Recherche directe de matière noire avec le détecteur à argon liquide DarkSide

Anyssa Navrer-Agasson

Anyssa Navrer-Agasson. Recherche directe de matière noire avec le détecteur à argon liquide DarkSide. Physics [physics]. Université Paris Cité, 2019. English. NNT : 2019UNIP7113 . tel-03093848

Université de Paris

École doctorale STEP'UP - ED 560
Laboratoire de Physique Nucléaire et des Hautes Énergies

Direct Dark Matter Search With the DarkSide Liquid Argon Detector

par

Anyssa Navrer-Agasson

Thèse de doctorat de Physique de l'Univers

présentée et soutenue publiquement le
1er Octobre 2019

Dirigée par **Claudio Giganti**

Devant un jury composé de :

Claudio Giganti Chargé de recherches (CNRS - APC)	Directeur de thèse
Antoine Kouchner Professeur (Université Paris Diderot)	Président du jury
Jocelyn Monroe Professeur (Royal Holloway)	Rapporteur
Anselmo Meregaglia Chargé de recherches (CNRS - CENBG)	Rapporteur
Corinne Augier Professeure (Université Claude Bernad Lyon 1)	Examinateur
Sandro De Cecco Professeur adjoint (Université de Rome)	Examinateur

Résumé en français

Mot-clefs : matière noire, argon liquide, chambre à projection temporelle, WIMPs, axions, reculs nucléaires, DarkSide, ARIS.

L'existence de la matière noire est connue en raison de ses effets gravitationnels et, bien que sa nature reste inconnue, un des candidats principaux est une particule massive interagissant faiblement (WIMP) ayant une masse de l'ordre de 100 GeV/c^2 et un couplage avec la matière ordinaire à ou en dessous de l'échelle faible. Dans ce contexte, DarkSide-50 cherche à observer des collisions WIMP-nucléon dans une chambre de projection temporelle à double phase d'argon liquide située dans le sous-sol du Laboratoire National du Gran Sasso (LNGS), en Italie.

Le travail présenté ici porte d'abord sur une étude de la réponse de l'argon aux reculs nucléaires et électroniques à basse énergie, réalisée par l'expérience ARIS. Le quenching nucléaire a été mesuré avec la meilleure précision à cette date et la probabilité de recombinaison a été comparée aux différents modèles décrivant le comportement de l'argon en présence d'un champ éléctrique.

Une recherche de WIMP de faible masse effectuée avec les données DarkSide-50 est également présentée. Cette recherche porte sur le signal d'ionisation du TPC, conduisant à un seuil de détection beaucoup plus bas qu'en utilisant la scintillation. Les limites d'exclusion atteintes figurent parmi les meilleures pour des masses de WIMPs entre 2 et 6 GeV/c2 et sont les plus strictes pour une cible d'argon liquide.

Enfin, une recherche préliminaire d'axions est discutée. Les axions sont un candidat alternatif à la matière noire, proposés comme solution au "problème CP fort". Ils sont détectables dans DarkSide via leur couplage aux électrons. Cette recherche nécessitait l'amélioration de la modélisation des sources de fond en prenant en compte les effets atomiques dans les spectres d'émission bêta, ainsi qu'une redéfinition de l'échelle d'énergie convertissant l'énergie déposée dans l'argon en un certain nombre d'électrons extraits. Les résultats présentés montrent une sensibilité encourageante aux axions solaires et galactiques.

English abstract

Keywords: dark matter, liquid argon, time projection chamber, WIMPs, axions, nuclear recoils, DarkSide, ARIS.

The existence of dark matter is known because of its gravitational effects, and although its nature remains undisclosed, one of the leading candidate is the weakly interacting massive particle (WIMP) with mass of the order of 100 GeV/c^2 and coupling with ordinary matter at or below the weak scale. In this context, DarkSide-50 aims to direct observe WIMP-nucleon collisions in a liquid argon dual phase time-projection chamber located deep underground at Gran Sasso National Laboratory, in Italy.

This work first details the argon calibration realised by the ARIS experiment. ARIS characterised the argon response to low energy nuclear and electronic recoils, down to unprecedented energies. The nuclear quenching was measured with the best precision to this date, and the recombination probability extracted was compared to different models describing the behaviour of argon in presence of an electric field.

A search for low mass WIMPs performed with DarkSide-50 data is also presented. This search focuses on the ionisation signal from the TPC, leading much to much lower detection threshold. The achieved exclusion limits are amongst the leading ones, and the most stringent for a liquid argon target.

Finally a preliminary search for axions is presented. Axions are an alternative candidate to dark matter, proposed as a solution to the strong CP problem. They are detectable in DarkSide via their coupling to electrons. This search required the improvement of the modelling of the background sources, by taking into account atomic effects in beta emission spectra, as well as a redefinition of the energy scale converting the energy deposited into a number of extracted electrons. The results presented show an encouraging sensitivity to both solar and galactic axions.

Contents

Acknowledgements

First of all, I would like to thank my PhD advisor, **Claudio Giganti**, for this unique opportunity. During the past three years, I discovered the thrilling field of dark matter search, joined a wonderful collaboration and learned how to perform a physics experiment. All this would not have been possible without him. I take this occasion to thank the DarkSide Collaboration for welcoming me into their ranks. I really enjoyed the relaxed atmosphere and the accessibility of the people.

Beside my advisor, I want to thank the members of my thesis committee: **Antoine Kouchner**, **Jocelyn Monroe**, **Anselmo Meregaglia**, **Corinne Augier** and **Sandro De Cecco**. I really appreciated your comments and questions during the defense, that lead to a very interesting discussion. I want to thank my two referees **Jocelyn Monroe** and **Anselmo Meregaglia**, for taking the time to review my work and for their insightful comments that helped improve my manuscript and opened new perspectives in my research.

I am also particularly grateful to you, **Sandro** ! My journey towards this thesis began when you took me as a master intern. Thank you for always caring about my studies and career, and for helping me to succeed as a master then PhD student.

Thank you **Davide** for always checking that I understood what I was doing and pointing the areas I needed to improve. You always pushed me to reflect upon my work and trained my scientific reasoning.

Alessandra, thank you for your availability to answer all my questions and for being present when I needed to talk.

I also want to thank you **Quentin** for the considerable amount of time you spent explaining me everything. You always had helpful tips about everything: coding, dealing with administraion, PhD life, ... For a new PhD it is really important to have someone to introduce them into the world of research, and you did that for me.

J'ai découvert le LPNHE en 2015 lors de mon stage de Master 1, et je n'ai plus voulu le quitter ! J'y ai passé trois années de thèse extraordinaires grâce à tous le personnel du labo. Merci notamment à **François, Véra** et **Aurélien** pour avoir ruiné à jamais le mot "pyrex" dans mon esprit. Je tiens aussi à remercier tous les doctorants du labo pour l'ambiance géniale qu'ils ont su créer.

Je tiens à remercier toute l'équipe de l'unité de physique du Palais de la Découverte. Devenir médiatrice là-bas était un rêve d'enfant (ma mère s'en souvient encore), et je vous suis reconnaissante de m'avoir permis de le réaliser. Cette mission fut réellement une expérience inoubliable.

Je n'oublie pas **Ludo, Aurélie** et **Véro** : merci pour votre coaching d'enfer lors de la Semaine des Jeunes Chercheurs. Les journées de formation rigolade ansi que la Semaine en elle-même furent parmi les meilleurs moments de ma thèse. Et grâce à vous trois fut formé le groupe de doctorants le plus fou du monde : les Anges du Palais, dodécacouple de l'extrême !

Merci **Miléna, Oriane, Mehdi, Nicolas, Caro, Lydie, Clémence, Greg, Audrey, Camille** et **Antoine** ! Merci pour les soirées, les storytime (je n'oublierai jamais la feuille de menthe) et autres karaokés mémorables. Cette thèse aurait beaucoup manqué de fun sans la TeamToujoursPlus. Et vous m'avez appris que TOUT VA BIEN SE PASSER !

Merci **Camille** pour... tout ! Il est dur de nouer de réelles amitiés et je ne pourrai jamais assez te remercier d'être là. La thèse aurait été bien plus dure à traverser sans mon photon.

Papa et **Maman**, c'est toujours le doctorant que l'on félicite, mais pour moi vous méritez tous les honneurs. Merci de vous être toujours pliés en quatre pour moi et de m'avoir fourni l'amour et le soutien dont j'ai toujours eu besoin. J'en suis là aujourd'hui grâce à vous, et aucun mots ne sauraient exprimer ma reconnaissance.

Enfin, merci à toi **Antoine** pour ton soutien et tes encouragements constants. Merci de toujours veiller sur moi, de toujours m'aider à m'améliorer et de me donner confiance en moi. Nous avons traversé la thèse ensemble et je sais que nous serons là l'un pour l'autres dans les aventures à venir.

Introduction

Everything we can see when looking at the Universe with our eyes, telescopes, and detectors accounts for barely 5% of its total energy content. The rest is divided between dark energy ($\sim$70%) and dark matter ($\sim$25%). This alone is a good reason to dedicate our minds to the study of the "dark universe". But there is more. Dark energy is the reason why the expansion of the Universe is accelerating. Uncovering its properties and nature would give us information about the future evolution of the cosmos. As for dark matter, according to the models of the early Universe, it played a key role in the formation of the structures (galaxies, galaxy clusters, etc). Contrary to what its name suggests, dark matter can shine light on the history of our Universe. This thesis focuses on the hunt for dark matter particles.

Dark matter has yet to be observed. However, astrophysical probes have provided constraints on its properties. We know that dark matter is stable, non-luminous, non-relativistic, and couples very weakly with Standard Model (SM) matter. We also have information about its distribution throughout the Universe. But other parameters like its mass are almost completely unconstrained. This leaves a lot of room for experiments to try and detect dark matter and many techniques have been developed to finally "see" dark matter.

The DM halo surrounding the Milky Way combined with the Earth motion within this halo makes possible DM-nucleon interaction, detectable with Earth-based detectors. This is the strategy of direct detection. Due to the very small energy deposited, it requires detectors with a very low threshold, large active masses, and strong background suppression.

Noble liquids are excellent materials for direct dark matter search, thanks to their high ionization and scintillation yields and their scalability to large masses. Noble liquid Time Projection Chambers (TPCs) is the leading technology in the range of high mass dark matter detection. These detectors rely on the detection of the scintillation and ionization light produced when a dark matter particle scatters off a nucleus (nuclear recoil). Liquid Argon (LAr) in particular offers an impressive background rejection method against electronic recoils (matter scattering off electrons in the target) based on the study of the pulse shape.

The DarkSide Collaboration developed a staged program of direct dark matter search using LAr TPCs. The current stage of the program, DarkSide-50, started running at Laboratori Nazionali del Gran Sasso (LNGS, in Italy) in October 2013 and produced its last physics results in 2018 [1, 2]. It is the first detector to used argon extracted from underground sources, greatly reducing its internal radioactivity.

Many dark matter candidates have been proposed. For a long time, the leading hypothesis has been the Weakly Interacting Massive Particle (WIMP). WIMPs are massive particles (GeV - TeV), that interact via weak interaction. However, while it remains strongly motivated, the lack of positive WIMP signal is pushing towards other interesting possibilities. In particular, less massive particles like axions appear as a more and more promising eventuality.

During my Ph.D., I have been involved in the characterization of the response of liquid argon to nuclear and electronic recoils, as well as the search for low mass dark matter in DarkSide-50.

- The first part of this thesis will focus on the motivations for dark matter as well as the technologies employed to detect it.
  - Chapter 1 will introduce the astrophysical observations that led to the hypothesis of dark matter. There is a significant number of astrophysical evidence for the existence of dark matter. Despite all this, dark matter still escapes detection. This chapter will also detail the different strategies developed to hunt dark matter.
  - Chapter 2 will present the DarkSide experiment. DarkSide uses a dual-phase LAr TPC, making use of the outstanding background rejection capabilities of LAr. The high mass WIMPs exclusion limits will be discussed in this chapter.
- The second part of the manuscript will describe the ARIS experiment of calibration of the argon response. ARIS (for Argon Response to Ionisation and Scintillation) was designed to characterise LAr response to nuclear recoils.
  - Chapter 3 will present the issue of the calibration of the argon response before introducing the ARIS experimental setup. The experiment consisted of a small scale dual-phase LAr TPC exposed to a highly collimated neutron beam, designed to measure parameters like the scintillation and ionisation energy scales, the nuclear quenching factor, the recombination probability, and the time response.
  - ARIS performed the lowest energy and most precise measurement of LAr response parameters. Data were acquired with and without an electric, allowing to study the nuclear recoil quenching and the recombination probability. The results obtained by ARIS will be discussed in Chapter 4
- Finally the last part will discuss low mass dark matter searches in DarkSide-50. A better understanding of the argon behavior, thanks to experiments like ARIS, opens new doors in the use of LAr TPCs.
  - Despite noble liquid detector being designed for high mass WIMPs searches, several recent attempts have been made to look for lower mass dark matter. DarkSide-50 is the first LAr based experiment to perform this kind of search. LAr proved to be extremely

performant in the low mass WIMPs search (~ 2 to ~ 10 GeV$\cdot c^{-2}$), providing better limits than other technologies and liquid Xenon experiments of the same mass scale [2]. This analysis id detailed in Chapter 5.

- Chapter 6 will be devoted to axion searches. Axions are one of the primary alternatives to WIMP dark matter. They have been postulated in response to the strong CP problem by Peccei and Quinn [3]. Several different axion models have been developed. In some of them, axions can couple to electrons, which would make them visible in DarkSide as electronic recoils. The framework of the low mass dark matter search of DarkSide can then be adapted to axion searches. It, however, requires some improvements in the background model that will be discussed. We will be interested in axions produced in the Sun, as well as cold galactic axions, that could be dark matter. I will also present preliminary results on the exclusion limits on the coupling of axions to electrons for both solar and galactic axions.

Part I

DarkSide, a tool for dark matter search

Chapter 1

The dark matter hypothesis

Contents

Nearly a century after the first signs of its existence were discovered in the 1930s, dark matter remains an enigma for the scientific community.

However, the existence of dark matter is stll hypothetical and there are many fundamental questions still to be answered, such as:

- What is the nature of dark matter?

- How was it produced?

- How does it interact with ordinary matter?

In order to close the debate on dark matter, an observation is necessary.

I will present different astrophysical observations supporting the dark matter hypothesis. Then, I will focus on two candidate particles for dark matter. And finally, I will detail the dark matter search strategies, with an emphasis on direct detection.

1.1 Evidence for dark matter existence: from local to cosmological scale

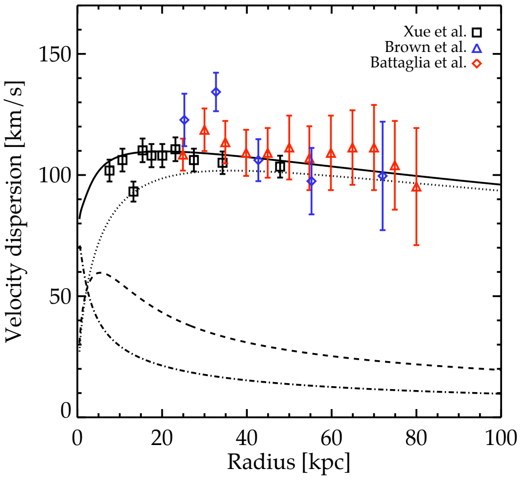

Figure 1.1 – Velocity dispersion of the stars in the Milky Way as a function of the distance from the galactic center [4] with the contributions from the bulge (dot-dashed), disk (dashed) and dark matter halo (dots). Measurements from [5, 6, 7]. The velocity dispersion of the dark matter halo is assumed isotropic.

1.1.1 Local scale: galactic rotation curves

The most well-known evidence of the existence of dark matter was revealed during the 1960s and 70s, in the work of Vera Rubin [8]. She studied the motion of the stars in spiral galaxies and compared it with the predictions from the theory of gravitation. Spiral galaxies typically consist of a central bulge with a high concentration of stars, surrounded by a disk containing gas, stars, and dust. The progress in telescope technologies made possible the measurement of the velocity of the galactic disk as a function of the radius. Such measurements usually rely on the Doppler shift of characteristic emission lines.

Since stars in galaxies are collision-less, their motion is entirely dictated by the laws of gravitation. This allows to predict the rotation velocity with respect to the orbiting radius. The expected velocity, v_c, for an object orbiting at radius r from the center of the galaxy is,

$$v_c(r) = \sqrt{\frac{GM(r)}{r}} \tag{1.1}$$

where G is the gravitational constant and $M(r)$ is the total mass enclosed in a sphere of radius r. For very large radii, far away from the central bulb, ($r \gg R_{bulge}$), the enclosed mass is approximately constant, so we expect the velocity to decrease as $v(r) \propto r^{-1/2}$, according to Equation 1.1. Rubin measured the rotation curves of different galaxies. But the observed rotation curves actually flatten for large radii, instead of decreasing. This study has been repeated in the Milky Way, yielding similar results [9, 4], as shown in Figure 1.1.

The straightforward explanation for such behavior is the addition of an ”invisible mass” in the form of a spherical halo surrounding the galaxies, increasing the gravitational potential. The study of the galactic rotation curves suggests that a dark matter density distributed as, $\rho(r) \propto r^{-2}$ allows to recover the correct curves. This corresponds to dark matter halo with a spherically symmetric distribution around the galactic center. There are still discussions about the dark matter halos density profiles.

1.1.2 Galaxy clusters

The first hint suggesting the existence of dark matter was given by Fritz Zwicky in the 1930s [10, 11]. He observed the velocity dispersion of the galaxies in the Coma cluster, containing over 1000 galaxies, and derived the mass of the cluster using two different methods. One was based on the virial theorem, starting from the measure of the velocities of the galaxies at the edge of the cluster. Since there must be enough gravity in the cluster to bind the edge galaxies, we can infer the mass that must be present. The second method relied on the luminosity of the objects in the cluster, estimating the mass from a counting of the objects that can be seen. The virial method leads to a much higher mass estimate than the luminosity method. To explain this phenomenon, Zwicky proposed the existence of a ”dark matter” in the cluster, a matter that could not be seen (thus escaping the luminosity count), but which gravitational influence was holding the galaxies together. His article made the term famous.

1.1.3 Gravitational lensing

Gravitational lensing provides an additional way to estimate the mass of an astrophysical object. According to general relativity, light that passes near a massive object is bent, due to the space-time perturbation caused by the object. The amount of bending depends on the mass of the object. Thus, the light emitted by faraway objects can be perturbed by this effect, which will distort the image we observe. It can result in multiple observed images (strong lensing), or a deformed image (weak lensing) [13]. Studying the deformation allows us to reconstruct the mass of the object inducing it. In many occurrences, the reconstructed mass is higher than the luminous mass, suggesting the presence of dark matter.

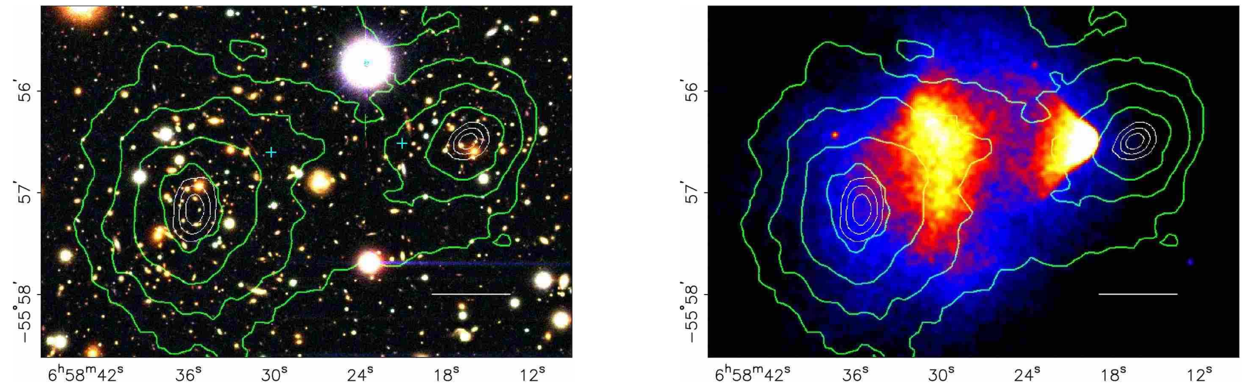

Figure 1.2 – Bullet cluster seen in the visible range by the Magellan telescope (left panel) and in X-rays by the Chandra satellite (right panel). On both pictures, the gravitational potential contours, calculated using the gravitational lensing, are drawn in green. Figure extracted from [12]

.

Lensing can also be applied to collisions of galactic clusters. In some cases, it indicates that the gravitational centers of the colliding objects do not correspond to the ones associated with ordinary matter, as in the famous example of the Bullet cluster(1E0657-56) [12]. The Bullet cluster consists of a pair of galactic clusters that have collided with each other. Since the mass of these clusters is dominated by interstellar gas and stars, optical techniques such as X-ray photography can be used to track the center of mass of the baryonic matter in both galaxies. Measurements of gravitational lensing caused by these galaxies can provide an independent measure of the center of mass of all matter (dark and baryonic alike) in each galaxy. As shown in Figure 1.2, results from optical techniques and gravitational lensing techniques significantly differ from each other, implying that the center of mass of baryonic matter differs from the total center of mass. The mass estimates from lensing techniques match those obtained with the virial theorem, rather than with the luminosity method.

Gravitational lensing also allows to pose upper limits on dark matter self-interaction, thanks to detailed hydrodynamical simulations and theoretical models [14],

$$\frac{\sigma_{\chi\chi}}{m_\chi} < 1{,}25\,\mathrm{cm}^2\cdot\mathrm{g}^{-1} \tag{1.2}$$

where $\sigma_{\chi\chi}$ is the dark matter self-interaction cross-section and m_χ is the dark matter particle mass. This result is in agreement with other measurements like in [15].

1.1.4 Cosmological parameters

To discuss dark matter at the cosmological scale, I will first present the current status of our understanding of our cosmological history.

1.1.4.1 The standard model of cosmology

The current standard model is called the Lambda Cold Dark Matter Model (Λ-CDM). The name reflects the fact that, in this parametrisation, the energy density of the Universe is dominated by dark energy (the Λ part) and dark matter. It describes remarkably well the formation of the large scale structures of the Universe. At small scales, matter is distributed very irregularly, being accumulated in galaxies, or galaxy clusters, leaving large areas of under-densities. However, if we consider the Universe in its larger scales, we observe that matter tends to be homogeneously and isotropically distributed.

Λ-CDM divides the total energy density of the Universe, ρ_T in three components [16]:

$$\rho_T = \rho_m + \rho_r + \rho_\Lambda \tag{1.3}$$

where ρ_m is the matter density, ρ_r is the radiation density and ρ_Λ represents the dark energy density. The matter density can be seen as the sum of a baryonic and non-baryonic contributions : $\rho_m = \rho_b + \rho_{nb}$. The radiation density ρ_m includes all relativistic components (photons, neutrinos, etc). The dark energy density, ρ_Λ has been introduced to explain the acceleration of the expansion of the Universe [17, 18].

Those quantities are usually normalised using the total density parameter $\Omega = \sum \Omega_i$, where $\Omega_i = \rho_i/\rho_c$, $i = m, r, \Lambda$. ρ_c is the so-called critical density, the density required for a flat, homogeneous and isotropic Universe.

The Λ-CDM model has 6 free parameters that are constrained by astrophysical probes.

1.1.4.2 Cosmic Microwave Background

Shortly after the Big Bang, the Universe was in such a hot and dense state that photons could not travel far before interacting with other particles. This lead to a period where the Universe was largely opaque. As the Universe expanded and cooled down, various forms of matter began to ”freeze out” as the available energy density dropped below the chemical potential needed to further create and destroy that form of matter.

Roughly 380,000 years after the Big Bang, the temperature of the Universe allowed the formation of the first hydrogen atoms, and the Universe became transparent to radiation, resulting in a fossil photon emission. This is the matter-radiation decoupling. The relic photons formed what is known as the Cosmic Microwave Background (CMB), and can still be observed today. The first measurements showing the existence of the CMB have been realised by Penzias and Wilson [20], as simple noise from an antenna. Since then several satellites have surveyed the CMB and its black body emission has been fitted at 2.276 ± 0.010 K(at 95% C.L.) [21]. A picture of the temperature map of the CMB as produced by Planck [19] is shown in Figure 1.3.

While the CMB is mostly isotropic, showing that the Universe is largely homogeneous, small anisotropies (∼ 10 µK [22]) are driven almost entirely by the temperature fluctuations in the early Universe that were caused by the under-densities and over-densities in different regions as particles

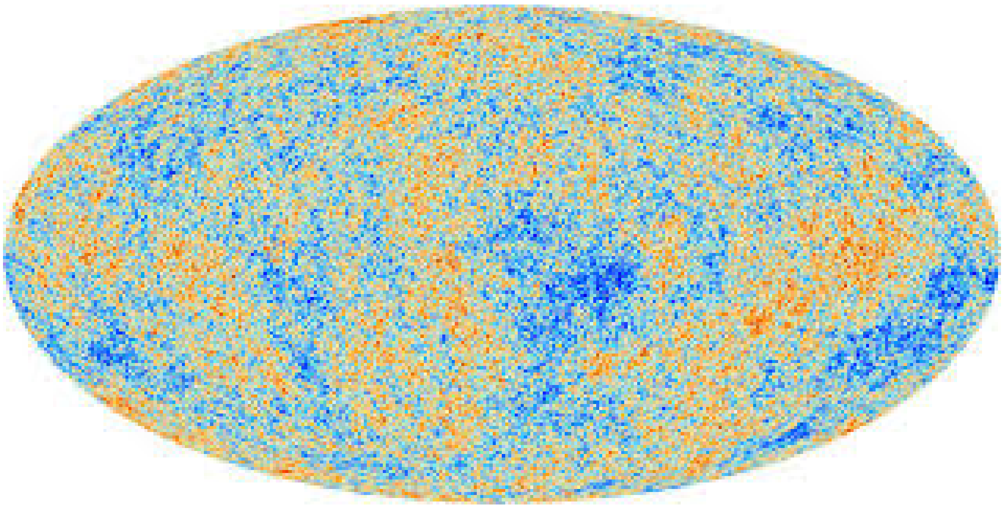

Figure 1.3 – Cosmic Microwave Background as measured by PLANCK [19].

began to freeze out at different times. The intensity and size of these fluctuations depend entirely on the particle physics that was happening at this time, making the CMB a very powerful probe into the fundamental properties of different species of particles. Baryonic matter couples to photons substantially more strongly than dark matter does. This means that while fluctuations in baryonic density in the over-dense and under-dense regions of the early Universe drive anisotropies in the CMB, fluctuations in the presence of dark matter have a much weaker effect. Planck measured the CMB anisotropies to remarkable precision, and thus was able to constrain the cosmological density parameters [22] by fitting the CMB power spectrum. Complementary observations are required to break the degeneracy between Ω_Λ and Ω_m.

1.1.4.3 Baryon acoustic oscillations

In the primordial plasma, over-density zones appeared, due to the presence of matter. Before the matter-radiation decoupling, acoustic waves were propagating in the plasma, causing the over-densities to oscillate between gravitational collapse and escape due to radiation pressure. These oscillations are referred to as Baryon Acoustic Oscillations (BAOs). BAOs left a trace that should be found in the distribution of galaxies throughout the Universe. By measuring the matter distribution, the Sloan Digital Sky Survey (SDSS) showed the existence of BAOs [23, 24]. The identification and the fit of the acoustic peaks provide an independent measurement of the Ω_m and Ω_λ parameters.

1.1.4.4 Type Ia supernovae

Type Ia supernovae (SNe Ia) are used as ”standard candles”. Since the physical parameters of the explosion of SNe Ia are always close, the luminosity curve of the supernovas is approximately the same and well-calibrated: their occurrence makes it possible to accurately evaluate their distance and, consequently, that of their host galaxy [25].

Hubble constant H_0 is the proportionality coefficient between the recessional velocity[1] and the

---

[1] The rate at which an astronomical object is moving away.

proper distance of an astrophysical object.

Thus, measuring the distance and redshift of SNe Ia allows us to precisely obtain Hubble's constant [26].

$$H_0 = 100h = 73.52 \pm 1.62 \text{ km}\cdot\text{s}^{-1}\cdot\text{Mpc}^{-1} \tag{1.4}$$

where $h \equiv H_0/(100 \text{ km}\cdot\text{s}^{-1}\cdot\text{Mpc}^{-1})$ is the reduced Hubble constant. This value is in tension with Planck's independent measurement [22]. The origin of this discrepancy is still in discussion to this day.

Fitting SNe Ia data allows to constrain the ratio between the matter and dark energy density as reported in [27]. They found $\Omega_m = 0.295 \pm 0.034(\text{stat+sym})$. Combining the SNe Ia data with the CMB data, it is possible to constrain the baryonic contribution to Ω_m.

1.1.5 Baryon density: the Big Bang nucleosynthesis (BBN)

All the known matter in the Universe is essentially in the form of baryons. So, we can naturally wonder if the dark matter is not actually made of "hidden" baryons. The answer can be found in the cosmological parameters. Indeed, it is possible to constrain both the total matter density and baryon density in the Universe. If the numbers are not matching, it will mean that there is non-baryonic matter present.

There are several ways to measure the baryon density, Ω_b. Big-Bang nucleosynthesis (BBN) offers the deepest reliable probe of the early Universe, being based on well-understood Standard Model physics. Measuring the abundance of light elements like D, ^{3}He, ^{4}He and ^{7}Li allows to constrain the baryon to photon ratio, and thus, to have information about Ω_b.

The production of light elements is highly sensitive to the physical conditions in the Universe during the radiation era. While the temperature T of the Universe was higher than $\sim$ 1 MeV, protons and neutrons are at thermal equilibrium and the proton to neutron density is given by

$$\frac{n}{p} = e^{-Q/T} \tag{1.5}$$

where $Q = 1.293$ MeV is the mass difference between protons and neutrons. When the temperature decreases, the neutron-proton conversion rate diminishes more rapidly than the Hubble expansion rate. At the freeze-out temperature, $T_{fr} \sim 1$ MeV, the neutron to proton ration becomes constant, fixed at $n/p = e^{-Q/T_{fr}} = 1/6$. Neutrons are then free to decay until nuclear reactions can take place and the nucleosynthesis starts. At that moment, $n/p \simeq 1/7$.

The nuclei formation starts with deuterium production via $p(n,\gamma)D$ reaction. However, photodissociation prevents the production of deuterium until well after T drops below the binding energy of deuterium. Then, heavier elements like ^{3}He, ^{4}He and ^{7}Li are produced similarly. The rate of the nuclear reactions involved depends directly on the baryon density, n_b. We can use measurements of abundance ratios of different elements, like D/H or Li/H to constrain the baryon density.

BBN is the only significant source of deuterium, which is entirely destroyed when it is cycled

Component	Symbol	Measured density
Photons	Ω_r	$\sim 5.46 \times 10^{-5}$
Dark Energy	Ω_Λ	0.6911 ± 0.0062
Matter	Ω_m	0.3089 ± 0.0062
Baryonic matter	Ω_b	0.0486 ± 0.00072
Non-baryonic matter	Ω_c	0.2589 ± 0.0041

Table 1.1 – Measurements of the cosmological parameters, obtained from the Planck CMB measurements [22], combined with BAOs and supernovae. These results are obtained assuming the Λ-CDM model with six free parameters and a flat Universe

into stars [28]. Thus, any detection provides a lower limit on the primordial D/H and the baryon density. D/H has been measured in [29], and translates into a limit on the baryon density fraction Ω_b,

$$0.021 \leq \Omega_b h^2 \leq 0.024 \ (95\% \ C.L.) \tag{1.6}$$

This result is consistent with Planck's measure of Ω_b. Given that $\Omega_m \sim 0.3$ [22], we can deduce that most matter in the Universe is non-baryonic.

1.2 Dark matter halo

The calculation of the DM event rate will require the expression of the velocity distribution of the DM particles. Let us then get interested in the different modelisations of the dark matter distribution. The geometry and velocity distribution in the dark matter halo are unknown. However, it is possible to model the halo of dark matter either by solving the Boltzmann equation or by Monte-Carlo simulation.

1.2.1 Modeling the dark matter halo

The dark matter halo can be considered as a self-gravitating gas of non-collisional particles. Its distribution $f(\mathbf{r}, \mathbf{v}, t)$ then follows the Boltzmann equation [30],

$$\frac{\partial f}{\partial t} + \mathbf{v} \cdot \nabla f - \nabla \phi \cdot \frac{\partial f}{\partial \mathbf{v}} = 0 \tag{1.7}$$

where ϕ is the gravitational potential. Since a detector would have a small volume compared to the halo, it would only be sensitive to the local velocity distribution

$$f(\mathbf{v}) = \frac{1}{V} \int f(\mathbf{r}, \mathbf{v}, t_0) d^3 r \tag{1.8}$$

where t_0 is the current time. Furthermore, the dark matter density $\rho(\mathbf{r})$, the gravitational potential and the dark matter distribution are linked by the Poisson equation,

$$\nabla^2 \phi = 4\pi G \rho(\mathbf{r}) = 4\pi G \int f(\mathbf{r}, \mathbf{v}, t_0) d^3 r \tag{1.9}$$

1.2.2 Standard halo model

As discussed in Section 1.1.1, a spherical dark matter density distributed as $\rho(r) \propto r^{-2}$ allows to recover flat rotation curves. The velocity distribution can then simply be expressed as a Maxwell-Boltzmann distribution,

$$f(\mathbf{v}) = \frac{1}{(3\pi\sigma_v)^{1/2}} exp\left(-\frac{\mathbf{v}^2}{2\sigma_v^2}\right) \tag{1.10}$$

where σ_v is the velocity dispersion of the particles in the halo.

The Standard Halo Model (SHM) assumes the distibution of Equation 1.10, as well as the following characterictics:

- **Static halo:** The DM halo is often considered static. There is no definitive proof of this assumption, but it is coherent with the non-collisional nature of DM particles. N-body simulations [31] also confirm this hypothesis.

- **Local dark matter density:** A value of $\rho_0 = 0.3$ GeV$\cdot c^{-2}\cdot$cm^{-3} is usually adopted [32].

- **Solar system velocity:** The Sun is orbiting towards the Cygnus constellation at a speed $v_\odot = 220 \pm 20$ km$\cdot$s^{-1}. This is the traditional value, that is still in use for the analysis of experimental results. However, the current standard value is $v_\odot = 254 \pm 16$ km$\cdot$s^{-1} [33], for a distance $R_0 = 8.4 \pm 0.6$ kpc.

- **Velocity dispersion in the halo:** The model considers $\sigma_v = v_\odot/\sqrt{2} \approx 270$ km$\cdot$s^{-1}. The velocity dispersion is related to the solar system velocity. The local circular speed and the peak speed are also considered identical [34].

- **Escape velocity:** The escape velocity corresponds to the maximal speed of a DM particle gravitationally linked to the halo. In the framework of the SHM, it is common to consider $v_{esc} \lesssim \infty$. However, the RAVE collaboration determined a 90% C.L. interval for v_{esc} with a median value at $v_{esc} = 544$ km$\cdot$s^{-1} [35].

1.3 Dark matter non-baryonic candidates

Baryonic particles have been ruled out as the main component of the dark matter. Besides, the Standard Model of particle physics is known to have some inconsistencies, like the strong CP violation, or the Higgs boson mass, that prove it is incomplete. Therefore, it is straightforward to resort to new, Beyond Standard Model (BSM) theories. Those theories often naturally introduce new particles with characteristics in agreement with dark matter requirements.

In this section, I will present two dark matter candidates motivated by BSM theories: WIMPs and axions.

1.3.1 Weakly Interacting Massive Particles

Among all the dark matter candidates, the Weakly Interacting Massive Particle (WIMP) is the most extensively researched at the moment. WIMPs are hypothetical elementary particles, interacting only through gravity and weak nuclear force. The weak interaction makes them detectable through non-gravitational methods. The introduction of a new particle with mass at the weak scale (m_{weak} $\sim$10 GeV - 1 TeV) would justify the mass of the Higgs boson to be smaller than the Planck mass [36] (solving the so-called gauge hierarchy problem), giving it another motivation.

1.3.1.1 Supersymmetry and extra dimensions

Particles with the characteristics of a WIMP naturally arise in several beyond Standard Model (BSM) theories, like supersymmetry (SUSY) or models with extra dimensions.

SUSY [37] was proposed to solve the gauge hierarchy problem and to allow the unification of the strong, weak and electromagnetic couplings at high energy. It introduces a supersymmetric partner to all SM fermions and bosons. Fermions have boson super-partner and vice-versa. The symmetry must be broken, otherwise, the SM particle and their partners would have the same mass. A new parity, the R parity is introduced:

$$R = (-1)^{3(B-L)+2S} \tag{1.11}$$

where B and L are the baryonic and leptonic number, and S, the spin. $R = 1$ for SM particles and $R = -1$ for their super-partners. The conservation of this number prevents a super-symmetric particle to decay into SM products, implying that the lightest SUSY particle (LSP) is stable. In fact in much of SUSY parameter space, the neutralino - an electrically neutral, weakly interacting, and colorless particle - is taken to be the LSP, with a mass of a few hundred GeV/c^2 [38].

Another possibility is models with extra-dimensions [39]. They were proposed in the 1920s to unify electromagnetism with gravity. They add n extra spatial dimensions to the classical (3+1) space-time dimensions. Among the particles proffered by models of extra-dimensions, the stable lightest Kaluza particle (LKP) is often considered a good WIMP candidate.

1.3.1.2 Dark Matter relic density: the WIMP miracle

In the first moments of the Universe, all the particles, including dark matter, are at thermal equilibrium (the annihilation rate is equal to the production rate):

$$\chi + \bar{\chi} \leftrightharpoons X + \bar{X}$$

As the Universe expands, it also cools down, thus decreasing the kinetic energy of its particles. When the temperature T drops below the dark matter particle mass m_χ, the X particles energy becomes too low to lead to the production of χ, it is the chemical decoupling. The number of dark matter particles then decreases exponentially as $e^{-m_\chi/T}$. The dark matter gas dilutes in the growing Universe, to the point that the annihilation rate becomes negligible. The time evolution of

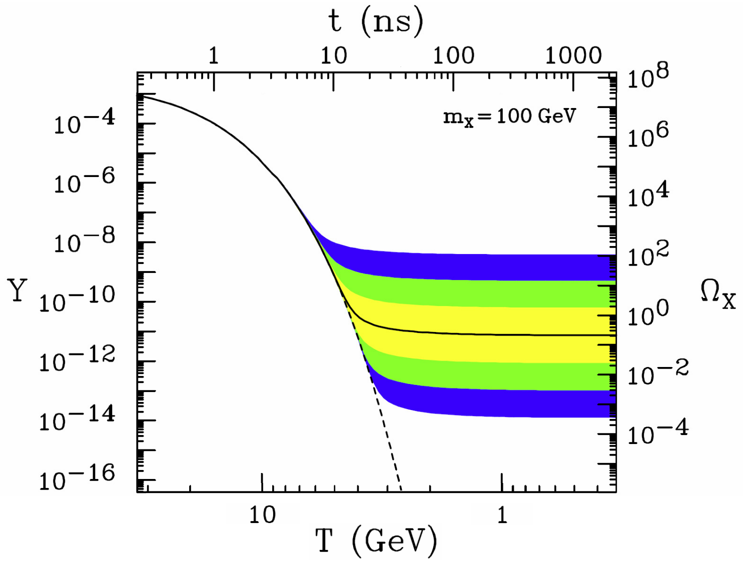

Figure 1.4 – Comoving density Y (left) and the resulting relic density Ω_χ (right) for a 100 GeV WIMP as a function of temperature T (bottom) and time t(top). The solid contour corresponds to the annihilation cross-section which leads to the correct relic density. Color regions are for cross sections that differ 10, 100 and 1000 times from this value. Picture extracted from [36]

.

the dark matter number density n in the Universe is then described by the Boltzmann equation :

$$\frac{dn}{dt} = -3Hn - \langle \sigma_A v \rangle (n^2 - n_{eq}^2) \tag{1.12}$$

where H[1] is the Hubble expansion rate of the Universe, $\langle \sigma_A v \rangle$ represents the DM effective annihilation cross section and n_{eq} is the DM density at the equilibrium. We note that the evolution of density depends on the competition between the expansion of the Universe and the DM annihilation cross-section.

If the annihilation rate is higher than the expansion rate, the DM density will drastically drop. However, if the annihilation rate is lower than the expansion rate, the annihilation stops and the density will be asymptotically constant. The density is then decoupled from the rest of the Universe. This process (the freeze-out) leads to a relic density that is directly linked to the annihilation cross-section. We can roughly define the freeze-out time to be the time when $n \langle \sigma_A v \rangle = H$ [36]. Solving this equation gives us the relic density at freeze-out,

$$n_f \sim (m_\chi T_f)^{3/2} exp(-\frac{m_\chi}{T_f}) \sim \frac{T_f^2}{M_{Pl} \langle \sigma_A v \rangle} \tag{1.13}$$

where T_f is the temperature at freeze-out and M_{Pl} the Planck mass. The thermal relic density in the current Universe can be written,

$$\Omega_\chi h^2 = \frac{m_\chi n_0}{\rho_c} = \frac{m_\chi T_0^3}{\rho_c} \frac{n_0}{T_0^3} \tag{1.14}$$

---

[1] $H = \dot{a}/a$, where $a(t)$ is the scale factor for a distance $d(t)$ with respect to its value at the Big Bang d_0: $d(t) = a(t) d_0$

where h is the reduced Hubble constant, and n_0 and T_0 are the present-day number density and temperature.

In an iso-entropic Universe, $aT \sim$ const so,

$$\frac{n_0}{T_0^3} \sim \frac{n_f}{T_f^3}$$

and we have

$$\Omega_\chi h^2 \simeq \frac{m_\chi T_0^3}{\rho_c} \frac{n_f}{T_f^3} \sim \frac{x_f T_0^3}{\rho_c M_{Pl}} \langle \sigma_A v \rangle^{-1} \tag{1.15}$$

This expression is independent of the mass of the dark matter particle. Figure 1.4 illustrates the evolution of the dark matter density.

From measurements of the CMB (see Table 1.1), we can derive a typical value for the annihilation cross-section.

$$\langle \sigma_A v \rangle \simeq \frac{3 \times 10^{-27}\ \mathrm{cm}^3{\cdot}\mathrm{s}^{-1}}{\Omega_\chi h^2} \simeq 2.5 \times 10^{-26}\ \mathrm{cm}^3{\cdot}\mathrm{s}^{-1} \tag{1.16}$$

The ”miracle” resides in the fact that this typical value is extremely close to the typical weak cross-section.

$$< \sigma_W > \simeq \frac{\alpha_{weak}^2}{m_W^2} \simeq 1.5 \times 10^{-26}\ \mathrm{cm}^3{\cdot}\mathrm{s}^{-1} \tag{1.17}$$

where $\alpha_{weak} \simeq 0.01$ is the coupling contant of the weak interaction and m_W the W boson mass. Thus, a Big Bang relic population of weakly interacting DM particles with masses in the GeV - TeV range, would naturally have the right present density, providing a strong motivation for WIMP dark matter.

1.3.2 Axions and axion-like particles

As the parameter space for WIMP searches starts to be more and more excluded, dark matter search turns to alternative candidates. An interesting one is the axion. One major weakness of the Standard Model is the absence of a mechanism to explain the lack of charge-parity (CP) violation in strong interactions. A solution, introduced by Peccei and Quinn [3], postulates an additional symmetry that is broken at some large energy scale f_a. This results in a new particle called the axion. This original axion has been ruled out by experimental results, but axions arising from symmetry-breaking at a much higher scale, the ”invisible” axions are still allowed [40]. In addition to QCD axions, axion-like particles (ALPs) are pseudo-scalars that do not necessarily solve the strong CP problem but have been introduced by many string-theory driven BSM models [41, 42, 43].

Both axions and ALPs make interesting candidates for dark matter. They may have been produced as a non-thermal relic by the misalignment mechanism [44], and while very light, are predicted to be produced essentially at rest, thus satisfying the criteria for cold dark matter. More details about axions and ALPs (theory and detection) will be given in Chapter 6.

1.4 WIMP detection strategies

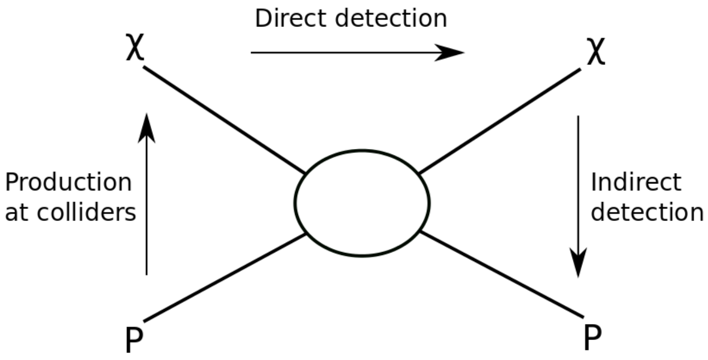

Figure 1.5 – Schematic description of the different dark matter detection strategies.

Dark matter can potentially interact with any known particle, or with a dark sector. Thus, there are several ways to detect it. Figure 1.5 illustrates the different types of interaction between dark matter and ordinary matter. All these methods give access to different information and explore different parameter spaces, therefore they are complementary to ensure a certain detection and identification of dark matter particles. In order to fully characterize dark matter, we then need a balanced program based on all the different detection techniques.

1.4.1 Indirect detection

Reading figure 1.5 from top to bottom, we obtain the annihilation of dark matter particles, which leads to indirect detection. Indirect detection uses astronomical observations to detect annihilation products of dark matter. There are actually two processes to consider :

- the pair annihilation of dark matter particles : $\chi + \chi \longrightarrow SM$
- the decay of dark matter particles into SM particles : $\chi \longrightarrow SM$

The searches usually focuses on three of these possible products photons (γ and X), neutrinos, and anti-matter [45]. Telescopes look for an excess of these particles coming from a region where a high density of dark matter is expected, as the center of the Milky Way, or the center of the Sun.

The γ and X astronomy give the cleanest signatures since the photons will be weakly disturbed during their propagation into the interstellar medium. The spectrum of the emitted photons is given by the DM annihilation model. There are two different possible channels. First, if the photons are directly emitted by dark matter annihilation, there will be a peak at $E_\gamma = m_\chi$. This channel is often referred to as ”smoking gun” thanks to its easily recognizable signature. Second, if the photons are emitted by the disintegration of the products of the annihilation, the photon spectrum will present an increasing distribution with an end-point energy depending on the dark matter particle mass. Photons can be detected by imaging atmospheric Cherenkov telescopes (MAGIC [46], H.E.S.S. [47], and VERITAS [48]) or by satellite-based experiments (Fermi-LAT [49]). So far no significant signal from DM annihilation has been observed [45], leading to strict upper limits on the DM annihilation cross section [49, 47].

In the case of a DM particle decay, the photon spectrum will present a peak at $E_\gamma = m_\chi/2$. This approach allows us to pose a limit on the WIMP lifetime. FERMI-LAT [49] posed a limit for the WIMP lifetime between 4×10^{28} and 3×10^{29} s for a WIMP mass between 14 and 400 GeV. MAGIC [50] also derived a DM lifetime $\gtrsim 10^{26}$ s.

Neutrinos are a complementary probe to photons for dark matter searches. Since they interact very weakly, they can travel from their source without any perturbation along the way. WIMPs can gravitationally accumulate in large astrophysical objects (e.g. stars, galaxies, dwarf spheroidals, and the Sun), resulting in an enhancement of the local DM density and therefore an enhancement in the rate of self-annihilation/scattering, or decay. Among decay products, muon neutrinos can be produced and interact in the Earth. Taking into account the neutrino oscillation, detection efficiency and assuming a certain annihilation spectrum, it is possible to compute an expected neutrino spectrum from WIMP annihilation [51]. Neutrino telescopes such as SuperKamiokande [52] and IceCube [53], can then measure the neutrino flux via the reaction: $\nu_\mu + X \rightarrow \mu + X$, providing limits on WIMP annihilation into b-meson, τ and W pairs.

WIMPs can also annihilate into charged particles such as protons, anti-protons, electrons, and positrons which can be detected by satellites as PAMELA [54] and AMS-02 [55, 56]. Excesses in the flux of these particles have been detected but can be concealed by the activity of astrophysical objects like pulsars or secondary production due to cosmic ray collisions with the interstellar medium [57]. Hence these excesses cannot be considered as a clear indication of DM.

1.4.2 Dark matter production at colliders

Particle colliders such as the LHC at CERN are also very useful tools to look for dark matter [58]. SUSY and extra-dimension can both be tested at LHC. To this day, no signs of these theories have been found in LHC. See [40] for reviews about SUSY and extra-dimensions searches at LHC.

Dark matter may also be produced in high-energy particle collisions, arising from proton-proton collision via the fusion of two quarks. DM particles are likely to pass through the detector without leaving a trace. Therefore a large energy imbalance observed in the plane transverse to the colliding proton beams, known as missing transverse momentum, can be a signature of DM. However, it is possible that, in the initial state, one of the quark radiates a photon or a gluon. We can then look for DM particles in events with a mono-photon or mono-jet associated with lar missing energy. Because backgrounds are typically smaller for larger values of missing momentum, collider searches tend to be most effective for low-mass dark matter particles, which are more easily produced with high momentum. Using effective field theories, it is possible to constrain the coupling constants of the effective operators describing the interaction [59]. However, a direct comparison of these experimental results to other detection methods is, in general, model dependent. Figure 1.6 shows the comparison of LHC spin-independent limits to results from direct detection experiments.

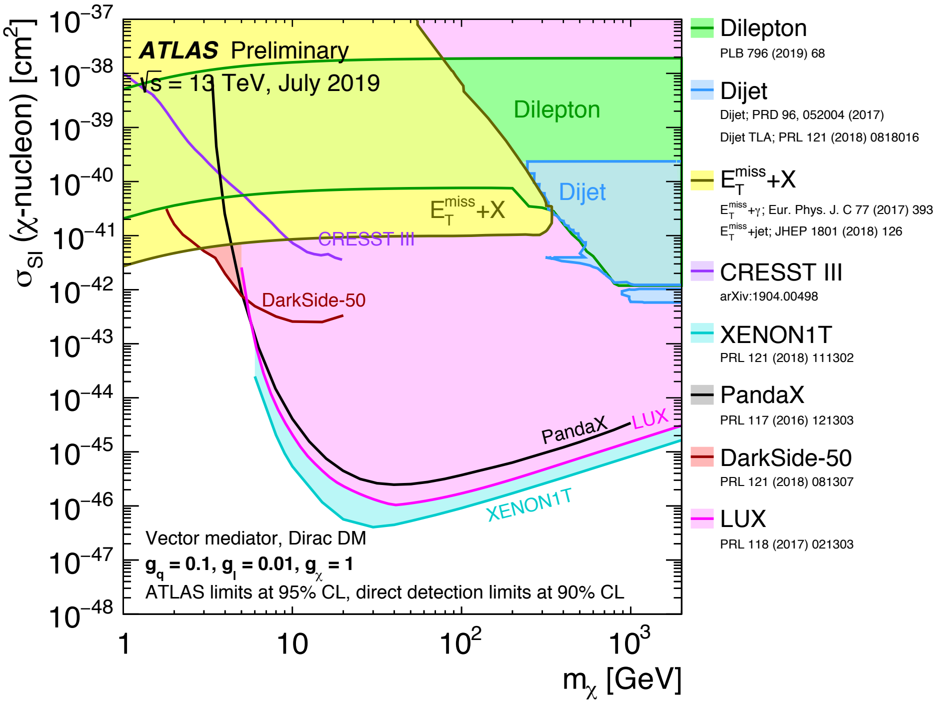

Figure 1.6 – Comparison of the LHC limits on spin-independent WIMP-nucleon cross-section with diect detection experiments. LHC limits are shown at 95% CL and direct-detection limits at 90% CL. The model considered in this plot assumes a DM coupling $g_\chi = 1$, quark coupling $g_q = 0.1$, and lepton coupling $g_l = 0.01$. LHC searches and direct-detection experiments exclude the shaded areas. Exclusions of smaller scattering cross-sections do not imply that larger scattering cross-sections are also excluded. Figure extracted from [60].

1.5 Direct detection of WIMPs

Since the galactic dark matter is supposed to be distributed in a spherical halo, the motion of the Earth will cause a WIMP flux. Such flux would be detectable by measuring the energy spectrum of nuclear recoils caused by the elastic diffusion of WIMPs of target nuclei. Assuming a cross-section of 10^{-47} cm^2, we expect $\sim$ 1 events/ton/year in a noble liquid detctor The typical energy of the recoils is $\sim$ 100 keV. This requires very low energy threshold detectors and large target masses. This strategy has been proposed in 1985 by M.W. Goodman and E. Witten [61].

1.5.1 Event rate calculation

The event rate depends on the local density on WIMPs, $\frac{\rho_0}{m_\chi}$, the elastic WIMP-nucleon cross-section σ, the velocity of WIMPs in the lab frame, and the energy transferred during the collision.

In the lab frame, the WIMPs have a velocity of 330 km·s^{-1}. Thus, we can consider WIMPs as non-relativistic particles. We can then demonstrate that energy transferred to the nucleus during an elastic scattering is expressed, in the center-of-mass frame, as following,

$$E_R = \frac{q^2}{2m_N} = \frac{\mu_N^2}{m_N} v(1 - cos(\theta_R)) \tag{1.18}$$

where q is the transferred energy, $\mu_R = m_\chi m_N/(m_\chi + m_N)$ is the reduced mass of the system, m_N is the mass of the nucleus, m_χ is the mass of the WIMP, v is the velocity of the WIMP and θ_R is the scattering angle of the WIMP.

From Eq. 1.18, we deduce the minimum velocity for a given E_R, corresponding to a backscattering,

$$v_{min} = \sqrt{\frac{m_N E_R}{2\mu_N^2}} \tag{1.19}$$

The WIMP events per unit mass of the detector can be written

$$\frac{dR}{dE_R} = \frac{\rho_0}{m_\chi m_N} \left\langle v \frac{d\sigma}{dE_R} \right\rangle \tag{1.20}$$

where ρ_0 is the local DM density, $d\sigma/dE_R$ and the term between brackets represents the average over DM velocities.

Writing explicitly the velocity average,

$$\frac{dR}{dE_R} = \frac{\rho_0}{m_\chi m_N} \int_{v_{min}}^{v_{esc}} \frac{d\sigma}{dE_R} v f(v) d^3 v \tag{1.21}$$

where $f(v)$ is the velocity distribution of the dark matter halo.

At a given velocity v, the differential recoil energy is

$$dE_R = \frac{\mu_N^2}{m_N} v^2 dcos(\theta_R) \tag{1.22}$$

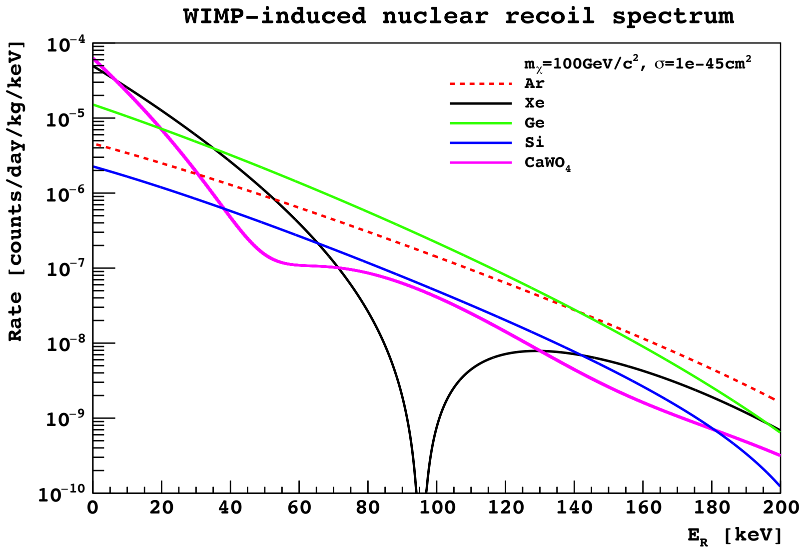

Figure 1.7 – Expected recoil energy spectrum, ER, for xenon (black), argon (red), germanium (green), silicon (blue) and CaWO$_4$ (magenta) targets assuming a WIMP with $m_\chi = 100$ GeV$\cdot c^{-2}$, $\sigma = 1045$ cm, and SHM parameters.

If we substitute Eq. 1.22 in Eq. 1.21, we get

$$\frac{dR}{dE_R} = \frac{\rho_0}{\mu^2 m_\chi} \int_{v_{min}}^{v_{esc}} \frac{d\sigma}{dcos(\theta_R)} \frac{f(v)}{v} d^3v \tag{1.23}$$

The cross-section σ can be expressed as

$$\sigma(q) = \sigma_0 F^2(q) \tag{1.24}$$

where σ_0 is the cross-section at zero momentum transfer and F(q) is the nuclear form factor.

The form factor is needed to describe the decrease of the effective total cross-section when the transferred momentum is such that the wavelength h/q becomes much smaller than the nucleus radius. On the contrary, the $_0$ factor takes into account all the dependence on the specific physics model. In general, both the zero momentum cross-section and the form factor differ for even and odd nuclei, because of the target nucleus spin. In general, the cross-section can be written as the sum of a spin-dependent and spin-independent part, each being associated with a form factor. If the target nucleus has spin different from 0, both the spin-dependent and spin-independent contributions must be taken into account when computing the WIMP-nucleus cross-section.

Figure 1.7 shows the WIMP event rate for different target materials, assuming $m_\chi = 100$ GeV^2 and standard SHM parameters.

1.5.2 Annual modulation

One of the possible signatures of a dark matter signal is the annual modulation. Because of the motion of the Earth around the Sun, the velocity of the observatory in the galactic reference system v_{obs} can be expressed as:

$$v_{obs(t)} = v_{Sun} + v_E[\hat{\epsilon}_1 cos\omega(t - t_1) + \hat{\epsilon}_2 cos\omega(t - t_1)] \tag{1.25}$$

where v_{Sun} is the Sun velocity, v_E is the orbital velocity of the Earth around the Sun, $\omega = 2\pi/\text{year}$ and t_1 the fraction of the year before the Spring equinox. The $\hat{\epsilon}_1$ and $\hat{\epsilon}_2$ are unitary vectors describing the direction of the Earth at the Spring equinox and the Summer solstice respectively in the galactic reference system. The time dependence of the v_{obs} magnitude can be written as:

$$v_{obs}(t) = \sqrt{v_{Sun}^2 + v_E^2 + 2bv_E v_{Sun} cos\omega(t - t_c)} \tag{1.26}$$

where b =0.49 is a geometrical factor, accounting for the different inclinations of the Earth orbit with respect to the Sun orbit plane and t_c is the time of the year at which v_{obs} is maximized. Since $v_{Sun} \gg v_E$, the above equation can be approximated by:

$$v_{obs}(t) \simeq v_{Sun}[1 + b\frac{v_E}{v_{Sun}} cos\omega(t - t_c)] \tag{1.27}$$

This few-% variation in the velocity of the Earth through the WIMP static halo implies a time-dependent change in the inverse mean speed, which reflects in a modulation of the event rate. The time-dependent event rate can be parametrized as the sum of a time-averaged component and a modulation one:

$$R(t) = R_0 + R_m(t) = R_0[1 + \chi_m(t)] \tag{1.28}$$

where $\chi_m(t) = R_m(t)/R_0$ is the magnitude of the relative modulation.

This few-% annual modulation represents a strong signature of a WIMP signal (if the background does not show the same behavior). Nonetheless, to be exploited, a large statistics data sample is required.

1.5.3 Directionality

Directional detection of WIMPs was proposed in 1988 by D. Spergel [62]. Given the assumed dark matter halo model and Solar System orbital velocity, there should be a preference for nuclear recoils appearing to come from the Cygnus constellation. The angular distribution of recoils will take the form of a dipole whose maximum is centered on the Cygnus constellation, as shown in Figure 1.8. This feature would be a way to go beyond the neutrino floor.

For a detector able to discriminate the direction of the recoil, the anisotropy in the angular distribution can be exploited to distinguish between DM events and background. The majority of the backgrounds are expected to be isotropic in the Galactic reference frame. A directional detector could make use of non-isotropic response scintillators or gaseous targets in an electric field. In the latter case, the amount of collected ionization charges depends on the inclination of the track with respect to the drift field. To improve the spatial resolution of the track, one can lower the pressure of the target, at the cost of a large sensitive mass (and thus exposure). The direction signal is

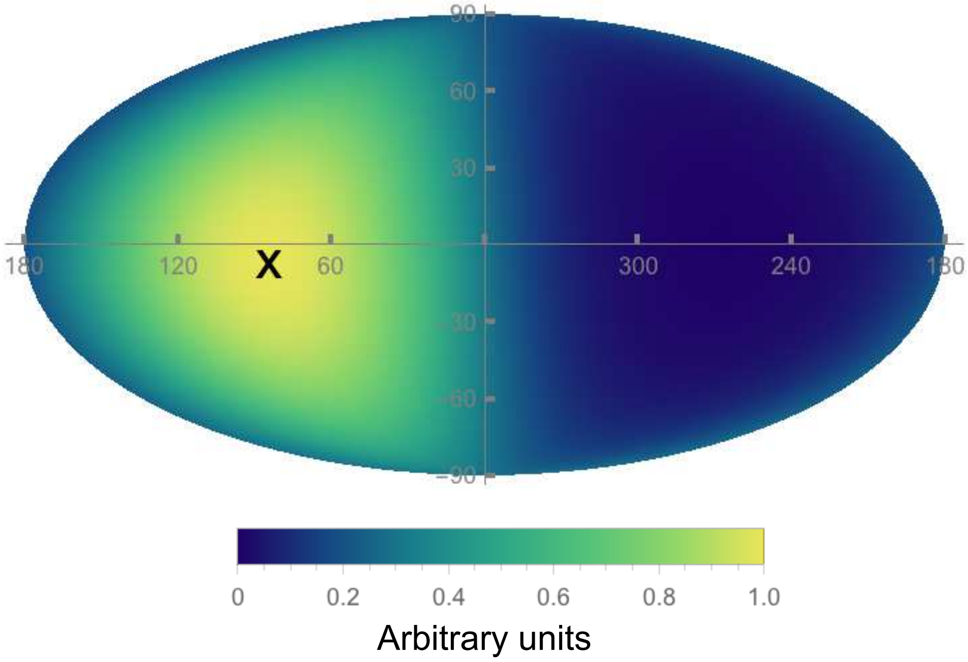

Figure 1.8 – Angular distribution of the energy differential recoil rate in F for WIMP mass 100 GeV, and recoil energy of 25 keV, plotted in galactic coordinates. Figure extracted from [63].

much larger than the one coming from the annual modulation (the back-scattering probability for an elastic collision is several times larger than the forward one).

1.5.4 Direct WIMP detection experiments

I will discuss here the different technologies used for direct dark matter search. Figure 1.9 shows the different signals that can be produced by WIMP-induced nuclear recoils and the detector technologies to observe them. Experiments are essentially looking into three channels: phonons, scintillation photons or ionisation of the target atoms. Most of the recent experiments collect signals from more than one channel.

Phonons In a crystal, recoiling nuclei or electrons deposit energy through collisions with nuclei and electrons in the crystal lattice. Phonon excitations matrix arise as the multiple collisions convert the kinetic energy into collective excitation of the crystal. When the phonon distribution thermalise, it is possible to measure the temperature increase of the material. These kind of detectors are usually bolometers, which permits very low thresholds and excellent energy resolution. The SuperCDMS [64], CRESST [65, 66] and EDELWEISS [67] detectors are observing phonons signals.

Scintillation In a scintillator, a fraction of the incident particle energy is transferred through excitation of the atoms of the medium. The de-excitation produces photons with a characteristic

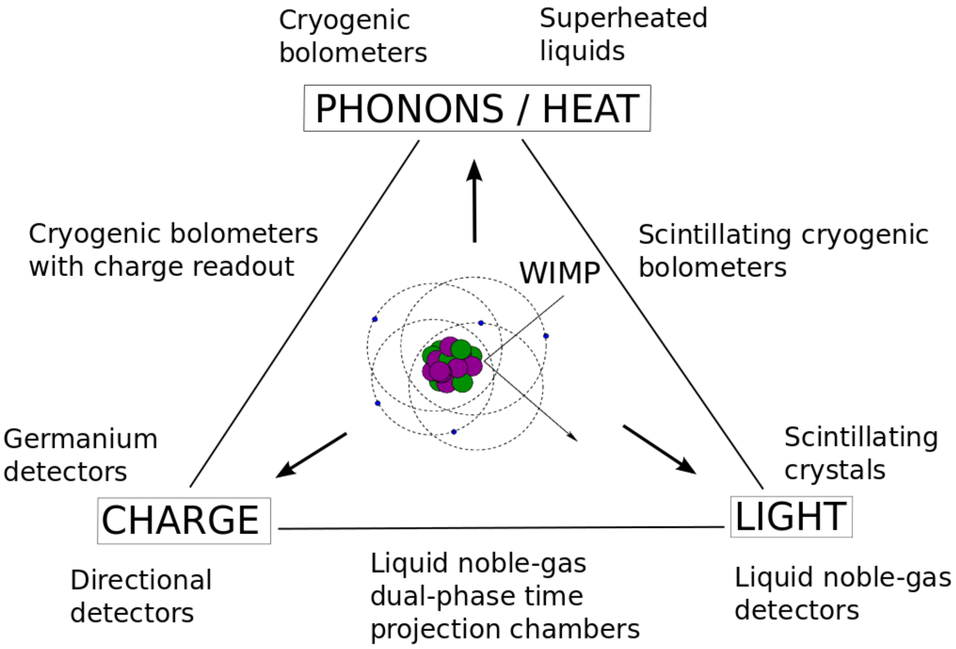

Figure 1.9 – Schematic of possible signals that can be measured in direct detection experiments depending on the technology in use.

decay time and wavelength. The amount of scintillation photons produced depends on the deposited energy, so the energy can be reconstructed from the collected light. There are several scintillators in use in direct dark matter searches, like scintillating crystals and noble liquids. Scintillating crystals benefit from an attractive combination of low target costs and existing well-understood technologies for light collection and detection over wide areas. In noble gases, the time. The DarkSide (see Chapter 2), LUX [68], DEAP [69], XENON [70] and PandaX [71] detectors chose noble liquids as scintillators, DAMA/LIBRA [72] uses sodium iodine (NaI), CRESST [65, 66] relies on calcium tungstate crystals ($CaWO_4$).

Ionisation The last type of signal that can be collected is ionisation. If enough energy is transferred to an atomic electron, the atom will ionise and the liberated electrons and ions can be collected using a strong electric field. The charge from these particles can be observed by a variety of techniques. In analogy with the scintillation process, the amount of ionization surviving recombination depends on the particular type of particle that interacts, again allowing for particle discrimination.

In semiconductor detectors, electrons are collected at the crystal surface and their charge is measured with charge amplifiers. In dual-phase noble gas detectors, the charge drifts to a gaseous region where a strong electric field accelerates the electrons, producing electroluminescence which is then collected by light sensors.

Examples of such detectors are: CoGeNT [73], DAMIC [74] and NEWS-G [75].

Superheated liquids In bubble chambers and superheated droplet detectors, a nuclear recoil will induce bubble nucleation. These bubbles can then be observed with imaging or acoustic sensors. By tuning the temperature and pressure of the fluid, it is possible to make sure that bubble nucleation only arises for a given stopping power. Particles which lose their energy over a comparatively longer range, will not induce bubbles. PICASSO [76], PICO [77] made use of this technique.

Directional detectors In recent years, efforts have been devoted to the development of detectors sensitive to the direction of nuclear recoils. The NEW-AGE [78], MIMAC [79] and DRIFT [80] collaborations are giving promising results in this direction, operating TPC filled with gaseous mixtures. They are however limited by their small target masses, which prevents them from exploring parts of the parameter space that have not already been excluded by bigger experiments.

1.5.4.1 State-of-the-art

High mass WIMPs In the high-mass WIMPs region, the best limits are given by the noble liquids experiments (see Table 1.2).

Experiment	σ_χ [cm^2]	M_χ [GeV/c^2]	Reference
XENON1T	4.1×10^{47}	30	[81]
PandaX-II	8.6×10^{-47}	50	[71]
LUX	1.1×10^{-46}	50	[68]
DarkSide-50	1.1×10^{-44}	100	[1]

Table 1.2 – 90% C.L spin-independent cross-sections for high mass WIMPs.

The noble liquids again proved extremely powerful in the case of spin-dependent interactions. The WIMP-proton limit is given by XENON1T [82] at 30 GeV/c^2 and 90% confidence level, while the best limit for WIMP-proton cross-section is given by PICO [83]. The leading limits are summarized in Table 1.3.

Experiment	σ_n [cm^2]	σ_p [cm^2]	M_χ [GeV/c^2]	
XENON1T	6.3×10^{-42}	-	30	[84]
PICO	-	2.5×10^{-41}	25	[83]
PandaX-II	1.6×10^{-41}	4.4×10^{-40}	40	[85]
LUX	1.6×10^{-41}	5×10^{-40}	35	[86]

Table 1.3 – 90% C.L spin-dependent cross-sections for high mass WIMPs.

Low mass WIMPs In the low mass region, noble liquids have made significant progress in terms of sensitivity, enough to be now leading the domain. The XENON collaboration has always been a leader in the field of low mass WIMPs searches in noble liquid TPC, proposing some of the earliest attempts. Now, with the exposure of XENON1T [82], XENON poses the most stringent limits on cross-sections for low mass WIMPs. The DarkSide-50 [2] detector demonstrated encouraging possibilities in LAr for WIMPs of similar masses, with a much lower exposure. The

DAMA/LIBRA [72] experiment observes an annual modulation signal that can be interpreted as due to WIMPs with masses of few GeV/c^2 and a cross-section $\sim 10^{-40}$ cm^2 [87], but this scenario has been excluded by several other experiments under simple models of SHM.

Chapter 2

The DarkSide Experiment

Contents

The DarkSide program is a staged series of WIMP direct detection experiments housed at Gran Sasso National Laboratory (LNGS) in Italy [88, 89], the final goal being a multi-ton exposure. All the experiments exploit the technology of dual-phase (liquid-gas) time projection chamber (TPC) with a liquid argon (LAr) target. The design of the detector has been directed towards performing a background-free WIMP search. In order to achieve that goal, both strict material selection and efficient background suppression are required.

In this chapter, I will introduce WIMP detection with noble liquids. I will then focus on the current stage of the DarkSide program, DarkSide-50 and its results, before introducing DarkSide-20k, the next phase of the DarkSide experiment.

2.1 Direct dark matter search with noble liquids

Noble liquids are excellent targets for direct high mass WIMP detection: they are relatively inexpensive, naturally stable, intrinsically more pure than other materials, and scalable to masses in the multiton range. They are also dense and easy to be chemically purified, have large ionization and scintillation yields, are transparent to the scintillation light and have large electron mobility.

2.1.1 LAr/LXe complementarity

Argon and Xenon are the most widely used noble liquids. Xenon has a high density (∼3 kg/L) [90] and a very high intrinsic radio-purity. It is also self-shielded against external radiation: the mean free path of thermal neutrons is of the order of the cm and the range of 50 keV gammas is less than 1 mm. In liquid argon, these quantities are respectively 50 cm and 1 cm [91]. These are the reasons why the Xenon-based experiments are leading the field of high-mass WIMP direct detection. On the other hand, argon properties make it highly efficient in discrimination between nuclear and electronic recoils. In LAr, the time distribution of the primary scintillation pulse is strongly dependent on the nature of the recoiling particle (see Section 2.3.1.4). The active mass of a LAr detector was so far limited by the presence of ^{39}Ar radioactivity, which is present in atmospheric argon (∼1 Bq/kg). However, the use of low-radioactivity underground argon allows to reduce the fraction of ^{39}Ar by a factor ∼1400 as shown in [92] (see Section 2.3.1.2).

2.2 Dual-phase moble liquids Time Projection Chamber

The leading technology exploiting noble liquids for direct dark matter searches is the Time Projection Chamber (TPC). In this section, we will first describe the principle of the noble liquid TPC. We will then discuss the interaction of energetic particles in noble liquids, before detailing the process of electron extraction and electroluminescence in noble gases.

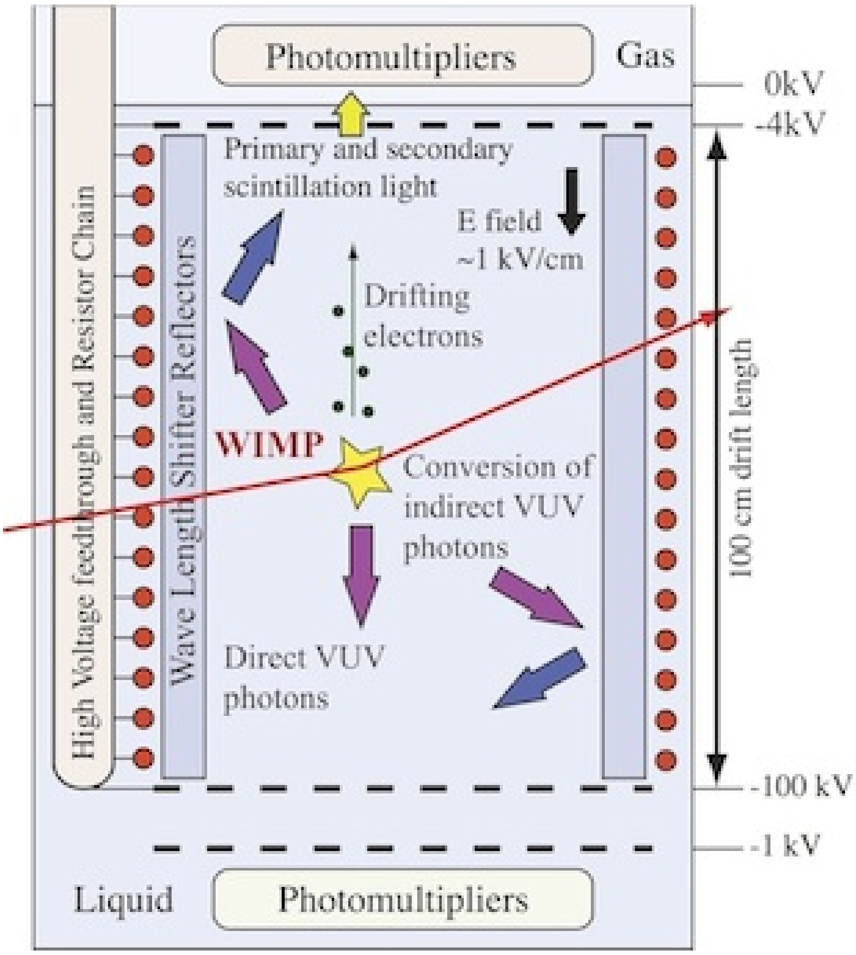

Figure 2.1 – Principle of a dual-phase TPC.

2.2.1 Principle of the TPC

This device consists of a noble liquid target with (dual phase) or without(single-phase) the adjunction of a gas layer. The dual-phase configuration allows access to both the ionisation and scintillation signals of the recoils. These combined signals contribute to background discrimination and allows 3D reconstruction of the recoil position.

Typically, a dual-phase TPC contains a thin layer ($\sim$1 cm) of gaseous argon above a larger monolithic cylindrical body of liquid. Adding a gaseous layer has a double advantage: it provides an amplification of the signal in the gas (see Section 2.2.4) and transforms the ionisation signal into an optical signal, observable with the same photon detectors as the scintillation output.

The liquid volume is immersed in a uniform electric field applied to drift the electrons that survive recombination towards the gas layer. From the liquid, they are extracted into the gas thanks to the extraction electric field. In the gas a stronger electric field causes the electrons to excite argon atoms which then de-excite and emit UV scintillation light due to electroluminescence processes. The production of light in the gas is similar to the liquid: excited argon dimers de-excite and produce light according to a two-component exponential (with decay times of 11 ns and 3.2 μs) [93]. This process is illustrated in Figure 2.1.

One or more arrays of photodetectors (usually photomultipliers) view the active volume recording both the primary scintillation signal, commonly referred to as S1, and the electroluminescence signal, commonly called S2. The amount of scintillation light produced, usually measured in units of photoelectron (PE), is proportional to the energy deposited in the argon (details in Chapter 3). Likewise, the amount of electroluminescence light produced, and consequently, the size of S2 is proportional to the amount of ionization. The scintillation light of noble liquids being in the VUV region, the inner walls of the TPC need to be coated with a wavelength shifter. Electrons drift time in the TPC is generally long, between tens to hundreds of μs. The time difference between S1 and S2 is proportional to the z position (considering the z-axis pointing along the drift direction) of the event while the hit pattern of the S2 over the top PMTs can be used to reconstruct the position of the primary interaction in the (x, y) plane. In this way a 3D position reconstruction of the interaction inside the TPC is possible.

Let us now detail the process of energy deposition in liquid and gaseous argon.

2.2.2 Particle interactions in noble liquids

The light emission processes are here described for liquid argon but are similar in other noble liquids.

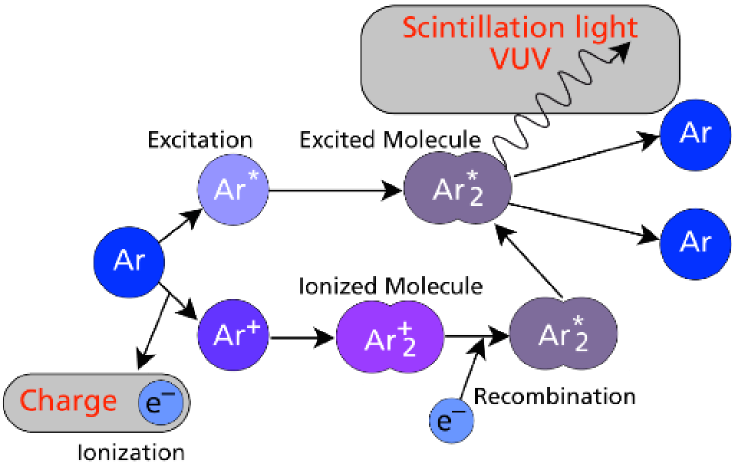

Figure 2.2 – Argon scintillation process.

Figure 2.2 illustrates the scintillation process in LAr (and other noble liquids). When an energetic particle interacts in a LAr volume, its energy is transferred to the atoms and molecules of the medium as either excitation or ionization. The particle can elastically scatter off an electron orbiting around an argon nucleus (electronic recoil or ER) or off the nucleus itself (nuclear recoil or NR), producing a free electron or a nucleus recoiling through the liquid argon. As the charged particle moves through the argon, it will continuously lose energy, either through ionization or excitation of argon electrons or by scattering off of more argon nuclei, causing them to recoil as well. This creates a track of excited and ionized atoms. In this latter case, some of the energy given to argon nuclei will end up being transferred to electrons (directly by the recoiling nucleus or by a nucleus sent recoiling by this nucleus, and so on in a cascade of recoils) while a significant fraction will ultimately be dissipated as heat.

Scintillation light can be produced either by excitation of the medium or via the recombination of free electrons with ions. The two channels lead to the formation of excited dimers, that will ultimately emit light. The processes of energy loss, electron-ion pair creation, and recombination will be discussed in more detail in Chapter 3.

2.2.2.1 Scintillation light emission

The first mechanism leading to scintillation light in LAr relies on the excitation of argon atoms by the interacting particle. The excited argon atoms combine with neutral atoms to form excited dimers that subsequently decay by radiative emission, emitting scintillation photons [94]:

$$\mathrm{Ar}^* + \mathrm{Ar} \rightarrow \mathrm{Ar}_2^* \tag{2.1}$$

$$\mathrm{Ar}_2^* \rightarrow 2\mathrm{Ar} + \gamma \tag{2.2}$$

This process is called the *excitation luminescence*.

The ions that recombine with electrons along the track also lead to scintillation light, the so-called *recombination luminescence*. They first go through non-radiative de-excitations and then radiate (with the same process described in equation 2.2):

$$\begin{aligned}
\mathrm{Ar}^+ + \mathrm{Ar} &\rightarrow \mathrm{Ar}_2^+ \\
\mathrm{Ar}_2^+ + e &\rightarrow 2\mathrm{Ar}^{**} + \mathrm{Ar} \\
\mathrm{Ar}^{**} &\rightarrow \mathrm{Ar} * + heat \\
\mathrm{Ar}^* + \mathrm{Ar} &\rightarrow \mathrm{Ar}_2^* \\
\mathrm{Ar}_2^* &\rightarrow 2\mathrm{Ar} + \gamma
\end{aligned}$$

The wavelength of the emitted photons peaks around $\lambda_{Ar} = 128$ nm [95].

Liquid argon (LAr) produces 40,000 UV photons per MeV of energy deposited from ERs. Photons are emitted from what is called a ”molecular continuum”, making argon transparent to its own light [90].

2.2.3 Extraction of electrons in the gas phase

It is known that in semiconductors and dielectrics the potential barrier on the surface of the material, which prevents the escape of free electrons. Thus scintillation electrons cannot travel to the gas phase at the top of the TPC. However, free electrons can cross the liquid/gas interface in

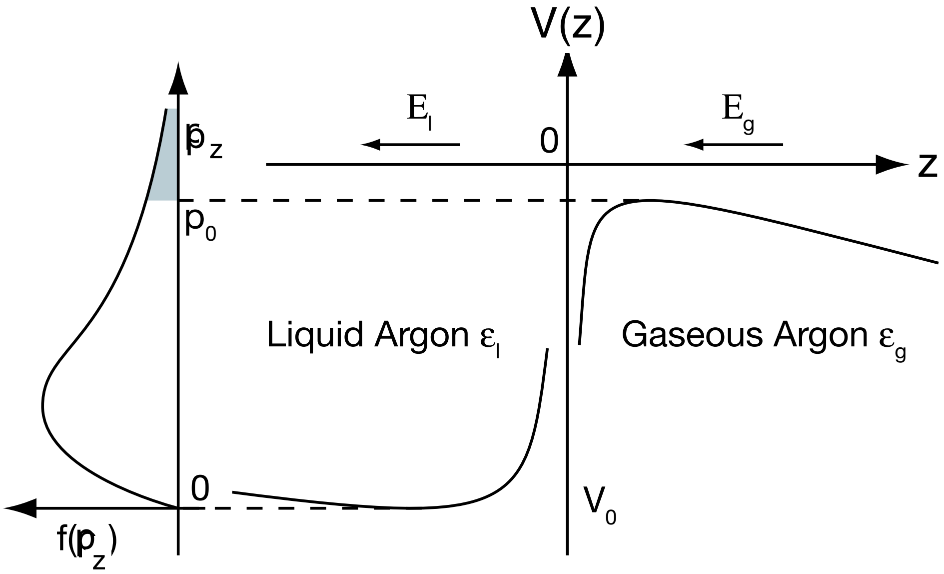

Figure 2.3 – Potential distribution near the liquid/gas interface. An indicative momentum distribution (not in scale) is reported on the left.

the presence of a moderate electric field [96]. The extraction process depends on the value of V_0, the potential energy of an electron in the liquid. If we assume that the energy level of argon in the gas is close to the one in the vacuum, then V_0 is also the energy gap between the conduction band in the liquid and gas phase. For argon, $V_0 = 0.2 \pm 0.03$ at 83 K [97]. See Figure 2.3 for an illustration.

The potential energy of an electron at a distance z from the interface and in presence of an electric field normal to the interface can be expressed as [97],

$$V_l(z) = V_0 - eE_l z + A_l \qquad \text{for z < 0} \quad \text{(liquid)} \tag{2.3}$$

$$V_g(z) = -eE_g z + A_g \qquad \text{for z > 0} \quad \text{(gas)} \tag{2.4}$$

where e is the electron charge, E_l and E_g are the electric fields in the liquid and gas phases respectively, and

$$A_{l,g} = -\frac{e^2(\epsilon_l - \epsilon_g)}{4\epsilon_{l,g}(\epsilon_l + \epsilon_g)} \frac{1}{x + \beta\frac{x}{|x|}} \tag{2.5}$$

where ϵ_l and ϵ_g are the dielectric constants of the liquid and gas phase and β represents the physical thickness of the interface (few times the inter-atomic distance). $A_{l,g}$ is derived by applying the Schottky model. In this model, the barrier is described as an interaction between the electron and its dielectric image [98].

It is usually considered that electron emission occurs through two mechanisms: emission of 'hot' electrons and 'thermal' emission. The first mechanism refers to the case when the electron has a momentum projection along the z axis $p_x \geq 2m_e V_0$, so that it has sufficient kinetic energy

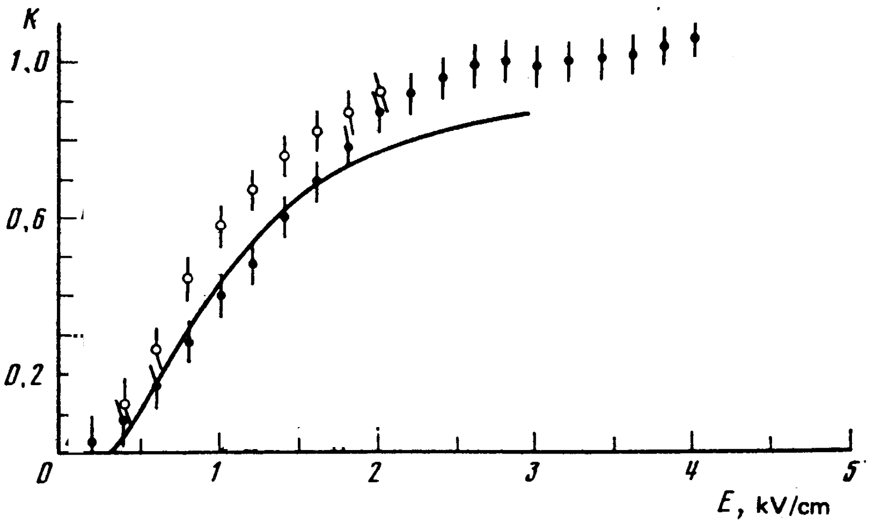

Figure 2.4 – Probability of extraction for electron in argon as a function of the electric field. The hollow dots are the sum of the fast and slow component, while the black dots represent the fast component. Figure extracted from [98].

to overcome the potential barrier and pass immediately into the gas phase (see Figure 2.3). These electrons are emitted very fast.

However, if the electron's momentum is too low, it will not cross the surface barrier at the first attempt. It will be reflected in the bulk of the liquid and, after several scatterings, and then return to the surface, guided by the field and have another chance of crossing the barrier. This process can be repeated several times and leads to the "thermalisation" of the electron. This process is much slower than the previous one. Besides, depending on the electron lifetime in the liquid phase, electronegative impurities could capture some of the electrons.

The relative contribution of these two processes depends on the extraction field: a higher field will provide a higher average number of electrons with the required momentum to pass directly in the gas phase. Figure 2.4 illustrates the probability of extraction of electrons as a function of the electric field in argon. It appears that the slow component vanishes for fields of the order of 2.5 kV/cm. At such an extraction field, all the electrons are extracted immediately in the gas phase.

2.2.4 Light emission in the gas phase

If the electrons extracted in the gas phase are placed within a high enough electric field, they can gain enough energy to excite or ionize the atoms of the gas. The Ar^* excitons produced will then form excited dimers that will de-excite emitting 128 nm photons, similarly to the scintillation process in the liquid. If sufficient energy for ionisation is reached, secondary electrons are created, starting an avalanche process. However, the use of the avalanche regime is not straightforward in a dual-phase TPC (see discussion below). Between the excitation threshold and ionisation threshold, the electroluminescence mechanism should proceed linearly.

Electroluminescence photons are emitted all along the electron drift path. This can lead to the

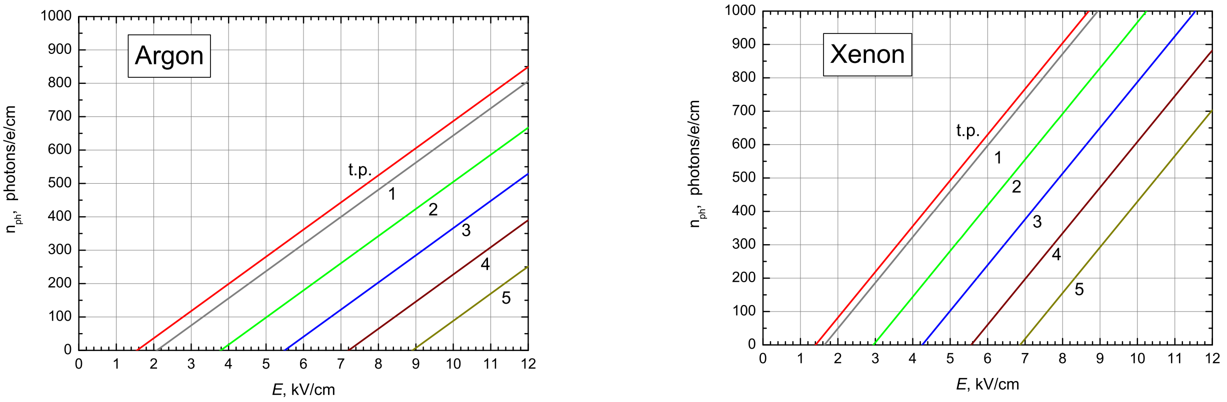

Figure 2.5 – Number of secondary scintillation (electroluminescence) photons generated by an electron travelling 1 cm in saturated gas at different gas pressure (indicated next to each curve, in bar) as a function of electric field in argon (left) and xenon(right). 't.p.' stands for triple point and corresponds to a pressure of 0.6889 bar for Ar and 0.8175 bar for Xe. Figure extracted from [100].

production of hundreds of photons. The number of photons emitted by an electron in a uniform electric field is proportional to the drift path length. Considering an electric field E (V/cm) and the pressure P of the gas, the light yield per cm is well described by a linear function of E/P [99],

$$\frac{1}{n}\frac{dN_{ph}}{dx} = a\frac{E}{P} - b \tag{2.6}$$

Secondary scintillation is a threshold process, therefore, there is a minimal value for E/P. Eq. 2.6 is valid at a given temperature, T, being used to convert the density into pressure.

Measurements at room temperature have been performed in liquid argon[99], while data at $T =$ 183 K are available in xenon. The measured values are $a = 81$ and $b = 47$ in argon. Extrapolating to zero scintilation then gives a minimum $E/P = 0.7 \pm 0.1$ kV/cm/bar. The resulting light yields are shown in Figure 2.5.

The problem of the avalanche in dual-phase TPCs When operating an avalanche device with a double-phase medium, two issues have to be addressed. First, VUV photons cause photoelectric feedback effects at cathode electrodes with high probability, resulting in secondary avalanches. Since the purity of the medium is very important, usual solutions, like adding quenching molecules, cannot be used. Second, the high gas density affects the maximum achievable multiplication gain.

As has been shown recently [101], micro-pattern avalanche detectors such as GEM (Gaseous Electron Multiplier), THGEM (THick GEM), LEM (Large Electron Multiplier) or similar devices may offer a promising solution for this problem. As an example, WA105 [102] will test the association of LEMs with a double-phase liquid argon TPC.

2.3 Backgrounds in noble liquid TPCs

Current limits on the WIMP-nucleon scattering cross-section require to detect ~1 evt/ton/year. To perform such rare event searches, the backgrounds have to be kept at a minimum and be extensively studied. The background discrimination features of LAr and the design of DarkSide allow for a background free WIMP search. The possible backgrounds include:

- electron recoils (ER) from internal and external contamination.
- NR's induced by radiogenic and cosmogenic neutrons;
- α particles emitted from the detector surfaces;

2.3.1 Electronic recoils and Pulse Shape discrimination

The electronic recoils backgrounds can be separated in two different origins: the external ERs, originating from the materials of the detector, and the internal ERs, induced by the contamination of LAr by ^{39}Ar.

2.3.1.1 Internal ERs : ^{39}Ar

2.3.1.2 Low-radioactivity underground argon

Argon is relatively abundant in Earth's atmosphere (0.94%) and this makes the extraction of this gas from the air convenient. The majority of argon in the atmosphere is stable ^{40}Ar, produced by electron capture on ^{40}K. However, because of cosmogenic activation through the reaction ^{40}Ar(n,2n)^{39}Ar, there is a significant amount of ^{39}Ar in atmospheric argon (^{39}Ar/^{40}Ar $\sim 8\times10^{-16}$). The ^{39}Ar isotope is a beta-emitter, with half-life of 269 years and endpoint at 565 keV. As a result, the total activity of atmospheric argon is $A_{atm} = 1.01 \pm 0.02 \pm 0.08$ Bq/kg [103]. Even if this background could be fully removed by PSD (see details in Section 2.3.1.4), such large activity would introduce dead times due to saturation or pile-up that would make the scaling to multi-ton LAr detectors unfeasible.

Underground argon, extracted from deep wells, is shielded from cosmic rays. As a result, its ^{39}Ar contamination is greatly depleted. In April 2015 the DarkSide TPC was filled for the first time with a batch of underground argon and a new data taking was started. As it will be described in Chapter 5, a spectral fit combining single and multiple scatter events allowed to measure the residual ^{39}Ar contamination, resulting in a depletion factor of 1400 ± 200. Thanks to this impressive result, the LAr technology can be scaled to multi-ton detectors.

2.3.1.3 External ERs

Most of the background due to γ-ray radiation originates from the decays in natural uranium and thorium chains, as well as from decays of common isotopes such as ^{40}K, ^{60}Co and ^{137}Cs which are present in the materials surrounding the detector. Many α- and γ-decays in the uranium and thorium chains' are followed by the emission of several γ-rays with energies from tens of keV to few MeV. When interacting with the target medium, these γ-rays deposit energy in the energy region expected for DM. External γ-rays can be reduced and suppressed both by selecting materials with low radioactive traces of contaminants and by surrounding the detector by materials with high atomic number and high density (i.e. good stopping power) and low internal contamination. This material could be lead, xenon, or water (even if Z is low, a huge amount of water acts as a very good passive shield against gamma radiation). Moreover, to reduce the γ-ray activity from radon in the air most of the operations on the inner parts of the detector should be done in a clean room environment with a radon trap facility.

2.3.1.4 Pulse Shape Discrimination in LAr

	Xenon	Argon
τ_1	4 ns	7 ns
τ_2	22 ns	1.6μs

Table 2.1 – Decay time constant for singlet and triplet states in xenon and argon

A noble element atom can be excited on two different states, the singlet $^1\Sigma_u^+$ and the triplet $^3\Sigma_u^+$. The energy difference between the two states is small, so that they cannot be distinguished spectroscopically, but the decay time constants τ_1 and τ_2 of the two states are different as summarized in Table 2.1 (the subscript 1 stands for the singlet and 2 for the triplet). While in liquid xenon the two decay constants are similar, they differ by more than a factor of 200 in liquid argon [104]. It was shown that the relative intensity of the singlet (or prompt) component is smaller for higher deposited energy density [105, 106]. Nuclear recoils typically have a higher density track than electronic recoils, so their prompt fraction will be higher. The typical singlet fraction for electron recoils is about 0.3 and about 0.7 for nuclear recoils in liquid argon. One can measure the fraction of prompt component (which decays completely in a few tens of nanoseconds) by computing the ratio between the integral of a scintillation pulse in the first tens of nanoseconds and the total integral. The SCENE collaboration [107] has shown that the maximum separation is achieved by defining f_{90} as estimator of the prompt fraction of the signal $S(t)$:

$$f_{90} = \frac{\int_0^{90ns} S(t)dt}{\int_0^{7\mu s} S(t)dt} \tag{2.7}$$

where the upper limit of 7 μs is chosen to allow the late part of the signal to fully decay. Using the f_{90} parameter it is possible to achieve discrimination between nuclear and electron recoils up to a factor 10^8 in liquid argon. It must be noted that the separation is less accentuated at low energy (few keV$_{ee}$) when the mean value of the prompt fraction for electronic and nuclear recoils tends to approach the intermediate value of 0.5, while it is larger at higher energies. The pulse shape discrimination (PSD) is a prerogative of liquid argon and offers a unique tool for the background rejection. An argon detector can in principle be free from all the known β and γ backgrounds to an unprecedented level in the region of interest for DM searches. DarkSide-50 demonstrated a discrimination power of 10^7 using PSD alone [89] and the DEAP collaboration reached 10^8 [108]. The exploitation of PSD in DarkSide-50 will be discussed in Section 2.6. Also, the observed ratio between ionization and scintillation depends on the NR or ER nature of the event and can be used as an additional tool to discriminate between these two types of event improving the discrimination power.

In xenon, PSD is not feasible since the decay times for singlet and triplet states are very similar. For dual-phase TPC based on liquid xenon, the discrimination power relies only on the ratio between ionization and scintillation (S2/S1) and is of the order of 10^3. S2/S1 can also be used in LAr for dual-phase TPC, to provide additional discrimination power at high energy.

2.3.2 Nuclear recoils induced by neutrons

Neutrons scattering off the argon nuclei exactly mimic a WIMP interaction.

Neutrons can be produced cosmogenically or radiogenically. Cosmogenic neutrons are produced by muon spallation reactions with the detector materials or with the surrounding rocks. Radiogenic neutrons are emitted in (α,n)-reaction and spontaneous fission reactions from natural radioactivity. Both types of neutrons can produce nuclear recoils in the energy region relevant to DM searches. To mitigate this problem, DM experiments are typically placed in deep underground laboratories. The rock coverage greatly reduces the muon flux and so the number of muon-induced neutrons. Moreover, significant work has been done to select materials with low uranium and thorium content thereby reducing the rate of α-emission and spontaneous fission. Additionally, detectors have passive or active shields that can moderate and tag external neutrons. Often water or polyethylene layers are installed around the detector setup and/or active vetoes are designed to record the muon interactions and the eventual neutron production. The latter approach is effective when such detectors are used in anti-coincidence: data acquired in the DM detector simultaneously to a muon or neutron event are discarded. Usually, plastic scintillator plates, water Cherenkov detectors, and liquid scintillator detectors are used.

2.3.3 Alpha particles

Contamination from heavy nuclei can lead to signals from α-decays in the detector. Some of these heavy nuclei may be found in higher concentrations on the inner surfaces of the detector; these nuclei can give rise to surface backgrounds. The backgrounds that a detector sees from these decays can result directly from signals produced by the emitted α particles, or by the recoiling daughter nucleus after the decay. α particles can also produce neutrons via (α, n) reactions. Understanding the α-decays in the experiment and the signals they may produce in the detector is, therefore, an important part in understanding the experiment's backgrounds. In particular, these signals often appear as nuclear recoils, which may produce WIMP-like signals inside of a detector. The alpha-induced backgrounds can be eliminated via fiducial cuts. Indeed alpha particles originate from the walls of the TPC and interact on the border of the volume, as shown in Figure 2.6.

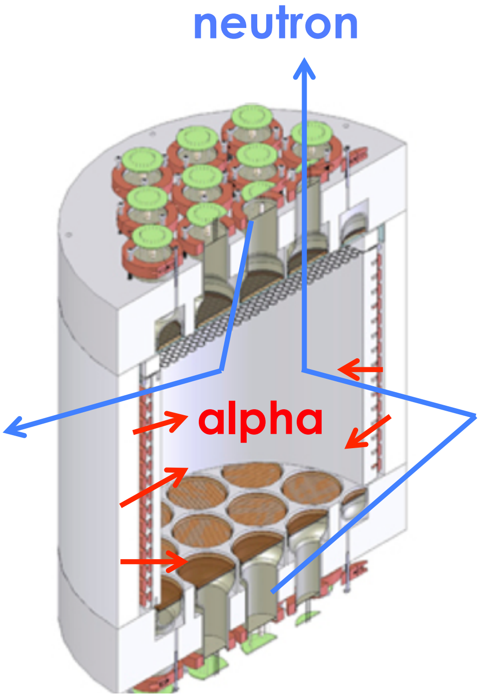

Figure 2.6 – Illustration of the alpha and radiogenic neutron backgrounds origins.

2.4 The DarkSide-50 detectors

DarkSide consists of three nested detectors. The innermost is the dual-phase LAr TPC, being engulfed in two veto envelopes for background shielding and tagging. These detectors are installed in the Hall C of the LNGS, under ∼3400 m.w.e. of rock. They are here described from the innermost to the outermost.

2.4.1 DarkSide-50 TPC

The TPC is housed inside a cylindrical stainless steel, vacuum insulated, cryostat to keep the argon in liquid state. The DarkSide-50 TPC is made of a monolithic 1" thick PTFE (Teflon) reflector cylinder of 36cm diameter and height. The active volume of (46.4±0.7) kg of liquid argon is seen by 38 Hamamatsu R11065 3" PMTs, arranged in two hexagonal arrays (19 on the top and 19 on the bottom). The large uncertainty on the LAr volume is mainly due to the uncertainty on the shrinking factor of Teflon at the liquid argon temperature. The top and bottom surfaces of the sensitive volume are fused silica windows, 6 mm and 12 mm thick respectively. PMT photocathodes directly face the windows. Indium tin oxide (ITO) is evaporated on both surfaces of the windows, making them high voltage electrodes. The inner faces of the fused silica windows are then the anode (top) and cathode (bottom) of the TPC field cage. A 50 µm thick stainless steel grid with hexagonal mesh sits 5mm below the liquid surface. Negative high voltage is applied between the grid and cathode to produce the vertical electric field that drifts the ionization electrons upward. Voltage is also applied between the anode and the grid to extract the drift electrons out of the liquid and produce the electroluminescence signal in the gas pocket. The nominal fields are: 200 V/cm for

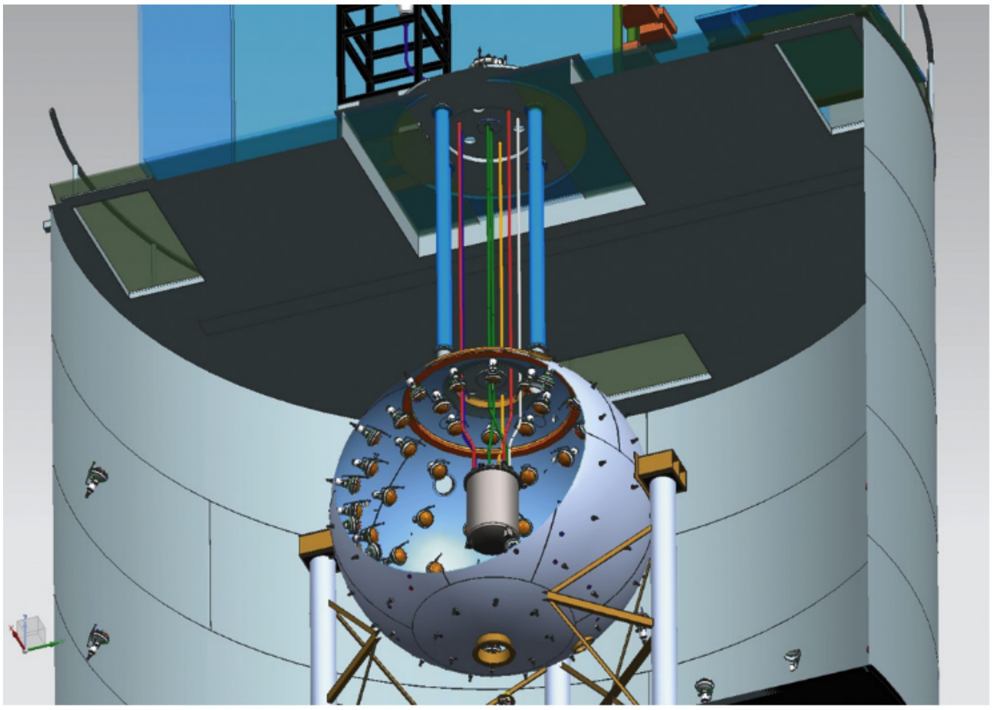

Figure 2.7 – DarkSide-50 nested detectors.

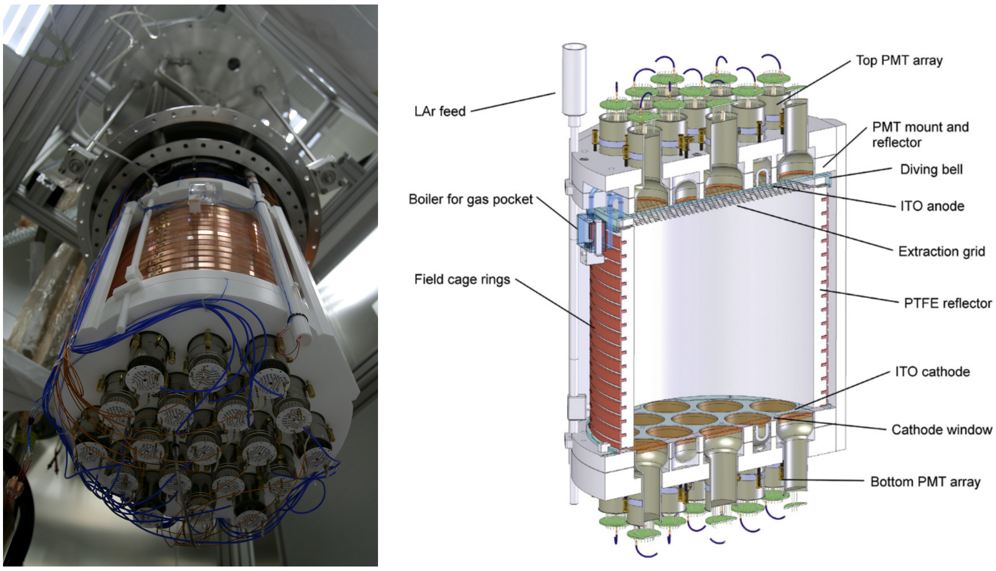

(a) Picture of the DarkSide-50 detector during commissioning.

(b) Scheme of the DarkSide-50 TPC.

Figure 2.8 – The DarkSide-50 TPC.

the drift field, 2.8 kV/cm for the extraction field and 4.2 kV/cm for the electroluminescence field. At 200 V/cm, the electron drift velocity is 0.93 ± 0.01 mm·µs^{-1} Since the LAr emits scintillation light at 128 nm, the inner surface of the TPC walls and the windows are coated with tetraphenyl butadiene (TPB), posing as a wavelength shifter. It converts the scintillation photons into a 420 nm light, visible by the PMTs.

Outside the cylindrical PTFE wall, 15 T-shaped copper rings at graded potentials keep the drift field uniform throughout the active volume.

2.4.1.1 TPC Electronics

Due to sporadic light emissions induced by charge accumulations on internal components, the PMTs have to be operated at low gain. This operation mode is defined by DarkSide custom-made local pre-amplifiers. The pre-amplified PMT signal is split into two copies. One is directly sent to a 14-bit 100MHz digitizer channel while the second is amplified and split again. One amplified signal is used to form the TPC trigger and the other is sent to a 12-bit 250 MHz digitizer channel. The usage of two digitizer types extends the dynamic range, providing a linear response between 1 PE to 10,000 PE. The TPC trigger is a majority trigger: a given number of PMTs are required to fire within a 100 ns window. For each trigger, the DAQ records a 440 μs gate of waveform data for each of the 38 channels. The raw data is then passed to the reconstruction software and are available for analysis.

2.4.2 Veto detectors

The veto system of the DarkSide-50 experiment is described in detail in [109].

2.4.2.1 Liquid Scintillator Veto

The TPC cryostat is completely enclosed in a Liquid Scintillator Veto (LSV). The 4π coverage allows the LSV to detect γ-rays and neutrons that scatter in the TPC and the LSV and produce coincident signals, making it possible to veto and make in situ measurements of backgrounds in DarkSide-50 (see Figure 2.9a).

The LSV detector is a 4 m diameter stainless steel sphere filled with 30 tonnes of boron-loaded liquid scintillator. The scintillator is a mixture of pseudocumene (PC) for the primary scintillator, trimethyl borate (TMB, $B(OCH_3)3$) for boron-loading and with 2,5-diphenyloxazole (PPO) as a wavelength shifter. Two different mixtures were used during the operation of DS-50:

- Phase-I (AAr search): 50% mass fraction of PC, 50% TMB, 2.5 g/L PPO
- Phase-II (UAr search): 95% mass fraction of PC, 5% TMB, 1.4g/L PPO

The light collection efficiency is increased by the Lumirror reflecting foils covering the inside of the LSV. 110 Hamamatsu R5912 8” PMTs are mounted on the inner surface. Those PMTs present

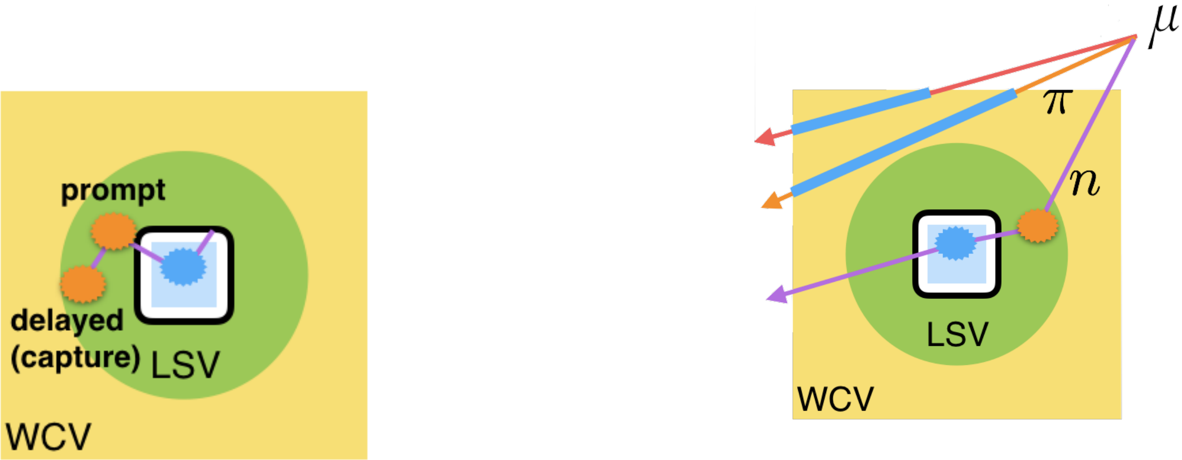

(a) Tagging process of radiogenic neutrons in LSV

(b) Tagging process of cosmogenic neutrons in WCD

Figure 2.9 – Tagging process of neutrons in LSV(left) and WCD(right). The veto observes either the thermalization of neutrons or their capture.

ow radioactivity glass bulbs and high quantum-efficiency photocathodes (37% average quantum efficiency (QE) at 408 nm).

The LSV is designed to identify and veto neutrons that might enter or exit the LAr TPC. Neutrons thermalize by scattering on protons in the liquid scintillator and are efficiently captured by ^{10}B nuclei via two channels (see Figure 2.10):

$$\begin{aligned} \text{BR: } 6.4\% \; ^{10}B + n \rightarrow ^{7}\text{Li}(1015\text{ keV}) + \alpha(1775\text{ keV}) \\ \text{BR: } 93.6\% \; ^{10}B + n \rightarrow ^{7}\text{Li}^{*} + \alpha(1471\text{ keV})^{7}\text{Li}^{*} \rightarrow ^{7}\text{Li}(839\text{ keV}) + \gamma(478\text{ keV}) \end{aligned} \tag{2.8}$$

Neutrons can also be captured on hydrogen, which causes the emission of a 2.2 MeV γ-ray. The TMB contains natural boron with a 20% natural abundance of ^{10}B, which has a thermal neutron capture cross-section of 3840 b. Loading TMB in the PC thus shortens the thermal neutron capture time.

As shown in Eq 2.4, neutrons can be tagged in the LSV by detecting both the γ-ray, as long as it does not escape into the cryostat before interacting in the scintillator, and the α and the ^{7}Li nucleus which is always contained (due to their high stopping power and consequently short track length), as long as their quenched energy of 50-60 keV$_{ee}$ is detectable. The measured light yield of the DS-50 LSV is (0.54±0.04) PE/keV allowing the detection of neutrons with an efficiency of 99.8%.

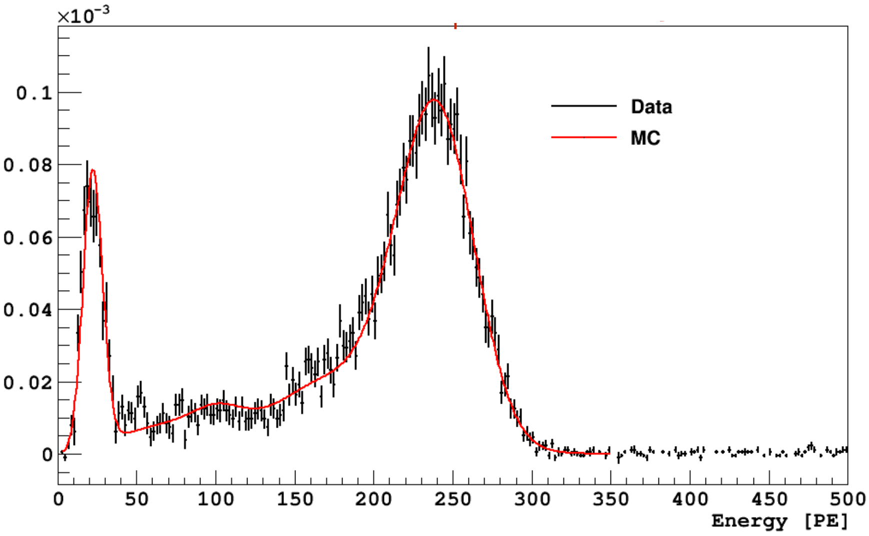

Figure 2.10 – LSV neutron capture spectrum.

2.4.2.2 Water Cherenkov Detector

The WCD is a cylindrical stainless steel tank, 11 m in diameter and 10 m high, filled with 1000 tonnes of ultra-pure water. The WCD serves two functions: it is a passive shield against external γ-rays and neutrons, and it is an active Cherenkov detector for muons crossing the LAr TPC or passing close enough to produce dangerous background events (see Figure 2.9b). It is designed to detect Cerenkov light produced by muons or other relativistic particles going through the water. Indeed, those particles can lead to the production of neutrons via spallation reactions, that will contribute to the nuclear recoils backgrounds. The WCD allows to tag the neutrons induced by those processes and discard them. The muon flux at the 3800 m.w.e. depth of the LNGS, although reduced from that at the Earth's surface by a factor 10^6, is of the order of 1.1 muons/m2/h [110]. This corresponds to about 2000 muons per day crossing the WCD, about 380 muons per day crossing the LSV, and about 4 muons per day crossing the LAr TPC. Cosmogenic muons can produce high energy neutrons, which can penetrate several meters of shielding. The internal surface of the tank is covered by reflecting Tyvek sheets for light collection enhancing. An array of 80 ETL 9351 8" PMTs, with 27% average QE at 420 nm observe the light produced.

2.5 G4DS the Geant4 based DarkSide simulation

G4DS is a GEANT4-based simulation toolkit specifically developed by DarkSide. G4DS provides a rich set of particle generators, detailed geometry descriptions, properly tuned physical processes and the full optical propagation of photons produced by scintillation in liquid argon and by electroluminescence in gaseous argon. The main goals of G4DS are: the accurate description of the light response (to calibrate the energy responses in S1 and S2 and the time response expressed by the f90 variable); the tuning of the analysis cuts and the estimate of their efficiencies; the prediction of the electron and nuclear recoil backgrounds. Each DarkSide experiment simulation is composed of

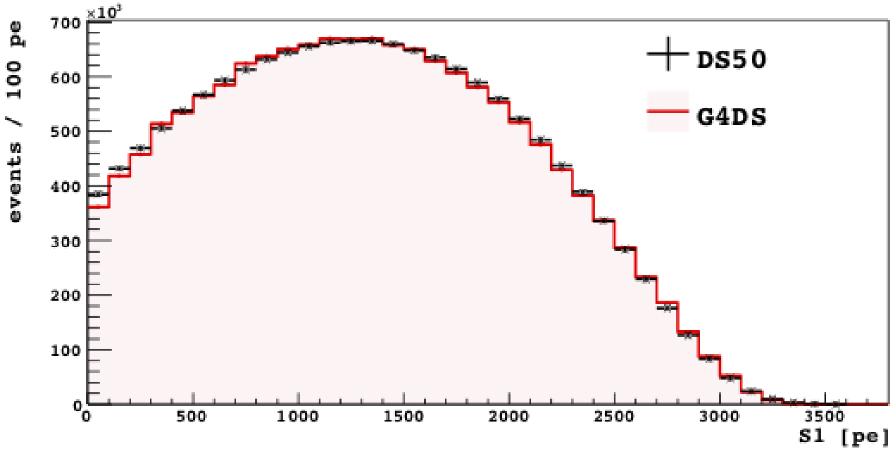

Figure 2.11 – Comparison of G4DS model (red) to ^{39}Ar data(black)

the TPC and a veto system. However, each part is independent, allowing to disable some of them to reduce the CPU time required for the simulation.

A particular attention was dedicated to the description of the physical processes. G4DS permits the use of different physics lists, including all the GEANT4 standard lists. The default electromagnetic physics list used in DarkSide is the *G4EmLivermorePhysics*, since it fits the energy range and accuracy required. A custom made hadronic physics list has been designed to account for the need for very high accuracy in the low energy neutron propagation, from a fraction of eV to a few MeV.

For background estimation, G4DS needs to be able to simulate large panels of decays. That is why G4DS provides several custom made event generators, in addition to the classical GEANT4 Particle Gun, in order to meet the specific needs of each physics goal. G4DS also accepts as input custom made FLUKA [111, 112] and TALYS [113] simulation outputs: the first one to study cosmogenic isotope productions and the second for the prediction of (α,n) neutron energy spectra and hence the evaluation of the nuclear recoil background.

The light generation in liquid and gaseous argon required a dedicated custom–made new GEANT4 physical process, since effects like excitation, ionization, nuclear quenching, and electron-ion recombination effects are poorly known in argon, especially in presence of electric fields. We developed a custom-made liquid argon response model called PARIS (Precision Argon Recoil Ionization and Scintillation), based on an effective description of the recombination effect, which, once opportunely tuned on calibration data, can provide an accurate description of the light response in both S1 and S2. Figure 2.11 shows the agreement between the data and the G4DS simulation. This model will be used also for the ARIS data and will be described in Chapter 3.

2.6 DarkSide-50 WIMP searches

2.6.1 S1, S2 and f_{90} in DarkSide-50

Two types of signals are recorded by the PMTs: the primary scintillation signal, S1, and the electroluminescence signal, S2. For each pulse identified in the raw waveform of an event, the estimators for the light produced by the primary scintillation and for the electroluminescence are specific integrals with fixed windows. The S1 size is estimated as the integral in a fixed window of 7 μs from the start of the pulse. The integration time is chosen to include several de-excitation decay times of the liquid argon slow component of 1.6 μs. Similarly, the S2 size is estimated as the integral in a fixed window of 30 μs from the start of the pulse: here the integration time is chosen to include nine de-excitation decay times of the argon gas slow component of 3.2 μs since electrons are not all extracted at the same time from the liquid-gas interface. The S2 pulse also has a slower rise time, since light is emitted all along the path of the electron in the gas.

Given the dual-phase technology and the geometry of the TPC, some corrections need to be taken into account when estimating the size of S1 and S2. For S1, a correction dependent on the depth at which the event takes place must be applied. In fact, due to total internal reflection at the liquid-surface interface and partial transparency of the extraction grid, more S1 light is collected in the bottom PMTs array than in the top one (the light collection efficiency can vary up to 14% from top to bottom). This correction can be applied both knowing the z-position of the event and/or, in the absence of the electric drift field, by the top-bottom asymmetry (referred to as TBA) in the light collection which provides an averaged z-position of the event. Concerning electroluminescence, the S2 response is found to have a strong dependency on the (x,y) position: PMTs in the center of the TPC see larger (about three times more)S2 signals than side and corner ones. The cause of the radial dependence has not been firmly established: possible explanations include a sagging anode window or electromechanical deflection of the grid. The S2 detector response depends also on the depth of the event due to the presence of impurities in the LAr which can soak electrons, thus reducing the observed S2 signal. The survival probability for electrons to drift all the way to the gas phase follows an exponential distribution, whose mean is referred to as the electron drift lifetime. The electron drift lifetime in DarkSide-50 is estimated to be>5ms. Considering the maximum drift time of 376 μs in the TPC the total z variation of S2 is <7%.

2.6.1.1 The PSD parameter, f_{90}

Recalling Section 2.3.1.4, NRs, and ERs have a different scintillation time profile allowing for PSD. DarkSide-50 uses the parameter f_{90} as a discriminator between NRs and ERs. f_{90} is defined as the fraction of the primary scintillation light seen in the first 90 ns of the S1 pulse. Since only a small fraction of the slow component (with a time constant of 1.6 μs) is integrated within this small time window (0.5%), f_{90} is almost equal to the ratio between singlet and triplet. The ratio between singlet and triplet is about 0.3 for ER and 0.7 for NR, for energies above 10 keV as illustrated on Figure 2.12.

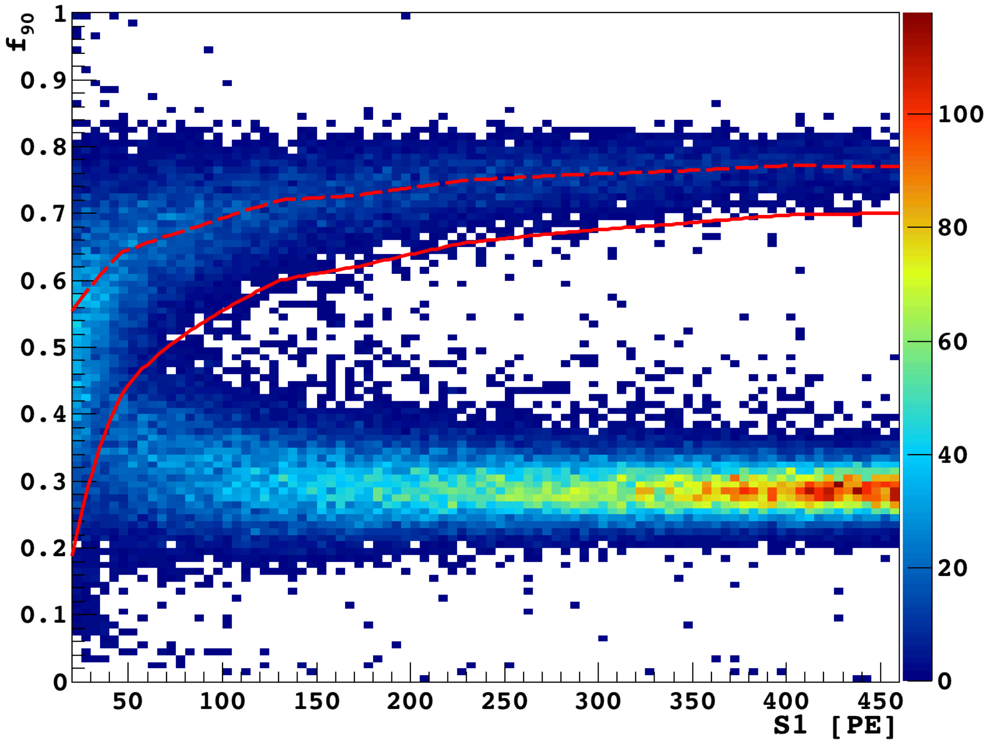

Figure 2.12 – f_{90} distributions for ER and NR over DM search range.

2.6.2 Blind analysis scheme

The latest DarkSide results come from a blind analysis performed on 532.4 live days of data. The goal of the blind analysis is to reduce the unintended biasing of a result in a particular direction. Several techniques of blind analysis exist for particle physics, and it is important to correctly choose the one that corresponds to a particular search. The *hidden signal box* technique chosen by DarkSide is well suited for rare events searches, where the signal region is known in advance [114].

In this technique, a ”blinding box” is defined, hiding events falling into the signal region. The box is usually chosen to be larger than the signal region, to prevent bias in the choice of the final signal cuts. Once the selection cuts and background estimates are finalized, the box is opened and the upper limit can be set. We choose a pre-determined level of background in the WIMP signal box to reach and design our cuts accordingly. We chose 0.1 event of expected background as an acceptable level, giving a <10% Poisson probability of seeing one or more background events in the search box.

Two categories of events were ”blinded” : events with S1 and f_{90} falling within the ”blinding box” and events chosen randomly with a probability of 2×10^{-5}. The random fraction was chosen to have enough fluctuations to obscure the counting of possible candidate events in the final analysis stages, where it was anticipated that the number of candidates would be small or zero when final cuts were applied.

Blinded events appear in the output files, but with all TPC data except the event ID, timestamps, and the livetime associated with the event set to -1.

2.6.3 Event selection

The data selection cuts for this analysis are based on the set of analysis cuts developed for previous DarkSide analyses [89, 92].

I present here a list of the cuts used, including the new cuts developed and the ones modified for this analysis. We distinguish between quality cuts (that imply a loss of lifetime) and physics cuts.

2.6.3.1 Quality cuts

- **AllChan:** data are present for all TPC channels in the event.
- **Baseline:** baselines for the digitized waveforms are successfully found in all TPC channels.
- **VetoPresent:** the event has GPS-timestamp-matched veto data.
- **TimePrev:** the event occurs at least 400 μs after the end of the inhibit window of the previous trigger (that is, at least 1.21 ms after the previous trigger). This removes events that triggered on an S2 whose S1 occurred during the inhibit window.

2.6.3.2 TPC events cuts

These cuts are designed to ensure that passing events are single-scatter events that triggered on S1 and have a single valid S2.

- **S1start:** the first pulse occurs at trigger time.
- **Npulse:** there is a second pulse, presumed to be S2. A third pulse is allowed only if its timing is consistent with the small tertiary pulses produced when S2 light photoionizes the TPC cathode.
- **S1sat:** the first pulse does not saturate the digitizers.
- **MinS2uncorr:** the second pulse is required to be at least 200 PE before position-based corrections, the approximate threshold for successful reconstruction of the event's radial position. For reference, the uncorrected S2's of interest in this analysis are >400 PE.
- **S2f90:** the second pulse has f90<0.20, consistent with the slow rise-time of S2 pulses.
- **xyRecon:** the x-y reconstruction algorithm successfully derives transverse coordinates of the event from S2.
- **MinS2/S1:** a more refined S2 cut that removes events with unphysically small S2/S1. The cut is set to remove events in the lowest 1% of the S2/S1 distribution of 241AmBe NRs.

2.6.3.3 Backgrounds estimates and selection cuts

The first step of the blind analysis procedure is to estimate the background levels and corresponding cuts. We defined a goal of < 0.1 background events within the WIMP search box. There are different types of backgrounds that have to be estimated differently and need different sets of cuts.

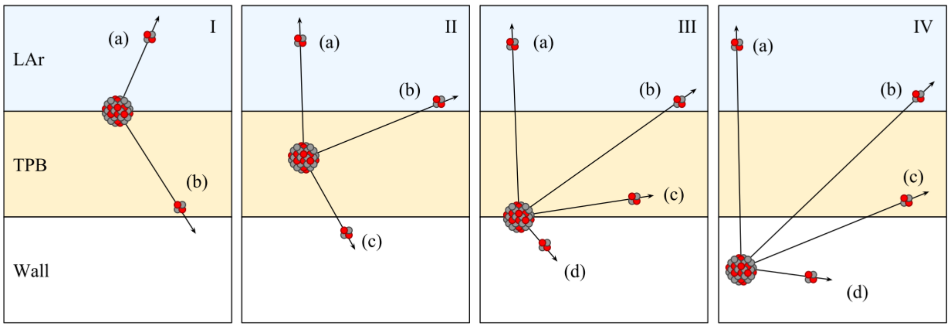

Figure 2.13 – Alphas decay modes on the surface of a liquid argon detector depending on the origin of the radioisotope. In each panel, the different possible trajectories of the alpha particle are labeled (a) to (d).

Surface events Surface backgrounds are undesired scintillation events originating on the surface of the detector — such as a wall or a window — that is containing the target volume. As described earlier, α particles can induce signal falling in the WIMP search region. Since α-induced events happen within or close to the TPC walls, they can be classified as "surface events". The presence of TPB coating on the inner TPC walls disturbs the α decays pattern. The different decay modes are shown in Figure 2.13. Signifi

cant scintillation is expected whenever an alpha travels through LAr or TPB, or when the nucleus travels through LAr. Of particular concern for DarkSide are the decay mode I(b), which has a low energy signal produced in the liquid by the recoiling nucleus, as well as decay modes (II-IV)(b), which have low energy signals produced in the liquid by a degraded alpha. Modes in which the alpha deposits a large fraction of its energy in the LAr (MeV), leading to a signal well above DarkSide's search region or where the recoiling nucleus does not have enough energy to reach the LAr do not pose problems.

For the decay modes that could lead to a problematic signal, two cases are possible. First, if the S2 signal is large enough to pass the analysis cuts (Type 1). The large majority of surface events do not show any detectable S2, and even then, the S2 signal often does not pass the analysis cuts. They are then called "S1-only" events. It could be due to the loss of drifting electrons very close to the side reflector of the TPC. The other problematic events are S1-only events that happen closely in time with an S2-only event. The combined event can then be accounted for as a real S1 + S2 event (Type 2). Each type of background is estimated separately.

Type 1 Thanks to the low electron collection efficiency along the walls, surface events only pass analysis cuts for S1 > 20 000 PE, which well above the signal region. This estimate is based on the open data with S1 > 600 PE. Considering that the acceptance decreases with S1, the extrapolation into the WIMP signal region yields an estimate of < 0.07 events passing the S2 cuts. Further rejection of Type 1 events is achieved by the use of the TPB coating. Indeed, it has been discovered that alpha particles interacting in the TPB lead to a millisecond long scintillation. It is then possible to tag S1 events followed by this slow component as originating from the TPB. This lead to the development of the *LongS1tail* cut. Applying the cut to a sample of surface decays results in a rejection factor of more than 100, giving an expectation of <0.0007 Type 1 surface background events in the current data set.

Type 2 In some events happening near the top of the TPC, S1 and S2 can be so close in time ($t_{drift}3\mu$s) that they are not resolved by our reconstruction. These S2-only events and the S1-only surface events are uncorrelated and of constant rate, allowing the use of Poisson statistics to predict the expected number of S1+S2 pileup background events. As it will be discussed in the following, three cuts (*MaxS2/S1, S2LEshape* and *S1TBA*), are designed to reject the Type 2 background events, each targeting a different feature of these events. After application all the cuts, we expect 0.00092 ± 0.00004 surviving Type 2 surface background events in the current data set.

Cuts designed:

- **LongS1tail:** removes events with S1 with a long tail, consistent with laboratory measurements of α-induced scintillation in TPB wavelength shifter. We count the individual photoelectrons in the region between S1 and S2 and define a cut based on this count, that accepts 99% of ^{241}AmBe NR events.
- **MaxS2/S1:** removes events in the highest 1% of the S2/S1 distribution of 241AmBe NRs. This cut targets the "Type 2" surface background with uncorrelated S1 and S2 described above. This can also be a powerful discriminant between NR and ER and is the basis of WIMP discrimination in LXe TPCs. In LAr TPCs it is effective against high-energy ERs, but it is not effective at low S1, where further rejection is most needed.
- **S2LEshape:** removes events in which the shape of the leading edge of the second pulse is not consistent with the shape of a true S2 pulse. It relies on the risetime of the S2 pulses and removes unresolved S1 and S2 by requiring that the apparent S2 pulse have the ~2 μs risetime of a true S2 pulse rather than the few-ns risetime of S1. This S2 shape cut is applied via the ratio of the integrals of the first 90 ns and first 1 μs of the S2 pulse.
- **S1TBA:** removes events with S1 and S2 pulses that originate from different positions. We require that the z positions inferred from the top-bottom asymmetry in the detected S1 light and from t_{drift} differ by no more than 3σ, as determined from uniform ^{39}Ar events from AAr.

2.6.3.4 Radiogenic neutrons

Radiogenic neutrons that leave a WIMP-like signal in the TPC are tagged and captured by the LSV as described in Section 2.4.2. Because of the γ-rays emitted by AmBecoincidently with the neutrons, calibrating the prompt neutron thermalization in the LSV is impossible. To overcome this obstacle a ^{214}Am^{13}C source was realised. With lead shielding to absorb the ^{241}Am x-rays, this results in a neutron source very low in coincident γ-rays, allowing the study of isolated neutrons. Estimating the radiogenic background levels is then equivalent to measuring the efficiency of the LSV.

The ^{214}Am^{13}C campaign was taken in the same trigger configuration as in WIMP-search mode, with the TPC triggering both vetoes. A standard nuclear recoil search is then conducted in the data. The neutron veto efficiency is then calculated as the fraction of TPC NR candidates that fail the standard WIMP-search LSV cuts. With an acceptance of 0.79 for the neutron counting and a veto efficiency greater than $\epsilon_{AmC}^{data} = 0.9964 \pm 0.0004$, we predict a radiogenic neutron background <0.005 events, with 100% statistical error.

Cuts designed:

- **LSVprompt:** rejects events with >1 PE in the interval [-50,250] ns relative to the TPC trigger time. This targets the thermalization signal from neutrons giving NR in the TPC.
- **LSVdelayed:** rejects events with >6PE in a 500 ns sliding window covering [0,189.5]μs after a TPC trigger. This interval can be compared to the capture lifetime of 22μs in the boron-loaded liquid scintillator. The long acquisition window and search interval allow us to veto efficiently via the emitted γ-rays even when the neutron captures in TPC materials with long capture lifetimes.
- **LSVpre:** rejects events with >3 PE in a 500 ns sliding window covering [-10.5,0] μs before a TPC interaction.

2.6.3.5 Cosmogenic neutrons

The rate of cosmogenic neutron background is estimated via simulation using FLUKA [112]. The simulation is carried out in multiple steps. In the first and most time-consuming step, cosmic-ray muons are started 7 m above the ceiling of LNGS Hall C and propagated through the 7 m of rock. The muon and any produced secondaries are stopped and stored when they reach the ceiling of Hall C. The stored events are restarted and propagated onto the WCV and are only processed further if no muons are entering the water tank with energy higher than 4 GeV and projected path length in the water superior to 2 m since these would be rejected by the WCV. We find that for a generated livetime of 48.7 yr, the FLUKA simulation predicts 1388 events in which any particle reaches the TPC. None of the 1388 events passes the simulated veto cuts. Only one event is a single neutron in the TPC with no other accompanying particles. In 6 more events, a neutron is accompanied by one

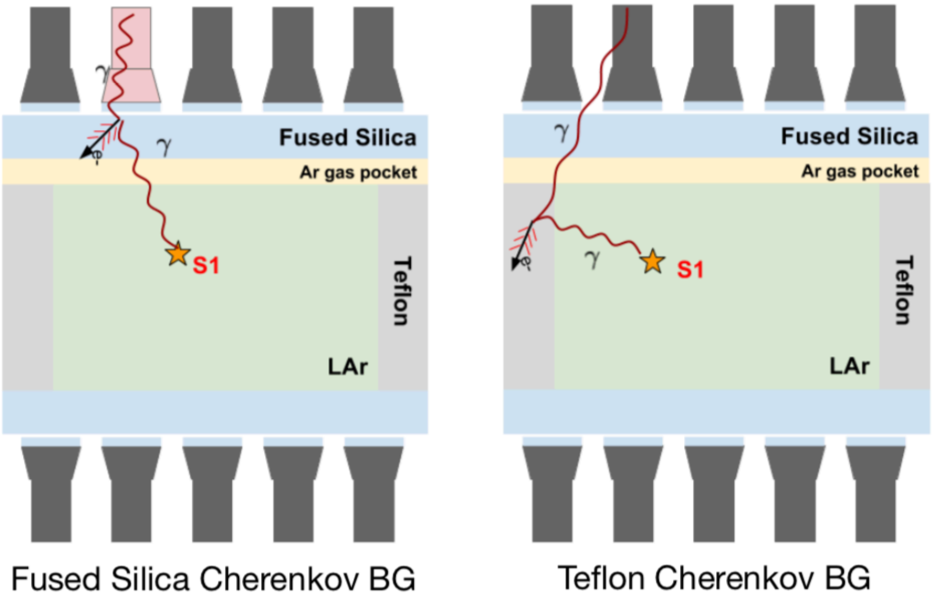

Figure 2.14 – Schematic illustrating the process of Cerenkov backgrounds production in DarkSide-50.

other particle that is not an easily rejected muon, typically a γ-ray or another neutron. None of these 7 events have TPC energy deposits in our WIMP-search region. If we take a 90% CL upper limit of 2.3 of 1388 events reaching the TPC passing the veto cuts and take the 7 (neutron+ $\leq$1 particle) events as a conservative upper limit on the number of neutron events passing TPC cuts in 48.7 yr, we predict < 0.00035 cosmogenic neutron events passing all cuts in the present WIMP search. When we include the muons with long path lengths and high energies in the WCV, the rate of simulated single-scatter neutron events in the TPC depositing energy in the WIMP search region rises to $\sim$2 per year.

Cuts designed:

- **CosmicMu:** rejects events with a WCV signal higher than 400PE or an LSV signal higher than 2000 PE, integrated over the full 200 μs acquisition window. This vetos cosmic-ray muons or their showers and thus cosmogenic neutrons.
- **CosmoActiv*:** a"cosmic ray activation veto" is applied if a TPC event occurs within 0.6 s (shorter than in previous analyses) following a triggered event failing the CosmicMu cut. This removes some delayed neutrons produced by cosmic-ray-activated isotopes in the detectors.

2.6.3.6 Cerenkov events

Cerenkov events are not an obvious background source for dual-phase TPCs. The Cerenkov light production of electrons in the active argon itself is small compared to scintillation light, and Cerenkov electrons produced in detector components besides argon have f_{90} = 1.0 and S2/S1 = 0, different from both electron- and nuclear-recoils. However, in a small subset of events, for

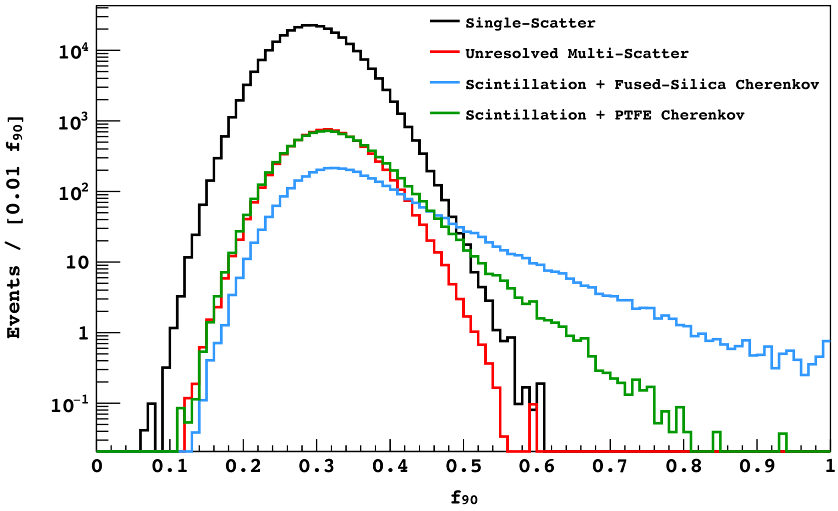

Figure 2.15 – f_{90} profiles computed from G4DS for of single-scatter, unresolved multiple-scatter, scintillation+fused silica (FS) Cerenkov, and scintillation+Teflon Cerenkov 2-pulse events with 100 < S1 < 180 events.

example beta decays followed by the production of a bremsstrahlung photon, gamma rays which produce multiple Compton scatters, or gamma-ray cascades, a relatively energetic beta is produced in an inert detector component,and another, lower energy, electron is produced in the argon active volume. In this situation, the Cerenkov light from the first electron combines with the argon scintillation event from the second to produce a ”real-looking” event with both a higher f_{90} and a lower S2/S1 than an electron recoil. Figure 2.14 highlights the process of Cerenkov backgrounds production. Studies have been conducted with G4DS to estimate the shape of f_{90} including the Cerenkov contribution, as shown in Figure 2.15.The increase of f_{90} due to Cerenkov light is clearly visible on the figure.

The cuts designed to remove Cerenkov backgrounds are detailed below.

ER and Cerenkov cuts:

- **tdrift:** vertical fiducialization via the time between S1 and S2 (t_{drift}) is effective against γ rays from the PMTs, their primary source. We use the same vertical fiducialization as in the previous analyses, removing 40μs of drift time (4 cm) from the top and bottom of the active volume. Though the ER background determined the location of the cut, it is also clearly important for surface background, notably serving to eliminate α decays occurring on the TPC cathode and grid.

- **S1pMaxFrac:** removes events with S1 too concentrated in any one PMT. These events are likely to have interactions giving Cherenkov light in the fused silica PMT and TPC windows. A variant of this cut was used in past analyses, but it was modified for the current analysis to use only prompt light, boosting its effectiveness as a Cherenkov discriminant. This cut is extremely effective against fused silica Cherenkov, leaving scintillation+Cerenkov in the Teflon reflector as the main surviving ER background.

- **S1NLL:** squeezes further rejection from the S1 PMT pattern, targeting the multi-sited nature of scintillation+Teflon Cerenkov events. The pattern of S1 light on the PMT arrays is required to be consistent with the reconstructed x-y position via a negative-log-likelihood comparison to templates derived from AAr data (dominated by single-sited ^{39}Ar β decays).
- **RadialFid*:** a radial fiducial cut. The radial cut is a drift-time-dependent radial contour chosen to reject a fixed fraction of G4DS-simulated scintillation+Teflon Cerenkov events in each drift time bin. The final cut varies from 23 mm from the wall at the top and bottom of the TPC to 4 mm from the wall at the center.

2.6.3.7 Surviving background summary

Background	Events surviving all cuts
Surface Type 1	0.0006 ± 0.0001
Surface Type 2	0.00092 ± 0.00004
Radiogenic neutrons	< 0.005
Cosmogenic neutrons	< 0.00035
Electron recoil	0.08 ± 0.04
Total	**0:09 ± 0.04**

Table 2.2 – Predicted backgrounds surviving all cuts. Note that the ER background includes the scintillation+Cherenkov background. The f_{90} vs. S1 search box is defined to give 0.08± 0.04 surviving ER background events.

A summary of the predicted backgrounds surviving all cuts in the full exposure is given in Table 2.2.

2.6.4 High mass WIMPs search results

Once the backgrounds design goal was achieved and the WIMP box defined, data were unblinded. Unblinding basically meant changing the access permissions for the data files. Figure 2.16 presents the full dataset after full unblinding and selection cuts, the blue shaded region representing the WIMP box. As it is clearly visible, no events were observed in the WIMP search region.

Considering the absence of signal in the WIMP search region, a limit on the spin-independent DM-nucleon scattering. This limit was derived assuming the standard isothermal WIMP halo model (see Chapter 1). The background- and signal-free result is consistent with up to 2.3 expected DM-nucleon scatters (90% C.L.), which sets an upper limit on the spin-independent scattering cross-section at $1.14 \times 10^{44} cm^2$) for $M_{WIMP} = 100 GeV/c^2$. Figure 2.17 compares this limit to those obtained by other experiments.

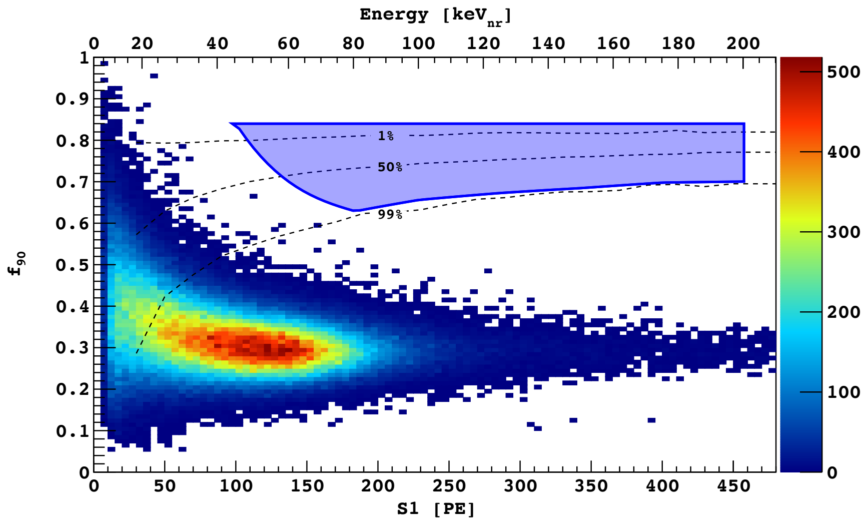

Figure 2.16 – Final 532.4 live days high mass WIMPs search dataset. The solid blue outline indicates the DM search region. The 1%, 50%, and 99% f_{90} acceptance contours for nuclear recoils, as derived from fits to our ^{241}AmBe calibration data, are shown as the dashed lines.

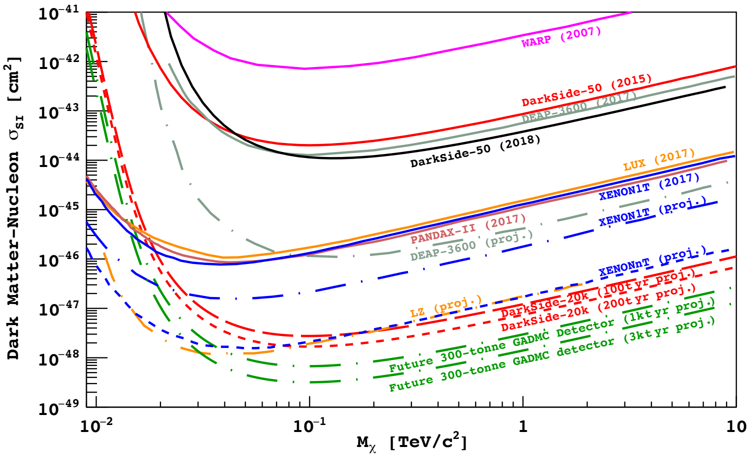

Figure 2.17 – Spin-independent DM-nucleon cross section 90% C.L. exclusion limits, compared with selected results and projections.

2.7 Towards the future: the Global Argon Dark Matter Collaboration

Given the strong potential for the LAr technology to push the sensitivity for WIMP detection several orders of magnitude beyond current levels, scientists from all the major groups currently working with this technology (ArDM, DarkSide-50, DEAP-3600, and MiniCLEAN) have joined the Global Argon Dark Matter Collaboration (GADMC) to pursue a sequence of future experiments to follow this potential. DarkSide-20k will be the first step of this new collaboration.

2.7.1 DarkSide-20k

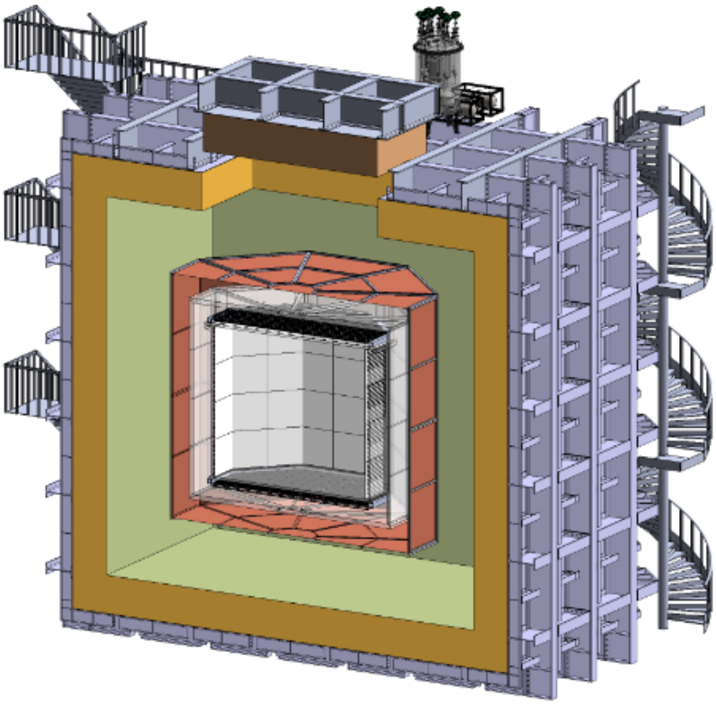

Figure 2.18 – Layout of the design of the DarkSide-20k detector.

DarkSide is a staged program to detect dark matter. The current running detector, DarkSide-50, will be replaced in 2021 by the next generation: DarkSide-20k. DarkSide-20k will be filled with 30 tonnes of underground purified liquid argon. DS-20k will also be installed in the LNGS facilities. The light will be collected by Silicon PhotoMultipliers (SiPM). This technology has higher photo-detection efficiency and a much better single-photon resolution than regular PMTs, they also operate at lower bias voltages. They also emit less neutrons than regular PMTs. To minimize environmental impact, DS-20k will not rely on an organic scintillator for its veto. We will build a cryostat based on the technology developed for ProtoDUNE, filled with AAr and that will also act as neutron veto.

DarkSide-20k will have ultra-low backgrounds, with the ability to measure its backgrounds in situ, and sensitivity to WIMP-nucleon cross sections of $1.2 \times 10^{-XXX47} cm^2$ ($1.1 \times 10^{-XXX46} cm^2$) for WIMPs of 1 TeV/$c^2$(10 TeV/$c^2$) mass, to be achieved during 5 yr run with exposure of 100 t yr as shown on Figure 2.17.

A 1 ton prototype, DarkSide-Proto, is under construction to be installed at CERN. This prototype will allow for the testing of the technologies that will be deployed for DarkSide-20k.

During my Ph.D., I participated in the design studies to ensure that DS-20k will be background-free.

2.7.2 DarkSide-20k veto design study

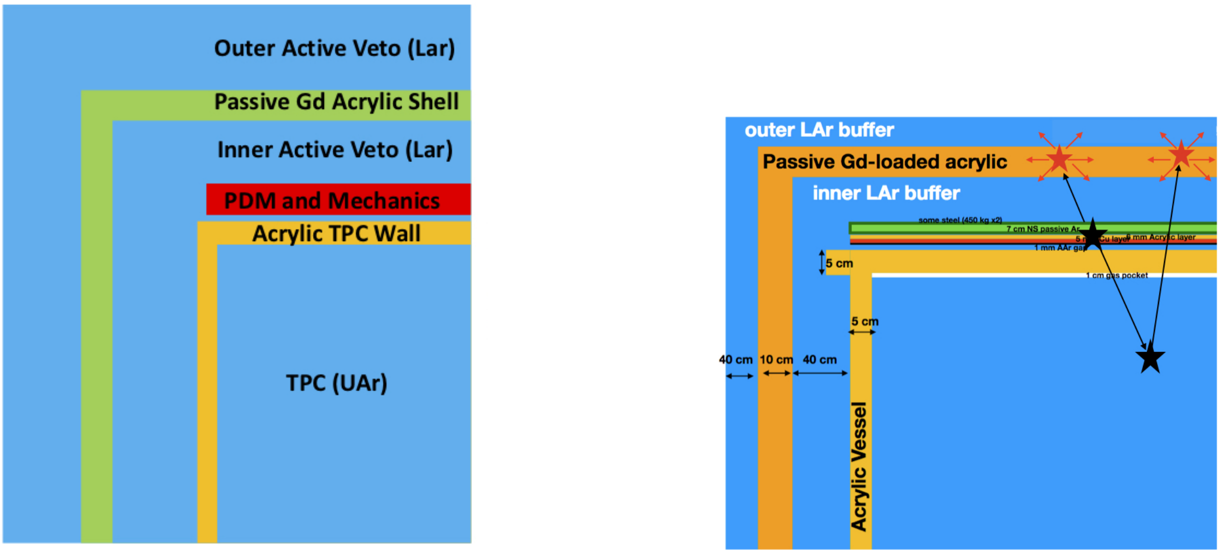

(a) Schematic view of the DarkSide-20k veto detector

(b) Simulation pattern of neutrons in the SiPMs

Figure 2.19

Relying on the implementation of the ProtoDUNE cryostat, DarkSide-20k will use AAr as its veto material. The veto design includes three different volumes: a passive octagonal acrylic shell loaded with gadolinium called the GdA and mounted around the TPC and providing 4πcoverage, a 40 cm thick inner volume of active liquid AAr called the Inner Argon Buffer (IAB) and sandwiched between the TPC vessel and the GdA, a 40 cm thick outer active volume of AAr called the Outer Argon Buffer (OAB) contained between the GdA (see Figure 2.19b).

One of the key points is to determine the optimal thicknesses for each of these elements. To study that, we generated neutrons in the SIPM (see Figure 2.19b), varying the acrylic shell and buffers thicknesses. We then applied cuts to the energy deposited in the TPC and the veto, to determine the fraction of surviving events. We selected single scatter neutrons in the TPC, with an energy comprised between 7.5 keV and 50 keV, and a fiducial cut of 30 cm. We also selected neutrons in the veto by requiring to have less than 800 keV (100 keV) deposited in the IAB (OAB).

Figure 2.20 shows the events that are discarded by the applied cuts, which are the events that will be tagged by the veto.

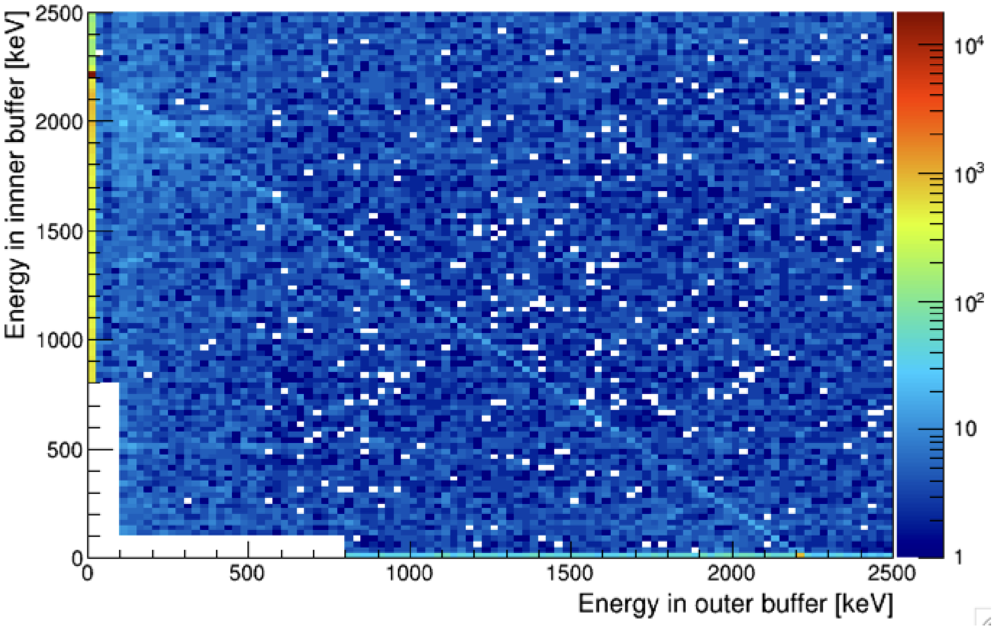

Figure 2.20 – Cuts applied to the energy deposited in the veto for the veto dimensions study. The white region represents the event that are not tagged by the veto.

Table 2.3 summarizes the fraction of surviving events for the different tested configurations. We can straightforwardly exclude the possibilities of a 5 or 20 cm plastic shell since it gives the worst results. The best option, according to this study, seems to be a 10 cm thick GdA. Also, we can note the limited influence of the AAr buffers' thickness.

	5 cm plastic	10 cm plastic	15 cm plastic	20 cm plastic
20 cm LAr		2.63×10^5	2.77×10^5	3.13×10^5
25 cm LAr		2.57×10^5	2.58×10^5	2.91×10^5
30 cm LAr		2.53×10^5	2.71×10^5	2.91×10^5
35 cm LAr	3.96×10^5	2.41×10^5	2.56×10^5	
40 cm LAr	3.91×10^5	2.43×10^5	2.58×10^5	
45 cm LAr	3.64×10^5	2.45×10^5	2.4×10^5	
50 cm LAr	3.49×10^5	2.33×10^5	2.42×10^5	

Table 2.3 – Fraction of surviving events after veto cuts, for different veto configurations.

The possibility of applying cuts to only one of the buffers has also been studied. Indeed, it would allow to instrument only one of the buffers, leading to reduced cost and internal radioactivity.

Figure 2.21 shows the fraction of surviving events cutting only on the IAB. A GdA thickness of 10 cm has been considered for this study. The drop found in veto efficiency is not dramatic. The results are a factor 1.5 to 3 worse than the two buffers cut case, but are still within expected performances. However, further studies of this cut are required.

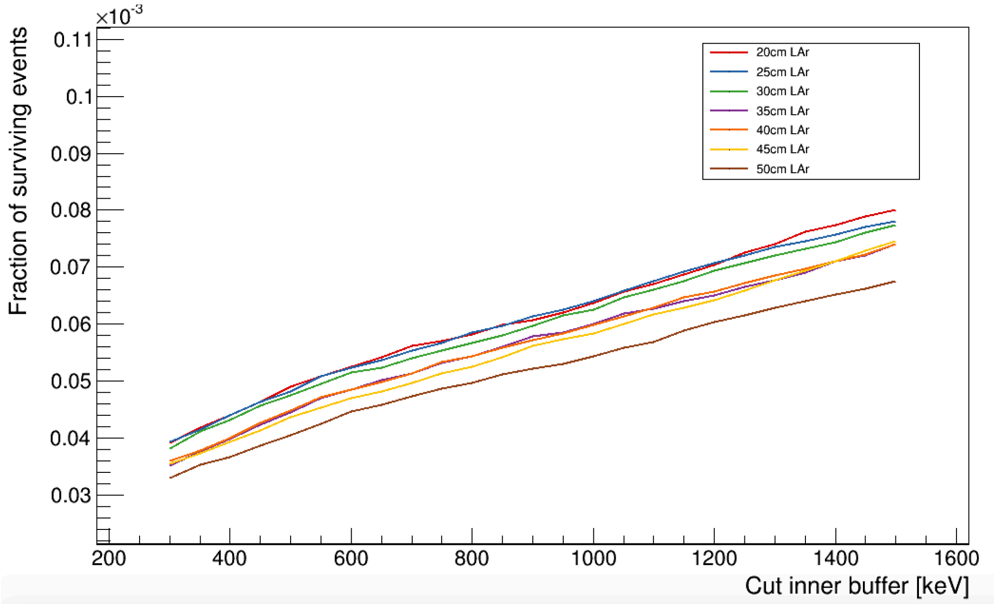

Figure 2.21 – Fraction of surviving events after veto cuts in the case of a single buffer cut, as the function of the cut threshold and buffer thickness. A GdA thickness of 10 cm has been considered for this study.

2.7.3 DarkSide-Proto and low mass dark matter searches

The DarkSide-Proto detector will be a demonstrator for the technologies implemented in DarkSide-20k, in particular for the photo-detection modules (PDMs), and will be installed at CERN. Since it will use low-background SiPM-based PDMs, a low-background cryostat, and an ultra-low background argon target purified by the Aria cryogenic distillation column, DS-Proto will be an excellent target for low mass dark matter searches. The world-leading low-mass results of DS-50 were enabled by the study of the (sole) ionization signal from very low energy events (see Chapter 5). The analysis threshold is of 100 eV_{ee}(600 eV_{nr}), corresponding to 4 electrons extracted from the liquid target, with each electron producing, on average, 23 PE. The residual background above 7 electrons(1.2 keV_{nr}) in DS-50 is completely characterized and accounted for by known sources. The DS-LM TPC will be a scaled-down version of that of DS-20k, operated in a low radioactivity copper container, and within an AAr active veto. Thanks to the Aria cryogenic distillation column, we are able to project the complete removal of ^{85}Kr and the reduction of ^{39}Ar, for small, tonne-size batches, to the level of 1 μBq/kg. The limiting low-energy background from PDMs can be reduced by the use of ultra-pure light guides and by planned abatements of the radioactivity of the PDMs components.

2.7.4 Argo

In the farther future, a 300t LAr detector, Argo, should be built to explore even more of the dark matter parameter space. It will increase the sensitivity of DS-20k by a factor 15, with an exposure of 3000 t yr.The experiment is scheduled to start around 2028. Argo will have a strong potential for discovery, and if dark matter interactions are observed with cross-sections above the neutrino floor, the potential for elucidating the nature of the dark matter particle, namely its mass and interaction cross-section. Argo would allow other important measurements beyond the dark matter search, such as measurement of medium-energy solar neutrinos or the flavour-blind measurement of neutrino bursts associated with supernovae.

2.8 Conclusion

Noble liquids are excellent targets for WIMPs direct detection. Liquid xenon based dual-phase TPCs are the leading technology in this domain. However, the DarkSide experiment demonstrated the promising possibilities of liquid argon. Indeed, the extraction of underground argon, reducing the ER activity and the impressive discrimination power of the pulse shape discrimination are pleading in favor of LAr-based detectors.

The DarkSide collaboration, and now the Global Argon Dark Matter Collaboration, has an ambitious goal of becoming leaders in the direct dark matter search field. They advance towards this with a staged program, which most recent phase came to a conclusion in 2018. I presented in this chapter the high mass WIMP search analysis and results of the DarkSide-50 detector.

The next step of the DarkSide program is the DarkSide-20k detector. I discussed the design and new technologies that will be implemented in this detector, as well as a study of the optimisation of its veto dimensions.

Part II

Characterisation of the LAr response: the ARIS experiment

Chapter 3

The ARIS experiment

Contents

A critical aspect to LAr TPC dark matter search experiments is the limited knowledge of the LAr response for recoil energies below 100 keV, in both the scintillation and ionisation channels and as a function of the drift electric field. It is particularly important to understand the energy scale of nuclear and electronic recoils, in other words, how we relate the energy reconstructed by the detector (S1) to the real recoil energy. This relation depends on different parameters, like the photoelectron yield, the electric field or the relative scintillation efficiency between nuclear and electronic recoils. In particular, the effect of the recombination probability is non-linear with the recoil energy and has to be measured. There are discrepancies in the measurement of the LAr response parameters at low energies, like the relative scintillation efficiency of NR compared to ER. These discrepancies are a huge source of systematics for WIMP searches in LAr.

I will here present a characterisation of the LAr response for low energy recoils done by the ARIS collaboration in 2016. I will first describe the energy scale in noble liquids. I will then discuss the different calibration methods, before detailing the ARIS calibration experiment and its results. I, in particular, participated in the commissioning, data taking, data selection, study of systematics and decommissioning of the detector.

3.1 Energy response in noble liquids

3.1.1 Ionisation and scintillation in noble liquids

As discussed in Chapter 2, the measured S1 and S2 signals are not an exact representation of the recoil energy. When a particle interacts in a noble liquid, its energy can be deposited via two channels: ionisation, excitation. It will result in the creation of N_{ex} excited (excitons) and N_i ionised (ions) atoms together. Some sub-excitation free electrons are also released. Secondary elastic collisions can be induced by secondary nuclear recoils or sub-excitation electrons. These interactions will increase the temperature of the medium and dissipate some of the energy as heat, which is the so-called *quenching*. I will here be interested in the repartition of the energy between these different processes.

In the case of an electron recoil, the energy lost in the LAr by an energetic particle, E_{dep}, can be split between excitation and ionisation,

$$E_{dep} = N_i E_i + N_{ex} E_{ex} \tag{3.1}$$

with N_i and N_{ex} the number of produced excitons and electron-ion pairs respectively, and E_i and E_{ex} are the average conversion energies for ionisation and excitation. It is possible to define the ionisation and excitation work functions $W_i = E/N_i$. We can also define an effective work function W, as

$$W = \frac{E}{N_i + N_{ex}} = \frac{W_i}{1 + \frac{N_{ex}}{N_i}} \tag{3.2}$$

We can fix $W = 19.5$ eV as suggested in [115].

Excitons can be produced either directly along the interaction track and at the interaction site or through recombination of the ionised electrons. Excitons then decay via the formation of an excited dimer, producing photons. When an electric field is applied, some electrons can escape recombination, at the expense of the scintillation light. The number of scintillation photons is then given by

$$N_\gamma = N_{ex} + R \times N_i \tag{3.3}$$

where R is the recombination probability of free electrons. R is expected to vary as a function of the electric field and the local ionisation density. The recombination probability plays an important role in the determination of the recoil energy from the visible signals in the TPC.

Let us define $\alpha = \frac{N_{ex}}{N_i}$. The value of α does not depend on the recoil energy, but varies with the track, and therefore on the particle type. For an electronic recoil, $\alpha = 0.21$ and for a nuclear recoil $\alpha = 1$.

The S1 signal seen in the TPC can then be expressed as a function of α:

$$S1 = \epsilon \ (\alpha + R) \times N_i \tag{3.4}$$

where ϵ is the light collection efficiency of the detector, and R the electron-ion recombination probability.

S1 depends on the light yield (LY), which is the amount of scintillation light produced. LY is measured using calibration sources. S1 also depends on the nature of the particle. In ERs, all the energy deposited goes into excitation or ionisation. But in NRs, some energy goes into heat, reducing the visible energy.

To be able to correctly reconstruct the recoil energy from the visible energy, it is then mandatory to constrain the energy scale parameters. In order to achieve that goal, calibration campaigns are performed in every noble liquid-based experiment.

3.2 Calibration methods

There are several methods available to calibrate the response of noble liquids. The ideal setup would be to insert a homogeneously distributed or isotropic source of nuclear/electronic recoils inside the TPC. However, it is extremely challenging in practice. The number of injectable sources is limited and can pose a problem of internal background afterwards. Introducing an arm with an isotropic source is also technically extremely difficult. Some methods also employ sources placed just outside the cryostat of the TPC, but then, the passive materials crossed by gammas and neutrons are disturbing the reconstruction of the deposited energy. Furthermore, the neutron sources are not always monochromatic, also leading to energy reconstruction issues.

3.2.1 Calibration with neutron sources

In recent years, the particle physics simulation libraries have become increasingly accurate for modeling low energy neutron interactions in matter. The full simulation of neutron source exposures to the large underground WIMP detectors, either with a mono-energetic neutron source, such as a D-D generator or with a broad spectrum neutron source, such as ^{252}Cf and ^{241}AmBe, can be used to compare with actual spectra from data. Due to the large sizes of those detectors compared to the neutron mean free path, both the data and the Monte Carlo simulations include single- and multiple-interaction events within the spectra. Fitting the experimentally obtained spectra to the simulated spectra allows the extraction of crucial energy scale calibration factors such as scintillation, ionisation or phonon yields of the WIMP detectors. The drawback of this method is the lack of features in the spectra of neutron energy deposition, as the neutron interactions are dominated by elastic scattering. The uncertainties in many inputs of the simulation, for instance, the neutron-nucleus differential cross sections and the WIMP detector trigger efficiencies at near-threshold energies, limits the precision of those energy scale calibrations.

3.2.2 Calibration with a neutron beam

Due to the many challenges of *in-situ* calibrations, most experiments rely on external calibrations, where a small scale test cell is exposed to a neutron source, in a controlled environment. A typical calibration detector is a few centimeters in each dimension and features a design with as little material as possible along the path of neutrons to reduce the chance that neutrons scatter another time before or after their interaction in the active volume of the detector. The recoil energy is then obtained by tagging the neutrons elastically scattered at known angles with neutron detectors. The gamma rays produced in association with the neutron beam pose a major challenge. Separating neutrons from gammas requires either a nanosecond resolution in the WIMP detector or a mean to tag gammas from the beam. To reach lower recoil energy means to narrow the neutron scattering angle. But this implies a higher uncertainty on the scattering angle. There are several production methods for the neutron beam. One is the D-D gun (deuterium onto a deuterated target). It produces relatively high energy neutrons (2.4 MeV). Besides large uncertainties for small recoil energies, the large neutron energy of the D-D generator will also result in inelastic scatterings of most targets. Despite these disadvantages and a lack of neutron bunching, not requiring the use of a proton accelerator makes the setup of the experiment more convenient. Neutrons can also be produced by the interaction of a heavy ion with protons. This method is exploited in two different types of setups: direct and inverse kinematics. In the first case, the protons are accelerated and projected onto the ion target. It produces an isotropic beam as well as neutrons of various energies. In the second case, the process is reversed, and the ions are the projectiles. In this configuration, the beam produced is highly collimated and quasi-monochromatic, depending on the ion energy. The inverse kinematics is the method used by the ARIS experiment. A variation on this method does not require the use of neutron tagging detectors. The full nuclear recoil spectrum is recorded and the calibration is determined using the correspondence between the endpoint of the nuclear recoil energy spectrum and the endpoint of the detector's response spectrum. Both endpoints are given by the elastic backscatter of the incident neutrons. This technique does not require the detector to bear good timing resolution for TOF selection, but a background subtraction is necessary for determining the endpoint. Measuring or modeling the background sometimes is a difficult task and subject to many uncertainties.

3.3 Previous experiments

I will here present the latest results in Xenon and Argon TPC calibrations.

3.3.1 In liquid Xenon: LUX D-D gun calibration

The LUX collaboration demonstrated the possibility to reconstruct the positions of twice-scattered neutron events to determine the nuclear recoil energy of the first neutron scatter in a large LXe TPC [116]. They measured the low energy ionisation and scintillation yield of liquid xenon down to unprecedented energies, the xenon scintillation endpoint and the ionisation to scintillation ratio.

The neutron source used was a D-D neutron gun, producing a collimated beam of 2.45 MeV neutrons. Neutrons produced by the D-D source were introduced into the TPC via an air-filled conduit spanning the LUX water tank.

The ionisation yield was measured as a function of nuclear recoil energy from 0.7 to 24.2 keV$_{nr}$, using neutrons that scatter twice in the active liquid xenon volume. The recoil energy was reconstructed directly from the scattering angle of the neutrons.

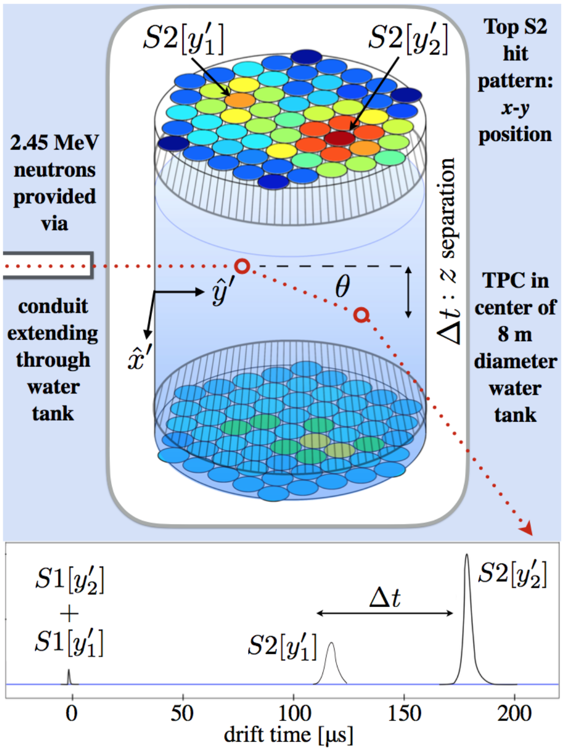

Figure 3.1 – LUX calibration setup

As single scatter model was developed, using the measured ionisation yield as an input. This model was then fitted onto single scatter data, using the observed S2 as a measure of energy.

This method allows us to avoid systematic errors due to the translation of an *ex-situ* measurement. However, this scheme can only be applied if there is a short path for neutrons to enter the sensitive volume. The spread in the direction and kinetic energy of the incoming neutrons and the uncertainties in the position reconstruction eventually limit the precision of the results.

Figure 3.2 shows different measurements of the relative scintillation efficiency in LXe.

3.3.2 In liquid Argon: SCENE

The reference external calibration in LAr was done by the SCENE collaboration, and is presented in [117].

They have used an isotropic neutron beam to characterise scintillation and ionisation signals produced by nuclear recoils between 10.3 and 57.3 keV in a LAr TPC with and without an elec-

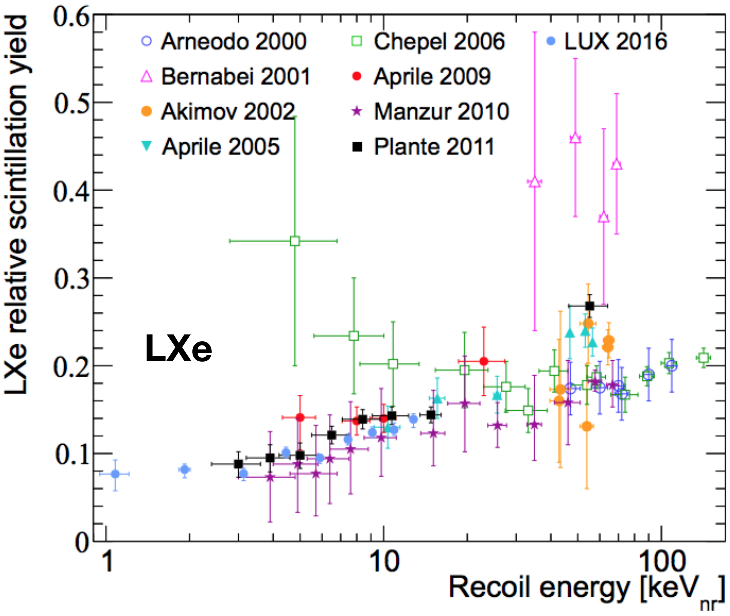

Figure 3.2 – Relative scintillation efficiency measured in LXe by several experiments. The LUX point are in light blue.

tric field. Scattered neutrons were detected in three liquid scintillator neutron detectors. These detectors were placed on a two-angle goniometer-style stand at a distance of 71 cm from the LAr target and at selected angles with respect to the beam direction. The angles determined both the energy of the nuclear recoils and the direction of the initial momentum of the recoils. A layout of the experimental setup is shown in Figure 3.3.

However, SCENE results were limited by the neutron beam characteristics. An isotropic neutron beam means a low neutron flux on the TPC and therefore low neutron scatter statistics. The beam not being collimated, neutrons reflected in the experimental room and then interacting in the TPC are an additional source of backgrounds. SCENE did not use a monochromatic neutron beam, so there was an incertitude on the initial energy of the scattering neutrons, increasing the incertitude on the recoil energy in the TPC.

Figure 3.4 presents nuclear recoils quenching measurements in LAr. A clear tension between experiments can be seen at low energy recoils. The results from SCENE suggest a quenching increasing at low energies, while MicroCLEAN and Creus et al. [118] hints a decreasing quenching effect. Each of these tendencies tend to agree with either the Mei model (see Section 4.2) or the NEST simulation (tuned for LXe). Further tests are required to determine precisely the behavior of the quenching down to very low energies.

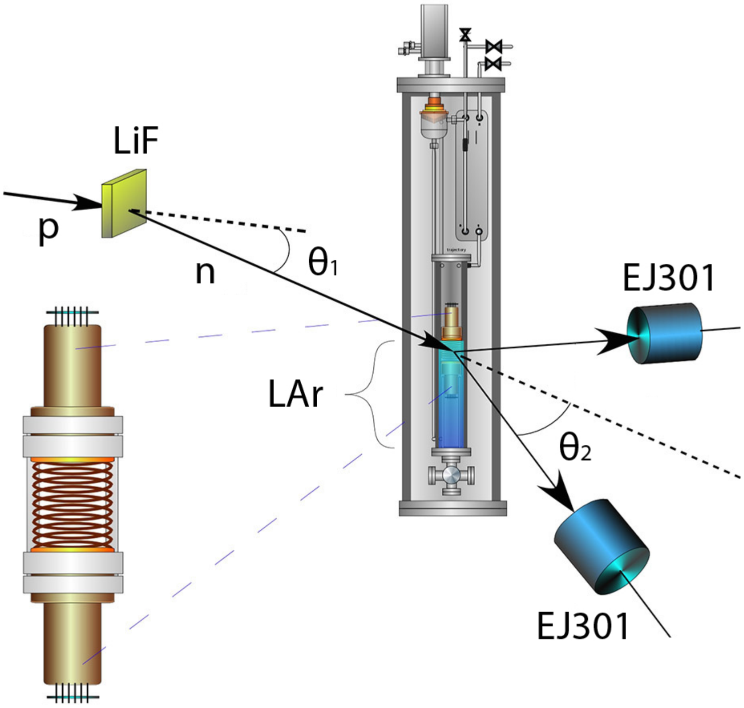

Figure 3.3 – Layout of the SCENE experiment apparatus.

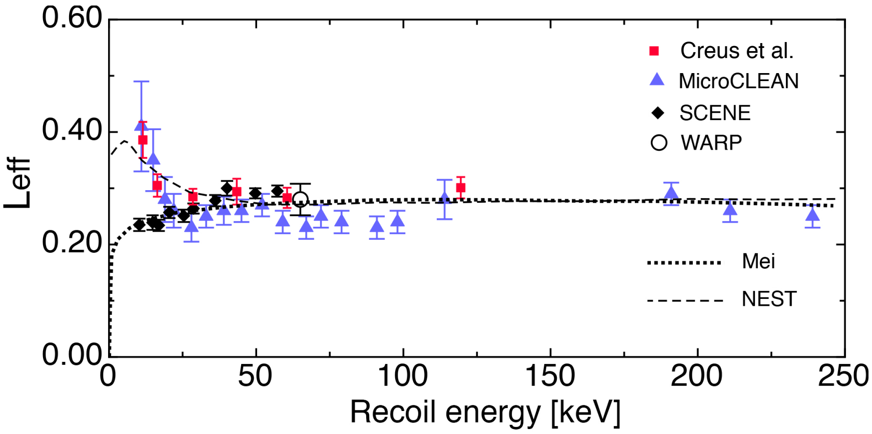

Figure 3.4 – Relative scintillation efficiency measured in LAr by several experiments.

3.4 ARIS experimental setup

The ARIS experiment was designed to study nuclear and electronic recoils in LAr, especially at low energies by exposing a small scale TPC to a neutron beam. Learning from the SCENE experiment, particular attention was given to the neutron beam in order to maximise the neutron flux and facilitate the recoil energy reconstruction. A complete simulation of the ARIS setup has been implemented in G4DS for purpose of design and analysis.

3.4.1 TPC and neutron detectors

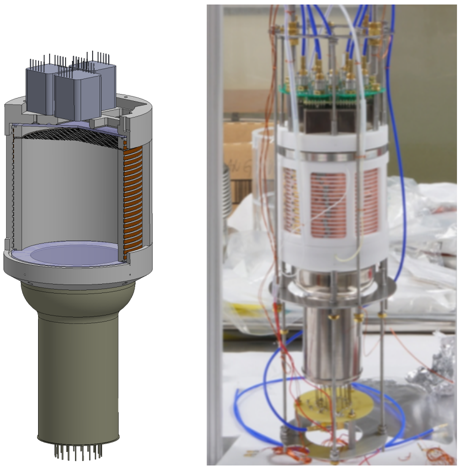

Figure 3.5 – Left panel: 3D drawing of the TPC. Right panel: picture of the TPC.

The ARIS TPC was designed to minimise multiple scatter interactions non-active materials along the beam line. The layout of the detector was based on the one of DarkSide-50, at a smaller scale, as shown on Figure 3.5. The ∼0.5 kg LAr active mass was housed in a 7.6 cm diameter, ∼1 cm thick PTFE cylinder. The inner surface of the PTFE is coated with TPB acting as a wavelength shifter.

The electric field is created by two 1.6 mm thick fused silica windows plated with indium tin oxide (ITO) and placed at the end-caps of the cylindrical volume. Outside the Teflon sleeve, a set of 2.5 mm thick copper rings connected by resistors in series ensures the field uniformity. The extraction field is created by a hexagonal stainless steel grid of 0.05 mm placed 1 cm below the anode. A stainless steel lipped ring pressed against the anode creates a diving bell to hold the gas pocket, which is produced by a PT100 acting as a bubbler underneath the diving bell. Evaporated argon is continuously purified with a getter and re-condensed by mean of a custom cold head.

Photons are collected by one 3-inch R11065 PMT below the cathode and an array of seven 1-inch R8520 PMTs above the anode. An optical fiber connected to a LED, powered by a pulse generator, is used to calibrate PMTs in single photoelectron regime, as shown in Figure 3.6.

Eight neutron detectors (NDs) are placed around the TPC to observe scattered neutrons, labeled from A0 to A7. The EDEN [119] NE213 liquid scintillator detectors cells are 20 cm diameter and

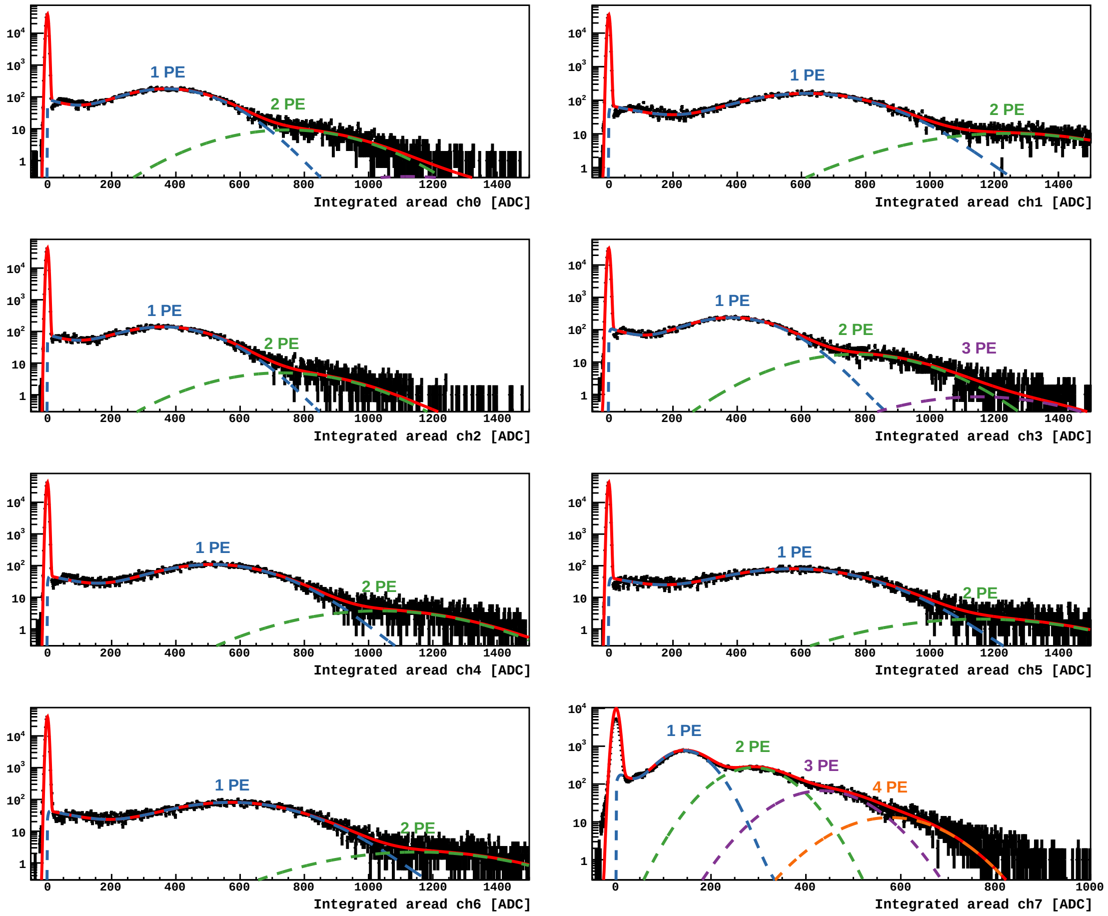

Figure 3.6 – Response of the ARIS PMTs to the LED pulses.

5 cm height cylinders. The walls of the cells are coated with NE561 reflector. At the back of the cell, a 6 mm thick glass window allows a PMT to observe the light output. Pulse shape discrimination is available for the NDs signal, providing a good neutron/γ discrimination (see Section 3.4.3.6). Distances between the NDs and the TPC range from 1.3 to 2.5 m, and angles with respect from beam direction range from 25.5 to 133.1 degrees. The NDs positions were thought to scan energies of interest considering WIMP searches while taking into account the experimental room constrains. The ND positions were determined with an accuracy of 2-3 mm depending on the ND. An inspection after the data taking identified a mismatch in the position of A2, that is reflected in larger systematics as it will be described in section 4.2. Table 3.1 summarises the recoil energies scanned by ARIS.

In order to maximise the statistics, the gas pocket was suppressed during the entire data taking. The drift time requires an acquisition window up to hundreds of microseconds, depending on the electric field, exposing the TPC to a large pile-up with accidental background. The lack of S2 signal, although preserving the electric field, allows to reduce the acquisition window to 10 μs and hence the background. At the same time, it does not prevent to infer the amplitude of the ionisation component thanks to the accurate determination of the recoil energy and recombination

	Scattering Angle [deg]	Mean NR Energy [keV]	Mean ER Energy [keV]
A0	25.5	7.1	42.0
A1	35.8	13.7	75.9
A2	41.2	17.8	85.8
A3	45.7	21.7	110.3
A4	64.2	40.5	174.5
A5	85.5	65.4	232.0
A6	113.2	98.1	282.7
A7	133.1	117.8	304.9

Table 3.1 – Scattering angles, NR mean energies for neutrons from $^7\text{Li}(p,n)^7\text{Be}$ reaction, and ER mean energies for γs emitted by $^7\text{Li}^*$ de-excitation, determined with Monte Carlo.

probability.

Signals from the TPC PMTs and A0–A7 are digitised by two CAEN V1720 boards at a 250 MHz frequency. The time of the beam pulses is also digitised at a 250 MHz frequency by a CAEN V1731 board. The board timestamps are synchronised by an external clock to allow time of flight measurements. The TPC trigger requires at least two PMTs fired in a 100 ns window. For each trigger, the TPC PMT waveforms, the neutron detectors waveforms, and the signal from the beam pulse are recorded. The acquisition window was 10 µs for the TPC PMTs and 7 µs for each ND. These signals are analysed by a reconstruction software based on the art framework [120] to extract observables from the recorded waveforms. First, fluctuations and drift of the baseline are tracked and subtracted from the raw signal waveforms. Next, waveforms from each PMT in the TPC are corrected for their single photoelectron response and summed together. Figure 3.7 shows the resulting waveforms. A pulse finder algorithm is applied to each summed waveform to identify the magnitude and start time of TPC and ND pulses. Finally, the reconstructed waveform and pulse information is used to extract S1, pulse shape discrimination parameters for both the TPC and NDs and time-of-flight (TOF) parameters.

Data were taken in October 2016, for 12 days, in two modes: double coincidences between the beam pulse and TPC, and triple coincidence including NDs. The latter data set provides nuclear and electron recoils at defined energies, as quoted in table 3.1. The double coincidence data set, which provides continuous spectra, is useful for investigating the time response of LAr and for calibration purposes. For each running mode data were taken at various electric fields in the TPC, from 0 to 500 V/cm. A Geant4-based MC simulation of the experimental setup has been developed including the materials, size, and relative placement of the TPC, PMTs, dewar, and A0–A7 detectors as described above. This simulation provides a spectrum of nuclear and electron recoil energies from coincidences between the TPC and A0–A7 detectors, with mean values listed in table 3.1.

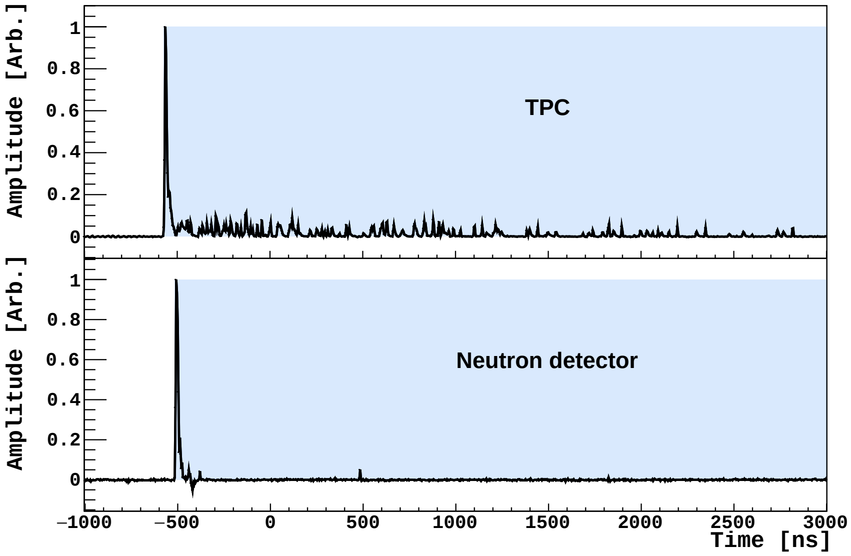

Figure 3.7 – Waveforms for the TPC and ND signals.

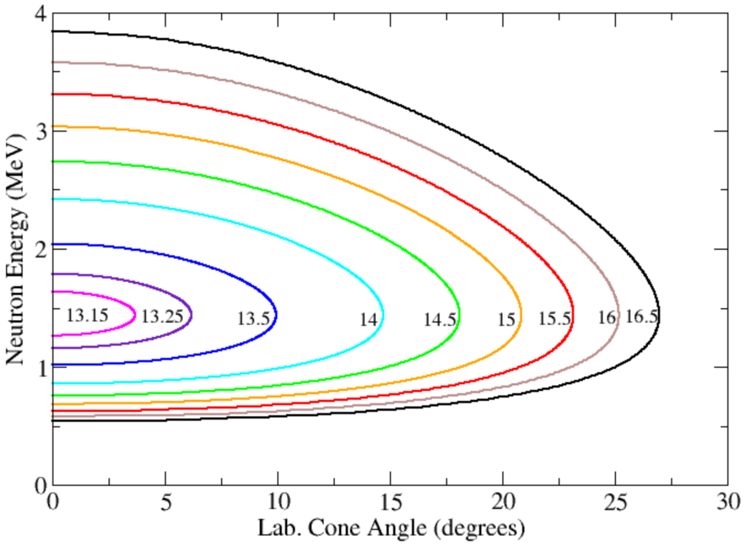

Figure 3.8 – Kinematic curves of the produced neutrons. Each curve is produced for a different ^{7}Li energy.

3.4.2 The LICORNE neutron beam

Neutrons were provided by the LICORNE beam of Institut de Physique Nucléaire d'Orsay (IPNO). LICORNE produces a very collimated neutron beam, thanks to the inverse kinematics reaction where heavy ions are projected onto a proton target (usually hydrogen). The Tandem accelerator of IPNO provides an intense beam of ^{7}Li ions, with energies ranging from 13 to 17 MeV. The energy of the ^{7}Li nucleus determines the characteristics (energy and cone opening angle) of the produced beam, as shown in Figure 3.8. The whole ARIS campaign was done with a ^{7}Li energy set at 14.63 MeV.

The proton target is a small hydrogen cell, separated from the beam pipe by a thin tantalum foil where ^{7}Li nuclei lose part of their energy. Since the foil thickness is unknown, the exact ^{7}Li energy at the entrance of the target, and hence the neutron kinematics, had to be measured in a dedicated campaign. To do this, one ND was placed at a distance of 3 m from the source at different angles, varying between 0 and 15°. The relative neutron beam intensity, with respect to the one at 0°, measured at each angle was compared with GEANT4 simulations, assuming different thicknesses of the tantalum foil.

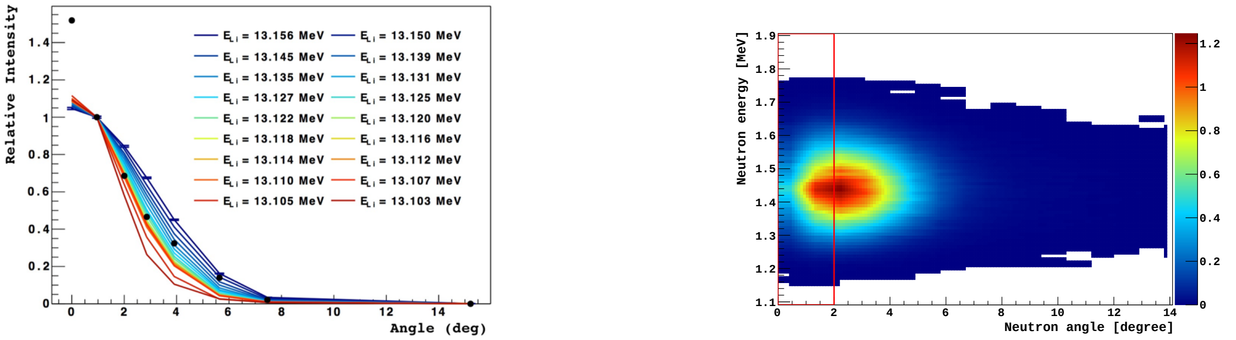

(a) Beam profile as a function of the opening angle for different ^{7}Li energies at the entrance of the gas cell. The black dots represent the profile measured by ARIS.

(b) Neutron kinematics for ^{7}Li energy of 13.13 MeV at the entrance of the Hydrogen target from Monte Carlo simulations. The red box defines the geometrical acceptance of the TPC.

Figure 3.9

The best fit of the beam profile was obtained for a thickness of $2.06 \pm 0.08\,\mu$m, corresponding to a mean ^{7}Li energy in the Hydrogen target of $13.13^{+0.02}_{-0.01}$ MeV, as shown on Figure 3.9a. The corresponding neutron kinematics is illustrated in Figure 3.9b. The uncertainties on the ^{7}Li energy include the statistical error and a conservative estimation of the systematics from the initial energy of the ^{7}Li beam.

In addition to neutrons, LICORNE emits an isotropic source of 478 keV γs in the center of mass from the de-excitation of ^{7}Li*. ^{7}Li*, which has a half-life of 105 fs, can be created either by ^{7}Be decay or by excitation of ^{7}Li while it is passing through the beam line materials. In the first case, given the ∼53 days half-life of the ^{7}Be, the γ emission is not correlated with the beam pulse and constitutes a uniformly distributed accidental background within the beam pulse. Considering the very short half-life of ^{7}Li*, we can consider that γ-rays from ^{7}Li* are emitted immediately after the excitation and then in correlation with the beam pulse. We refer to this component as the γ-flash. The γs are subjected to a relativistic boost due to the motion of the ^{7}Li* nuclei, which increases their energy up to 6% for a ^{7}Li energy of 14.63 MeV. Since ^{7}Li* atoms lose an unknown amount of energy in the source materials adding uncertainty on the energy at which the γs are emitted. A mean boost of 3% and, conservatively, a σ of 3% are then assumed, resulting in a γ energy of 492 ± 15 keV.

The distance between the beam and the TPC has been optimised to maximise the flux of neutrons reaching the LAr, using the GEANT4 simulation of the setup. The γ background has also been taken into account, with a requirement of 0.1 γ per acquisition gate. The distance of 1 m has been selected. This corresponds to a neutron flux reaching the TPC of the order of 10^4 Hz. The solid angle geometrically selected by the TPC is then of $<2°$, reducing the neutron kinematics available as shown in Figure 3.9b.

Time of flight measurements with a detector placed in front of the beam allowed to constrain the mean neutron energy. The mean neutron energy in this region is 1.45 MeV with an RMS of 85 keV, as shown in Figure 3.10.

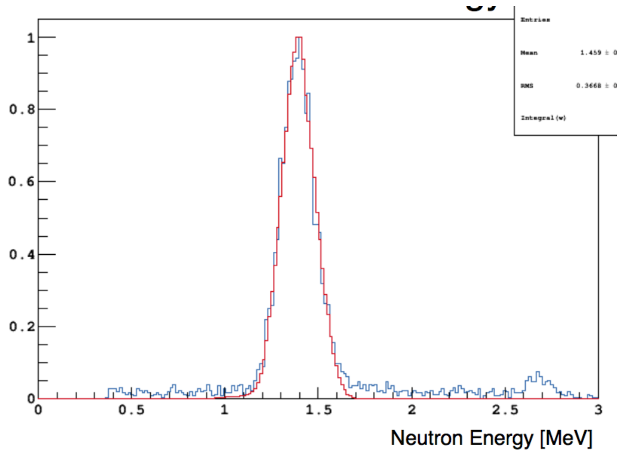

Figure 3.10 – Distribution of the beam neutrons energies from the conversion of the time of flight measurement.

3.4.3 Detectors calibration

3.4.3.1 Monte-Carlo and detector response modeling

The Monte-Carlo simulation of the detector can simulate the different energy deposits in the TPC and extract the energy deposited, E_{vis}. However, this energy has to be converted into an S1 signal, taking into account the different aspects of the detector response.

1- Poisson distribution: In the low energy regime, the number of photoelectrons n_{phe} for a given visible energy E_{vis} is expected to follow a Poisson distribution with a mean of $E_{vis} \times LY$. E_{vis} is uniformly distributed from 0 to 120 keV.

2- Top/bottom asymmetry: The vertical non-uniformity of the light collection, the top/bottom asymmetry, has to be considered as well. The light collection efficiency varies as a function of the event z-coordinate which contributes to the detector resolution. The light collection is expected to be larger at the bottom because the 3-inch PMT provides a larger optical coverage and quantum efficiency with respect to the 1-inch PMT array at the top. As the top/bottom asymmetry, noted TBA, is correlated with the z-coordinate, it can be used to extract variations of the light collection efficiency. Indeed, in ^{241}Am calibration data, a variation of the LY is observed as a function of the TBA. The TBA observable is defined as the ratio between the light collected by the bottom PMT with respect to the total.

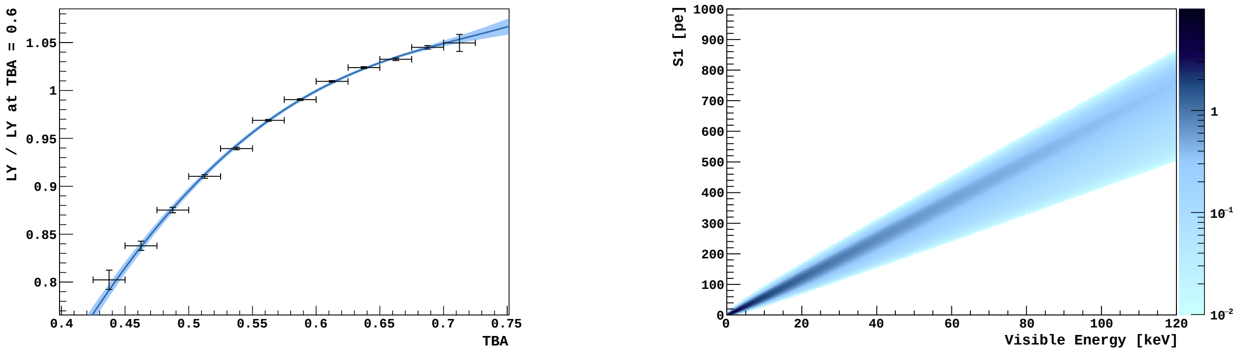

(a) Light collection efficiency as function of the TBA.

(b) TPC optical response as a function of visible energy, defined as proportional to the detected light, from the toy Monte Carlo approach described in the text.

Figure 3.11

Figure 3.11a shows the light response as a function of the TBA. It is determined as the ratio of the mean S1 of the fitted ^{241}Am γ peaks, with respect to TBA=0.6. This reference point has been chosen as it is where the maximum of events are collected for a source placed at the TPC center.

3- Single Electron Response: Finally, the PMT response is also included. It is measured by fitting the single electron response (SER), obtained with LED (see Figure 3.6), and constantly monitored along all the data taking. For the ith detected photoelectron, the associated PMT charge Q_i is randomly generated from the SER distribution. S1 is finally obtained by summing all the normalised PMT charge as: $\mathrm{S1} = n_{phe} \times Q_i/G$, where G is the PMT gain. It allows us to take into account the contribution of the SER to the detector resolution.

To easily include all these effects in the analysis, response maps are generated to model the detector behavior, as shown in Figure 3.11b.

3.4.3.2 Light yield

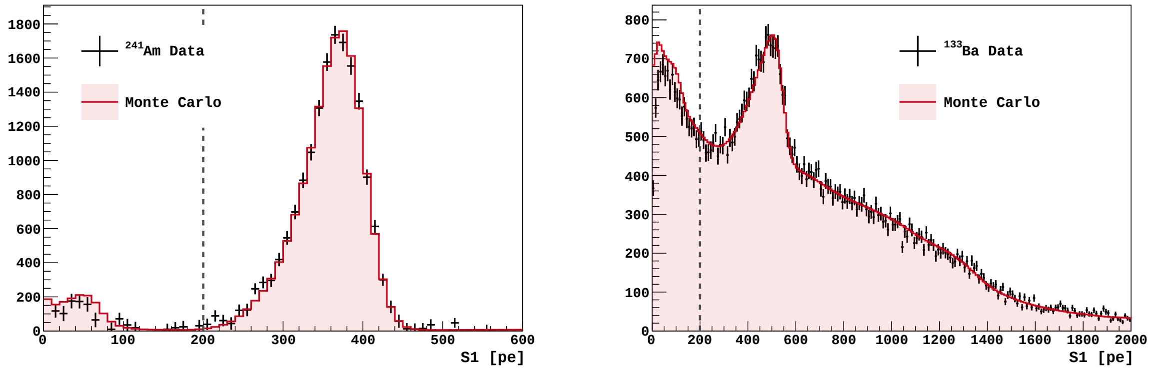

Figure 3.12 – ^{241}Am (left) and ^{133}Ba (right) sources calibration of the TPC light-yield at 0 V/cm and their best fit. Vertical dashed line represents the low threshold for the fit interval.

During the data taking, daily calibrations with ^{241}Am and ^{133}Ba sources were conducted. The data were then fitted with simulated distributions. To fit the data with the MC, the response maps have been generated for each data set by fixing the LY to an arbitrary value LY$_{ref}$. Thus, to generate the S1 spectrum for a given LY, the energy scale of the MC histogram must be rescaled by a factor LY/LY$_{ref}$. A standard χ^2 minimisation with two free parameters, i.e. the LY and a normalisation factor, has been used.

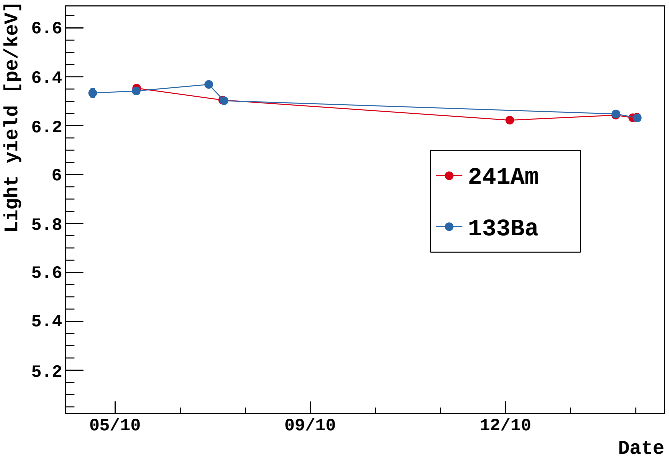

Figure 3.13 – Evolution of the measured light yield over the course of the data taking from ^{241}Am (red curve) and ^{133}Ba (blue curve).

The best-fit is obtained for LY = 6.35±0.05 pe/keV. As it is visible in Figure 3.12, data and Monte Carlo are in excellent agreement. This is confirmed by the $\chi^2/ndf \sim 1$ obtained for both sources. This result shows that all the main contributions to the detector resolution are included in our modeling. The main systematic error on the LY is due to LY decreasing of 1.8% observed during the data taking, as shown in Figure 3.13. This decrease is likely due to a degradation of the LAr purity.

The light yield obtained with this calibration is the reference light yield used in all the analyses.

3.4.3.3 TPC trigger efficiency

A specific campaign was performed to measure the TPC trigger efficiency. The TPC is triggered when at least two PMTs are fired within 100 ns. It required a slightly different setup compared to the main analysis, using the decays of a ^{22}Na source. In most cases (99.94%) ^{22}Na decays to excited ^{22}Ne emitting a positron. ^{22}Ne then goes to the ground state emitting a 1.27 MeV γ. The ^{22}Na source was placed on the external wall of the cryostat and two detectors, placed as shown in Figure 3.14a at a distance of $\sim$ 2 cm from the source, observed the photons exiting the TPC.

One was located on the TPC-^{22}Na source axis, in order to detect one of the two back-to-back 0.511 MeV γs from the positron annihilation, and the second rotated with respect to the same axis, to detect the isotropic 1.27 MeV γ. Since the excited state has a lifetime of only 3.7 ps, very fast

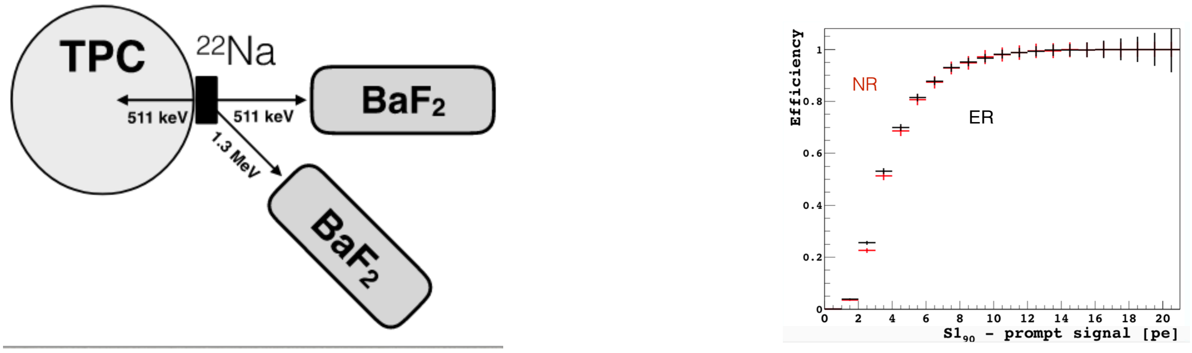

(a) Trigger efficiency measurement setup (top view).

(b) Toy Monte-Carlo for the efficiency as a function of $S1_{100}$ for ERs and NRs.

Figure 3.14

scintillators are needed. That is why ARIS used two BaF_2 scintillators, which fulfill this criterion, for this measurement.

This configuration ensures that the second 0.511 MeV γ is emitted toward the TPC center when both scintillators are triggered. Offline cuts on the BaF_2 signals optimise the selection of 0.511 MeV γ-rays directed toward the TPC center.

The trigger efficiency is then estimated looking at the number of events selected in the BaF_2 that also triggered the TPC. A dependence of the trigger efficiency on the TBA is expected since, as previously mentioned, the light collection is larger at the bottom. The trigger efficiency is then evaluated in three differents TBA regions.

Measuring the trigger efficiency with ER events presents a problem when applying the results to NR data because of the different pulse shapes. If we look at a NR and ER event with the same S1 value, the NR event will have a higher probability of exceeding the trigger threshold due to the pulse containing a higher percentage of the signal in the prompt region. To take into account this effect, we create a new light collection variable called $S1_{100}$. This is a measurement of the photoelectrons collected in the 100 ns of the majority trigger window.

Measuring trigger efficiency as a function of $S1_{100}$ produces a result that is independent of the interaction type, and thus can be applied from the calibration directly to the data, as illustrated in Figure 3.14b.

Figure 3.15 shows the trigger efficiency for the three TBA regions considered. Data are corrected on an event-by-event basis, by evaluating the correspondent $S1_{100}$ value, as shown in figure 3.16 for NR sample selected by A0 with the lowest mean energy (7.1 keV_{nr}), and where the impact of the trigger efficiency is expected to be maximal.

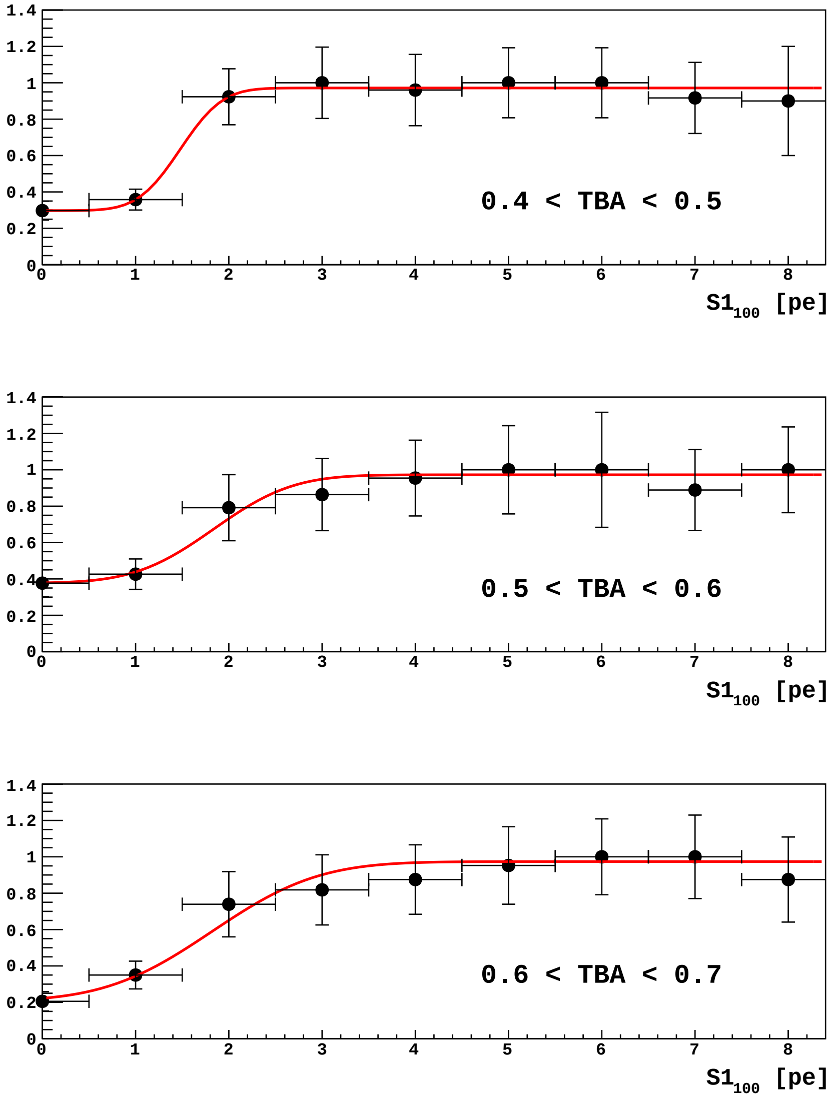

Figure 3.15 – Trigger efficiency, as a function of $S1_{100}$, measured with the ^{22}Na source for three regions of TBA. The plateau at high energies does not reach 1, because of the inhibition time of introduced after each trigger. Dark noise prevents the efficiency to reach 0 at very low values of $S1_{100}$.

3.4.3.4 TPC saturation

The TPC saturation has been investigated with the ^{22}Na source by comparing S1 with $S1_{late}$, the integral of the signal starting after the first 90 ns (the opposite of f_{90}). This range is not affected by saturation since it is dominated by the slow component of the scintillation emission with a characteristic time of ∼1.6 µss. A deviation from the linearity between S1 and $S1_{late}$ is observed from S1 = 4000 pe, corresponding to more than 600 keV_{ee}, as illustrated by Figure 3.17. A similar study has been done for NRs selected in double coincidence. Since the prompt scintillation component in NRs is larger, the effect of saturation is expected at lower S1. Up to 400 pe, corresponding to the maximum energy of NRs induced by 1.45 MeV neutrons, no deviations from linearity were observed

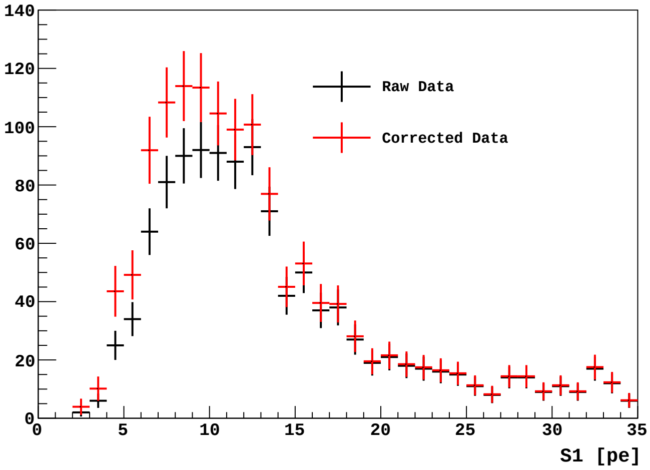

Figure 3.16 – Effect of the trigger efficiency correction on the NR energy spectrum, for events selected by A0 with the lowest mean energy of 7.1 keV$_{nr}$, and where the impact of the efficiency is maximal.

between S1 and S1$_{late}$.

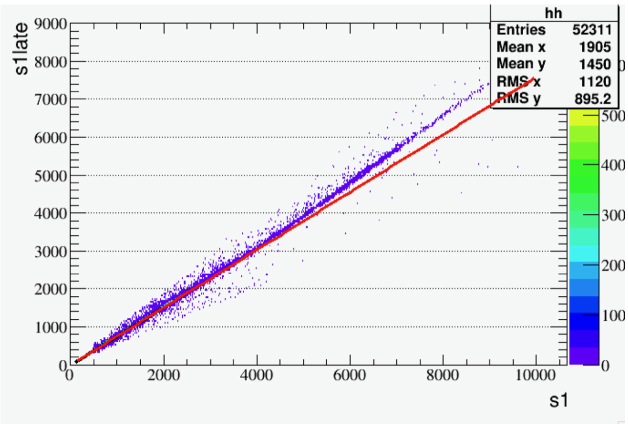

Figure 3.17 – S1$_{late}$ vs. S1 distribution highlighting the deviation from equality starting ∼ 4000 PE.

3.4.3.5 Time of flight variables

The analysis relies on time of flight (TOF) measurements to reconstruct the energy of scattered neutrons and then deduce the recoil energy in LAr. Two TOF variables are defined for ARIS :

- TOF$_{\mathrm{TPC}}$: the time between the beam pulse and the detected signal in the TPC
- TOF$_{\mathrm{ND}}$: the time between the beam pulse and the detected signal in one of the neutron detectors.

These two variables have been precisely characterised and constrained using the detector simulation.

Time alignment To overcome all the delays from the DAQ and the cables, we chose as a time reference the so-called γ-flash (see Section 3.4.2). The γ-flash peak is then by definition centered around 0. The alignment is done on a run-by-run basis. In order to align the runs, we define one offset value for $\mathrm{TOF}_{\mathrm{TPC}}$ and one for each ND for $\mathrm{TOF}_{\mathrm{ND}}$. For each run, the γ-flash $\mathrm{TOF}_{\mathrm{TPC}}$ and $\mathrm{TOF}_{\mathrm{ND}}$ distributions are fitted with a Gaussian. The peak of this Gaussian is considered our offset value.

A misalignment of the timestamps of the different CAEN boards was found for some runs. Indeed, for each event, there is a timestamp recorded from the digitiser boards. In the ideal case, the timestamps are equal among the boards. However, we sometimes observed a discrepancy between the timestamps of the different boards, leading to a time difference between the beam pulse clock time and the TPC or ND pulse event. This resulted in the splitting of the TOF distributions, as shown in Figure 3.18 for the γ-flash in $\mathrm{TOF}_{\mathrm{TPC}}$.

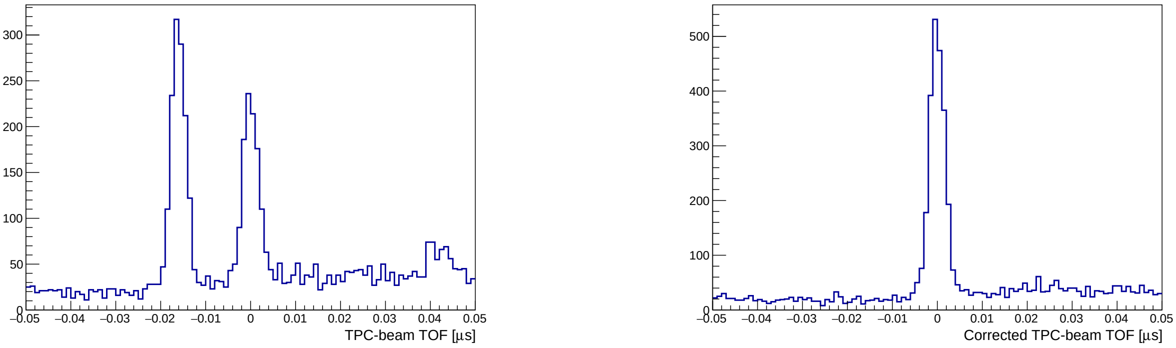

Figure 3.18 – $\mathrm{TOF}_{\mathrm{TPC}}$ before(left) and after (right) correction of the splitting due to the timestamps difference of the CAEN boards.

This was solved event per event by looking at the difference in timestamps: if a difference is found, the TOF is corrected by the value observed.

Resolution The TOF resolution was determined by adjusting MC distributions of the TOF to the γs from $^7\mathrm{Li}^*$ de-excitation data. The resolutions were found to be 1.8 ns for $\mathrm{TOF}_{\mathrm{TPC}}$ and ranging from 2 to 3 ns for $\mathrm{TOF}_{\mathrm{ND}}$.

The distributions for $\mathrm{TOF}_{\mathrm{TPC}}$ and NDs $\mathrm{TOF}_{\mathrm{ND}}$ are shown in figure 3.19, compared with Monte Carlo simulations of neutrons for the neutron detector A3. The agreement between data and Monte-Carlo confirms that the beam kinematics used for the simulation is correct.

3.4.3.6 PSD in the neutron detectors

In a similar process to the PSD in LAr, γ-rays and neutrons have different interactions in the NE213 liquid scintillator. γs interact with the electrons while neutrons interact mainly with nuclei, leading to much slower scintillation [121]. Thus, the ND signal exhibits (35 ns) a fast and a slow (270 ns) component. We defined an integration window for the slow component, starting 0.1 µs after the

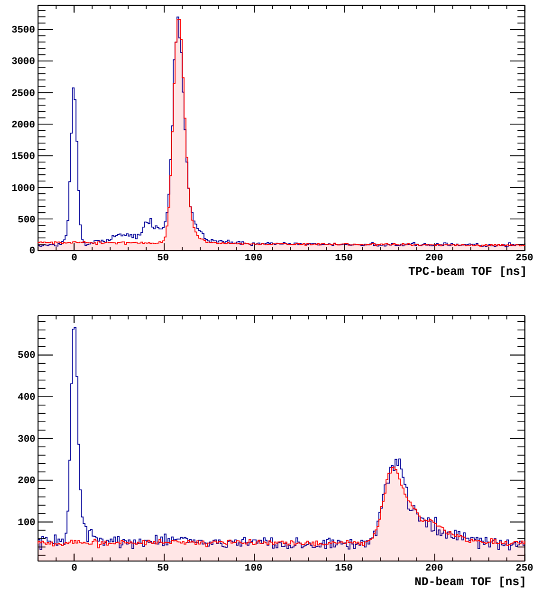

Figure 3.19 – Data (blue line) and Monte Carlo (red area) comparison of the $\mathrm{TOF}_{\mathrm{TPC}}$ (top) and $\mathrm{TOF}_{\mathrm{ND}}$ (bottom) distributions for the ND A0. The peak at 0 ns corresponds to the coincidence with $^7\mathrm{Li}^*$–γ. The flat background in both the simulation samples are produced with a toy Monte Carlo approach tuned on data.

start of the pulse. The neutron PSD variable, $\mathrm{PSD}_{\mathrm{ND}}$, is then the ratio of the slow component of the signal over the total charge. The distribution of $\mathrm{PSD}_{\mathrm{ND}}$ is shown in Figure 3.20.

The NR distribution for $\mathrm{PSD}_{\mathrm{ND}}$ is centered at ~ 0.35, while the ER one is around 0.09 This variable has been used to select clean samples of neutrons and γ events from our data.

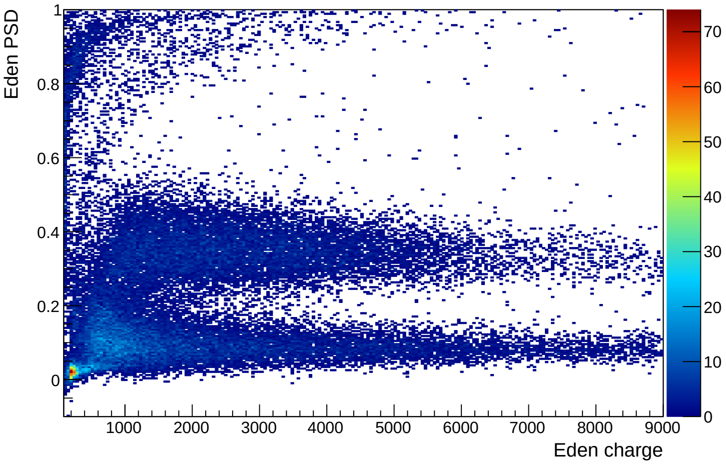

Figure 3.20 – Neutron detector PSD parameter as a function of the charge collected in the ND for the A3 detector.

3.5 Data selection

We select events with triple coincidence between the beam pulse, TPC and neutron detectors, with a ToF compatible with neutrons. Besides, similarly to the neutrons, the γs can produce triple coincidence interacting in both TPC and ND. In such configurations, the γ produces an ER in LAr by Compton scattering and a peak is observed in the S1 spectrum thanks to the angular selection of the outgoing γ. γ-flash photons then provide an excellent sample of single Compton electrons for investigating LAr response to ERs.

In this section, I present the selection criteria that are applied to the selection of NR and ER samples. For a matter of simplification, the discussion below is detailed only for the A3 detector (corresponding to 21.5 keV$_{nr}$) at null field, the conclusions being very similar for the other configurations and the other fields.

We want to select nuclear recoils produced by neutron elastic scattering in the TPC, in order to extract the S1 nuclear recoil energy spectra. As the neutron beam has an average energy of 1.47 MeV, a peak from these neutrons is expected at roughly 57 ns in TOF$_{\mathrm{TPC}}$ and roughly from 120 to 210 ns in beam-ND TOF. We can thus apply cuts on these two TOFs to select the relevant samples. We also cut onPSD$_{\mathrm{ND}}$ to discriminate between NRs and ERs. We decided to exclude any f$_{90}$ cut to select relevant events to avoid possible biases in the TPC energy spectra due to the correlation between S1 and f$_{90}$.

3.5.1 NR events selection

3.5.1.1 TOF cut

Different TOF cuts methods were tested for the NR population.

NR true energy [keV]	6.99	13.7	17.7	21.5	40.7	65.3	98.6	119
Compton								
Beam-ND TOF [ns]	[-2, 2]	[-2, 2]	[-0.5, 1.5]	[-1, 1.5]	[-1, 1.5]	[-1, 2]	[-1, 2]	[2, 5]
Neutrons								
Beam-ND TOF [ns]	[180, 220]	[180, 220]	[165, 200]	[130, 160]	[120, 160]	[128, 160]	[125, 160]	[140, 170]

Table 3.2 – Summary of all TOF_{ND} cut values for the neutron and Compton samples in all configurations.

Box cut We define a selection region around the neutron and Compton scattered gammas in each TOF distribution. The window chosen for the TOF_{TPC} cut is $53 \leq TOF \leq 70$ns. The same window is applied to every ND since the path between the beam and the TPC does not depend on the scattering angle considered. On the other hand, the cut on TOF_{ND} has to be tuned for each neutron detector, in order to take into account the differences due to kinematics and the variation of the distance between the beam and the neutron detectors. The intervals for the TOF_{ND} cut are summarised in Table 3.2.

Two-dimensional cut For this cut, we generate neutrons from the beam interacting in the TPC and select the single scatter population. The distribution of this pure sample of MC neutron single scatter is then plotted in the TOF_{TPC}- TOF_{ND} plane. We expect a correlation between the two variables, and this was confirmed by the MC simulations. This distribution can be used in several different ways.

- Mask: as a mask to accept/reject events
- Contour: defining a contour to a preset cut level
- Likelihood: a definition of weights for the events in the data

In the first case, a loop is made on the 2D distribution of the data and each bin is compared with the 2D MC distribution. If there is at least one event in the bin in the MC distribution, the bin content is preserved in the data distribution, otherwise, it is set to zero. For the likelihood method, the 2D MC distribution is normalised to 1. Then the bin contents of the MC are used as a weight applied to the 2D data.

The mask method revealed complicated to use and had too much background acceptance. The other 2D cuts were studied more extensively.

Figure 3.21 shows the data in the TOF_{TPC}- TOF_{ND} plane, with the MC single scatter distribution. Both 2D cuts have been applied to the data and compared to the one-dimensional ”box” cut.

The results of the different cuts have been compared as shown on Figure 3.22 The likelihood method has a lower acceptance than the other two and was abandoned. We also had trouble understanding the background selection with the contour cut. We, therefore, decided to continue the analysis with the 1D cut. The statistics available was sufficient to ensure good results despite the slight loss in acceptance.

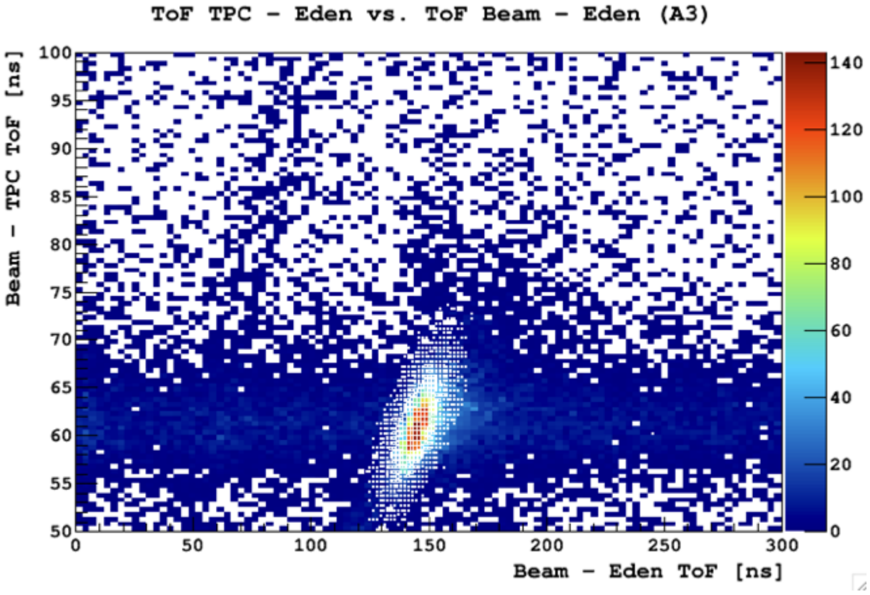

Figure 3.21 – $\mathrm{TOF_{ND}}$ vs $\mathrm{TOF_{TPC}}$. The white boxes are the neutron single scatter MC distribution, which is used to select the data.

3.5.1.2 Final set of cuts

Figure 3.23 shows different combinations of observables for triple coincidence events. On these distributions, some regions of interest are identified by red lines representing the selection cuts applied.

Four populations are emphasised in Figure 3.23:

- **D1 - Neutrons from the $^7\mathrm{Li}(p,n)^7\mathrm{Be}$ reaction:** Both the $\mathrm{TOF_{TPC}} \sim 60$ ns and $\mathrm{TOF_{ND}}$ ~ 150 ns peaks are the ones expected for scattered beam neutrons. Moreover, the large $\mathrm{f_{90}}$ values indicate these events are NRs. The $\mathrm{PSD_{ND}} \sim 0.35$ also confirms that these events are neutrons. This population contains daily single scatters due to the design of the TPC, but there is also a multiple scatter contamination.

- **D2 - Compton scattered γs:** This region corresponds to the γ-flash. The ER origin of the events is deduced from the small $\mathrm{f_{90}}$ and $\mathrm{PSD_{ND}}$. The TOF distributions are centered around 0 since this population has been chosen as the time reference. The little cluster beside this region is due to some γs interacting first in the ND and then in the TPC.

- **D3 - High-energy neutrons:** The $\mathrm{f_{90}}$ of this population classifies these events as neutrons, but the two TOFs are shorter than for the expected signal from ~1.5 MeV neutrons. These high energy neutrons are identified as byproducts of fusion-evaporation reactions between the different target materials and the accelerated $^7\mathrm{Li}$. Indeed, when accelerated $^7\mathrm{Li}$ nuclei pass through the beam cell, it can fuse with present nuclei (e.g. Al) and form an excited compound nucleus. This nucleus will then evaporate nucleons (preferably neutrons) before radiating to reach the ground state of the resulting nucleus. Those neutrons, having a higher energy than

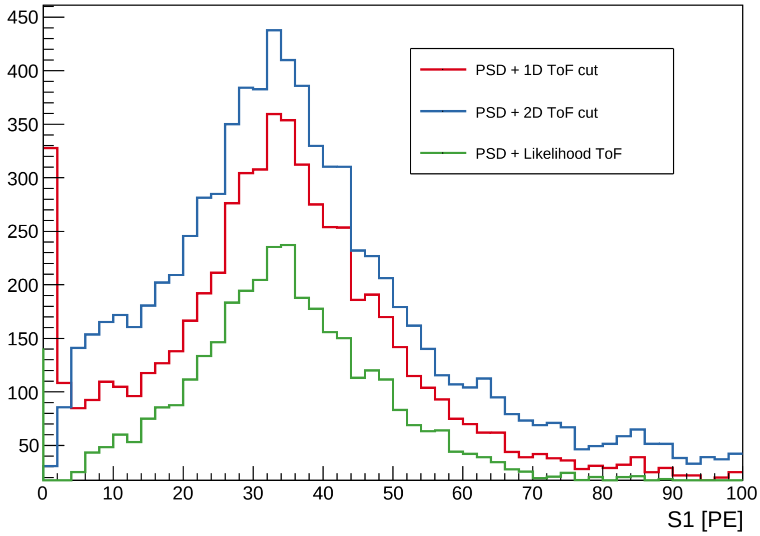

Figure 3.22 – Comparison of the different TOF cuts methods. The 2D contour cut is defined for a cut level of 0.65.

the beam neutrons, arrive before the neutrons from the ^{7}Li$(p,n)^7$Be reaction, resulting in this distribution centered slightly earlier than the ^{7}Li$(p,n)^7$Be distribution.

- **D4 - Accidental γs:** As indicated by their short TOF$_{\text{ND}}$ and long TOF$_{\text{TPC}}$, these events are random coincidences between a neutron interacting in the TPC and γ correlated with the beam pulse detected in the ND.

The right panel shows the ER selection for the same configuration. The single scatter acceptance of the TOF cuts has been estimated with a Monte-Carlo simulation. We applied the TOF selection cuts described above to the MC events and took the acceptance as being the ratio of the surviving single scatters over the total number of single scatters. We obtained acceptances for single scatter nuclear recoils between 0.93 and 0.95.

3.5.2 ER event selection

The Compton scattered gammas provide an easily identifiable ER sample, that will be used to study light yield linearity and recombination probability. Thus, a dedicated selection process has been developed for this population, based on the selection for nuclear recoils. We kept all the events with a PSD$_{\text{ND}}$ ≤ 0.2. According to the description above, selecting the TOF region for the Compton scattered γ is just selecting the γ-flash in the two TOF distributions. The γ-flash being always centered around 0, we just select the events in a given window around 0. We chose a window of ± 2 ns around 0 for the TOF$_{\text{TPC}}$ cut and the values for TOF$_{\text{ND}}$ are summed up in Table 3.2.

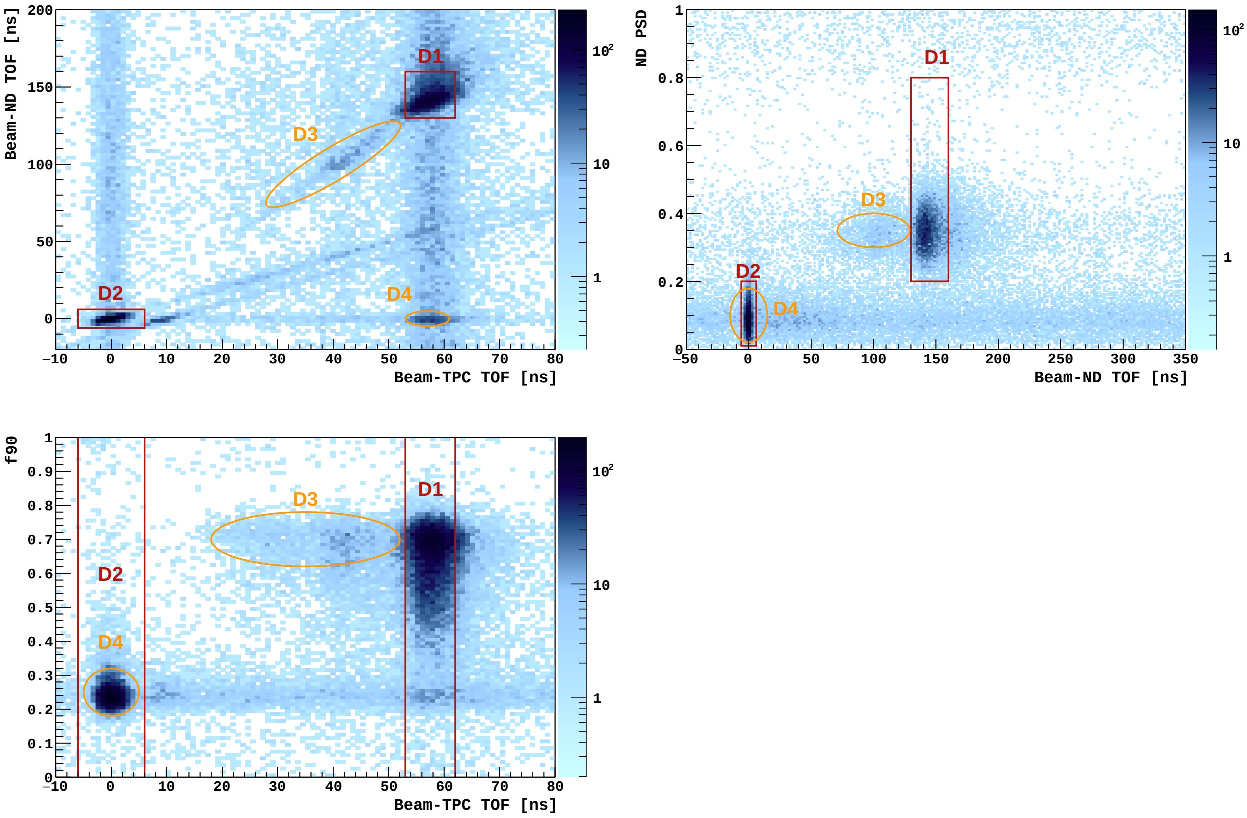

Figure 3.23 – $\mathrm{TOF_{ND}}$ vs. $\mathrm{TOF_{TPC}}$ (top), $\mathrm{PSD_{ND}}$ vs. $\mathrm{TOF_{ND}}$ (center), and f_{90} vs. $\mathrm{TOF_{TPC}}$ (bottom) for triple coincidences with the A3 detector. The numbered populations are described within the text. The red lines correspond to the selection cuts for NRs (D1) and ERs (D2). Yellow lines highlight two classes of NR (D3) and ER (D4) backgrounds.

3.5.3 Background subtraction

Once the selection is done, the final step to obtaining NR and ER spectra is to estimate and subtract the accidental background. We consider as accidental background the random coincidences between a neutron in the TPC and a γ (not correlated with the beam pulse) in one of the neutron detectors. To have an estimation of this background, we apply the $\mathrm{TOF_{TPC}}$ to be sure to select a neutron in the TPC, and we relax the $\mathrm{TOF_{ND}}$ cut. We then exclude from the background selection regions D1 and D4 to make sure we avoid the triple coincidence of γs and neutrons. We assume a similar shape of the background in both the selected region and under the neutron peak.

In the case of ERs, the background from γs scattering multiple times in the TPC materials is dominant, making the accidental background subtraction irrelevant. The ER Compton background has been estimated by using the *TSpectrum Background* algorithm in ROOT [122].

These cuts remove background correlated with the beam pulse. Purely accidental background is shown in the continuous bands for $\mathrm{TOF_{ND}}$ at the expected $\mathrm{TOF_{TPC}}$ for neutrons or γs in figure 3.23.

Figure 3.24, presents the resulting NR and ER spectrum after application of all the cuts, as well as the accidental background for our reference configuration. The background will be subtracted from the spectrum for the following analyses.

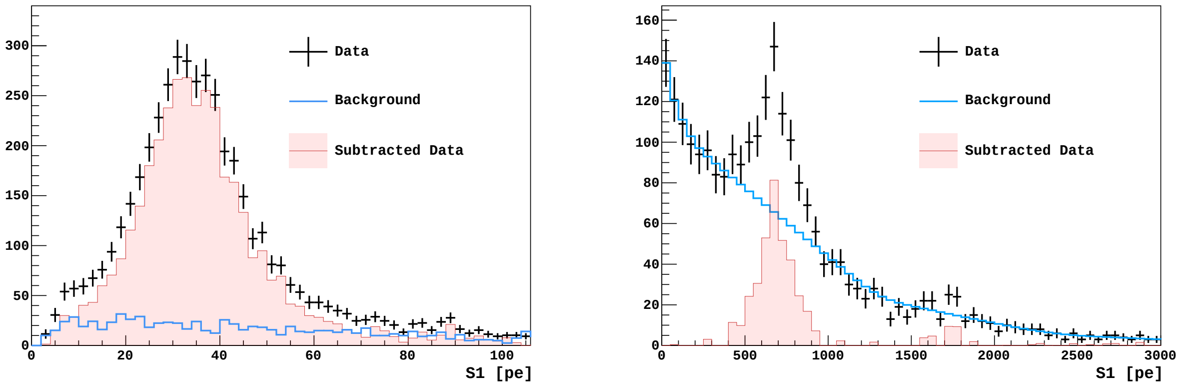

Figure 3.24 – Left: NR spectrum for detector A3 (21.5 keV recoil energy). Right: ER spectrum for Compton scattered electrons in detector A3. In black is the spectrum after all the selection cuts. The background is represented by the blue histogram.

Chapter 4

Extraction of the LAr scintillation parameters

Contents

ARIS acquired data with and without field and obtained well defined samples of both ER and NR. These data allow to extract different parameters of the argon scintillation:

- ER data at null field gives information about the light yield
- NR data at null field is used to extract the NR quenching
- ER and NR data with field shine light on the recombination probability and can be used to study the behaviour of f_{90} as a function of the electric field

Extracting all these paraneters allows to parametrise the LAr response, using adapted theoretical models.

4.1 Light yield linearity

Lippincott et al. [123] used different γ sources to measure the ER response of liquid argon. They observed that the light yield seemed to vary linearly with respect to the γ energy. This suggests that LAr is not subject to quenching effects for nuclear recoils. This would be interesting for future experiments, since it would mean that we can use any γ-ray source to calibrate the LAr response, without paying attention to the regime of the peaks used. Indeed, γs in the photoelectric regime will deposit their energy all at once, causing a single scatter event in the TPC, while γs in the Compton regime will scatter several times in the TPC. If the light yield is not linear, it means that the regime of the γs considered will have an incidence on the light yield measured, biasing the measurements. If the linearity of LAr is verified, it would differ from LXe, in which non-linear ER response has already been observed [124].

However, the *Lippincott et al.* result only relies on multiple scatter sources, like γ-rays in the Compton scattering dominated regime: no direct measurements with single electrons have confirmed yet the linearity.

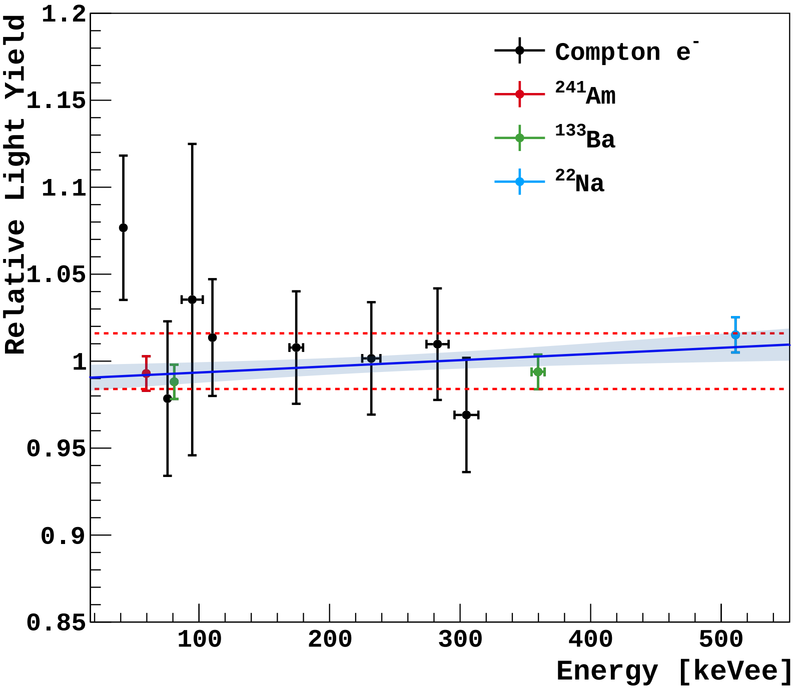

Figure 4.1 – Relative LY, with respect to the mean, as a function of the Compton electron energy from ^{7}Li* de-excitation, and from ^{241}Am (59.5 keV), ^{133}Ba (81 and 356 keV), and ^{22}Na (511 keV) γ-sources. Data points are fitted with a first-degree polynomial (blues line) to look for deviations from unity. The dashed red lines correspond to ±1.6% band and contains the fitted polynomial, including 1σ error (blue band), in the [41.5, 511] keV range.

The eight single ER energies selected by looking at the mono-energetic γ emitted by the ^{7}Li* de-excitation in triple coincidence are ideal candles for this test. For each ND, background subtraction is applied as described in section 3.5 and the resulting peak is fitted with a Gaussian function. The LY for each ND is evaluated as a function of the Compton electron energy determined with Monte Carlo. The so-obtained relative LYs, with respect to their mean value, are fitted with a first degree polynomial resulting in a maximum deviation from unity of 5% in the [41.5, 300] keV range, including the statistical error from the fit.

LYs independently extracted from the full absorption γ peaks, shown in figure 4.1, from ^{241}Am (59.5 keV), ^{133}Ba (81 and 356 keV), and ^{22}Na (511 keV), are fully compatible with the one derived from single Compton electrons. This is expected for the full absorption peaks of 59.5 and 81 keV γs since they are dominated by the photoelectric effect. The 356 and 511 keV γ interactions, instead, are dominated by the Compton scattering, producing multiple lower-energy electrons, each of them independently quenched. The total quenching effect for γs in the Compton regime would then be amplified with respect to single scatter events.

Fitting simultaneously the ^{241}Am, ^{133}Ba, ^{22}Na and Compton electrons, the LY in the [41.5, 511] keV range is constant within 1.6%, as shown in figure 4.1. This result confirms the linearity of LAr scintillation response at null field also observed in [125] at 2%, using multiple scatter sources in the [41.5, 662] keV range. This result suggests that, at null field, ERs are not subjected to non-linear quenching effects. Indeed, in that case, multiple scatter events would have an amplified quenching, due to the addition of single-electron quenching at each step, with respect to single scatter events. Since it is not the case, it means that calibrations of LAr detectors can be performed either with single or multiple scatter ER sources, without introducing any bias.

4.2 Nuclear recoil quenching at null field

The scintillation efficiency of nuclear recoils is reduced when compared to that of electronic recoils. In the case of electronic recoils at null field, all the deposited energy is converted into scintillation via electron-ion recombination. On the contrary, for nuclear recoils, a fraction of the particle energy is transferred to atoms of the medium in elastic collisions, i.e. lost to heat.

In addition, the high ionisation density of nuclear recoils tracks hinders the recombination and reduces the scintillation output. The process proposed, the *bi-excitonic quenching* involves exciton-exciton interactions [126],

$$\mathrm{Ar}^* + \mathrm{Ar}^* \rightarrow \mathrm{Ar} + \mathrm{Ar}^+ + e^- \tag{4.1}$$

Although the formed ion has a good chance of recombining with an electron to produce a new excited state, this would result, at best, in one emitted photon instead of two (one from each of the two excitons initially created) if these underwent a normal process.

In this case, the nuclear recoil scintillation efficiency, q_f is much smaller than one and can depend on the recoil energy.

A good indicator of q_f is the relative scintillation efficiency $\mathcal{L}_{eff}$. It is defined with respect to a particular gamma line and represents the ratio of scintillation light for NR with respect to ER.

Several theories have been proposed to model the reduction of scintillation for nuclear recoils. I will first discuss the discuss them before detailing ARIS's measure of $\mathcal{L}_{eff}$ and comparing the results with the different predictions.

4.2.0.1 Energy transfer to nuclei: Lindhard theory

The total average energy loss per unit path length by an ionizing particle during the nuclear recoil process can be expressed by the sum of the contribution of electronic and nuclear stopping powers:

$$\left(\frac{dE}{dx}\right)_{total} = \left(\frac{dE}{dx}\right)_{nucl} + \left(\frac{dE}{dx}\right)_{elec} \tag{4.2}$$

Electronic stopping power is defined as the energy deposited per unit distance by the nuclear recoil to excite or ionise the surrounding atoms. The nuclear stopping power is the energy loss per unit length caused by atomic collision. In such a collision the energy lost is transferred kinematically and does not contribute to the production of the scintillation light. Lindhard et al. [127] suggested that under the assumption that the recoiling nucleus loses all its energy in the detector, the total energy lost by the particle could be written as

$$E_R = \eta(E_R) + \nu(E_R) \tag{4.3}$$

where ν represents the average energy released to atomic motion and η the average energy released to the electrons of the medium.

Only the energy lost to electronic excitation or ionisation will lead to the production of excitons and electron-ion pairs. The electronic contribution is represented by

$$f_n(E_R) = \frac{\eta(E_R)}{E_R} = \frac{\eta(E_R)}{\eta(E_R) + \nu(E_R)} \tag{4.4}$$

where f_n is the energy reduction factor due to the nuclear stopping.

Using Eq 4.2, f_n can be expressed as

$$f_n(E_R) = \frac{\int_0^{E_R} (dE/dx)_{elec} dE}{\int_0^{E_R} ((dE/dx)_{elec} + (dE/dx)_{nucl}) dE} \tag{4.5}$$

Eq 4.5 has to be evaluated for each possible recoil energy and can be approximated by

$$f_n = \frac{kg(\epsilon)}{1 + kg(\epsilon)} \tag{4.6}$$

where, for a nucleus of atomic number Z, $\epsilon = 11.5 E_R Z^{-7/3}$, $k = 0.133 Z^{2/3} A^{-1/2}$, and $g(\epsilon)$ is well fitted by: $g(\epsilon) = 3\epsilon^{0.15} + 0.7\epsilon^{0.6} + \epsilon$.

4.2.0.2 Reduced Scintillation Yield due to High Ionisation Density

According to [104], a highly ionising recoiling particle produces a track of excitons and ionised atoms which can be described in terms of a core surrounded by a penumbra. The main difference between the two regions is their ionisation density, which is higher in the core. The bi-excitonic quenching or Penning processes (ionisation via the collision of an exciton with a neutral atom) are expected to occur only in the core, where the ionisation density is higher. The density of excitons and electron-ion pairs created along the track is proportional to the electronic energy loss, with a proportionality constant that we will name A. Without taking into account the quenching processes occurring in the core, the scintillation can then be written,

$$\frac{dS}{dx} = A\left(\frac{dE}{dx}\right)_{elec} \tag{4.7}$$

There is also a proportionality between the local concentration of the core and the electronic stopping power with constant B. The total collision probability in the core is denoted by k.

Then the scintillation light response can be written as a function of the electronic stopping power,

$$\frac{dS}{dx} = \frac{A\frac{dE}{dx}}{1 + kB\frac{dE}{dx}} \tag{4.8}$$

Eq 4.8 is Birk's saturation law. The values of A and kB can be obtained experimentally. Comparing it to Eq 4.7, we can see that the light yield is reduced for high ionisation density and we can define a quenching factor

$$f_l = \frac{1}{1 + kB\frac{dE}{dx}} \tag{4.9}$$

kB is also called Birk's constant and its value for LAr is $7.4 \times 10^{-4} MeV^{-1} gcm^{-2}$.

4.2.0.3 Mei model

Mei et al. [128] combine the Lindhard theory of energy loss (f_n) and Birk's saturation law (f_l) to explain the reduced scintillation efficiency for nuclear recoils in noble liquids. They represent the total scintillation efficiency in noble liquids by

$$q_f = f_n \times f_l = f_n \times \frac{1}{1 + k_B\frac{dE}{dx}} \tag{4.10}$$

This expression is possible due to the independence of the processes governing each factor.

4.2.1 ARIS measure

The reference gamma line chosen to measure $\mathcal{L}_{eff}$ in ARIS is the 59.5 keV γ from ^{241}Am at null field. The comparison with other measurements is made possible by the linearity of the light yield demonstrated in the previous section.

The S1 NR distribution for each configuration is fitted with a Monte-Carlo simulation. The results are shown in Figure 4.2. The amplitude and $\mathcal{L}_{eff}$ are considered as free parameters in the fits. $\mathcal{L}_{eff}$ is assumed constant in each data sample.

The different sources of systematic errors were studied, to quantify their impact. A list of the systematics can be found in Table 4.1. The dominant contributions are the uncertainties on the LY and the ND positions.

The first is evaluated with an analytical propagation of the error on the LY. To evaluate the systematics on the ND positions, MC simulations were produced, varying the ND positions in the direction that maximises the NR energy spread. The ND positions were obtained by measuring the distance of each ND from several reference points along the beam direction. A *a posteriori* cross-check was done by overlaying several photographs of the entire setup with the rendering of the geometry in the Monte Carlo using the BLENDER package. The TPC, the source position, and the ND support structures were used as reference anchors in the comparison. All the ND positions, except A2, were confirmed within a maximum shift of 4 cm. Indeed, the position of A2 in the survey appeared to be incorrect and required a shift of (-6,+7,+13) cm with respect to the survey position(the x direction being the beam-TPC direction). The uncertainty for the A2 position is conservatively assumed of the same size of the shift corresponding to an uncertainty of 5.6% on the NR energy. The uncertainty on the NR energy for the other NDs ranges from 0.8% to 2.6%. Such uncertainty also affects the second point in Figure 4.1.

Other systematics sources related to the setup geometry and materials are considered: the uncertainties on the Li energy and the TPC position, known within 1 cm. Systematics associated with the analysis, such as the trigger efficiency, the TOF cuts, binning and energy range in the fit and background subtractions were investigated. Their influence was found to be negligible, with the exceptions of the trigger efficiency and the TOF selection.

Figure 4.3 shows ARIS $\mathcal{L}_{eff}$ measurement as a function of the NR energy, compared with previous measurements [117, 129, 118] and with the Lindhard [127] and Mei [128]. In the ~[20, 60] keV$_{nr}$ region all the data sets are in good agreement, while discrepancies are observed outside this range. At low energies, ARIS provides a $\mathcal{L}_{eff}$ measurement down to ~7 keV$_{nr}$, the lowest NR energy among all the data sets.

Data are also compared to the PARIS model, which is a tuning of the Mei model using a fit to the DarkSide-50 data with kB as a free parameter. The fitted value for k_B is $k_B = 4.66^{+0.86}_{-0.84} \times 10^{-4} MeV^{-1} gcm^{-2}$, using DS-50 data.

As visible in Figure 4.3, the Mei model doesn't reproduce the data correctly. A fit of the model to the ARIS data has been performed, but the model is still disfavored at 2σ. However, a better agreement is achieved by adding a quadratic term to Mei's $\mathcal{L}_{eff}$, as in the extended version of Birk's formula for organic scintillators [131].

$$\mathcal{L}_{eff\,Mei^*} = f_n \times \frac{1}{1 + k_B \frac{dE}{dx} + k_B^* \frac{dE}{dx}^2} \tag{4.11}$$

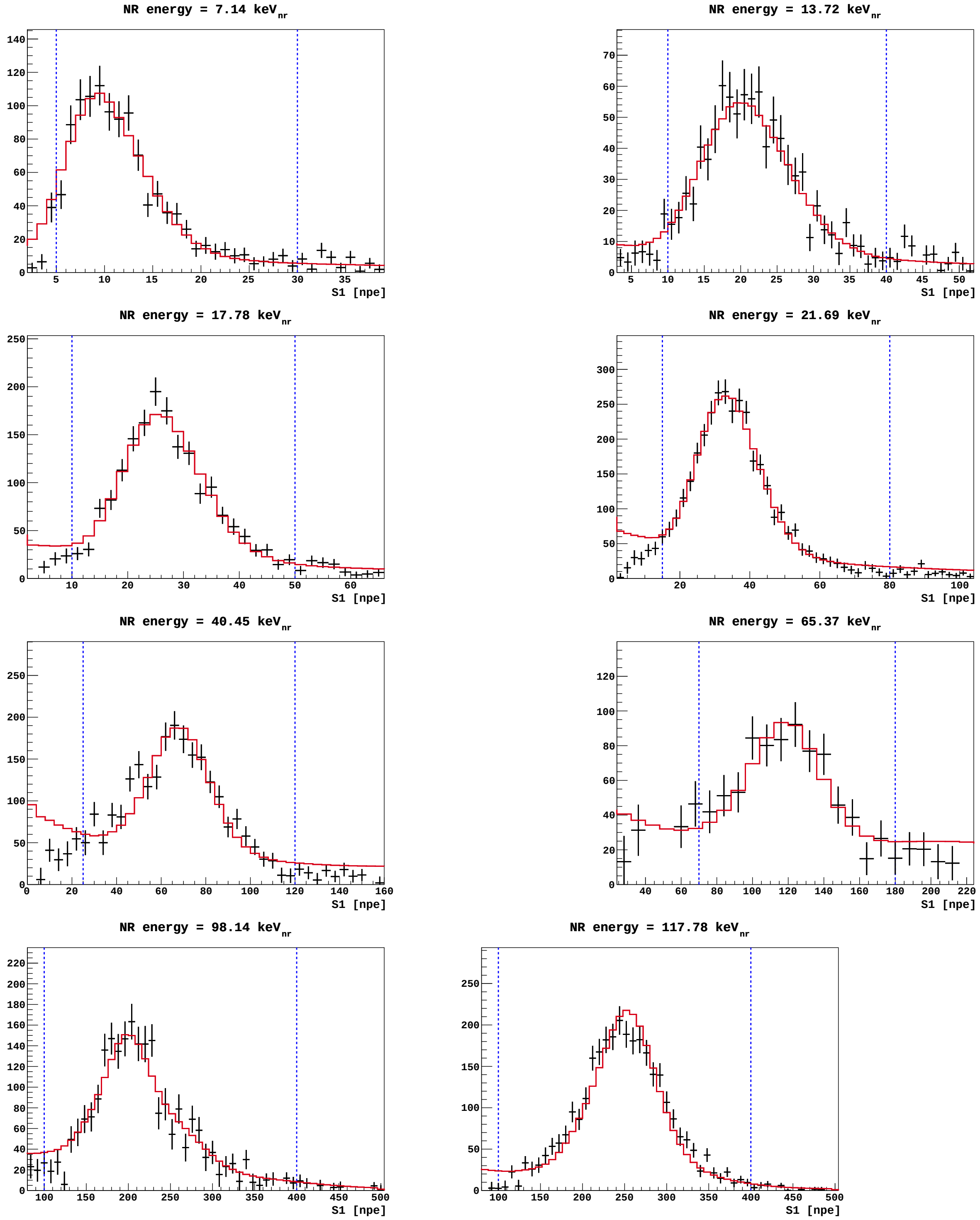

Figure 4.2 – Nuclear recoil data taken with zero electric field, fitted with the Monte Carlo-derived probability density functions for events in coincidence with the A0-7 detectors (red lines). The vertical dashed lines indicate the fitting range for each spectrum.

This modified Mei model is fitted to the ARIS data. The values fitted are: $k_B = (5 \pm 0.6) \times 10^{-4} MeV^{-1} gcm^{-2}$ and $k_B^* = (-2 \pm 0.7) \times 10^{-4} MeV^{-1} gcm^{-2}$.

Figure 4.4 shows the original (fitted to ARIS data) and modified Mei model against ARIS data.

NR energy [keV]	7.1	13.7	17.8	21.7	40.5	65.4	98.1	117.8
$\mathcal{L}_{eff}$	0.243	0.258	0.253	0.269	0.286	0.304	0.332	0.349
Light-yield	0.002	0.002	0.002	0.002	0.002	0.002	0.003	0.003
Beam kinematic	0.001	0.002	$o(10^{-3})$	$o(10^{-3})$	$o(10^{-3})$	$o(10^{-3})$	$o(10^{-3})$	$o(10^{-3})$
A0–A7 position	0.006	0.005	0.014	0.005	0.004	0.004	0.003	0.003
TPC position	$o(10^{-3})$	$o(10^{-3})$	$o(10^{-3})$	$o(10^{-3})$	$o(10^{-3})$	$o(10^{-3})$	$o(10^{-3})$	$o(10^{-3})$
A0–A7 TOF	$o(10^{-3})$	$o(10^{-3})$	0.001	0.001	$o(10^{-3})$	0.002	0.001	0.001
TPC TOF	0.002	0.001	0.001	0.001	0.002	0.002	0.002	0.002
Trigger efficiency	$o(10^{-3})$	$o(10^{-3})$	$o(10^{-3})$	$o(10^{-3})$	$o(10^{-3})$	$o(10^{-3})$	$o(10^{-3})$	$o(10^{-3})$
Total Syst.	0.007	0.006	0.014	0.006	0.005	0.005	0.005	0.005
Stat.	0.005	0.004	0.003	0.002	0.003	0.006	0.004	0.002
Combined	0.009	0.007	0.015	0.006	0.006	0.008	0.006	0.005
Combined relative [%]	3.8	2.7	5.8	2.3	2.1	2.6	1.8	1.5

Table 4.1 – Measured $\mathcal{L}_{eff}$ for each ND with the different sources of systematic uncertainties and the statistical uncertainty from the fit.

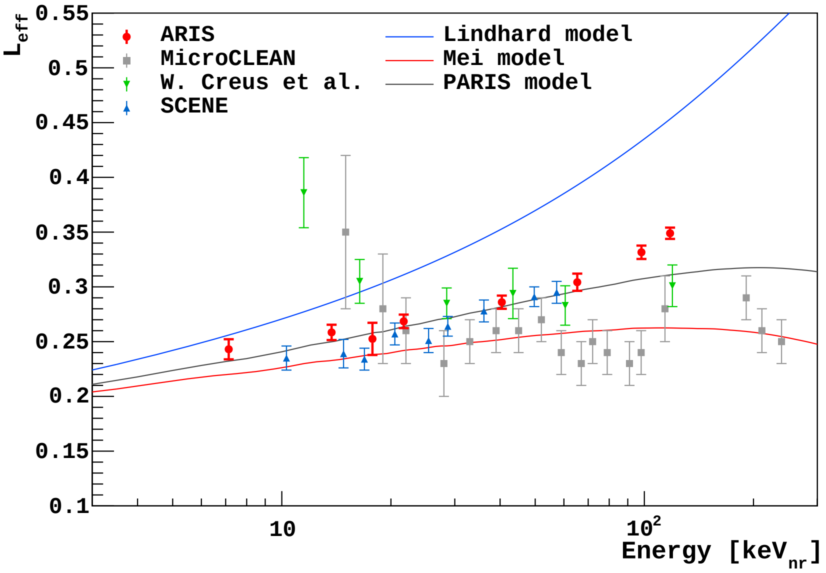

Figure 4.3 – $\mathcal{L}_{eff}$ dependence on NR energy as measured by this work and compared with other data sets [117, 129, 118] and models [127, 128, 130].

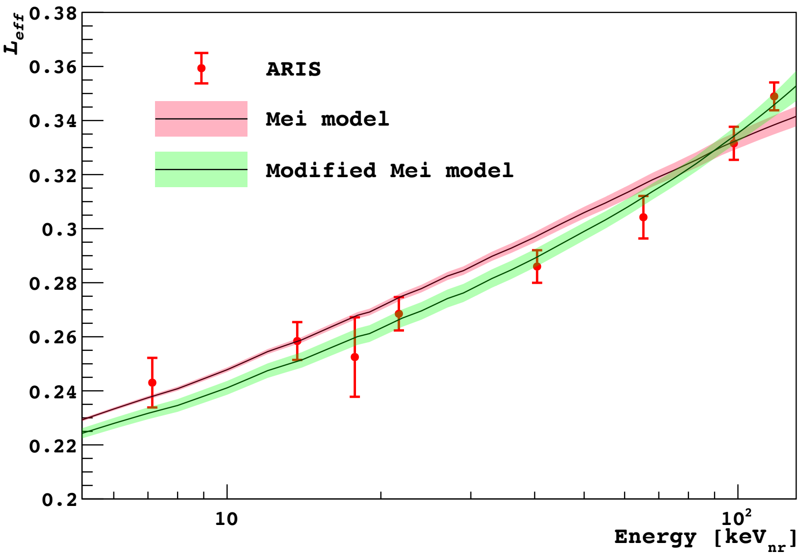

Figure 4.4 – $\mathcal{L}_{eff}$ values measured by ARIS fit with Mei and modified Mei models as described by Eq 4.10 and 4.11.

4.3 The influence of the electric field: recombination probability in LAr

When an electric field is applied, free electrons drift from the ionisation track, decreasing the probability of recombination and therefore affecting the scintillation signal. Therefore it is important to correct the scintillation loss for TPC detectors applying an electric field to collect ionisation signals.

4.3.1 Recombination models in noble liquids

Several theories exist to model the recombination probability in noble liquids. Different models are necessary to reproduce NR and ER since they leave very different tracks.

4.3.1.1 Thomas-Imel model

The Thomas-Imel [132] model is an extension of Jaffe's "box model" [133]. Jaffe developed a columnar theory of electron-ion recombination, describing the electrons and ions as two plasmas, the recombination being understood as interactions between them. He started from the following equations

$$\begin{aligned}\frac{\partial N_+}{\partial t} &= -\alpha N_+ N_- - u_+ \mathbf{E}\cdot\nabla N_+ + d_+\nabla^2 N_+\\ \frac{\partial N_-}{\partial t} &= -\alpha N_+ N_- - u_- \mathbf{E}\cdot\nabla N_- + d_-\nabla^2 N_-\end{aligned} \tag{4.12}$$

where N_+ and N_- are respectively the ion and electron charge distributions, u_+ and u_- are the mobilities,d_+,d_- and α are coefficients corresponding to the diffusion and recombination terms and $\mathbf{E}$ is the external electric field. Jaffe's solution for this model was to add a perturbation term for the recombination, with the boundary condition that the initial distribution is a column of charge around the primary track. In noble liquids like liquid argon, the diffusion term is very small since the electron diffusion rate is of the order of the mm per meter of drift [134] and the ion drift velocity is itself three to five orders of magnitude lower than the electron one [135, 136]. Considering a constant electric field along the z direction, classical for dual-phase TPCs, Eq 4.12 can be simplified as

$$\frac{\partial N_+}{\partial t} = -\alpha N_+ N_- \tag{4.13}$$

$$\frac{\partial N_-}{\partial t} = -\alpha N_+ N_- - u_- \mathbf{E}\frac{\partial N}{\partial z} \tag{4.14}$$

Thomas et al. argued that, if we assume that each electron-ion pair is isolated, the equations can be solved exactly. Indeed, integrating over time using the initial condition $N_+(t=0) = N_-(t=0)$ and substituting Eq4.13 into Eq4.14 yields

$$\frac{\partial \ln N_{+}(t)}{\partial t} = u_{-}E\frac{\partial}{\partial z}\left[\ln \frac{N_{+}(t)}{N_{+}(0)}\right] - \alpha N_{+}(t) \tag{4.15}$$

Another simplification can be done by defining $Y(t) \equiv \frac{N_{+}(0)}{N_{+}(t)}$, the variables transformations $v = t - \frac{z}{u_{-}E}$ and $w = t + \frac{z}{u_{-}E}$, and applying the boundary condition $Y(t=0) = 1 (v = -w)$, Eq 4.15 can be rewritten

$$\frac{\partial Y}{\partial v} = \frac{\alpha}{2}N_{+}(0) \tag{4.16}$$

Applying the box model boundary condition so that the electron-ion pairs are isolated and their initial distribution populates a box of dimension a ($i.e$ the box contains N_0 units of each charge at $t = 0$) and integrating over space yields,

$$\frac{Q}{Q_0} = \frac{\ln(1+\xi)}{\xi} \tag{4.17}$$

where

$$\xi \equiv \frac{N_0 \alpha}{4a^2 u_{-}\mathbf{E}} \tag{4.18}$$

and Q/Q_0 is the fraction of the charge collected. The theory is then characterised by the sole parameter ξ: $\xi \to 0$ for perfect charge collection and $\xi \to \infty$ for complete recombination.

The recombination parameter $\mathbf{R}$ can then be expressed as

$$\mathbf{R} = 1 - \frac{Q}{Q_0} = 1 - \frac{\ln(1+\xi)}{\xi} \tag{4.19}$$

We use for our analysis the parametrisation defined in [137], where

$$\xi = C_{box}\frac{N_0}{\mathbf{E}^{\beta}} \tag{4.20}$$

C_{box} and β are constants, and the dependence of ξ on the electric field has been modified to match a power law.

4.3.1.2 Doke-Birks model

Onsager [138] has developed a model for electron-ion recombination. It states that if an electron thermalises within an Onsager radius r_0 from the parent ion, it cannot escape the ion energy and the pair recombines. If the thermalisation point is outside the Onsager radius, the electron escapes, even in the absence of an electric field. The Onsager radius is defined as $r_0 \equiv \frac{e^2}{4\pi\epsilon_0\epsilon_r k_B T}$, where e is the electron charge, ϵ_0 and ϵ_r the dielectric constants respectively in the vacuum and in the medium, k_B is the Boltzmann constant and T the temperature. For LAr, $r_0 = 125$ nm [115] and the thermalisation range for electrons is estimated to be ~2 μm. Therefore, a significant fraction of the electrons are expected to escape recombination. Onsager's theory cannot by itself explain the entire recombination process in LAr since it doesn't account for the escaping electrons. To describe this part of the process, it is necessary to consider the so-called ”volume recombination”, where escaping electrons recombine with ions that are not their parent one.

Doke *et al.* divide the total scintillation response of the medium as a function of the interacting particle energy, $\frac{dL}{dE}$, into three parts : the first, $\left(\frac{dL}{dE}\right)_\nu$ is the scintillation yield for light produced by recombination of escaping electrons from the parent ions; the second, $\left(\frac{dL}{dE}\right)_g$, is the scintillation yield for light produced by geminate recombination, i.e. recombination with the parent ion; and the third, $\left(\frac{dL}{dE}\right)_g$, is the scintillation yield for light produced from the excited states directly produced by the ionizing particle. Both the second and third contributions are expected to be constant and their sum η_0 is the scintillation yield at zero electric field.

The rate of escaping electrons can be expressed as

$$\frac{dn_\pm}{dt} = -\alpha n_\pm^2 \tag{4.21}$$

where $n_\pm$ is the density of electrons or ions produced by an ionizing particle and α the recombination coefficient. According to [115], it is possible to estimate the number of recombination photons per unit path length by integrating Eq 4.21 over the observation time (from 0 to τ). The integration yields

$$\left(\frac{dL}{dx}\right)_\nu = -\sigma \int_0^\tau \frac{dn}{dt} dt = \frac{\alpha n_0^2 \sigma\tau}{1+\alpha\tau n_0} \tag{4.22}$$

where n_0 is the initial density of electrons or ions and σ is the cross-section of the electron-ion column. Assuming that n_0 is propotional to dE/dx, i.e. $n_0 = kdE/dx$, then Eq 4.22 can be rewritten

$$\left(\frac{dL}{dx}\right)_\nu = \frac{\alpha\sigma\tau k^2 (\frac{dE}{dx})^2}{1+k\alpha\tau\frac{dE}{dx}} \tag{4.23}$$

Using the fact that $\frac{dL}{dE} = \frac{dL}{dx} \times \frac{dx}{dE}$, the previous equation becomes,

$$\left(\frac{dL}{dE}\right)_\nu = \frac{A\frac{dE}{dx}}{1+B\frac{dE}{dx}} \tag{4.24}$$

where $A = \alpha\sigma\tau k^2$ and $B = k\alpha\tau$. The total scintillation response can then be expressed as

$$\frac{dL}{dE} = \frac{A\frac{dE}{dx}}{1+B\frac{dE}{dx}} + \eta_0 \tag{4.25}$$

In ARIS we introduced a dependence on the electric field, F, by defining

$$\eta_0 = \eta_0'\, e^{-D\times F}. \tag{4.26}$$

where D is a free parameter keeping the exponential dimensionless.

4.3.1.3 PARIS model

The PARIS model is based on an effective parameterisation of the recombination probability as a function of the recoil energy, extracted from DarkSide-50 data. Since Compton and photoelectric interactions both produce an electron, we did not distinguish between β decays and γ-induced electron recoils in liquid argon. We assume that all the fluctuations in the ratio between excitons and ions and the number of recombined ions are described by Poissonian smearing of the predicted number of scintillation photons. This is the simplest assumption on the statistics of photon emission. Since the optical propagation is properly tuned and the effect of the electronics on the energy response resolution is correctly simulated, any observation of an extra component in the resolution term, from data-MC comparison, should be addressed to the statistics governing the LAr photon emission. The results of this comparison are shown in the next section. In G4DS, the recombination probability is calculated as a function of the initial track energy (the GEANT4 vertex kinetic energy), while the number of produced species (excitons or ions) is computed for each energy deposit. The model is currently tuned on DarkSide-50 S1 data for both ER and NR and cross-checked with external calibration sources (^{57}Co and ^{133}Ba). PARIS used data at 200 V/cm only and was demonstrated to work from ~3 keV up to ~550 keV.

4.3.1.4 ARIS measure of the recombination probability in LAr

In addition to the null field data set, data were acquired at 50, 100, 200, and 500 V/cm drift fields in triple coincidence mode.

In ARIS, the recombination dependences on electron recoil equivalent energy E$_{ee}$ and field, F, are studied with respect to the observable:

$$\frac{S1}{S1_0} = \frac{\alpha + R(E_{ee}, F)}{1+\alpha}, \tag{4.27}$$

where S1$_0$ is the scintillation response at null field.

In case of NRs, E$_{ee}$ = $\mathcal{L}_{eff}$ (E$_{nr}$)×E$_{nr}$.

Eq 4.27 is expected to reproduce ARIS data in both ER and NR modes, by accordingly changing the α value, if the recombination probability $R(E,F)$ is correctly modeled. We compare the S1/S1$_0$ ratio, extracted from the data with the Thomas-Imel, Doke-Birks, and PARIS models. The first is an extension of the Jaffe "box" theory and was demonstrated to be accurate in the "short track" regime, like for NRs or low energy ERs. The Doke-Birks model is empirical and expected to reproduce data at higher energies.

ARIS data in ER mode were simultaneously fitted with the so–modified version of Doke-Birks in the [40,300] keV$_{ee}$ range, and the results are shown in Figure 4.5. The parameters returned by the fit are A=(2.5±0.2)×10^{-3} cm/MeV, η_0'=0.77±0.01, and D=(3.5±0.3)×10^{-3} cm/V. With these parameters, the model is able to reproduce data with energy from 40 keV at any field. However, while the Doke-Birks recombination tends to 1 at lower energies, different observations demonstrate it should decrease. The PARIS model, that was designed to solve this issue, does not require any

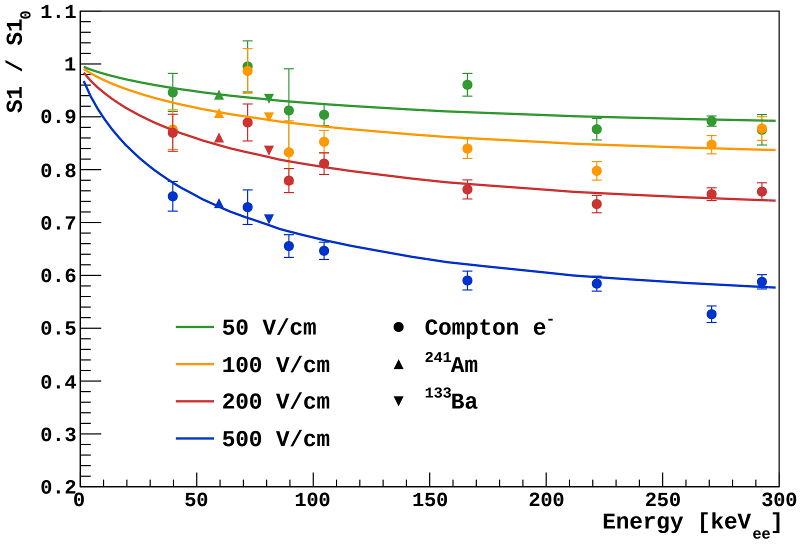

Figure 4.5 – Field induced quenching of S1 for ERs at different drift fields fitted with the Doke-Birks model.

tuning of the parameters and accurately matches the data at 200 V/cm, as shown in Figure 4.6. The difference between Doke-Birks and PARIS models appear for energies below 10 keV$_{ee}$.

NR data, converted in ER equivalent energy through the $\mathcal{L}_{eff}$ previously measured, is compared to the Thomas-Imel model.

Figure 4.7 shows the S1/S1$_0$ ratio, at different fields, for NRs, fitted with the Thomas-Imel model. The fit returns β=1.07±0.09, in good agreement with the Thomas-Imel prediction of β=1, and C_{box}=18.5±9.7. The resulting Thomas-Imel model for NRs is compared with Doke-Birks and PARIS, in the paradigma that, once fixed the recombination probability, models should be able to describe both ER and NR data sets, by changing the scintillation-to-ionisation ratio, α, from 0.21 (ER) to 1 (NR). This paradigm is confuted by the comparison between models and the NR data set at 200 V/cm, shown in figure 4.8, where Doke-Birks and PARIS predictions are rejected at more than 5 σ. The Doke-Birks and PARIS models are not recovered in NR mode, even by changing the α value.

An overall model requires then two separate recombination probabilities in order to describe both ERs and NRs. In the range of the dark matter search, the tuned Thomas-Imel model was demonstrated to correctly describe scintillation response to NRs, while PARIS is confirmed as a good modeling for ERs if operating at 200 V/cm. Doke-Birks provides a good description of ERs at different fields, but almost outside the range of interest (>40 keV$_{ee}$) for WIMP searches.

As a final check, the tuned Thomas-Imel model was compared with the ionisation signal measured by Joshi *et al.*, as function of the drift field, for 6.7 keV$_{nr}$ NRs, and assuming the $\mathcal{L}_{eff}$ measured by ARIS. Figure 4.9 shows the excellent agreement, suggesting that, apart from $\mathcal{L}_{eff}$, no extra quenching factor affects S2, which can be essentially modeled as complementary to S1.

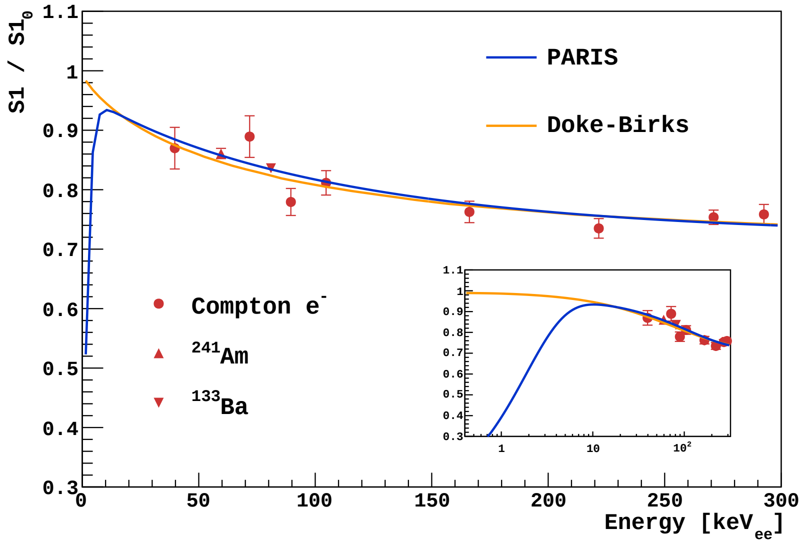

Figure 4.6 – Field induced quenching of S1 for ERs at 200 V/cm compared with the PARIS model and the fit of the Doke-Birks model.

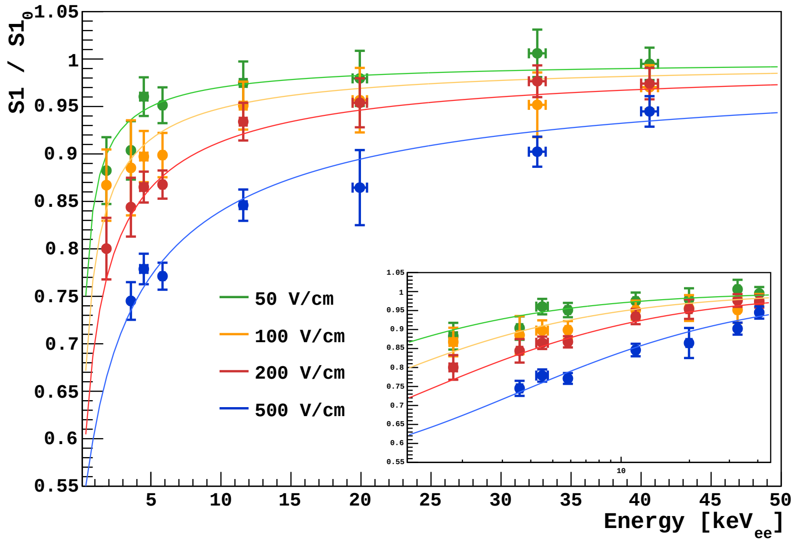

Figure 4.7 – Field induced quenching of S1 for NRs for different drift fields. The systematic uncertainties are included in the error bars.

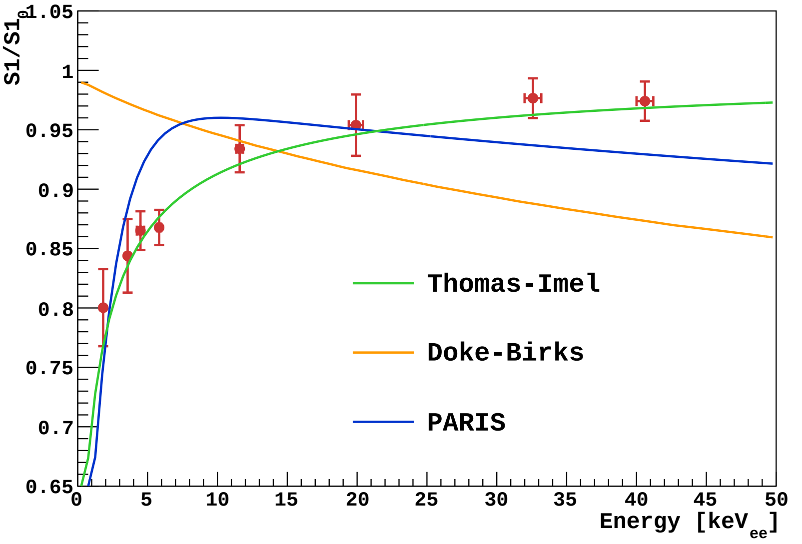

Figure 4.8 – Field induced quenching of S1 for NRs at 200 V/cm compared to model predictions from Thomas-Imel, tuned on the NR data set, and Doke-Birks and PARIS models, tuned on ERs, and assuming α=1.

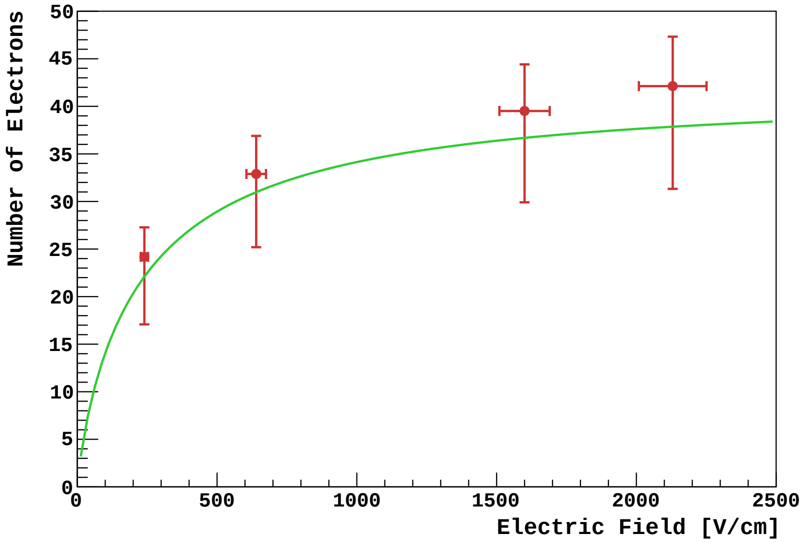

Figure 4.9 – Comparison of the S2 signal, expressed in number of ionisation electrons, between the *Joshi et al.* data set at 6.7 keV$_{nr}$ and the Thomas-Imel model prediction, as function of the drift field.

4.4 f$_{90}$ dependence on the electric field

Another study done with ARIS data was the dependence of f$_{90}$ on the electric field.

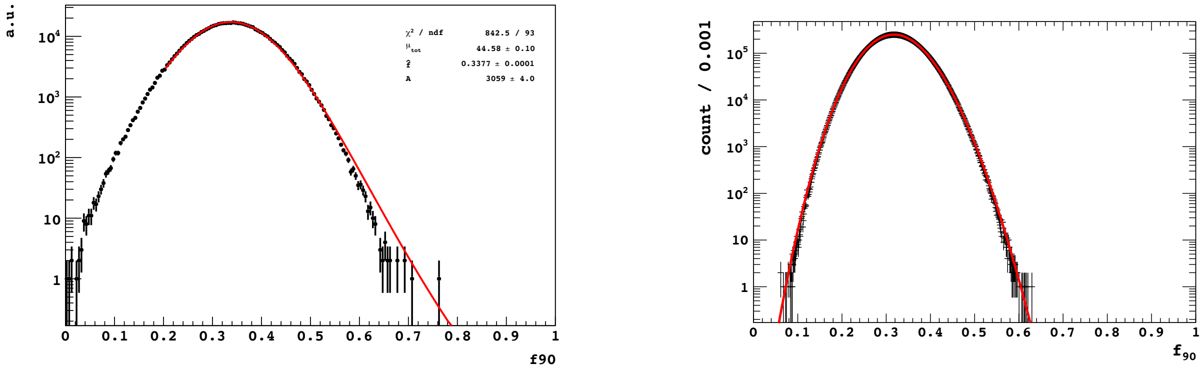

(a) Toy MC f$_{90}$ distribution fitted with DarkSide-50 f$_{90}$ model.

(b) Simulated f$_{90}$ distribution fitted with ARIS f_p model.

Figure 4.10 – Simulated f$_{90}$ distribution fitted with DS-50 (left) and ARIS (right) f$_{90}$ parametrisations.

4.4.1 Modeling the f_p distribution

If DarkSide uses f$_{90}$ as a PSD parameter, we can consider the general case of a parameter f_p, valid in any situation where the PSD is applicable. DarkSide-50 modeled f_p on the basis of the Hinkley function [139], describing the ratio of two correlated normal random variables. However, this model overestimates the tails of the f_p distribution, as illustrated with Figure 4.10a. ARIS proposes an alternative mathematical model of f_p, with the ability to reproduce f_p values also in the distribution tails.

Dark matter experiments analyze f_p distributions in very narrow ranges of photoelectrons. We place ourselves in the single photoelectron range, so that for a given value of S1=S1$_0$,

$$n_p + n_l = \mathrm{S1}_0 \tag{4.28}$$

where n_p and n_l are the prompt and late components of the signal. This means that n_p and n_l are fully anti-correlated.

The f_p distribution is then the ratio between n_p, constrained by $n_p \leq S1_0$, and S1$_0$

$$f_p = \frac{n_p}{n_p + n_l} = \frac{n_p}{\mathrm{S1}_0} \tag{4.29}$$

The second assumption at the basis of this model is that the statistics governing n_p fluctuations can be approximated with a normal distribution. Such an assumption is reasonable for sufficiently large values of n_p (>10) and is supported by the fact that scintillation photons are emitted with Poisson statistics, as shown in reference [130]. f_p will, as n_p follow a normal distribution.

By applying a change of variable so that $n_p = w\mathrm{S1}_0$, we get

$$f_p(w) \propto exp\left(-\frac{(w-w_0)^2}{2\sigma(w)^2}\right) \tag{4.30}$$

where w_0 is the peak of the f_p distribution. This parametrisaton allows to recover the tails of f_{90}, as shown on Figure 4.10b.

4.4.2 Application to ARIS data

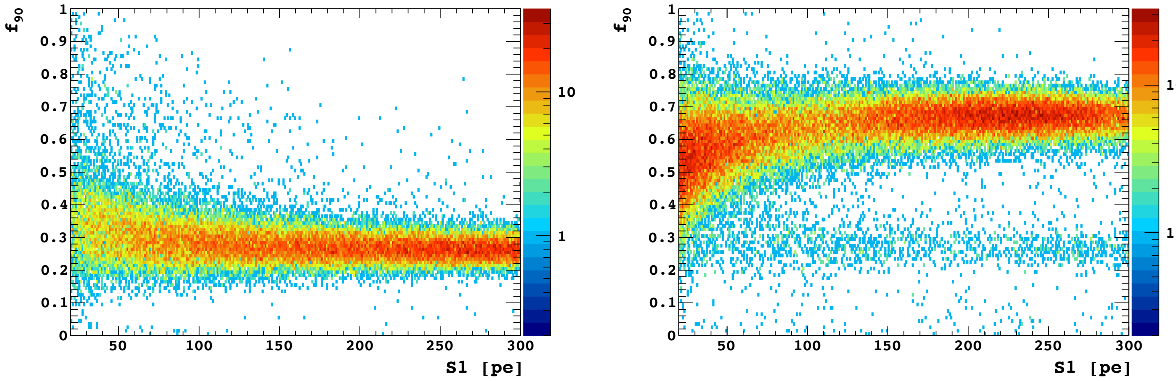

Figure 4.11 – f_{90} vs. S1 distribution in ARIS for ERs(left) and NRs(right) with null electric field.

Figure 4.11 shows the f_{90} distributions obtained in ARIS in the absence of an electric field. ERs data are obtained from a ^{133}Ba source and NRs data come from the ^{7}Li$(p,n)^7$Be neutrons taken in double coincidence mode. Data were also acquired at different drift fields, allowing for a study of the behavior of f_{90} as a function of the drift field.

Distributions at each field were split into S1 bin. Each bin was fitted with the model presented above and the peak of each distribution was extracted. Figure 4.12 shows the evolution of the f_{90} distribution as a function of the electric field for both ERs and NRs. Varying the electric field from 0 to 500 V/cm the ER moves up by 10% while NRs f_{90} decreases by 5%.

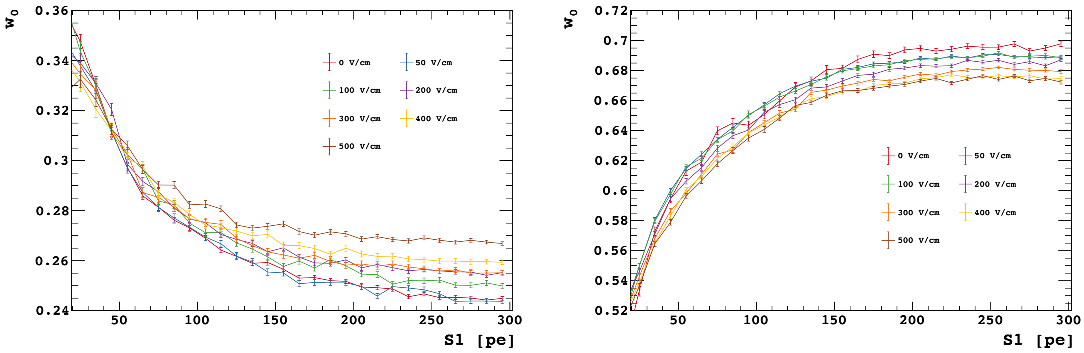

Figure 4.12 – Evolution of the peak of the f_{90} distribution, w_0 for ERs(left) and NRs(right).

4.5 Conclusion

The ARIS experiment was the first occurrence of the use of a collimated and monochromatic neutron beam to measure the response of LAr to nuclear and electronic recoils. We demonstrated the performances of such a technique in LAr. We measured the relative scintillation yield, $\mathcal{L}_{eff}$, of LAr between 7 keV$_{nr}$ and 120 keV$_{nr}$, at the lowest energy and with unprecedented precision.

We also had access to a clean ER sample thanks to the γ produced by ^{7}Li* de-excitation. This allowed us to study the light yield, which was found to be linear within 1.6% in the [40, 511] keV$_{ee}$ range, confirming the results of Lippincott et al [123]. Once again ARIS result is the most stringent test of the linearity of the LAr response.

We also tested the response of LAr in presence of an electric field, in particular, the recombination probability. ARIS data, at different drift fields, were compared to different models of recombination, tuned to our datasets. This confirmed that the PARIS model, developed by DarkSide is good for ERs at the DarkSide-50 operation drift field of 200 V/cm. The Doke-Birks recombination probability models the response to ERs at different fields, but only above 40 keV$_{ee}$, in the upper range of interest for dark matter searches. Finally, a comparison of the ionisation signal between the tuned Thomas-Imel model and an independent NR data set at 6.7 keV$_{nr}$ suggests that no extra quenching factors are required to predict the number of ionisation electrons.

In conclusion, ARIS results provide a fully comprehensive model of the LAr response in the range of interest for dark matter searches through measurement of the $\mathcal{L}_{eff}$ parameter as a function of NR energy, and by properly tuning the parametrisation of the electron-ion recombination probabilities for ERs and NRs.

These results have been used by the DarkSide collaboration to improve the limits on high mass WIMPs. The linearity of the electron recoil scintillation response measured by ARIS has allowed DarkSide-50 to derive the spectral shape of forbidden ^{39}Ar β decay, an important cosmogenic background intrinsic to LAr. The ARIS results have then impacted both the analyses by improving signal and background models.

Furthermore, ARIS results were of key importance in the development of the low mass dark matter searches in DarkSide. By offering measurements of the LAr response over an extended range and with excellent precision, the comprehension of the ionisation signals in LAr was improved, leading to the extraction of the ionisation yield in LAr. This analysis will be discussed in the following chapter.

Part III

Low mass dark matter searches in DarkSide-50

Chapter 5

Low-mass dark matter search in DS-50

Contents

Noble liquids DM experiments have always been aimed at high mass WIMPs [140]. The lower mass range was dominated by other technologies such as bolometers. This is mainly due to the fact that, at lower energies, the S1 signal detection efficiency drops, making the use of PSD or S2/S1 impossible. However, dropping the S1 signal, the high gain of the S2 signal ensures a good detection efficiency down to energies corresponding to one single electron ($\sim$ 20 eV). An analysis relying only on the S2 signal would then be able to have a much lower threshold. Previous similar analyses have been performed in dual-phase Xenon TPCs [141], demonstrating its feasibility and motivating our search.

Compared to xenon, argon has a lower atomic number and smaller quenching effect, making a similar search with DarkSide very attractive.

In this chapter, I will detail the low mass WIMP search in DarkSide-50. I contributed to the data selection, the study of the background shapes and realised a study of the ^{85}Kr activity.

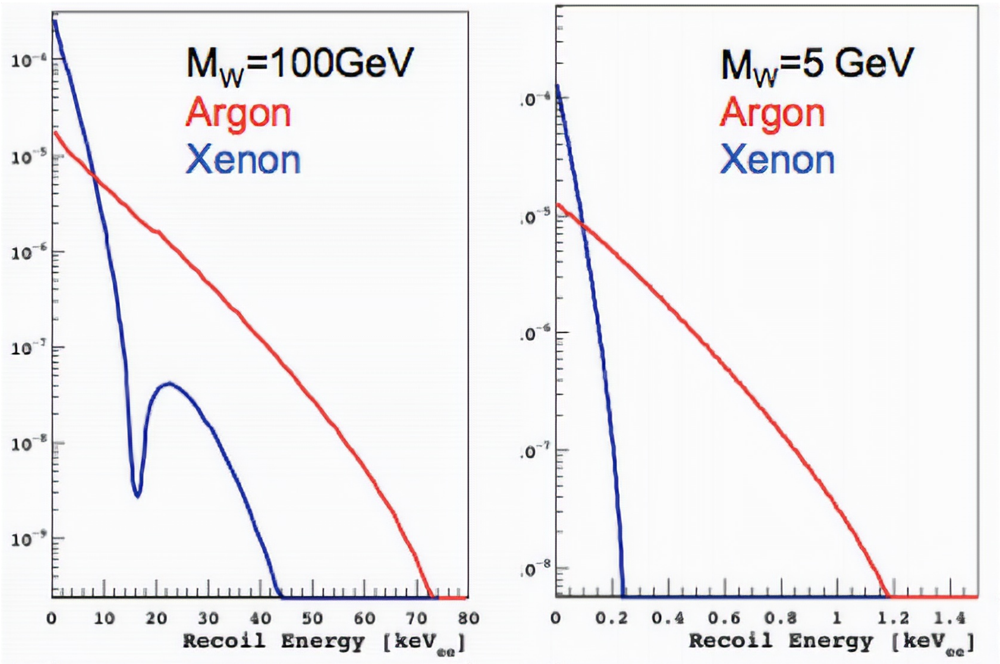

Figure 5.1 – Recoil energy spectra for a 100 GeV/c^2 (left panel) and a 5 GeV/c^2 (right panel) WIMP in LAr (red curve) and LXe (blue curve).

5.1 LAr for low mass WIMP searches

In LAr, the main tool for ER background discrimination, the PSD, cannot be used in the range of energies necessary for low-mass WIMPs searches. Indeed, the use of PSD requires the S1 signal, which detection threshold is ~6 keV$_{nr}$. Also, the separation between the NR and ER populations in the f$_{90}$ vs. S1 plane becomes less efficient as S1 decreases. These combined effects lead to a threshold of 13 keV$_{nr}$ for the use of PSD in DarkSide (see Figure 2.12). It is enough for a 100 GeV WIMP or higher, but the signal of a 5 GeV WIMP, for example, does not reach such energies, as can be seen on Figure 5.1.

However, the fact that low mass WIMP searches have been performed in LXe is a hint that it should also be possible in LAr. Indeed, argon is lighter than Xenon, and for a given WIMP mass the energy deposited will be higher, as shown in Figure 5.1.

Another advantage of LAr is that, as discussed int Chapter 3, the NR quenching is larger in LXe ($\mathcal{L}_{eff}$ <0.1) than in LAr ($\mathcal{L}_{eff} \sim 0.2$). This leads to a larger signal in LAr for a given NR energy.

LXe searches use the ionisation signal (S2) to reach the low energy region, but the possibility had never been studied in LAr before DarkSide.

5.1.1 ionisation signal

In order to access the low mass range, we cannot rely on the usual S1 + S2 signal. But the ionisation signal offers us an excellent alternative. It has a very high detection efficiency down to low energies and there is no dark rate in the PMTs at cryogenic temperatures. These combined effects allow us to set a much lower analysis threshold for S2. Such a threshold is sufficient to reach WIMP masses below 10 GeV/c^2. DarkSide used the number of electrons, Ne, as the observable for this analysis. All the usual ionisation energy variable, S2, has to be converted into Ne, requiring the calibration of the detector to determine the energy conversion scale for both electronic and nuclear recoils.

5.2 Response of DarkSide-50 to low ionisation signals

5.2.1 Generation of S2 signal in G4DS

The response of DarkSide-50 to low energy ionisation signals has been simulated through G4DS. We generate S2 pulses that correspond to a few electrons. The PE yield (the number of PEs per electron) depends on the distance to the center of the TPC due to the width of the gas pocket. The fraction of light seen by each of the PMTs depend on the XY position. We use the results from the XY position reconstruction algorithm to recreate the channel pattern in the simulation. The radial dependence of the S2 yield is extracted from ^{83m}Kr data [130], as shown on Figure 5.2. Events are generated randomly according to a uniform distribution in XY with $0 < r < 18$ cm. The simulated events are classified according to the PMT that registered the largest number of PEs, *s2 max chan*. This is the spatial tag that will be used in this analysis. We will only consider events with a *s2 max chan* that corresponds to the central PMT or the surrounding ones.

The reconstructed number of electrons is

$$N_e = \frac{S2}{f^i_{XY} f_{Central} \mathrm{g}^0_2} \tag{5.1}$$

where f^i_{XY} is the mean signal of a uniformly distributed mono-energetic source at a given PMT with respect to the central PMT (by definition, it is 1 for the central PMT); $f_{Central}$ is the ratio of the mean signal of a uniformly distributed mono-energetic source at the central PMT with respect to events at $r = 0$. The value of $f_{Central}$ has been derived from MC simulations and found to be 0.935. Finally g^0_2 is the PE yield at $r = 0$.

Because of an observed radial variation in the electroluminescence yield, a correction is applied to the S2 photoelectron yield for events that originate under the six PMTs surrounding the central one. This correction to the number of extracted electrons, Ne$^-$, was determined using calibrations performed to be $Ne^- = S2/(0.76 \times g_2)$.

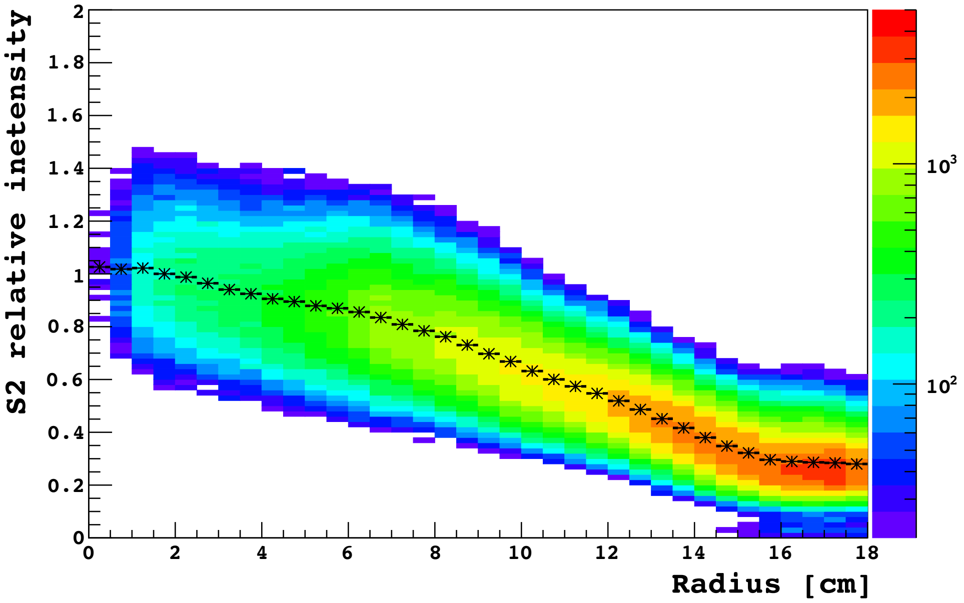

Figure 5.2 – Radial dependence of the S2 relative yield, extracted from ^{83m}Kr. Black dots correspond to the mean S2 value at fixed radii.

5.2.2 Classification of pulses

We use f_{90} to classify the pulses as S1 or S2. Indeed, the S2 signal is slow due to the electron drift time. As a result, the f_{90} of S2 only signals is pushed towards low values. The electron drift lifetime in DarkSide-50 is estimated to be > 5 ms. Considered the maximum drift time of 376 µs in the TPC the total z variation of S2 is $< 7\%$. The cut value is derived using AAr by fitting the low tails of the ER f_{90} distributions and requiring than less than 1% of events have an f_{90} below the cut. The optimum cut found is $f_{90} < 0.15$ (see Figure 5.3).

5.2.3 Single electron calibration

Single-electron events are defined as events where a single electron is extracted in the gas phase and emits electroluminescence light. Large S2 pulses can cause the emission of electrons from the cathode due to the photoelectric effect. These electrons are then extracted in the gas phase, causing electroluminescence pulses, which are actually echoes of S2's. Those events are referred to as ”S3”.

The S1 photons can also produce small S2 signals by photoelectric effect off materials present in the TPC. This process can happen in the argon itself, with impurity molecules (O_2, N_2, etc.) contained in the noble gas at the ppb level or with the detector components (the grid, the cathode, the field shaping rings, the TPB, etc.). argon UV photons, given their energy of ~9.7 eV, could either ionise negative O_2 ions created by the attachment of drift electrons with O_2 impurities or photo extract electrons from the TPB coating all the surfaces. The first scenario is possible since O_2 electron binding energy is 0.45 eV [142], while the first ionisation energy of O_2 and N_2 are above 12 eV [143, 144]. And the second case is likely since the UV photon energy could exceed the

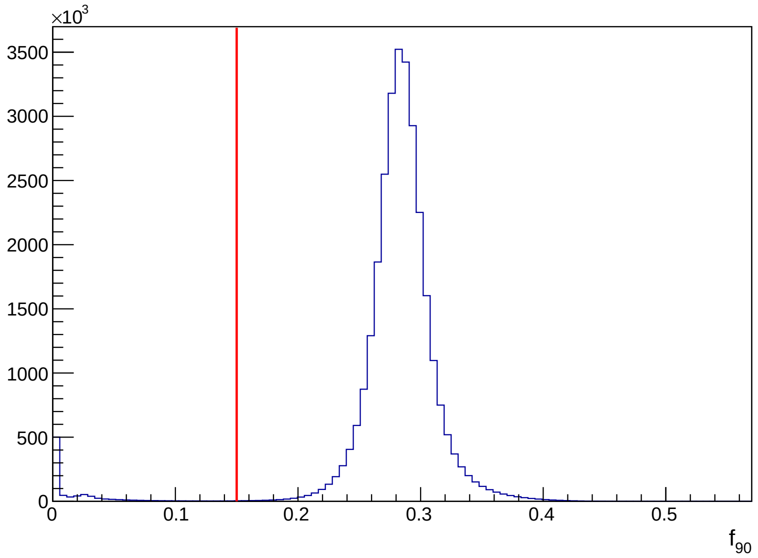

Figure 5.3 – f_{90} distribution for electronic recoils from the AAr data.

ionisation energy of the TPB (∼5.4 eV estimated indirectly) [145], thus producing free electrons. In all cases, the signature of the single pulses will be a small S2 signal.

There are then two ways to look for single-electron events in the data: S3 events or single electrons caused by UV photons.

For the second case, we use the time period during which the inline argon purification getter[1] was o ff for maintenance purposes. During this time, electronegative impurities like O_2 were not actively removed. The presence of electronegative impurities can produce single-electron S2 signals in the TPC.

Single-electron events allow us to determine the value of an important parameter: g_2. g_2 is the detector-dependent S2 photoelectron yield per drifted electron. Knowing the value of g_2 is necessary to convert the measured values of S2 into the corresponding number of electrons.

5.2.3.1 g_2 from S3 events.

S3 events are selected by requiring events triggered on S2 and looking in the region [372,405] μs since the start of the pulse, where we expect the echo. Indeed, at 200 V/cm (the nominal drift field in DarkSide), the maximum electron drift time is $t^{max}_{drift} \simeq 376$ μs. The selected data are then fitted with a Gaussian to extract the PE yield (see Figure 5.4a).

The resulting value is $g_2 = 22.76 \pm 0.15$ PE/e^-.

5.2.3.2 g_2 from getter-off data

The sample of single-electron events from the "getter-off" campaign is particularly valuable due to the tight correlation in XY positions between the parent event and the subsequent single-electron

---

[1] The argon is continuously recirculated in the detector both for cooling of the cryostat and purification. The argon is passed through a getter which reduces contaminants such as O_2 and N_2 to sub-ppb levels.

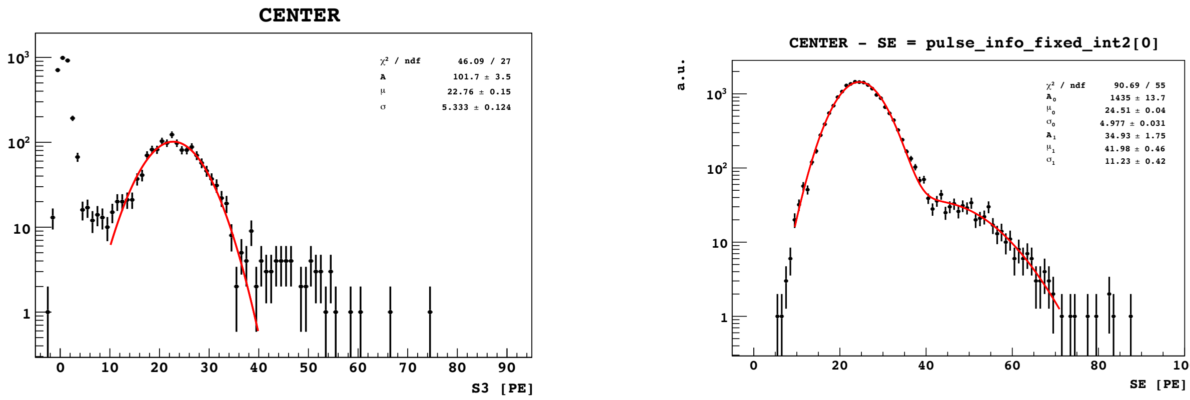

(a) S3 events spectrum with S2 triggers.

(b) Single electrons from the "getter-off"

Figure 5.4 – Single electron events from S3 echoes and getter-off data.

event. We dispose of a reliable reconstruction of the parent event, thus minimizing the bias in the estimation of g_2

In order to select single electrons, basic quality cuts are applied. We require that the time difference Δt between the event and its parent to be shorter than 0.04 s. There is a large excess of events between normal data taken with the getter on and the ones with the getter off for $Log_{10}(\Delta t)$ in [2.8,1.5]. Events in this bump could represent electrons released by impurities after the end of the time window for the previous events. We also ask $\text{f}_{90} < 0.25$ since single-electron events are S2-like pulses. We finally require only one pulse to be in the waveform as expected for a clean single electron released.

The data are then fitted with Gaussians to extract the value of g_2 (see Figure 5.4b). Figure 5.5 shows the distribution of the single-electron events during the getter-off campaign. The best estimate for g_2 gave $g2 = 24.51 \pm 0.04$ PE/e^- for events localised beneath the central PMT. This value differs from the one obtained with S2 echoes. For the following analysis, a value of 23 ± 1.0 PE/e^- has been chosen, in order to account for the discrepancy between the two values of g_2.

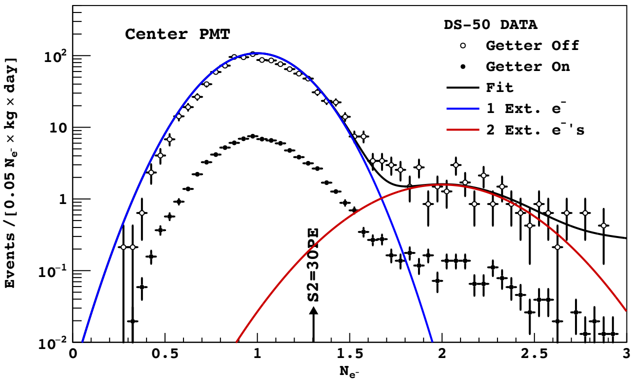

Figure 5.5 – Filled symbols show DarkSide-50 experimental Nespectra obtained during regular data taking and (open symbols) during the short period where the getter was off for maintenance. Both the single and double electron peaks are seen to be strongly enhanced in the absence of argon purification. Smooth curves show a weighted sum of the G4DS one- and two-electron responses.

5.3 Energy scale calibration

In order to calibrate the response of the detector, we need to relate the observable (S2 or Ne) and the visible energy in the argon. This has to be done by measuring the ionisation yield, which is the number of electrons produced for a given energy deposited in the liquid, as a function of the deposited energy (energy scale). Due to the quenching effects, the energy scales will be different for ER and NR. We, therefore, define two energy scales: one for ER and one for NR. The ER energy scale is obtained using peaks from ^{37}Ar and ^{83}Kr as anchor points. The NR scale comes from *in-situ* calibration data from ^{241}Am^{13}C and AmBe neutron sources, and neutron-beam scattering data from the SCENE [117] and ARIS [146] experiments.

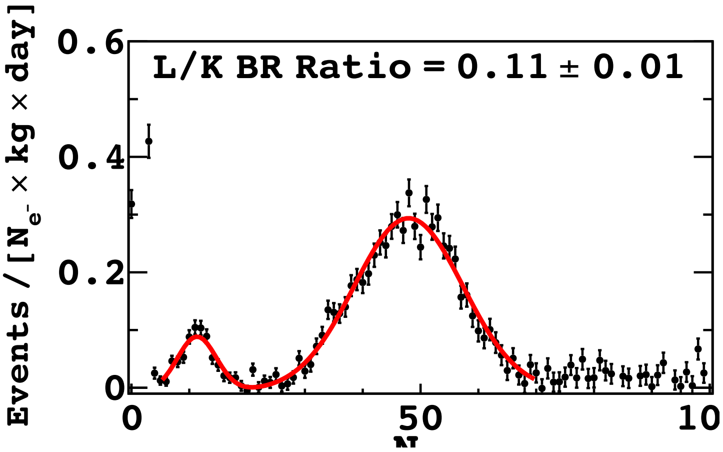

Figure 5.6 – First 100 days of the low mass dataset showing the two ^{37}Ar lines at 0.27 keV and 2.82 keV.

5.3.1 ER energy scale

The ER energy scale is calibrated at low energies thanks to the presence, in UAr, of ^{37}Ar, produced via cosmic activation. ^{37}Ar has a half-life of 35.04 days [147] and decays at 100% via electron capture [148, 149] to ^{37}Cl via the reaction,

$$^{37}\mathrm{Ar} \rightarrow ^{37}\mathrm{Cl} + \nu_e \tag{5.2}$$

Here we will be interested in the L-shell and K-shell electron captures, which emit respectively 0.27 keV and 2.82 keV X-rays, with respective branching ratios of 0.09 and 0.9 [150]. This makes ^{37}Ar an excellent source for the calibration of the ER scale in DarkSide since the lower energy line falls in the single S2 energy region while the higher peaks fall in the single scatter region (see Section 5.4). We can then calibrate both regions of our analysis with the same source. Due to its relatively short half-life, ^{37}Ar will only be present in the early days of the data taking. For this reason, we will only consider the first 100 days of the dataset to extract the ^{37}Ar points.

Figure 5.6 shows the UAr spectrum of ^{37}Ar. We fitted the data with Gaussians in order to check the branching ratio between the L-shell and K-shell decays. We find a value of 0.11 ± 0.01 for the

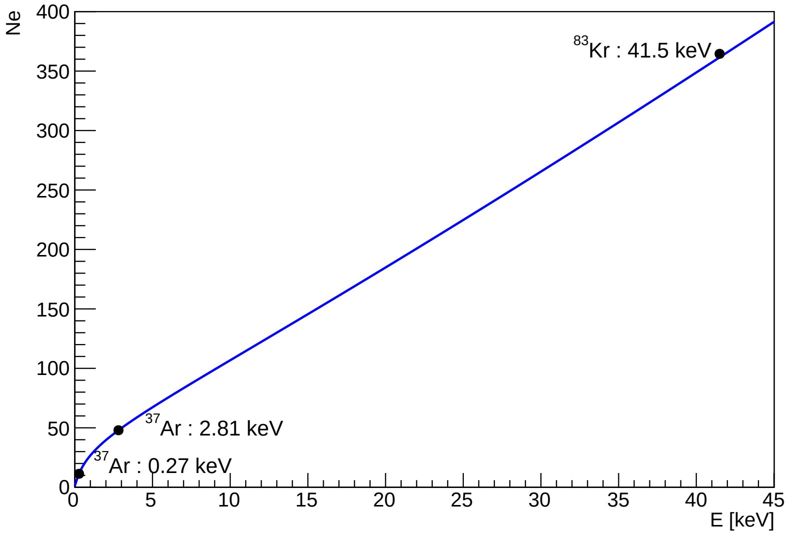

Figure 5.7 – ER energy scale over the low mass WIMPs energy range using the lines from ^{37}Ar and ^{83m}Kr.

L/K branching ratio. This value is compatible with the theoretical [151, 152] and experimental [153, 154] litterature. The fact that we recover the correct branching ratio confirms that the efficiency is indeed flat in this region.

To extend the energy range of the calibration, a point from ^{83m}Kr has been added to the calibration. Metastable ^{83m}Kr decays to ^{83}Kr in two transitions of 32.1 keV and 9.4 keV [147]. Since the two transitions happen with an intervening half-life of 154 ns, the two peaks are not resolved by the detector, and the spectrum shows a single peak at 41.5 keV.

We also fix Ne (E = 0) = 0. The points are then fitted with the following function

$$a \times (b + c \times E) \times ln(d \times E + 1) \tag{5.3}$$

where a, b, c, and d are free parameters. We find $a = 0.93 \pm 0.05$, $b = 16.94 \pm 0.98$, $c = 1.44 \pm 0.08$ and $d = 3.76 \pm 0.2$. Figure 5.7 shows the obtained energy scale for electronic recoils.

5.3.2 NR energy scale

The NR energy scale was obtained using both external and *in-situ* calibrations.

5.3.2.1 External calibration : ARIS and SCENE cross-calibration

Data from the ARIS and SCENE experiments were also used to calibrate the NR energy scale. SCENE directly measured the ionisation yield while ARIS only had access to the scintillation, but reached lower energies. The ionisation yield in ARIS was then extrapolated relatively to the S1 measurement in DS-50 for ^{83}Kr. The first step is to express the S1 in DS-50 as a function of the parameters measured in ARIS. The ionisation yield in ARIS can be expressed as

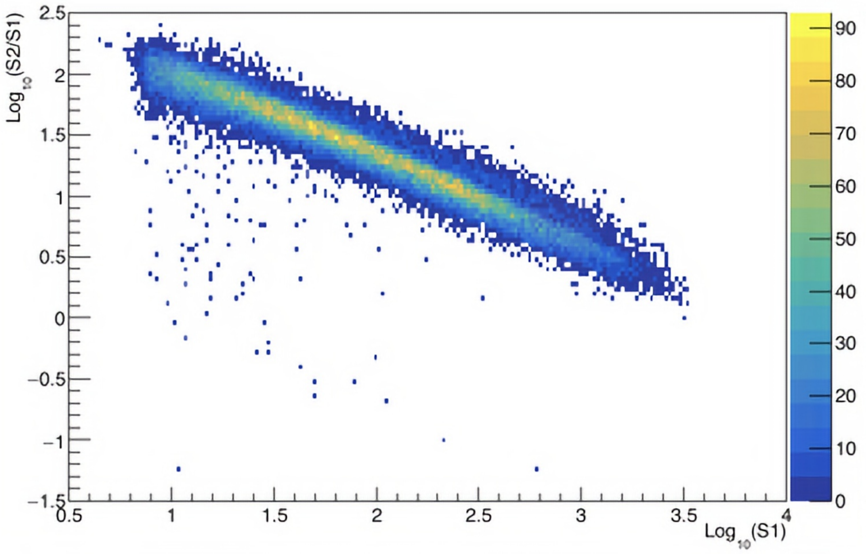

Figure 5.8 – S2/S1 as a function of S1 from AmBe data.

$$Q_y(E_{nr}) = \frac{\mathcal{L}_{eff} \times LY^{DS50}}{g_2} \cdot \frac{S1^{ARIS}_{200V}}{S1^{ARIS}_{0V}} \cdot \frac{S2^{DS50}}{S1^{DS50}} \tag{5.4}$$

In Eq. 5.4, $\mathcal{L}_{eff}$ and $\mathrm{S1}^{ARIS}_{200V}/\mathrm{S1}^{ARIS}_{0V}$ are taken directly from ARIS data; LY^{DS50} is the light yield at null field in DS-50, $LY^{DS50} = 8.1 \pm 0.2$ ph/keV$_{ee}$; g_2 is the photoelectron yield, determined in Section 5.2.3; and $S2^{DS50}/\mathrm{S1}^{DS50}$ is taken from Figure 5.8.

The obtained scale is then compared with the ionisation directly measured in SCENE at a drift field of 193 V/cm [107, 117]. As visible in Figure 5.9, the two measurements are in good agreement, reinforcing the ARIS result at lower energies.

However, even with ARIS extension of the energy range towards lower values, the scale obtained does not reach the energies of interest for low mass WIMP searches, where we are interested in energies below 3 keV$_{nr}$. That is why *in-situ* calibrations with neutrons sources have also been performed.

5.3.2.2 *In-situ* calibration

Two sources were used for the *in-situ* calibration of the ionisation response to NR : ^{241}Am^{7}Be and ^{214}Am^{14}C. Neutrons from both sources are generated in G4DS.

Event selection ^{241}Am^{7}Be has three different neutron emission channels:

- 36% with no γ emission
- 61% in coincidence with a 4.439 MeV γ
- 3% in coincidence with two γs of 4.439 MeV and 3.215 MeV

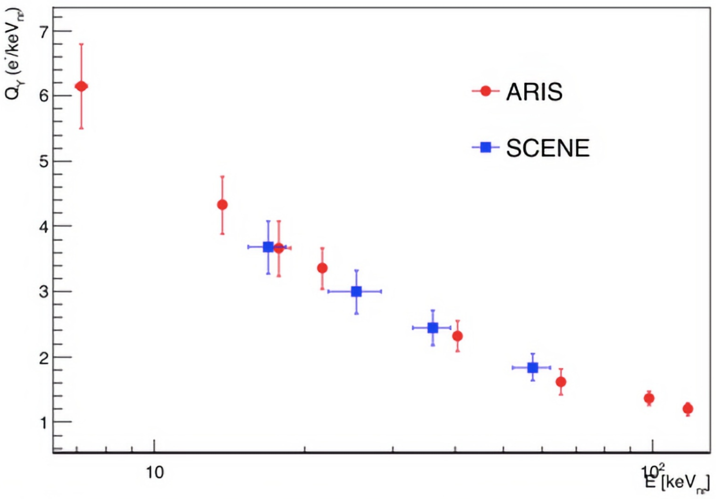

Figure 5.9 – NR ionisation yield from both ARIS and SCENE calibrations.

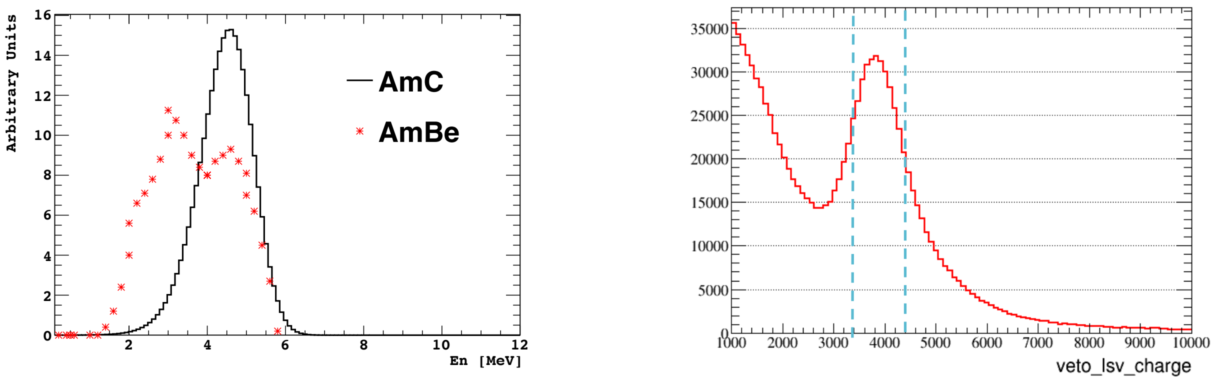

(a) Neutron spectra obtained for events from ^{241}Am^{7}Be in association with a single 4.439 MeV γ(red dots) and ^{214}Am^{14}C (black histogram).

(b) Energy spectrum measured in the LSV during the ^{241}Am^7Be campaign. The blue dashed lines represent the selection cuts used to identify the 4.439 MeV γ-ray.

Figure 5.10

We select the neutrons in the TPC in coincidence with a 4.439 MeV γ in the LSV as illustrated by Figure 5.10b. This allows to eliminate the γ and accidental backgrounds. Figure 5.10a shows the spectrum of neutrons from both sources that pass our selection cuts. However, in the case of S2-only data, the event in the veto arrives before the S2 since the veto signal is tuned to be in coincidence with the S1 (required for the high mass S1 + S2 searches). This induces a huge loss of efficiency: only 2% of the events are acquired, corresponding to the ones with small drift distance.

^{214}Am^{14}C does not emit neutrons and γs simultaneously, but the source is weaker. Therefore, there is no coincidence with the veto and we select the neutron events from ^{214}Am^{14}C without any veto cuts. This eliminates the decrease in the efficiency of the S2-only signal. However, a large fraction of events is due to background uncorrelated with the source. This background is statistically subtracted by using the 500 days UAr spectral shape, normalised in the higher Ne range from 600 Ne to 2500 Ne. No γs are emitted in association with the ^{214}Am^{14}C neutrons, but, α's from the ^{214}Am decay are very often emitted in association with X-rays and γ-rays. The dominant γ-ray component is the 59.5 keV line, with a 36% branching ratio. In addition, there are two groups of γ-ray lines centered around 330 keV and 670 keV, whose combined branching ratio sums to $\sim 2 \times 10^{-5}$. The 59.5 keV γs do not contribute in the DarkSide-50 LAr TPC as they are entirely suppressed by the 2 mm-thick Pb source shell, by the liquid scintillator, and by the passive materials surrounding the LAr active volume. Higher energy γ-rays provide a non-null contribution to the ER background. To reduce the γ background, only the four central PMTs (far away from the source) were considered. The residual γ background has been evaluated with a full G4DS simulation accounting for the 59.5 keV line and the two groups of lines centered around 330 keV and 670 keV.

Backgrounds from NRs correlated with these γ-rays can be safely neglected with respect, given the additional suppression factor of several orders of magnitude given by the low efficiency of neutron production in any (α ,n) reaction.

Conversion of the data to Ne Ne spectra for the data are produced by scaling S2 by $1./g_2$. The g_2 uncertainty is propagated directly in the data, by adding in quadrature the correspondent uncertainty in each bin of the data sets. We repeat the same procedure by scaling S2 by g2 within the 1 σ range. The average difference in each bin (1 Ne width) with respect to the data set produced with the central value of g_2 is accounted for as an additional systematic error.

Conversion of the MC to Ne Figure 5.11 shows the spectra of the energy deposited in the TPC for both AmBe and AmC distributions, requiring a single scatter in the TPC and $r < 12$ cm. To produce the MC spectra as a function of Ne, detector response and response model are applied on an event-by-event basis, according to the following sequence:

1. Number or quanta: $N_q = \text{Binomial}((E/W-1),\mathcal{L}_{eff})$
2. Number of ions: $N_i = \text{Binomial}(N_q, 1/1+\alpha)$
3. Number of electrons: $N_e = \text{Binomial}(N_i, 1-R)$
4. $\text{S2} = g_2 \times \text{Gaussian}(N_e, \sigma\sqrt{N_e})$

where $W = 19.5$ eV, R is the recombination probability and $\sigma \sim 0.2$ is the single electron resolution in PE. Quenching fluctuations can be turned off by substituting $N_q = e/W$ as the outcome of the first step.

The detector model is included at step 3, into the expression of the recombination probability.

The inefficiency on S2-only events in the ^{241}AmBe sample depends on trigger efficiency on S1: if S1 is detected, veto and TPC signals induced by the same particles, occur within a few tens of nanoseconds. If S1 is not detected, the coincidence between veto and S2 may be lost because the drift time is longer than the pre-trigger acquisition window. The trigger condition requires two PMTs fired within 100 ns. We use the product of f_{90} and S1 to evaluate if S1 has satisfied this

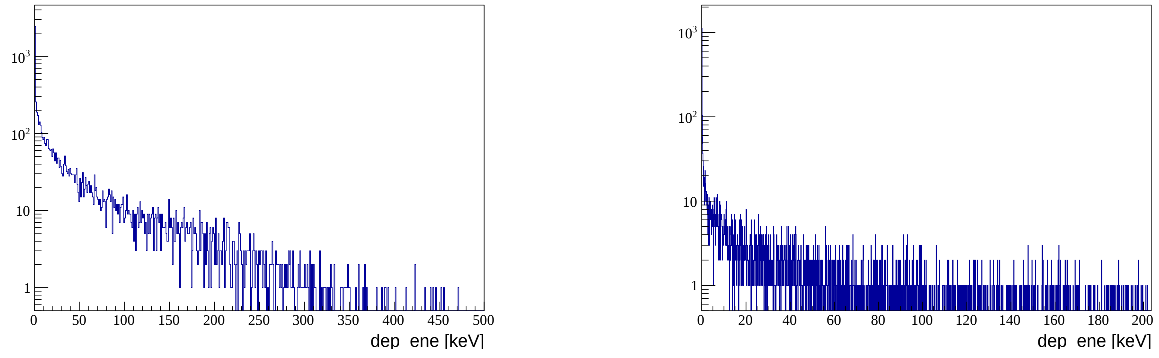

(a) (b)

Figure 5.11 – True energy deposited in the TPC from the AmBe (left) and AmC (right) MC simulations.

requirement, recognizing the approximate nature of this determination. For this reason, the region of the AmBe spectrum where the inefficiency is not negligible (Ne < 50) is excluded from the fit.

Fit and extraction of the ionisation yield The conversion of the MC distribution to Ne is done using the Lindhard-Ziegler-Bezrukov [127, 155, 156] recombination probability. The expression of the recombination probability of the LZB model is based on the Thomas-Imel theory (see Chapter 3).

Let's recall the Thomas-Imel recombination probability,

$$R = 1 - \frac{1+\xi}{\xi} \tag{5.5}$$

where

$$\xi = C_{box}\frac{N_i}{F^{\beta}} \tag{5.6}$$

where F is the electric field, $N_i = \frac{N_q}{1+\alpha}$ with N_q, the number of produced quanta. C_{box} and α are undetermined.

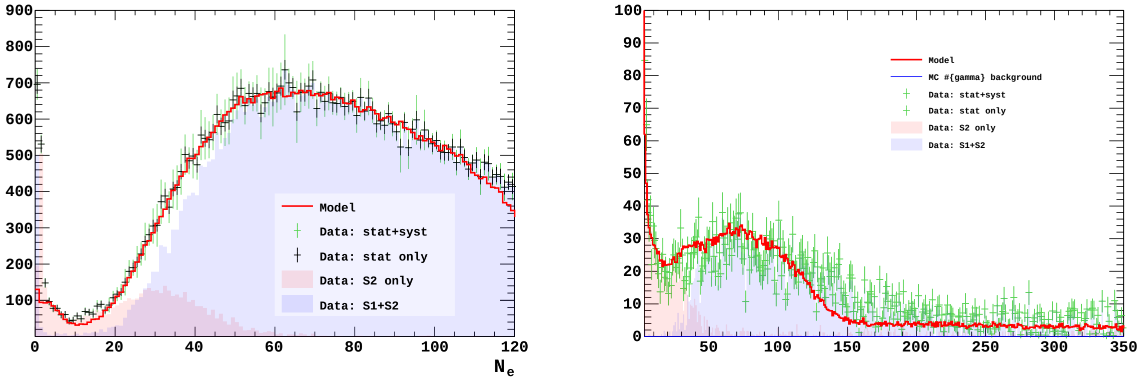

Figure 5.12 – Comparison of the AmBe (left) and AmC (right) data in DarkSide-50 to the MC assuming best fit of the LZB model.

The LZB model uses the universal stopping power from Ziegler et al. [156]. The formalism of the LZB model is also slightly different from Thomas-Imel and introduces a new parameter. In [155],

$$N_{ex} + N_i = \beta\epsilon\xi(\epsilon)$$

where β is a constant, ϵ is the reduced energy[1] and $\xi(\epsilon)$ is the ratio of the electronic over nuclear stopping powers. The recombination probability is expressed as

$$R = 1 - \frac{4}{\gamma N_i} ln\left(1 + \frac{\gamma N_i}{4}\right) \tag{5.7}$$

Equating it with the Joshi [137] parametrisation of the Thomas-Imel model, we have

$$\xi = \frac{\gamma N_i}{4} = C_{box}\frac{N_i}{F^\beta} \tag{5.8}$$

and then

$$\gamma = \frac{4C_{box}}{N_i} = \frac{\alpha}{a^2 v} \tag{5.9}$$

where α is a recombination coefficient and v is the electron velocity.

In the fit of this model to the data that we perform, the free parameters are C_{box} and $k = \beta/(1+\alpha)$. The parameter k is defined to avoid any degeneracy between $\gamma \propto \alpha$ and β when converting the reduced energy into energy.

In order to avoid effects related to the model of the trigger efficiency affecting S2-only data, the AmBe spectrum is fitted only in the region of Ne$> 50e^-$. A threshold of Ne$> 4e^-$, equivalent to the low mass analysis threshold that will be introduced later, is instead used for the AmC spectra. The upper limit of the fit is set at Ne$= 120e^-$, beyond which limit uncertainties from the presence of ER background in the AmC campaign could bias the result. Figure 5.12 shows the fit of the AmBe (left panel) and AmC (right panel) data with the model.

We found values of $C_{box} = 10.71$ and $k = 0.746 \times 10^4$.

Figure 5.13 shows the resulting NR energy scale. The ionisation yield found is 20% lower with respect to ARIS cross-calibration and SCENE data. The origin of this tension was not identified. It is possibly due to systematic errors still unaccounted in the cross-calibration procedure, for example, due to the lack of consideration of the finite energy width of each ARIS measurement campaign. In order to get a conservative limit on the low mass WIMPs cross-section, the analysis was performed using the lowest ionisation yield, given by this *in-situ* calibration, while the difference between the two was taken as a systematic.

---

[1] The reduced energy is defined as $\epsilon \equiv \frac{a}{2e^2 Z^2}E$, where $a = 0.626 a_0 Z^{-1/3}$ s the Thomas-Fermi screening length. In [156], the definition of the reduced energy, ϵ_Z is slightly different since they assume a different screening length.

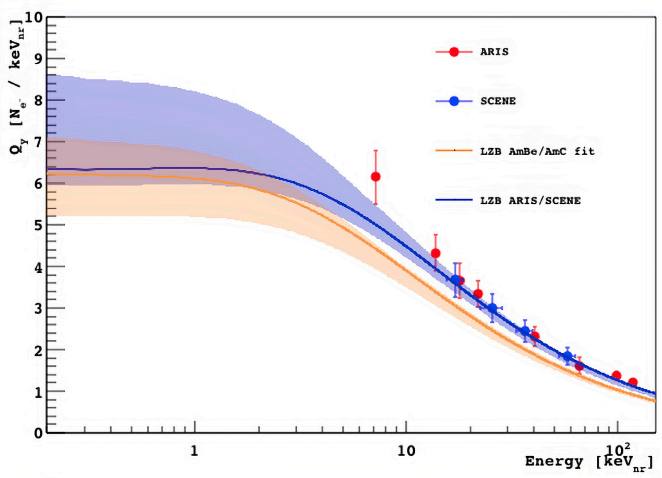

Figure 5.13 – Energy scale for nuclear recoils extracted from the fit the AmBe/AmC and ARIS/SCENE.

5.4 Data selection

Two populations of events are used for this analysis: the S2 only events with no detected S1 and the single scatters with both S1 and S2 signals. Some simple quality cuts are applied to the data before analysis. Flawed runs and runs with abnormal trigger rates or excessive noise in the PMTs were eliminated from the analysis.

npulses cut: Events with either one (single S2) or two (S1 + S2) pulses are selected.

TPCcore cut: Fiducialization is complicated by the fact that in this very low recoil energy region, the S1 signal is often not detectable. This means that the reconstruction of the z position of the interaction via the drift time is not accessible. The x-y position reconstruction via the S2 light pattern analysis is also flawed by the low PE statistics. To circumvent this obstacle, the XY position of each event is reconstructed at the center of the top PMT receiving the highest quantity of light. This is possible thanks to the fact that while S1 light is isotropic, S2 is concentrated on the top PMTs closest to the interaction site. This can be explained geometrically by the short distance between the interaction site and the PMTs. The fiducialization is then done by only accepting events with the highest number of PE in one of the central PMTs (see Figure 5.14a). The effect of this cut is illustrated by Figure 5.14b

f_{90} cut: We use f_{90} to classify events as either S1 or S2. The optimal cut value is determined by fitting the low tails in the f_{90} ER distribution and was determined to be 0.15. The events are tagged as S2 only or single scatter according to their value with respect to $f_{90} = 0.15$

Figure 5.16 shows the data distribution with the separated contributions from the S2 only and S1 + S2 events. The tail of S2 only events is due to unresolved S1 + S2.

The data are also labeled as either *first 100 days* or *last 500 days*. The first region corresponds

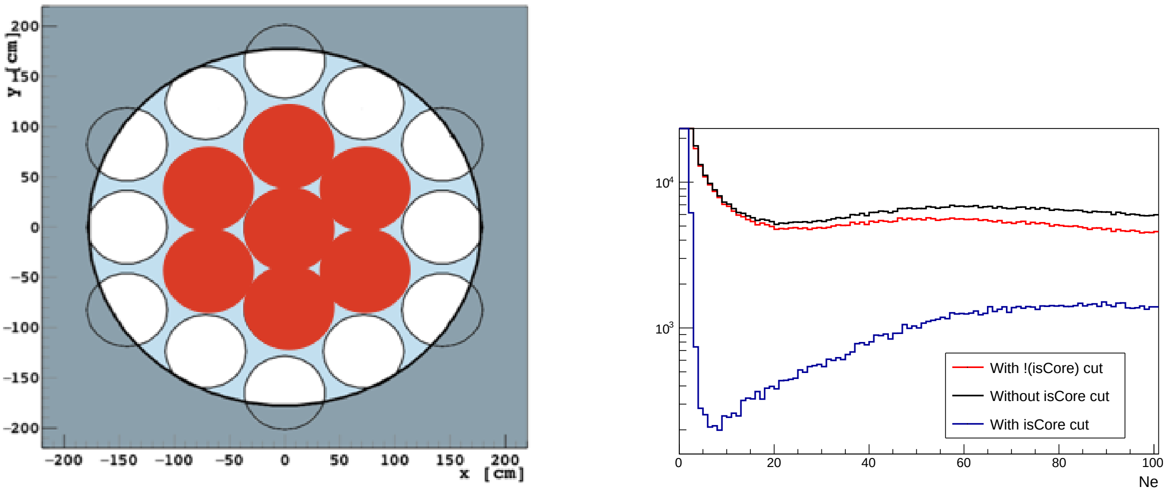

(a) Top PMT array of DarkSide-50. The red PMTs are the one requested to have the highest quantity of light for fiducialization.

(b) Effect of the TPCcore cut.

Figure 5.14

to the first 100 days after the UAr fill, while the latter corresponds to the last 500 days of running. The second period starts roughly 80 days after the end of the 100 days. This separation of the data is made to remove the ^{37}Ar background from the data sample.

The acceptance of the above cuts is estimated with a dedicated MC simulation, as shown in Figure 5.15. The extraction field allows for a 99.99% efficiency of the ionisation electrons into the gas layer. In addition, the pulse finder algorithm has a 100% efficiency for S2 pulse above 30 PE.

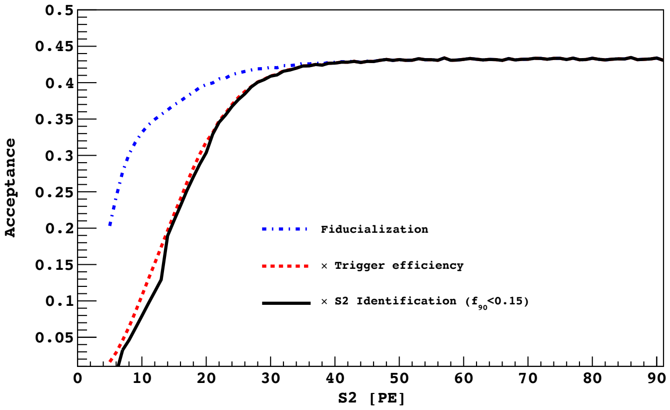

Figure 5.15 – Acceptance of the basic cuts described in the text as a function of S2.

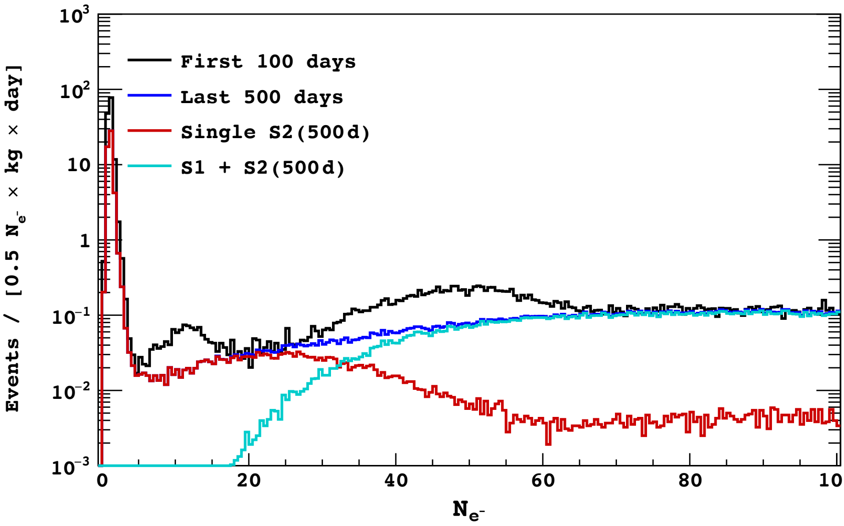

Figure 5.16 – Distribution of the data after the selection cuts.

5.5 Low energy background model

Since, in this region, we are no longer able to efficiently discriminate against the backgrounds, it is necessary to have a profound understanding of both the ER and NR backgrounds in the low energy region. At low energy, the dominant backgrounds are induced by the decay of ^{39}Ar and ^{85}Kr. The two following components are the radioactivity from the PMTs and the cryostat.

At high energies, a spectral fit including all background components allows to adjust the background activities. The starting values are provided by screening measurements of the detector materials.

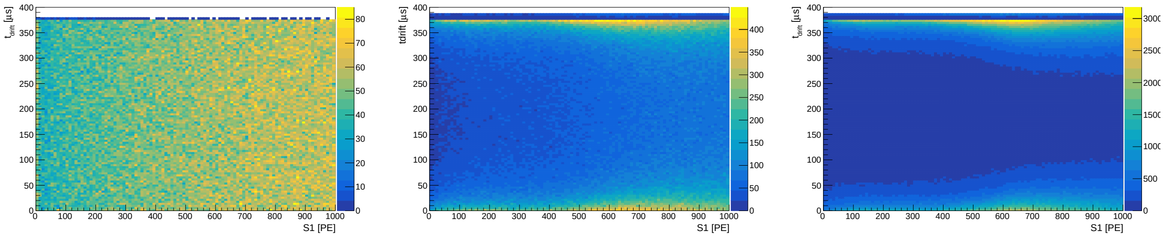

(a) Internal

(b) Cryostat

(c) PMTs

Figure 5.17 – t_{drift} vs. S1 distributions of the different background origins.

5.5.1 Spectral fit

Understanding the mix of various backgrounds in the detector is essential to making a background estimate in any WIMP-search region. In order to characterise the γ backgrounds in DS-50 and evaluate the residual ^{39}Ar contamination, we developed a fit procedure based on MC spectra. In particular, we simulated with G4DS all the β and γ radioactivity coming from different detector components (TPC, cryostats, PMTs, and fused silica windows).

Single scatter events give information on the spatial repartition of the events, while multiple scatters contain the full absorption peaks. However, the full absorption peaks often induces a saturated signal.

In order to get rid of the saturation, we used a new variable, called $\mathrm{S1}_{late}$, defined as

$$\mathrm{S1}_{late} = (1 - \mathrm{f}_{90}) \times \mathrm{S1}$$

. Indeed, the saturation is expected to be present only during the first tens of nanosecond of the typical scintillation pulse, because the fast component of the scintillation pulse is concentrated in this time window, while the slow component is emitted on a several microsecond time scale. The effect of saturation is totally absorbed in the f_{90} deviation from the true value. In this sense, the $\mathrm{S1}_{late}$ variable is free from saturation-induced distortions. $\mathrm{S1}_{late}$ is used to build the full energy spectrum.

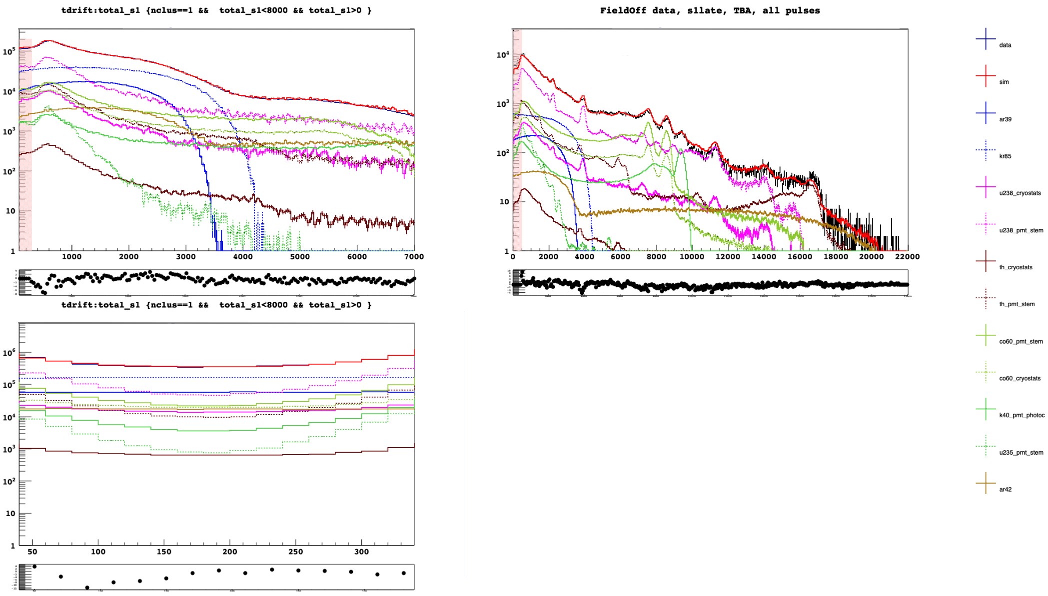

Figure 5.18 – Exemple of the multidimensional fit. Data in in black, the sum of the G4DS background contributions is in red. **Top left:** S1. **Bottom left:** *tdrift*. **Top right:** $\mathrm{S1}_{late}$. The shaded area is not included in the fit.

We perform a multidimensional fit with three observables: S1 for single scatters, $\mathrm{S1}_{late}$ for multiple scatter, and the electron drift time, t_{drift}. The use of the t_{drift} variable allows to distinguish the backgrounds from the cryostat and the PMTs. The t_{drift} distribution for the cryostat is flat,

Background	Rate[mBq]
$^{232}\mathrm{Th}_{PMT}$ [/PMT]	8.505 ± 0.358
$^{232}\mathrm{Th}_{cryo}$ [/kg]	0.117 ± 0.007
$^{40}\mathrm{K}_{PMT}$ [/PMT]	19.269 ± 0.870
$^{60}\mathrm{Co}_{PMT}$ [/PMT]	16.696 ± 0.517
$^{60}\mathrm{Co}_{cryo}$ [/kg]	3.747 ± 0.197
$^{235}\mathrm{U}_{PMT}$ [/PMT]	1.590 ± 0.263
$^{238}\mathrm{U}_{PMT}$ [/PMT]	49.924 ± 0.580
$^{238}\mathrm{U}_{Cryo}$ [/kg]	3.171 ± 0.011
$^{85}\mathrm{Kr}$ [/kg]	1.902 ± 0.009
$^{39}\mathrm{Ar}$ [/kg]	0.682 ± 0.010

Table 5.1 – Background rates, obtained by fitting the different background components.

since the cryostat is surrounding the TPC, whereas the t_{drift} for PMT background are clustered on the top and bottom.

Figure 5.18 shows the results of the multidimensional fit. The left panel concentrates on the [0,6000] PE region of the spectrum.

This region, ending roughly at the endpoint of ^{39}Ar, is observed with the S1 (top) and $tdrift$ (bottom) variables. The top right panel shows the full spectrum as a function of $\mathrm{S1}_{late}$.

The results of the multidimensional fit have been compared to the screening measurements, and a good agreement has been found [157]. The fitted activities are summarised in Table 5.1.

5.5.2 ^{85}Kr activity study

The presence of ^{85}Kr in UAr was totally unexpected and no specific purification procedure has been put in place before the filling of the detector. ^{85}Kr is the dominant background at low energies. It mostly undergoes beta decay to stable ^{85}Rb, with a 687 keV endpoint. However, it can also decay to excited ^{85}Rb with a branching ratio of 0.43% and a 173 keV endpoint. ^{85}Rb has a half-life of 1.015 μs which gives a decay time constant of 1.464 μs. It de-excites by emitting a 514 keV γ-ray as shown on Figure 5.19.

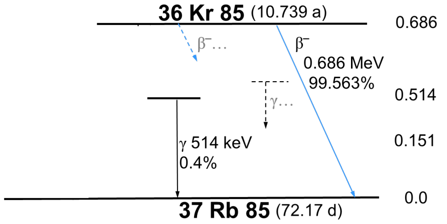

Figure 5.19 – ^{85}Kr decay scheme

This second decay mode will leave a very particular $\beta + \gamma$ signature in the detector that we can use to estimate the ^{85}Kr activity. We look for events with two S1 pulses, very close in time, the

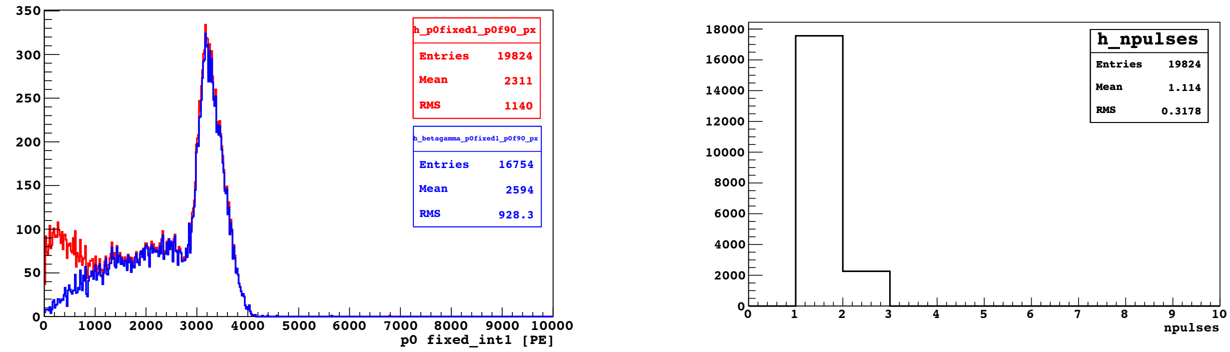

(a) Simulated ^{85}Kr spectrum. The red histogram is the total, whereas the blue one contains only the events with $\beta + \gamma$.

(b) Number of pulses for the ^{85}Kr events simulated in G4DS.

Figure 5.20

first pulse being smaller than the second (the γ energy is higher). Since the pulses are so close in time, it is possible that they will not be resolved by the pulse finder algorithm. We also have to take into account that the γ has a 15% probability to escape detection (see Figure 5.20a).

MC studies with G4DS were conducted to evaluate the detection efficiency of ^{85}Kr through this channel. According to these studies, only 11% of such events are reconstructed as separate pulses, as illustrated by Figure 5.20b. Since most events are reconstructed as one pulse, it is necessary to find a way to separate events with both β and γ signals from events where the γ escapes detection. The method to select such events relies on the pulse peak timing. The pulse peak time is determined by the time bin with the highest number of counts. Indeed, since the second pulse is much higher than the first, the reconstructed pulse peak time will be shifted.

5.5.2.1 Event selection

The activity of ^{85}Kr was studied using 432 live days of data (631 real days). Some quality cuts are applied to the data to eliminated bad runs (baseline, number of active PMTs, livetime and start time of the events).

npulses: The physics cut applied is the number of pulses. Since $\beta+\gamma$ events can be reconstructed as either one or two pulses, this cut has to take both possibilities into account. We require to always have at least two pulses.

- **Unresolved $\beta + \gamma$:** In this case, we assume that the first pulse is an unresolved S1$_\beta$+S1$_\gamma$, all the other pulses being S2s. The first pulse has to be at trigger time and all the other have to start more than 5 μs later to be identified as S2s.

- **Separated $\beta + \gamma$:** We assume that the first pulse is S1$_\beta$, the second is S1$_\gamma$ and all the other are S2s. This time, we require the first two pulses to be within 5 μs of the trigger time and all the other to happen more than 5 μs later.

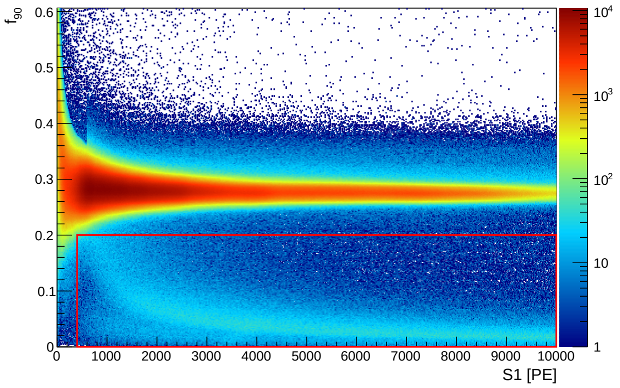

Figure 5.21 – f_{90} vs. S1 distribution. The red box represents the cuts applied.

f_{90} and S1 cut: The ^{85}Kr search box is defined on the f_{90} vs. S1 plane as shown on Figure 5.21. We take 400 PE $<$ S1 $<$ 10000 PE and $f_{90} < 0.2$.

Peaktime cut: The most important cut for this search is the one on the peak time. The definition of the peak time is different whereas the $\beta + \gamma$ is resolved or not. If only one pulse is reconstructed, the peak time is the peak time of the first pulse. In the other case, the peak time is the peak time of the highest amplitude peak between the first two pulses. However, this cut is limited by events where the S1 and the S2 are very close. The cut is defined as 0.05 μs $<$ peaktime $<$ 5 μs.

f_{5000} cut: In addition to the peak time cut, a cut has been designed on the model of the f_{90} cut. Since there is a high probability that the γ pulse will be contained within the first 5 μs of the pulse, the cut relies on the ratio of the integral of the first 5 μs of the pulse over the total 7 μs window. The ideal cut value has been tuned with G4DS and determined to be $f_{5000} > 0.9$, as illustrated on Figure 5.22a. The population highlighted by the red box corresponds to the $\beta + \gamma$ events.

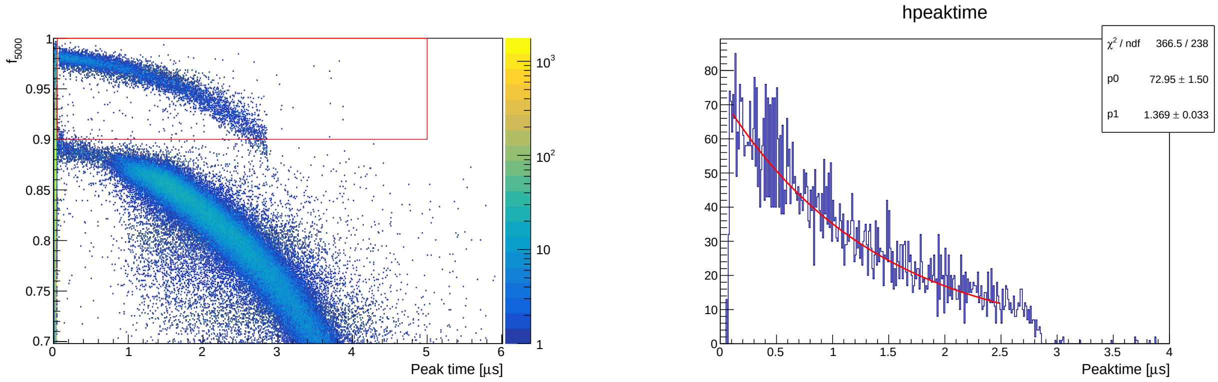

(a) Distribution of the f_{5000} variable with respect to the peaktime variable. The box shows the cuts applied on the peak time and f_5000 variables.

(b) Distribution of the peaktime variable after the f_{5000} cut

Figure 5.22

Fitting the peak time distribution in Figure 5.22b with an exponential gives us a measure of the ^{85}Rb* decay constant. We obtain a measure of 1.369 ± 0.033 µs, which is close to the expected value of 1.464 µs.

We found 8589 events passing the cuts in the dataset. The spectrum of these events is shown in Figure 5.23a.

5.5.2.2 Activity determination

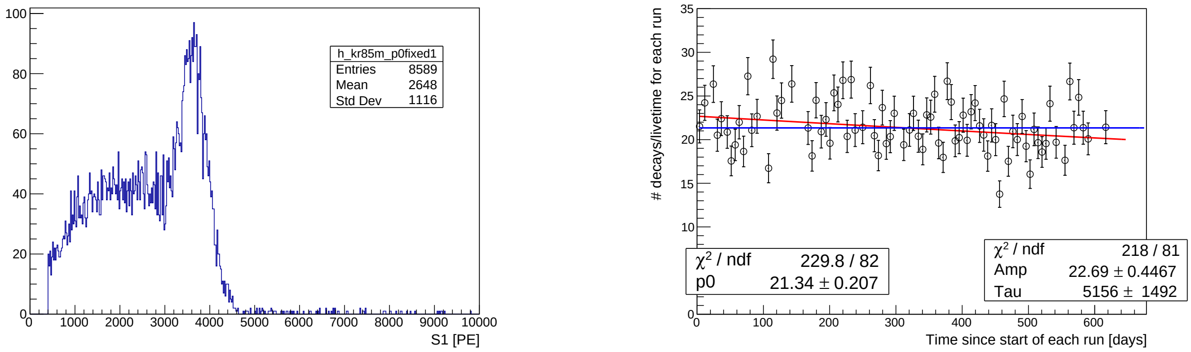

(a) Spectrum of the ^{85}Kr candidate events passing the selection cuts.

(b) Number of ^{85}Kr decays per day via the $\beta + \gamma$ channel as a function of the livetime.

Figure 5.23

Once the right set of events is selected, we can study the rate of events as a function of the livetime, as shown on Figure 5.23b. It allows us to perform fit to evaluate the number of decays per day. It is then converted into an activity in mBq/kg, taking into account the detection efficiency determined with MC studies, and the mass of the detector.

Linear fit We first performed a linear fit to determine the average number of detected decays per day as well as the decay rate of ^{85}Kr. We found 21.3 ± 0.21 detected decays per day on average. MC studies evaluated the detection efficiency of ^{85}Kr events to be $\sim 67\%$ after the selection cuts. Adding the efficiency tot he calculation, we obtain 31.8 ± 0.3 decays per day. And then adding the branching ratio of 0.463% for this channel, we arrive at 7407 ± 70 ^{85}Kr decays per day. From this we deduce a 1.85 ± 0.02 mBq/kg activity, considering the 46.7 kg of LAr in the detector. This value is slightly lower than the value found in the spectral fit.

Exponential fit We also performed an exponential fit, allowing us to evaluate both the number of decays per day and the decay rate of ^{85}Kr. We found 22.69 ± 0.45 detected decays per day. Multiplying by efficiency, it gives us 33.9 ± 0.7 decays per day. And then adding the branching ration of 0.463% for this channel, we arrive at 7876 ± 156 ^{85}Kr decays per day. And thus, a 1.95 ± 0.04 mBq/kg activity. This value is compatible with the spectral fit value, within error bars. However, since it comes from an exponential fit, it actually represents the activity at the beginning of the dataset considered.

From the exponential fit, we also deduce the decay constant of ^{85}Kr. The fit gives us 5156±1492 days, which is compatible with the expected value of 5655 days [147].

5.5.3 Background shapes at low energy

Most of the simulated radioactivity, originated in various materials, is due to the same decays or decay chains, so that the TPC energy spectrum shows some similarities. In order to limit the number of parameters to adjust in the analysis, we decided to regroup the background contributions in three components: internal (39Ar + ^{85}Kr), PMT and cryostat.

We checked that the different components had compatible shapes over the analysis range, ensuring that grouping them would not bias the profile likelihood. Figure 5.24 shows the superposition of the different background contributions. As visible on the Figure, the shapes of ^{39}Ar and ^{85}Kr are similar. All the other components also have similar shapes, allowing us to group them.

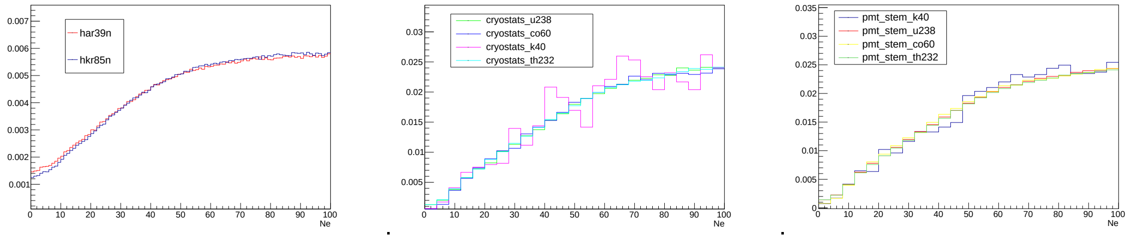

(a) Internal (b) Cryostat (c) PMTs

Figure 5.24 – Shapes of the different background component. Each panel represents one of the three final background components used for the analysis.

5.6 Profile likelihood analysis

The limit on the WIMP-nucleon cross-section in the low mass range was obtained using a Profile Likelihood method. It has the advantage of treating and tracking systematics in the calculation of exclusion limits. Dedicated ROOT [122] packages,*RooStats* and *HistFactory*, were used in order to develop the analysis. In these frameworks, systematics are introduced in two categories: spectrum shape uncertainties and normalization uncertainties. Each uncertainty is assigned with a nuisance parameter, which is constrained by Gaussian likelihood. Input values to the method are the mean and 1σ value of the Gaussian constraint for each nuisance parameter. HistFactory interpolates and extrapolates between them while minimizing the likelihood. The systematics accounted for in our calculation of the limit are listed in Table 5.2.

The S2 yield g_2 plays a role only in the scaling to the Ne$^-$ scale of experimental data. The Qy and S2 RMS are factors affecting the signal spectrum shape. The spectra are calculated based on $Q_y(E_{nr})$ with binomial fluctuations and then smeared in the final S2 response with a Gaussian function with the S2 RMS as its standard deviation. Instead of a full MC calculation, the WIMP spectra are convoluted with those binomial and Gaussian distribution before putting in *HistFactory*.

Systematics	Category	Mean	$\pm 1\sigma$
g_2	Shape	23 PE	$\pm 1PE$
Q_y	Shape	AmBe/AmC fit	$\pm 1\sigma$ from fit
Internal γ-rays	Normalization	Spectral fit	±15% of mean
PMT γ-rays	Normalization	Spectral fit	±15% of mean
Cryostat γ-rays	Normalization	Spectral fit	±15% of mean

Table 5.2 – List of the systematics included in the low mass analysis.

The normalization uncertainties on the different background components have been conservatively set at 15%.

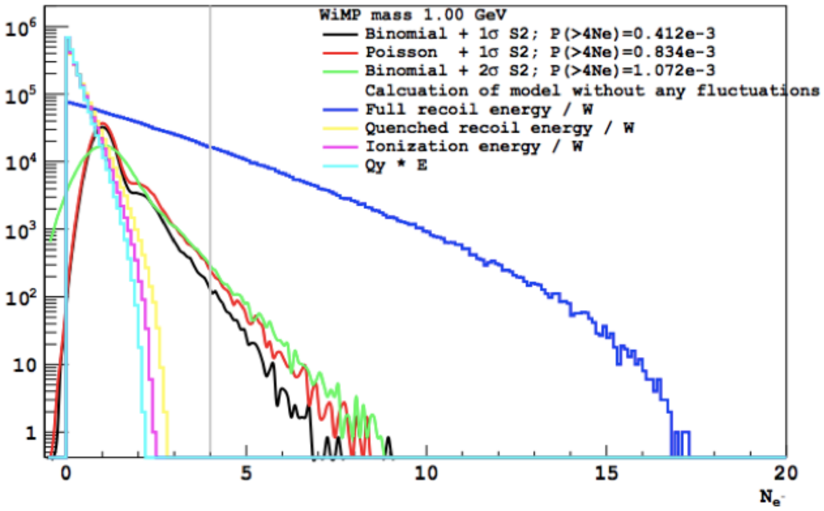

Figure 5.25 – WIMP spectra when including fluctuations in the low energy processes.

At low energies, there can be fluctuations in the quenching, recombination or ionisation processes, that could spread the wimp signal to higher energies, giving us access to lower masses. However, due to the lack of knowledge of these processes, we do not have a model for them. We considered two scenarios: the most conservative one involves no fluctuations and the other involves binomial fluctuations. WIMP spectra were produced for both cases and the analysis was run under both hypotheses.

As illustrated in Figure 5.26, several regions are treated differently. Below 4 Ne, the background is dominated by trapped electrons due to impurities, and this region is not used. Above 7 Ne, backgrounds are dominated by ^{85}Kr and ^{39}Ar, and this region is well reproduced using the MC component measured by the high energy spectral fit. Between 4 and 7 Ne^{-}, there is an excess of the data with respect to the MC. This is likely due to the tail of the trapped electrons that is not modeled.

Figure 5.27 shows the 90% C.L. limits achieved by DarkSide-50 in the low mass range (red curves). No result is claimed below $M_{WIMP} = 1.8 GeV/c^2$, which is the mass attainable when quenching fluctuations are not included. We improve the existing limits by one order of magnitude below $M_{WIMP} = 6$ GeV/c^2. The curve including binomial fluctuations is also shown, highlighting

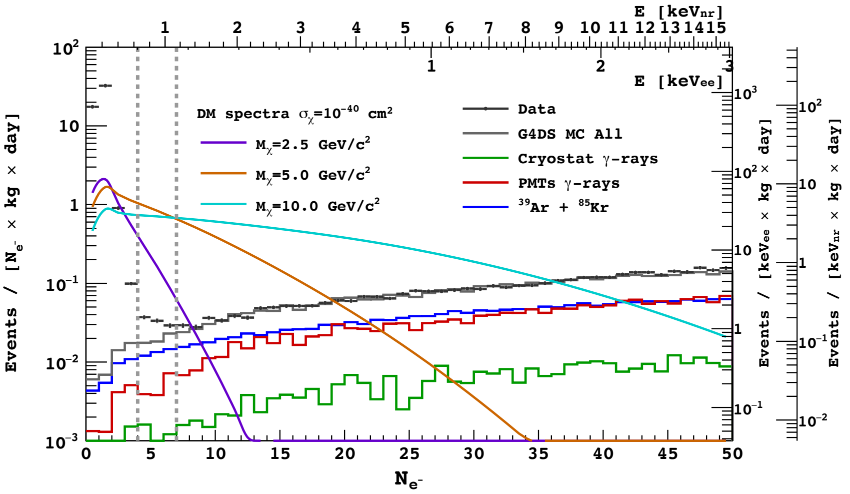

Figure 5.26 – The DarkSide-50 Ne spectra at low recoil energy from the analysis of the last 500 days of exposure compared with a G4DS simulation of the background components from known radioactive contaminants. Also dark matter particles of masses 2.5, 5, and 10 GeV/c^2 shown are the spectra expected for recoils induced by with a cross section per nucleon of 1040 cm^2 convolved with the binomial fluctuation model and detector resolution. The y-axis scales at right hand side are approximate event rates normalised at Ne = 10.

the gain in sensitivity that these processes could represent, in case we can model them. However, supplementary measurements of the properties of LAr are necessary. Above 1.8 GeV/c^2, the limit is almost insensitive to the choice of fluctuation models.

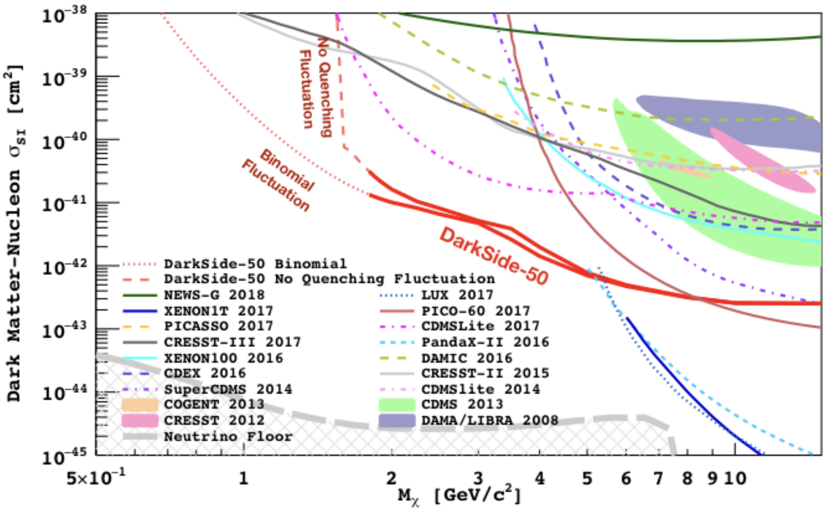

Figure 5.27 – 90% upper limits on spin independent DM-nucleon cross sections from DarkSide-50 in the range above 1.8 GeV/c^2.

5.7 Conclusions

DarkSide-50 was able to provide the most stringent limits on WIMP-nucleon cross-section for WIMPs mass in the range $1.8 < M_{WIMP} < 6$ GeV/c^2. This result was achievable both thanks to the intrinsic properties of argon and to the great effort that has been developed by DarkSide to characterise the argon response as well as the backgrounds.

An improved knowledge of the ionisation distribution of nuclear recoils is needed to reduce the uncertainties in the expected signal yield above the analysis threshold and thus improve the sensitivity at the lowest masses.

We plan to study low energy nuclear recoils performing direct measurements of scintillation and ionisation yield using a neutron beam, and to perform dedicated studies in the energy range of interest for low mass DM detection (<1 keV$_{nr}$), with the specific goal of a first direct measurement of the ionisation yield in liquid argon and, possibly, of establishing a realistic and detailed model for fluctuations of ionisation of nuclear recoils.

Chapter 6

Axions searches in DarkSide-50

Contents

Given the stronger and stronger limits on WIMP interactions, the natural question is: ”What if dark matter is made of something else ?” And a natural candidate to turn to is the axion. Axions are one the most extensively studied dark matter candidates. Most of the searches focus on its coupling to photons, but recently, searches exploiting the coupling to electrons have been performed. Axion coupling to electrons allows us to detect them in noble liquid TPCs, where they will appear as electronic recoils.

In this chapter, I will first present the motivation for the existence of axions, their production mechanisms, and their emission fluxes. I will then discuss improvements made to the background model of DS-50, in order to achieve a better agreement between data and MC. And finally, I will detail a preliminary axion search with DS-50 data.

6.1 Axions, a solution to the strong CP problem

The lagrangian of Quantum Chromdynamics (QCD) can be written,

$$\mathcal{L}_{QCD} = -\frac{1}{4}G^{a}_{\mu\nu}G^{a\mu\nu} + \sum_{j=1}^{n}[\bar{q}_j\gamma^{\mu}iD_{\mu}q_j - (m_j q^{\dagger}_{Lj}q_{Rj} + h.c)] + \frac{\theta g^2}{32\pi^2}G^{a}_{\mu\nu}\tilde{G}^{a\mu\nu} \tag{6.1}$$

with an implicit summation over suppressed color indices and an explicit one over n quark flavours, and where

$$\tilde{G}^{\mu\nu} \equiv \frac{1}{2}\epsilon^{\mu\nu\rho\sigma}G_{\rho\sigma}$$

The last term of the equation, known as the *theta term* is a total derivative and therefore does not contribute to the perturbative aspects of QCD. The Adler-Bell-Jackiw [158, 159] anomaly ensures that the theta term must be present if none of the quark masses vanish and that QCD depends on θ through the combination of parameters

$$\bar{\theta} = \theta + arg(det(\mathcal{M})) \tag{6.2}$$

where $\mathcal{M}$ is the quark mass matrix. If $\bar{\theta} = 0$, QCD violates P and CP. The lack of observation of CP violation in QCD therefore puts a limit on $\bar{\theta}$. The CP violation has important consequences for cosmology. Present theories of particle physics and cosmology predict that our universe was formed with equal parts matter and antimatter, which should by now have annihilated into radiation. To explain the dominance of matter, CP violation must exist.

The most stringent probe of the strong CP problem is the electric dipole moment of the neutron. A non-zero electric dipole moment (EDM) of the neutron (or any fundamental particle) would be a violation of parity (P) and time-reversal (T) symmetry. This can be explained by the following picture: if the neutron has a finite EDM, the charge distribution is reversed under P; it is unchanged under T, but the orientation of a particle is specified by its spin, which is unchanged under P but reverses under T. Therefore if the EDM is not zero then P and T are not conserved. Since, according to the CPT theorem, T violation implies CP is also violated, a non-zero EDM also implies a CP violation. One can show that the neutron EDM, d_n can be written,

$$d_n \simeq 5 \times 10^{-16}\,\bar{\theta}\,e\,\mathrm{cm} \tag{6.3}$$

Experiments on the neutron electric dipole moment [160] yielded $\bar{\theta} < 10^{-9}$. There is theoretically no reason for $\bar{\theta}$ to be so small.

Peccei and Quinn [3] proposed a solution to explain the smallness of $\bar{\theta}$. The Peccei-Quinn (PQ) theory postulates the existence of a global $U_{PQ}(1)$ quasi-symmetry, which is a symmetry of the theory at the Lagrangian (i.e. classical) level. This symmetry must be broken explicitly by the non-perturbative effects that produce the theta term and spontaneously broken at a scale f_a. Being a spontaneously broken global symmetry, there must be a pseudo-Nambu-Goldstone boson, the axion a, associated with $U_{PQ}(1)$. One can show [161] that the ground state of the axion potential drives $\bar{\theta} \to 0$ and thus solves the strong CP problem.

More generally, one can consider Standard Model extensions with new global $\mathcal{U}(1)$ symmetries spontaneously broken by some (hidden) Higgs-type mechanism at a symmetry-breaking scale v_h much higher than the electroweak scale. It is then possible to extend the PQ theory to other scales, yielding particles similar to QCD axions. Theses particles can be generically called "axion-like particles" (ALPs). String theory, for example, predicts ALPs. The axion couples to hadrons, photons, and leptons with interaction strengths inversely proportional to f_a. Thus as the experiments failed to detect axions, the smallest values of f_a have been experimentally excluded.

6.2 Axion production mechanisms and fluxes

6.2.1 Solar axions

The most important parameters that determine the solar axion flux are the axion-two-photon coupling and the axion-electron coupling. The first drives the Primakoff production of axions in photon collisions with charged particles of the solar plasma,$\gamma + q \to a + q$. The Primakoff flux is dominant in hadronic axion models such as the KSVZ [162, 163] where the axion-electron coupling is absent at tree level. The axion-electron coupling, present in models such as DSFZ [164, 165], or in the original PQ theory, drives several reactions of comparable importance that completely overshadow the Primakoff flux in non-hadronic axion models. The most important are the ABC reactions:

- Atomic axio-recombination, also known as electron capture or free-bound electron transitions

$$e + I \to I^- + a$$

- Atomic axio-deexcitation

$$I^* \to I + a$$

- Elecrtron-ion Bremsstrahlung

$$e + I \to e + I + a$$

- Electron-electron Bremsstrahlung

$$e + e \to e + e + a$$

- Compton scattering

$$e + \gamma \to e + a$$

Axio-recombination and atomic de-excitation are significant only for ions of metals which are much less abundant than hydrogen, helium or electrons.

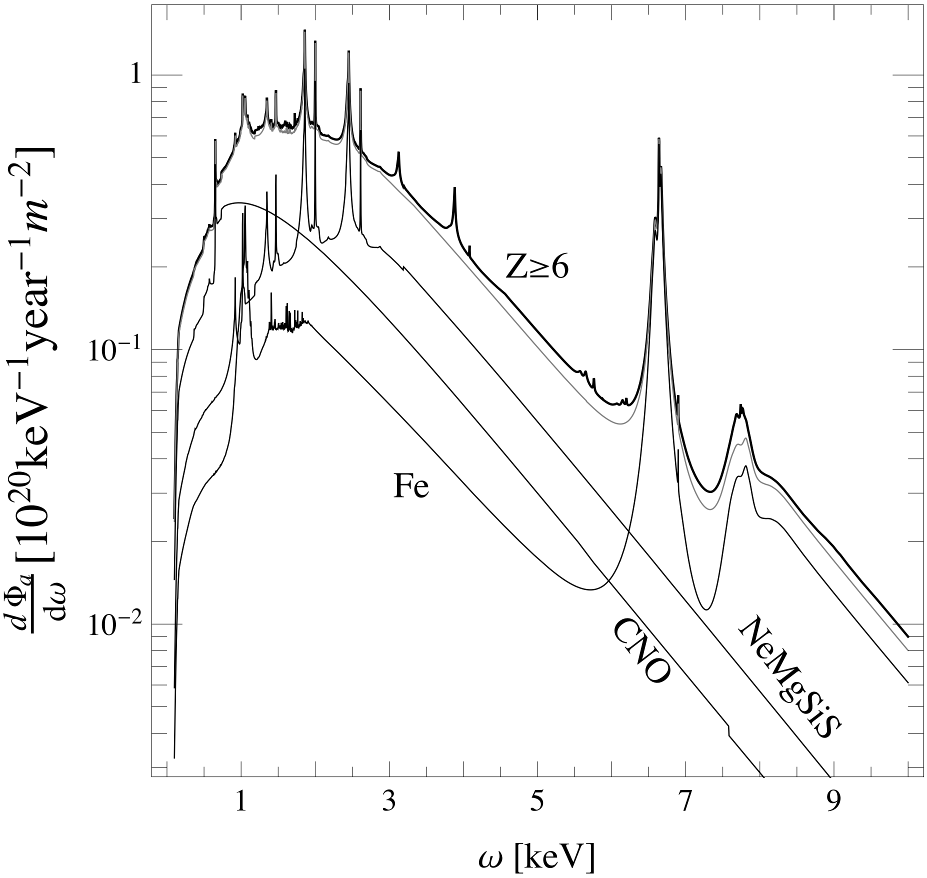

Figure 6.1 – Solar axion flux computed in [166] from the different ABC reactions, assuming $g_{Ae} = 10^{-13}$.

The solar axion flux has been computed by Redondo in [166], in the approximation of massless axions. This approximation is valid for axion masses up to 1 keV/c^2 without necessitating any correction to the flux. The flux can be expressed as

$$\frac{d\Phi_a}{d\omega} = \frac{1}{4\pi R^2_{Earth}} \int_{Sun} \frac{4\pi\omega^2}{(2\pi)^3} \Gamma^P_a(\omega) dV \tag{6.4}$$

where Γ^P_a is the axion emission rate from the different processes considered and ω the axion energy. T is the temperature, ρ is the density and X_Z is the mass-fraction density of the chemical element Z. Through those last three parameters, the resulting flux depends on the solar plasma model used. The resulting spectrum is shown on Figure 6.1.

6.2.2 Galactic axions

Galactic axions can be produced in the early universe via three mechanisms:

- thermal production of "hot" axions
- non-thermal production of "cold axions" via

- the misalignment mechanism
- cosmic axions strings decay

The temperature of thermal axions is of the order of the one of photons or neutrinos. Since thermal axions then move too fast to constitute the dark matter haloes in galaxies and clusters of galaxies, only cold axions will be discussed in this section.

There is controversy about the dominant production mechanism. Some sources say that the dominant production mechanism depends on the time when the symmetry giving rise to axions is broken [167, 168]. If it is broken before the end of inflation, the main contribution to the axion population will come from the misalignment mechanism. If the symmetry is broken after inflation, then most axions will be produced via axion strings decay.

Some other sources find comparable populations for the two mechanisms [169].

Misalignment mechanism $\bar{\theta}$ oscillates as it relaxes to 0. One can show that it leads to the axion mass m_a to depend on the temperature, T. Near the minimum, the potential will be quadratic in $\bar{\theta}$ and its curvature will be m_a^2 so that,

$$V(\bar{\theta}) \simeq m_a^2(T)\left(\frac{f_a}{N}\right)^2 \bar{\theta}$$

giving a Lagrangian

$$\mathcal{L} \simeq \left(\frac{f_a}{N}\right)^2 \left(\frac{\dot{\bar{\theta}}}{2} - m_a^2(T)\frac{\bar{\theta}}{2}\right)$$

The Lagrange equations of motion give

$$\ddot{\bar{\theta}} + 3H\dot{\bar{\theta}} + m_a^2(T)\bar{\theta} = 0 \tag{6.5}$$

At $T \gg \lambda_{QCD}$, $\bar{\theta} = constant = \bar{\theta}_1$. $\bar{\theta}_1$ is called the *misalignment angle*. For $m_a(T) \geq 3H$, the equation becomes the one of an harmonic oscillator, with frequency $\sim m_a(T)$. If we substitute $\dot{\bar{\theta}}$ for its average value over an oscillation, ρ_a,

Eq. 6.5 becomes

$$\dot{\rho_a} = \left(\frac{\dot{m_a}}{m_a} - 3H\right)\rho_a \tag{6.6}$$

In the adiabatic approximation, $\dot{m_a}/m_a \ll m_a$ and $H << m_a$, so the solution of Eq 6.6 is simply

$$\rho_a = Cst \times \frac{m_a(T)}{a^3} \tag{6.7}$$

This gives us a straightforward way to compute the present axion density.

Cosmic strings decay Let us now be interested in the second production mechanism of cold galactic axions. The distribution of θ_1 values in the universe is not necessarily uniform. Thus,

”axion strings” can appear in the Universe, with domain walls connecting them. The energy stored in a string per unit length depends on the axion properties via

$$\mu \sim f_a^2 log(f_a d) \tag{6.8}$$

where d is the typical distance between strings.

Over one Hubble time, the energy present in the strings can dissipate in only one way: the radiation of axions. As stated in [170], the change in the axion entropy density would be

$$\frac{n_a}{s} \sim \int_T {}_1^f {}_a \frac{1}{\omega M_{Pl}^2} dT \tag{6.9}$$

where ω is the average energy per radiated axion, and T_1 is the temperature such as $m_a(T_1) = 3H(T_1)$.

6.2.2.1 Axions and ALPs as cold dark matter

From the density formula computed previously (Eqs. 6.7, 6.9), we can deduce an order of magnitude for the axion mass required for them to be cold dark matter. Different groups have performed such computations, assuming different models(pre- and post-inflationary symmetry breaking) [171, 168, 172]. The mass range for axion dark matter goes from (∼ µeV to ∼ 200 µeV).

Such low axion masses are not accessible with a WIMP detector like DarkSide. However, as shown in in [173], axion-like particles can have masses in the keV range and be cold dark matter. These are the particles we can look for in the following analysis.

6.2.2.2 Galactic axion flux

If we assume that axions constitute the whole of the galactic dark matter density, then the total flux of dark matter axions $\Phi_{gal} = \rho_{DM} v_A / m_A$ is given by

$$\Phi_{gal}[/cm^2/s] = \left(\frac{9 \times 10^{15}}{m_A} \right) \beta_m \tag{6.10}$$

where $\beta_m = \sqrt{\frac{2E}{m_A}}$ is the mean velocity of the axion distribution relative to the Earth, and assuming a local dark matter density of $\rho_{DM} \sim 0.3$ GeV$\cdot c^{-2}$

6.3 Detection methods and constraints on axion properties

Constraints on axion properties come from both astrophysical observations and laboratory experiments. For a detailed review, see [40]. I will here present a non-exhaustive list of axion and ALPs constraints from various sources.

6.3.1 Astrophysical constraints

6.3.1.1 Globular clusters

If axions are present in stars, they would propagate more efficiently than photons, due to their very weak couplings to other particles. As a result, they would modify the stellar evolution. Globular clusters allow for a detailed study of the stellar evolution theory. Counting the number of stars on the horizontal branch (HB), compared to the number of red giants can provide constraints on the axion coupling to photons. Indeed, the radiation of axions from HB stars would reduce their number compared to red giants (that are not subjected to Primakoff effects). The upper bound with this method is $g_{a\gamma} < 0.66 \times 10^{-10}$ GeV^{-1}(95% C.L) [174]. Our good understanding of stellar evolution makes this limit one of the most robust.

6.3.1.2 Supernovae

Even if the physics of supernovae explosions is less well understood than stellar evolution, calculations of the duration of the neutrino signal are reliable. Axion emission would significantly reduce the duration of this pulse. The neutrino pulse of the Type II SN 1987A supernova has been studied, giving limits on the coupling of axions and axion-like particles to photons, neutrons and protons [175, 176, 177].

6.3.1.3 Cosmology

Axions may have been produced in the early Universe both thermally [178] or as cold particles [179, 172]. Using the precision measurements of the cosmological parameters, it is then possible to set a limit on the axion mass. In addition, for $m_A \gtrsim 20$ eV, axions decay rapidly (on a cosmic time scale), injecting photons. This excess radiation provides additional limits up to very large axion masses [180].

6.3.2 Laboratory constraints

Dedicated laboratory experiments have also been designed to explore the axion couplings. Currently, the most promising approaches rely on the axion-two-photon vertex, allowing for axion-photon conversion in external electric or magnetic fields.

6.3.2.1 Solar axions searches

Solar axions can be detected using ”axion helioscopes” as described in [181] to convert axions into photons. The most recent solar axion search is the CAST (CERN Axion Solar Telescope) experiment at CERN [182]. CAST uses a decommissioned LHC superconducting magnet (up to 9 T over a length of 9.3 m) to act as a catalyst to convert axions into X-rays. CAST sensitivity to the axion-photon coupling reaching the parameter space for KSVZ and DFSZ axions (see Figure 6.2).

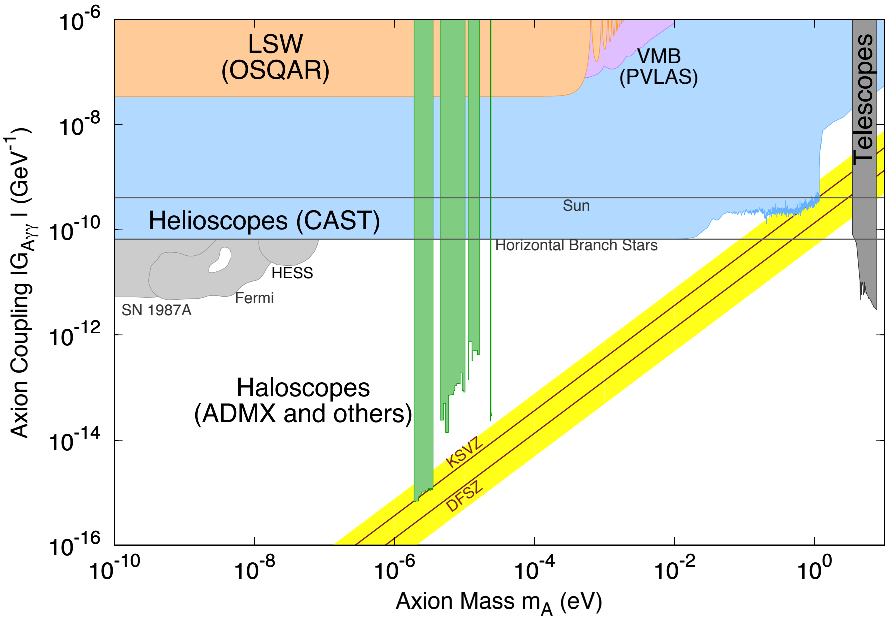

Figure 6.2 – Exclusion limits on the axion-photon coupling from various experiments. Figure extracted from [40].

6.3.2.2 Galactic axions searches

Microwave cavities Axion haloscopes were invented in 1983 by P. Sikivie [181]. The principle is to resonantly stimulate the conversion of axion to microwave photons a background magnetic field. When the cavity's resonant frequency is tuned to the axion mass, axions nearing the cavity can be converted into photons. This results in the deposit of a very tiny amount of power (of the order of $\sim 10^{-22}$ W) into the cavity. With large enough cavities, large enough magnetic fields ($B \sim 8$ T) and good noise reduction, detectors are able to reach good sensitivity. The ADMX [183], HAYSTAC [184] and ORGAN [185] rely on this detection mechanism.

Photon polarization Another way to probe axions is to measure the polarization of light propagating through a transverse magnetic field. This approach was used by the Rochester-BNL-FNAL (RBF) collaboration [186], then by the PVLAS collaboration [187] with a much higher sensitivity. PVLAS reported a signature for an axion in the mass range $m_a = 1 - 1.5$ meV, but it was later attributed to instrumental artifacts.

Photon regeneration: "light shining through a wall" Photon regeneration requires an axion to pass through an opaque barrier and be regenerated by the inverse process on the other side. Photons propagating through a transverse magnetic field may convert into axions. Then if we expose a photon beam to a magnetic field, and place another magnet inline with the first, but shielded by an optical barrier, photons may be regenerated from the pure axion beam. The OSQAR experiment is a representative example of this approach [188, 189]. An 18 W laser is polarized before traversing two 9 T superconducting magnets separated by an optical barrier. Improvements to this technique have been proposed in [190].

6.4 Improvements to the low energy background model of DS-50

Before detailing the analysis procedure for axion searches in DarkSide-50, I will discuss the modification made to the background model at low energy. Indeed, some improvements were needed in order to apply the profile likelihood to higher energies.

6.4.1 Modification of the energy scale

The spectrum for solar axions extends to $\sim$ 11 keV, or $\sim$ 100 Ne, while the galactic axions spectrum depends on the axion mass and can extend to even higher values. Therefore, in order to perform an axion search, we need to extend the fit range with respect to the low mass analysis. We decided to consider the spectra until Ne = 200, corresponding to an energy of $\sim$25 keV. When extending the range, we noticed a big mismatch between data and Monte-Carlo after Ne = 50, as shown in Figure 6.3. It is visibly a discrepancy in the shape of the distributions, so it is likely to be due to an error in the ER energy scale.

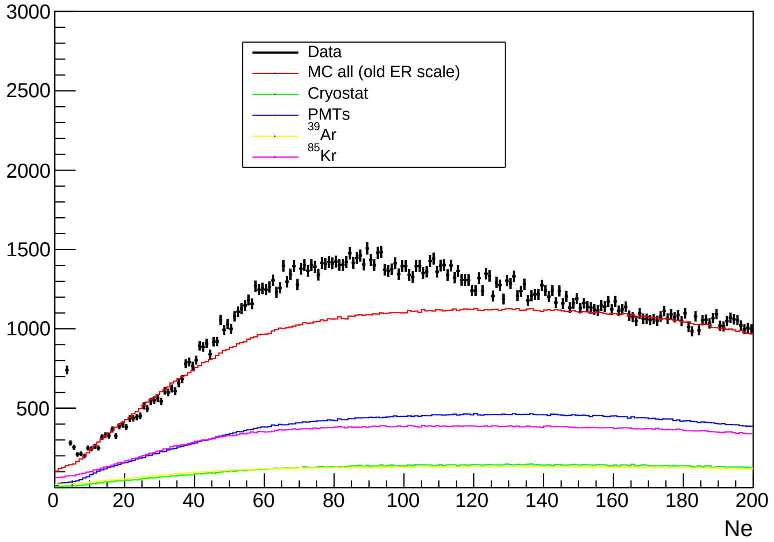

Figure 6.3 – Comparison between the data and DS-50 MC background model after the extension to 200 Ne.

Recalling Section 5.3, the ER energy scale was calculated using ^{37}Ar and ^{83}Kr as anchor points. These points allow us to establish an energy scale, but ^{37}Ar lines are relatively far from ^{83}Kr peaks. So we can miss some features in the shape of the scale.

To have a more precise energy scale, we decided to rely on more points. We select events in the

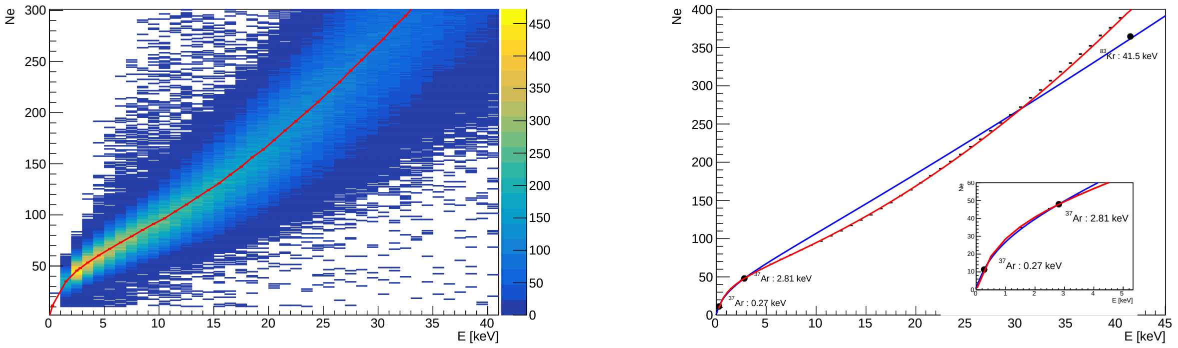

(a) Ne vs. E distribution. Each point of the red graph is the mean of the distribution in the energy bin.

(b) New energy scale (black dots) and fit function (red) compared to the old energy scale (blue line). The black dots represent the anchor points of the old energy scale.

Figure 6.4

data with two pulses and the correct f_{90} for S1 and convert S2 into Ne with

$$Ne = \frac{S2}{g_2}$$

. We then plot the 2D distribution in the Ne vs. E plane, with

$$E = W\left(\frac{S1}{g_1} + \frac{S2}{g_2}\right)$$

where $w = 19.5$ eV, $g_1 = 0.6$ and $g_2 = 24.5$ Th distribution is then divided in energy bins along the x axis and we extract the mean and RMS of each bin, as can be seen on Figure 6.4a. We can then construct a graph with y = Ne(E). This graph is fitted with the function

$$Ne = a \times (1 + E^{1.5} \times b) \times ln(cE + 1); \tag{6.11}$$

where a, b, c are the fit parameters. We find $a = 20.04 \pm 0.01$, $b = 3.12 \pm 0.05$, and $c = 1.17 \times 10^{-2} \pm 3.93 \times 10^{-5}$. This allows us to have an analytical function to convert energy into a number of electrons.

As can be seen in Figure 6.4b, the new energy scale is rather different from the old one, which was missing some features. The new scale also misses the ^{83m}Kr point. This peak is actually the sum of two different γ (see Section 5.3) and since the recombination probability, and then the electron yield depends on the photon energy, this peak cannot be considered as a valid calibration point.

However, as can be seen on the zoom-in Figure 6.4b shows that over the range of the DS-50 low mass WIMPs analysis [7,50] Ne, there is an excellent agreement between the two results. Thus the results of the low mass analysis are confirmed.

As shown in Figure 6.5, the modification of the energy allows to recover the shape of the data after 50 Ne. The data-MC shows now an excellent agreement, which was required to perform the

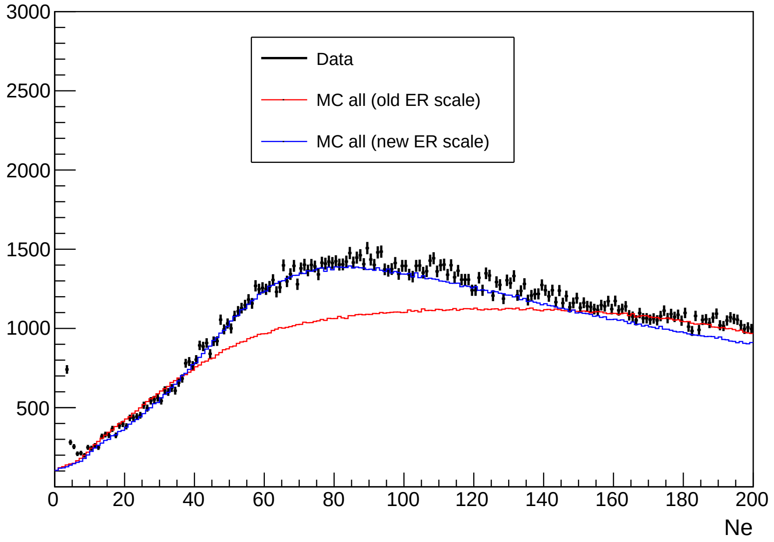

Figure 6.5 – Data/Monte-Carlo comparison of the background for the old (red histogram) and updated (blue histogram) ER energy scales.

axion searches.

6.4.2 Atomic effect in the ^{39}Ar and ^{85}Kr β-spectra shapes

Despite the excellent agreement achieved with the new energy scale, there is still the problem of the discrepancy at very low energies (see Figure 6.7a), where $\text{Ne} < 10$. New ideas have been proposed to solve, or at least attenuate this problem by modifying the shape of the ^{39}Ar and ^{85}Kr β spectra. This modification is motivated by the physics of β decays.

^{85}Kr and ^{39}Ar are both first forbidden unique β-decays. This makes them less probable than allowed decays and they have a higher half-life (265 and 11 years respectively). The "forbidenness" of the decays also affects the shape of the spectra, via a shape factor (see [191] for details).

Some atomic effects are neglected in the usual calculations of the β spectra shapes. In order to improve our background model, we decided to study the influence of these effects, and see if it could help us achieve a better agreement between data and Monte-Carlo.

6.4.2.1 Screening effects

In his original paper on beta decay, Fermi neglected the influence of the atomic electrons [192]. The general argument for this simplification is that the atomic electrons have only a small influence on the electric field of the nucleus, where the β particle is created. One expects the atomic electrons to be of importance only when the energy of the emitted beta particle is so small that the wavelength is comparable to the size of the atom. The atomic electrons make the effective electric field smaller than the field of the bare nucleus so that, when they are taken into account, a decreased electron emission and an increased positron emission are predicted by the theory.

R.H. Good [193] has calculated this screening effect for the forbidden beta spectra, of interest in our case.

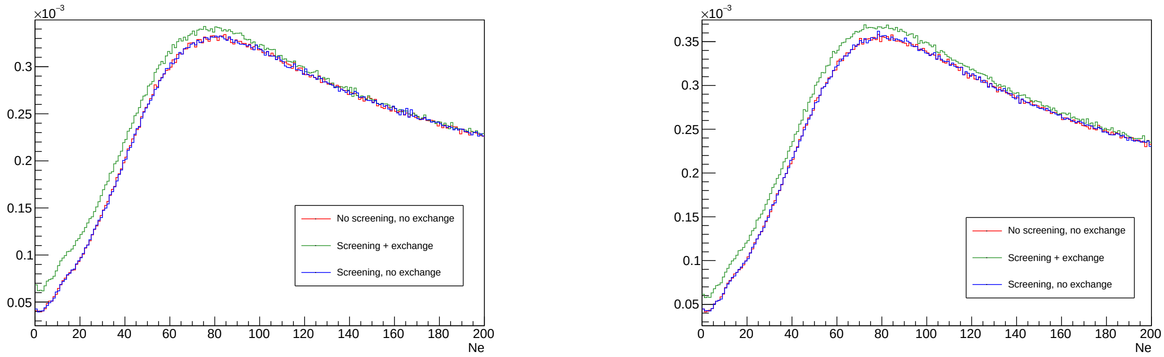

(a) Influence of screening and exchange effects on the ^{39}Ar β spectrum

(b) Influence of screening and exchange effects on the ^{85}Kr β spectrum

Figure 6.6 – Comparison of the background model with and without the addition of atomic screening and exchange effect into the ^{85}Kr and ^{39}Ar spectra.

6.4.2.2 Exchange effect

The non-orthogonality of initial and final state atomic wave functions in β decay allows for additional indirect processes through which electrons can be emitted into a continuum state. In the case of the exchange effect, this non-orthogonality leaves a possibility for a β particle to be emitted directly into a bound state of the daughter atom, thereby expelling an initially bound electron into the continuum. Experimentally it is impossible to distinguish this indirect process from regular β decay so that an additional correction to the experimentally measured spectrum is required. A calculation of the exchange effect is provided by [194].

6.4.2.3 Effect on the background model

As visible in Figure 6.6, the exchange effect, in particular, modifies the low energy shape of the spectra. This could help reduce the discrepancy between data and MC at low energies. X. Mougeot developed the *BetaShape* [195] code for analytical calculation of beta spectra. We used *BetaShape* to include these new effects in the ^{39}Ar and ^{85}Kr shapes of the DS-50 background spectra.

Figures 6.7 show the influence of the inclusion of the atomic effects mentioned before in the background model. The agreement between data and simulation is visibly better when the new atomic effects are taken into account.

6.4.2.4 Final background model

Figure 6.8 shows the data compared to the background model over the complete analysis range for axions.

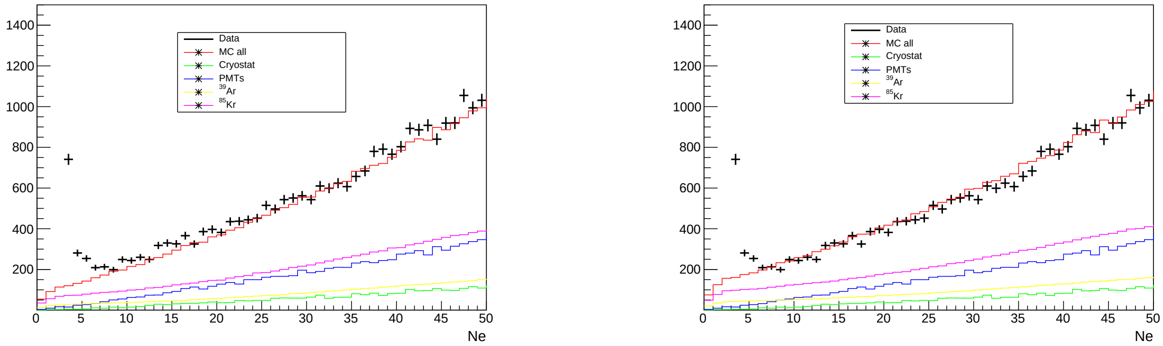

(a) Fit of the MC background over DS-50 data with the AR/Kr shapes used for the low mass analysis

(b) Fit of the MC background over DS-50 data with the Ar/Kr shapes including the new effects described in this section.

Figure 6.7 – Comparison of the background model with and without the addition of atomic screening and exchange effect into the ^{85}Kr and ^{39}Ar spectra.

Component	Fitted normalisation	Fitted activity [mBq]	Nominal activity [mBq]
^{39}Ar	1.14	0.78 ± 0.114 [/kg]	0.682 ± 0.010 [/kg]
^{85}Kr	0.97	1.845 ± 0.009 [/kg]	1.902 ± 0.009 [/kg]
PMTs	1.02	99.22 ± 2.11 [/PMT]	97.28 ± 2.07 [/PMT]
Cryostat	1.25	8.793 ± 0.231 [/kg]	7.035 ± 0.185 [/kg]

Table 6.1 – Results of the fit of the background components.

The improvements to the background model allow us to achieve an excellent agreement between the data and MC.

6.4.3 Fit of the background components

As visible on Figure 6.8, there is an excess of the data over the Monte-Carlo (blue histogram) after Ne = 80. We performed a fit with the normalisations of the background components as free parameters. This allows us to see how the activities should be modified in order to achieve a better agreement of the background model.

The fitted normalisations are summarized in Table 6.1. The fit tends to enlarge the activities of the background sources, thus reducing the space for axions at low energies. To account for this effect, we set large uncertainties over the background normalisations.

The fit impose modifications of the activities ranging from ∼3% to ∼25%. It is interesting to note that the fit makes the value of the ^{85}Kr activity very close to the value found in the study of 5.5.2, which was 1.85 ± 0.02. However, since we cannot use the results of a fit over the axion search region, we use the nominal activities from the spectral fit for the analysis.

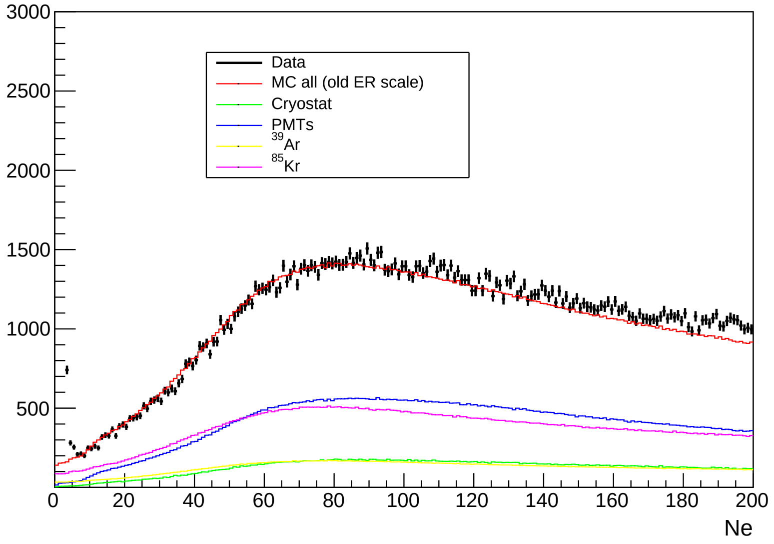

Figure 6.8 – Comparison of background model to data after the inclusion of atomic effects and modification of the energy scale.

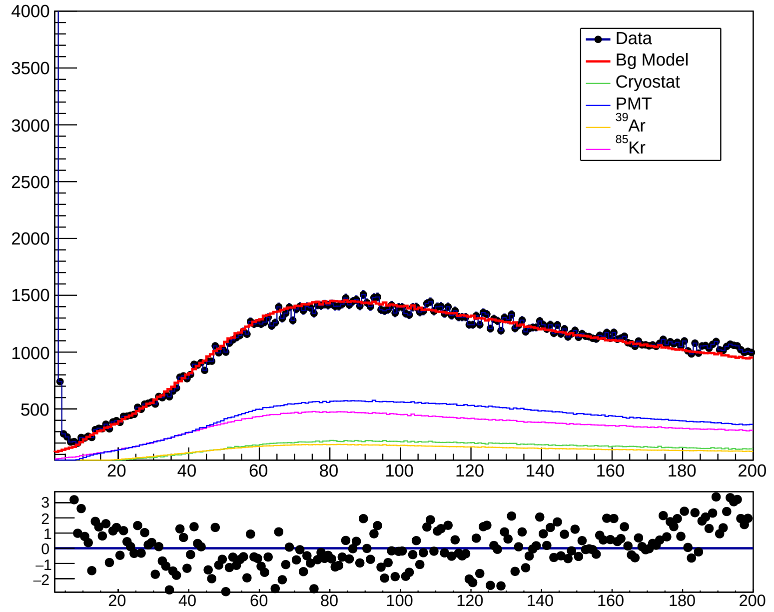

Figure 6.9 – Fit of the background components. The bottom panel shows the ratio of the devitaion of the data from the model over the statistical error.

6.5 Axion searches in DS-50

6.5.1 Axions searches in noble liquid detectors

Direct searches for axions in noble liquid detectors rely on the axio-electric effect, which is similar to the photo-electric effect, replacing the photon by an axion. Due to this effect, an axion or ALP interaction in the detector would lead to a visible electron recoil. The recoil energy is up to 15 keV for solar axions, while galactic axions distributions will peak around the axion mass, since the dark matter, halo is considered at rest with respect to the Earth.

The axio-electric cross section is given, for both axions and ALPs, by:

$$\sigma_{Ae} = \sigma_{pe}(E_A)\frac{g_{Ae}^2}{\beta_A}\frac{3E_A^2}{16\pi\alpha_{em}m_e^2}(1-\frac{\beta_A^{2/3}}{3}) \tag{6.12}$$

where σ_{pe} is the photoelectric cross section for LAr, E_A is the axion energy, α_{em} is the fine structure constant, m_e is the electron mass, β_A is the axion velocity over the speed of light and and $g_{Ae} = 2m_e/f_a$ is the dimensionless axion-electron coupling constant with the strength of the standard model-axion interaction f_a.

Figure 6.10 shows the photoelectric cross-section in argon.

The LUX [196] and XENON [197] experiments both have performed axions and ALPs searches in LXe. LUX currently has the best limits on g_{Ae} for both solar and galactic axions at respectively $g_{Ae} = 3.5 \times 10^{-12}$ and $g_{Ae} = 4.2 \times 10^{-13}$.

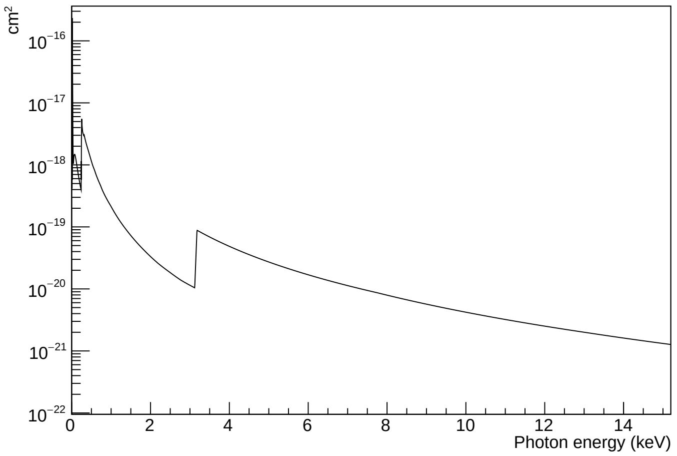

Figure 6.10 – Photo-electric cross-section for argon [198].

6.5.2 Production of the axion spectra

We generate the axion spectra visible in the detector by multiplying the fluxes from 6.2, with the axio-electric cross-section.

The interaction rate can then be written,

$$R[/kg/day] = \Phi \times 24 * 3600 \times \frac{6 \times 10^{23}}{A} \sigma_A(E) \tag{6.13}$$

with Φ, the emission flux, and A, the atomic number of argon. For solar axions both the flux and cross-section depend on g_{Ae}^2, so the event rate will scale with g_{Ae}^4.

We then include the influence of the detector response. We assume binomial fluctuations in the number of electrons produced by the interaction. We also include the smearing due to the response of the PMTs.

The spectra are produced assuming $g_{Ae} = 10^{-11}$, while the galactic ones are produced assuming $g_{Ae} = 10^{-12}$.

Figure 6.11 shows the resulting spectra for massless solar axions and galactic axions with masses ranging from 1 keV/c^2 to 13 keV/c^2.

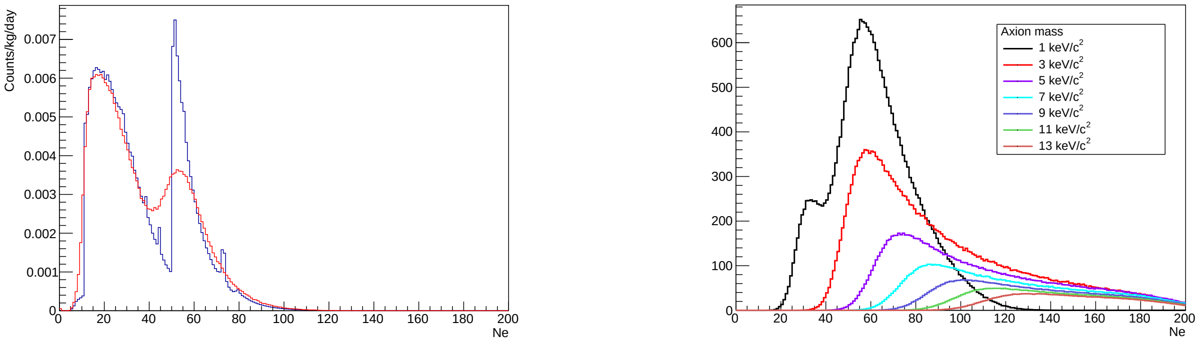

(a) Solar axion spectrum without fluctuations (black), and adding ER fluctuations and detector response (red). The spectrum is generated assuming $g_{Ae} = 10^{-11}$

(b) Galactic axion spectra. The spectra is generated assuming $g_{Ae} = 10^{-12}$

Figure 6.11 – Spectra for solar axions and galacti ALPs in the DarkSide-50 detector.

6.5.3 Massless solar axions limit

The data are then fitted using the same Profile Likelihood framework as the low mass analysis. The Low Mass analysis used a 15% uncertainty on the background normalisation. In order to account for the fit performed over the analysis range of axions, we enlarge these uncertainties to 30%. We also add a shape uncertainty on the background shape to account for the g_2 uncertainty.

6.5.3.1 Influence of the fit range

The sensitivity of the analysis relies on the agreement between the MC and the data. Because of that, any excess of data with respect to MC (and vice-versa) will influence the observed limit. To study this effect, we extracted the limit considering different ranges. The results are summarized in Table 6.2.

Range	Observed	Expected	1 σ band	2 σ band
[7, 50]	4.75e-12	5.49e-12	[6.59e-12, 4.20e-12]	[7.77e-12, 3.59e-12]
[7, 100]	3.12e-12	4.92e-12	[5.91e-12, 3.77e-12]	[6.96e-12, 3.22e-12]
[7, 150]	2.96e-12	4.89e-12	[5.84e-12, 3.73e-12]	[6.87e-12, 3.18e-12]
[7, 200]	2.51e-12	4.83e-12	[5.78e-12, 3.70e-12]	[6.77e-12, 3.16e-12]

Table 6.2 – 90% C.L. limits on solar axion coupling g_{Ae} for different fit ranges.

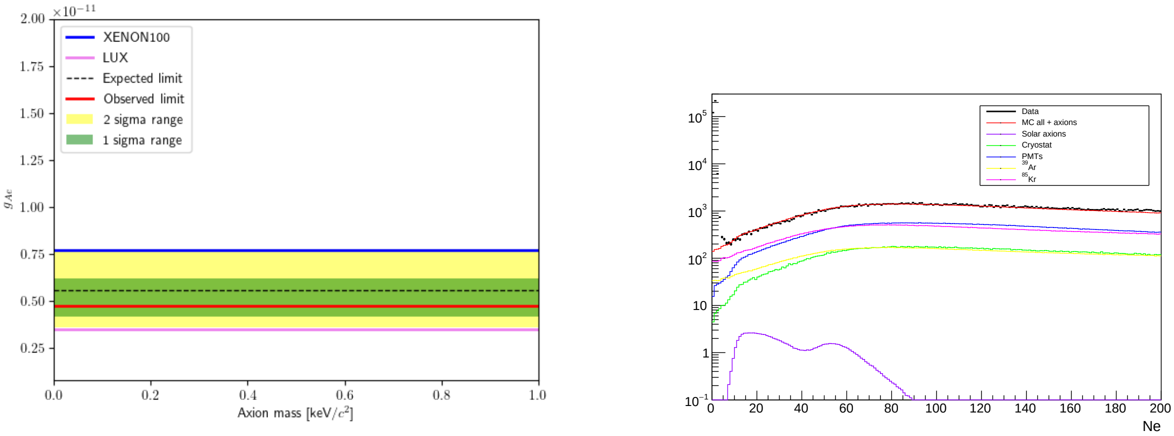

(a) Limit obtained for solar axions with the DS-50 low mass dark matter framework, compared to LUX and XENON results.

(b) Superposition of the background + axions distributions over data. The axion spectrum is generated at $g_{Ae} = 4.75 \times 10^{-12}$

After 100 Ne, there is a clear excess of the data with respect to the MC. This translates in the limits by an observed limit lower than the 2 σ band. For that reason, we can only claim a limit for the [7,50] range, at $g_{Ae} = 4.75 \times 10^{-12}$. This limit is $\sim$ 1.3 times worse than the LUX one.

6.5.3.2 Conclusions

Figure 6.12a shows the limit obtained for solar axions, and Figure 6.12b illustates the axion spectrum at the excluded coupling.

This result is still preliminary. There is still work to be done on the adjustment of the uncertainties and the background model.

6.5.4 Galactic ALPs limits

The treatment of the galactic ALPs is slightly different. Indeed, due to the great variation in the spectra for each mass, it is impossible to define a single fit range. Besides, the higher ALP masses fall in the energy range where the data are in excess with respect to the simulation.

This part of the analysis is still in development. For instance, we cite here the preliminary limits for a galactic ALP of 1 keV/c^2. For this mass, we exclude couplings higher than $g_{Ae} = 1.87 \times 10^{-13}$. Figure 6.12 shows the data, background and ALP distribution for the excluded g_{Ae}.

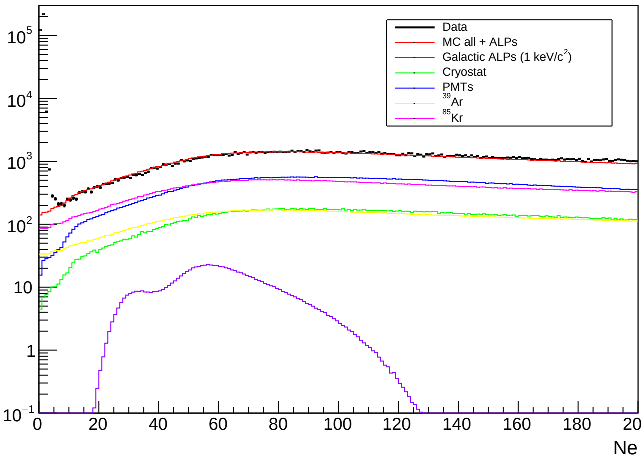

Figure 6.12 – Superposition of the background + axions distributions over data for a galactic ALP of 1 keV$\cdot c^{-2}$. The axion spectrum is generated at $g_{Ae} = 1.87 \times 10^{-13}$.

6.6 Conclusions

The preliminary results presented here are encouraging for axion searches in LAr TPCs. Indeed, we reached limits comparable to those of larger xenon detectors for solar axions. However, there is still room for improvement in the background model. As discussed above, there is a discrepancy between the MC and the data at high Ne. In order to reduce this deviation, the background activities have to be increased, thus reducing the available space for axions at low energies. Also, the spectral fit that gives the input activities is tuned at high energies, so there could be a variation of the results at lower energies.

These results are also an argument in favor of axion searches in the future DarkSide-20k detector. It is especially true for galactic axions, where the sensitivity scales with the fourth root of the target exposure. It would then be interesting to realise a sensitivity study to solar axions and galactic ALPs in the DarkSide-20k detector.

Conclusions and outlook

Noble liquid targets are extremely well suited to direct dark matter search and pose the most stringent limits down to WIMP masses of ∼1 GeV$\cdot c^{-1}$. Among the different noble elements available, argon stands out due to its extraordinary background rejection power, thanks to the PSD (see Chapter 2).

DarkSide-50 was the first LAr detector to run with low radioactivity underground argon. The results presented in Chapter 2 and published in [1] have confirmed the potential of LAr for high mass WIMP search. In Chapter 5, I discussed the DarkSide-50 results in the low mass WIMPs range [2]. DarkSide provides the best limits in the ∼ 2 to 6 GeV$\cdot c^{-2}$ range. This result was made possible thanks to the improvement of our knowledge of the argon ionisation response at low energies, provided by the ARIS external calibration and *in-situ* measurements.

The last part of this thesis focused on axions searches in DarkSide-50. Axions are a promising candidate for dark matter. Their coupling to electrons would make possible their detection in a LAr TPC. The preliminary results obtained are comparable to the current best limits, obtained with Xenon detectors. The sensitivity could be improved by further refinement of the background model. Sensitivity studies for axions and ALPs searches in DS-20k should be conducted. Other types of light dark matter should also be considered.

The DarkSide journey is not finished. The next phase of DarkSide, DarkSide-20k, should start its operations in 2021. Multiplying the target mass by 400 with respect to DarkSide-50, DS-20k will push the sensitivity to high mass WIMPs by several orders of magnitude. DS-20k will also use SiPMs to replace the PMTs. SiPMs are less radioactive and have better photo-detection efficiency and single-electron resolution.

Looking even farther in the future, the Global Argon Dark Matter Collaboration is planning a 300 t detector, Argo, which applications could extend beyond dark matter search to also be a neutrino observatory.

The unexpectedly good performance of LAr for low mass WIMP searches and the encouraging results fro axions also open a new door for LAr-based detectors. DarkSide has a project of small LAr TPC, DarkSide-LowMass, dedicated to low mass WIMP search. Other models of low mass dark matter could be explored, like leptophilic dark matter, hidden photons, etc.

List of Figures

List of Tables

References

[1] The DarkSide Collaboration et al. “DarkSide-50 532-day Dark Matter Search with Low-Radioactivity Argon”. In: (2018). arXiv: `1802.07198`. URL: `http://arxiv.org/abs/1802.07198` (cit. on pp. 1, 26, 152, 183).

[2] The DarkSide Collaboration et al. “Low-mass Dark Matter Search with the DarkSide-50 Experiment”. In: (2018), pp. 1–9. arXiv: `1802.06994`. URL: `http://arxiv.org/abs/1802.06994` (cit. on pp. 1, 3, 26, 152, 183).

[3] R.D. Peccei and Helen Quinn. “CP Conservation in the Presence of Pseudoparticles”. In: *Physical Review Letters - PHYS REV LETT* 38 (June 1977), pp. 1440–1443. DOI: `10.1103/PhysRevLett.38.1440` (cit. on pp. 3, 17, 135, 186, 200).

[4] Louis E. Strigari. “Galactic Searches for Dark Matter”. In: *Phys. Rept.* 531 (2013), pp. 1–88. DOI: `10.1016/j.physrep.2013.05.004`. arXiv: `1211.7090 [astro-ph.CO]` (cit. on pp. 7, 8, 184).

[5] X. X. Xue et al. “The Milky Way’s Circular Velocity Curve to 60 kpc and an Estimate of the Dark Matter Halo Mass from Kinematics of 2400 SDSS Blue Horizontal Branch Stars”. In: *Astrophys. J.* 684 (2008), pp. 1143–1158. DOI: `10.1086/589500`. arXiv: `0801.1232 [astro-ph]` (cit. on pp. 7, 184).

[6] Warren R. Brown, Margaret J. Geller, and Scott J. Kenyon. “MMT HYPERVELOCITY STAR SURVEY. III. THE COMPLETE SURVEY”. In: *The Astrophysical Journal* 787.1 (May 2014), p. 89. DOI: `10.1088/0004-637x/787/1/89`. URL: `https://doi.org/10.1088%2F0004-637x%2F787%2F1%2F89` (cit. on pp. 7, 184).

[7] Giuseppina Battaglia et al. “The Radial velocity dispersion profile of the Galactic Halo: Constraining the density profile of the dark halo of the Milky Way”. In: *Mon. Not. Roy. Astron. Soc.* 364 (2005). [Erratum: Mon. Not. Roy. Astron. Soc.370,1055(2006)], pp. 433–442. DOI: `10.1111/j.1365-2966.2006.10688.x,10.1111/j.1365-2966.2005.09367.x`. arXiv: `astro-ph/0506102 [astro-ph]` (cit. on pp. 7, 184).

[8] V. C. Rubin and W. K. Ford Jr. “Rotation of the Andromeda Nebula from a Spectroscopic Survey of Emission Regions”. In: 159 (Feb. 1970), p. 379. DOI: `10.1086/150317` (cit. on pp. 7, 183).

[9] Fabio Iocco, Miguel Pato, and Gianfranco Bertone. “Evidence for dark matter in the inner Milky Way”. In: *Nature Phys.* 11 (2015), pp. 245–248. DOI: `10.1038/nphys3237`. arXiv: `1502.03821 [astro-ph.GA]` (cit. on pp. 8, 184).

[10] Fritz Zwicky. “Die Rotverschiebung von extragalaktischen Nebeln”. In: *Helv. Phys. Acta* 6 (1933), pp. 110–127. URL: `http://adsabs.harvard.edu/abs/1933AcHPh...6..110Z` (cit. on pp. 8, 184).

[11] Fritz Zwicky. “On the Masses of Nebulae and of Clusters of Nebulae”. In: *Ap. J.* 86 (1937), p. 217. DOI: `10.1086/143864`. URL: `http://adsabs.harvard.edu/doi/10.1086/143864` (cit. on pp. 8, 184).

[12] Douglas Clowe et al. “A direct empirical proof of the existence of dark matter”. In: (2006). ISSN: 0004-637X. DOI: `10.1086/508162`. arXiv: `0608407 [astro-ph]`. URL: `http://arxiv.org/abs/astro-ph/0608407%7B%5C%%7D0Ahttp://dx.doi.org/10.1086/508162` (cit. on p. 9).

[13] Matthias Bartelmann and Peter Schneider. “Weak gravitational lensing”. In: *Phys. Rept.* 340 (2001), pp. 291–472. DOI: `10.1016/S0370-1573(00)00082-X`. arXiv: `astro-ph/9912508 [astro-ph]` (cit. on pp. 8, 185).

[14] Scott W. Randall et al. “Constraints on the Self-Interaction Cross-Section of Dark Matter from Numerical Simulations of the Merging Galaxy Cluster 1E 0657-56”. In: *Astrophys. J.* 679 (2008), pp. 1173–1180. DOI: `10.1086/587859`. arXiv: `0704.0261 [astro-ph]` (cit. on pp. 9, 185).

[15] Marusa Bradac et al. “Revealing the properties of dark matter in the merging cluster MACSJ0025.4-1222”. In: *Astrophys. J.* 687 (2008), p. 959. DOI: `10.1086/591246`. arXiv: `0806.2320 [astro-ph]` (cit. on p. 9).

[16] S. Dodelson. *Modern Cosmology*. Elsevier Science, 2003. ISBN: 9780080511979. URL: `https://books.google.fr/books?id=zk5e6XsY6nsC` (cit. on pp. 10, 185).

[17] Adam G. Riess et al. “BV RI light curves for 22 type Ia supernovae”. In: *Astron. J.* 117 (1999), pp. 707–724. DOI: `10.1086/300738`. arXiv: `astro-ph/9810291 [astro-ph]` (cit. on pp. 10, 185).

[18] Saul Perlmutter, Michael S. Turner, and Martin J. White. “Constraining dark energy with SNe Ia and large scale structure”. In: *Phys. Rev. Lett.* 83 (1999), pp. 670–673. DOI: `10.1103/PhysRevLett.83.670`. arXiv: `astro-ph/9901052 [astro-ph]` (cit. on pp. 10, 185).

[19] Planck Collaboration et al. “Planck 2015 results - I. Overview of products and scientific results”. In: *A&A* 594 (2016), A1. DOI: `10.1051/0004-6361/201527101`. URL: `https://doi.org/10.1051/0004-6361/201527101` (cit. on pp. 10, 11, 185).

[20] A. A. Penzias and R. W. Wilson. “A Measurement of Excess Antenna Temperature at 4080 Mc/s.” In: 142 (July 1965), pp. 419–421. DOI: `10.1086/148307` (cit. on pp. 10, 185).

[21] J. C. Mather et al. "Measurement of the cosmic microwave background spectrum by the COBE FIRAS instrument". In: 420 (Jan. 1994), pp. 439–444. DOI: `10.1086/173574` (cit. on p. 10).

[22] Planck Collaboration et al. "Planck 2015 results - XIII. Cosmological parameters". In: *A&A* 594 (2016), A13. DOI: `10.1051/0004-6361/201525830`. URL: `https://doi.org/10.1051/0004-6361/201525830` (cit. on pp. 10–13, 186).

[23] Will J. Percival et al. "Measuring the Baryon Acoustic Oscillation scale using the SDSS and 2dFGRS". In: *Mon. Not. Roy. Astron. Soc.* 381 (2007), pp. 1053–1066. DOI: `10.1111/j.1365-2966.2007.12268.x`. arXiv: `0705.3323 [astro-ph]` (cit. on pp. 11, 185).

[24] Metin Ata et al. "The clustering of the SDSS-IV extended Baryon Oscillation Spectroscopic Survey DR14 quasar sample: first measurement of baryon acoustic oscillations between redshift 0.8 and 2.2". In: *Mon. Not. Roy. Astron. Soc.* 473.4 (2018), pp. 4773–4794. DOI: `10.1093/mnras/stx2630`. arXiv: `1705.06373 [astro-ph.CO]` (cit. on pp. 11, 185).

[25] Bruno Leibundgut. "Cosmological Implications from Observations of Type Ia Supernovae". In: *Annual Review of Astronomy and Astrophysics* 39.1 (2001), pp. 67–98. DOI: `10.1146/annurev.astro.39.1.67`. eprint: `https://doi.org/10.1146/annurev.astro.39.1.67`. URL: `https://doi.org/10.1146/annurev.astro.39.1.67` (cit. on p. 11).

[26] Adam G. Riess et al. "Milky Way Cepheid Standards for Measuring Cosmic Distances and Application to Gaia DR2: Implications for the Hubble Constant". In: *Astrophys. J.* 861.2 (2018), p. 126. DOI: `10.3847/1538-4357/aac82e`. arXiv: `1804.10655 [astro-ph.CO]` (cit. on p. 12).

[27] M. Betoule et al. "Improved cosmological constraints from a joint analysis of the SDSS-II and SNLS supernova samples". In: *Astron. Astrophys.* 568 (2014), A22. DOI: `10.1051/0004-6361/201423413`. arXiv: `1401.4064 [astro-ph.CO]` (cit. on pp. 12, 185).

[28] Richard I. Epstein, James M. Lattimer, and David N. Schramm. "The origin of deuterium". In: *Nature* 198 (1976). DOI: `10.1038/263198a0`. URL: `https://doi.org/10.1038/263198a0` (cit. on p. 13).

[29] Ryan Cooke et al. "Precision measures of the primordial abundance of deuterium". In: *Astrophys. J.* 781.1 (2014), p. 31. DOI: `10.1088/0004-637X/781/1/31`. arXiv: `1308.3240 [astro-ph.CO]` (cit. on pp. 13, 185).

[30] J. Binney and S. Tremaine. *Galactic Dynamics: Second Edition*. Princeton University Press, 2008 (cit. on p. 13).

[31] F. -S. Ling et al. "Dark matter direct detection signals inferred from a cosmological N-body simulation with baryons". In: 2010.2, 012 (Feb. 2010), p. 012. DOI: `10.1088/1475-7516/2010/02/012`. arXiv: `0909.2028 [astro-ph.GA]` (cit. on p. 14).

[32] C. Patrignani et al. "Review of Particle Physics". In: *Chin. Phys.* C40.10 (2016), p. 100001. DOI: `10.1088/1674-1137/40/10/100001` (cit. on p. 14).

[33] M. J. Reid et al. "Trigonometric Parallaxes of Massive Star-Forming Regions. VI. Galactic Structure, Fundamental Parameters, and Noncircular Motions". In: 700.1 (July 2009), pp. 137–148. DOI: `10.1088/0004-637X/700/1/137`. arXiv: `0902.3913 [astro-ph.GA]` (cit. on p. 14).

[34] Anne M. Green. "Astrophysical uncertainties on direct detection experiments". In: *Mod. Phys. Lett.* A27 (2012), p. 1230004. DOI: `10.1142/S0217732312300042`. arXiv: `1112.0524 [astro-ph.CO]` (cit. on p. 14).

[35] Martin C. Smith et al. "The RAVE Survey: Constraining the Local Galactic Escape Speed". In: *Mon. Not. Roy. Astron. Soc.* 379 (2007), pp. 755–772. DOI: `10.1111/j.1365-2966.2007.11964.x`. arXiv: `astro-ph/0611671 [astro-ph]` (cit. on p. 14).

[36] Jonathan L. Feng. "Dark Matter Candidates from Particle Physics and Methods of Detection". In: *Ann. Rev. Astron. Astrophys.* 48 (2010), pp. 495–545. DOI: `10.1146/annurev-astro-082708-101659`. arXiv: `1003.0904 [astro-ph.CO]` (cit. on pp. 15, 16, 186).

[37] Adel Bilal. "Introduction to supersymmetry". In: (2001). arXiv: `hep-th/0101055 [hep-th]` (cit. on pp. 15, 186).

[38] Gerard Jungman, Marc Kamionkowski, and Kim Griest. "Supersymmetric dark matter". In: *Phys. Rept.* 267 (1996), pp. 195–373. DOI: `10.1016/0370-1573(95)00058-5`. arXiv: `hep-ph/9506380 [hep-ph]` (cit. on p. 15).

[39] T. Appelquist, A. Chodos, and P. G. O. Freund, eds. *MODERN KALUZA-KLEIN THEORIES*. 1987 (cit. on pp. 15, 186).

[40] M. Tanabashi et al. "Review of Particle Physics". In: *Phys. Rev.* D98.3 (2018), p. 030001. DOI: `10.1103/PhysRevD.98.030001` (cit. on pp. 17, 19, 139, 141, 186, 187).

[41] Edward Witten. "Some Properties of O(32) Superstrings". In: *Phys. Lett.* 149B (1984), pp. 351–356. DOI: `10.1016/0370-2693(84)90422-2` (cit. on pp. 17, 186).

[42] Joseph P. Conlon. "The QCD axion and moduli stabilisation". In: *JHEP* 05 (2006), p. 078. DOI: `10.1088/1126-6708/2006/05/078`. arXiv: `hep-th/0602233 [hep-th]` (cit. on pp. 17, 186).

[43] Asimina Arvanitaki et al. "String Axiverse". In: *Phys. Rev.* D81 (2010), p. 123530. DOI: `10.1103/PhysRevD.81.123530`. arXiv: `0905.4720 [hep-th]` (cit. on pp. 17, 186).

[44] Paola Arias et al. "WISPy Cold Dark Matter". In: *JCAP* 1206 (2012), p. 013. DOI: `10.1088/1475-7516/2012/06/013`. arXiv: `1201.5902 [hep-ph]` (cit. on pp. 17, 186).

[45] Jan Conrad, Johann Cohen-Tanugi, and Louis E. Strigari. "WIMP searches with gamma rays in the Fermi era: challenges, methods and results". In: *J. Exp. Theor. Phys.* 121.6 (2015). [Zh. Eksp. Teor. Fiz.148,no.6,1257(2015)], pp. 1104–1135. DOI: `10.1134/S1063776115130099`. arXiv: `1503.06348 [astro-ph.CO]` (cit. on pp. 18, 19, 187).

[46] M. L. Ahnen et al. "Indirect dark matter searches in the dwarf satellite galaxy Ursa Major II with the MAGIC Telescopes". In: *JCAP* 1803.03 (2018), p. 009. DOI: `10.1088/1475-7516/2018/03/009`. arXiv: `1712.03095 [astro-ph.HE]` (cit. on p. 18).

[47] A. Abramowski et al. "Constraints on an Annihilation Signal from a Core of Constant Dark Matter Density around the Milky Way Center with H.E.S.S." In: *Phys. Rev. Lett.* 114.8 (2015), p. 081301. DOI: `10.1103/PhysRevLett.114.081301`. arXiv: `1502.03244 [astro-ph.HE]` (cit. on pp. 18, 19).

[48] T. Arlen et al. "Constraints on Cosmic Rays, Magnetic Fields, and Dark Matter from Gamma-Ray Observations of the Coma Cluster of Galaxies with VERITAS and Fermi". In: *Astrophys. J.* 757 (2012), p. 123. DOI: `10.1088/0004-637X/757/2/123`. arXiv: `1208.0676 [astro-ph.HE]` (cit. on p. 19).

[49] M. Ackermann et al. "Fermi LAT Search for Dark Matter in Gamma-ray Lines and the Inclusive Photon Spectrum". In: *Phys. Rev.* D86 (2012), p. 022002. DOI: `10.1103/PhysRevD.86.022002`. arXiv: `1205.2739 [astro-ph.HE]` (cit. on p. 19).

[50] V. A. Acciari et al. "Constraining Dark Matter lifetime with a deep gamma-ray survey of the Perseus Galaxy Cluster with MAGIC". In: *Phys. Dark Univ.* 22 (2018), pp. 38–47. DOI: `10.1016/j.dark.2018.08.002`. arXiv: `1806.11063 [astro-ph.HE]` (cit. on p. 19).

[51] G. Wikström and J. Edsjö. "Limits on the WIMP-nucleon scattering cross-section from neutrino telescopes". In: 2009.4, 009 (Apr. 2009), p. 009. DOI: `10.1088/1475-7516/2009/04/009`. arXiv: `0903.2986 [astro-ph.CO]` (cit. on p. 19).

[52] K. Choi et al. "Search for neutrinos from annihilation of captured low-mass dark matter particles in the Sun by Super-Kamiokande". In: *Phys. Rev. Lett.* 114.14 (2015), p. 141301. DOI: `10.1103/PhysRevLett.114.141301`. arXiv: `1503.04858 [hep-ex]` (cit. on p. 19).

[53] M. G. Aartsen et al. "Search for annihilating dark matter in the Sun with 3 years of IceCube data". In: *Eur. Phys. J.* C77.3 (2017). [Erratum: Eur. Phys. J.C79,no.3,214(2019)], p. 146. DOI: `10.1140/epjc/s10052-019-6702-y,10.1140/epjc/s10052-017-4689-9`. arXiv: `1612.05949 [astro-ph.HE]` (cit. on p. 19).

[54] Oscar Adriani et al. "An anomalous positron abundance in cosmic rays with energies 1.5-100 GeV". In: *Nature* 458 (2009), pp. 607–609. DOI: `10.1038/nature07942`. arXiv: `0810.4995 [astro-ph]` (cit. on p. 19).

[55] M. Aguilar et al. "First Result from the Alpha Magnetic Spectrometer on the International Space Station: Precision Measurement of the Positron Fraction in Primary Cosmic Rays of 0.5–350 GeV". In: *Phys. Rev. Lett.* 110 (14 Apr. 2013), p. 141102. DOI: `10.1103/PhysRevLett.110.141102`. URL: `https://link.aps.org/doi/10.1103/PhysRevLett.110.141102` (cit. on p. 19).

[56] M. Aguilar et al. “Precision Measurement of the (e++e–) Flux in Primary Cosmic Rays from 0.5 GeV to 1 TeV with the Alpha Magnetic Spectrometer on the International Space Station”. In: *Physical Review Letters* 113 (2014). See paper for full list of authors –, p. 221102. DOI: `10.1103/PhysRevLett.113.221102`. URL: `http://hal.in2p3.fr/in2p3-01088104` (cit. on p. 19).

[57] Kfir Blum, Boaz Katz, and Eli Waxman. “AMS-02 Results Support the Secondary Origin of Cosmic Ray Positrons”. In: *Phys. Rev. Lett.* 111.21 (2013), p. 211101. DOI: `10.1103/PhysRevLett.111.211101`. arXiv: `1305.1324 [astro-ph.HE]` (cit. on p. 19).

[58] Antonio Boveia and Caterina Doglioni. “Dark Matter Searches at Colliders”. In: *Ann. Rev. Nucl. Part. Sci.* 68 (2018), pp. 429–459. DOI: `10.1146/annurev-nucl-101917-021008`. arXiv: `1810.12238 [hep-ex]` (cit. on pp. 19, 187).

[59] Prateek Agrawal and Vikram Rentala. “Identifying dark matter interactions in monojet searches”. In: *JHEP* 05 (2014), p. 098. DOI: `10.1007/JHEP05(2014)098`. arXiv: `1312.5325 [hep-ph]` (cit. on p. 19).

[60] *Dark matter summary plots.* Tech. rep. ATL-PHYS-PUB-2019-030. Geneva: CERN, Aug. 2019. URL: `https://cds.cern.ch/record/2684864` (cit. on p. 20).

[61] Mark W. Goodman and Edward Witten. “Detectability of certain dark-matter candidates”. In: *Phys. Rev. D* 31 (12 June 1985), pp. 3059–3063. DOI: `10.1103/PhysRevD.31.3059`. URL: `https://link.aps.org/doi/10.1103/PhysRevD.31.3059` (cit. on pp. 21, 188).

[62] David N. Spergel. “Motion of the Earth and the detection of weakly interacting massive particles”. In: *Phys. Rev. D* 37 (6 Mar. 1988), pp. 1353–1355. DOI: `10.1103/PhysRevD.37.1353`. URL: `https://link.aps.org/doi/10.1103/PhysRevD.37.1353` (cit. on p. 23).

[63] F. Mayet et al. “A review of the discovery reach of directional Dark Matter detection”. In: *Phys. Rept.* 627 (2016), pp. 1–49. DOI: `10.1016/j.physrep.2016.02.007`. arXiv: `1602.03781 [astro-ph.CO]` (cit. on p. 24).

[64] R. Agnese et al. “First Dark Matter Constraints from a SuperCDMS Single-Charge Sensitive Detector”. In: *Phys. Rev. Lett.* 121.5 (2018). [erratum: Phys. Rev. Lett.122,no.6,069901(2019)], p. 051301. DOI: `10.1103/PhysRevLett.122.069901,10.1103/PhysRevLett.121.051301`. arXiv: `1804.10697 [hep-ex]` (cit. on p. 24).

[65] G. Angloher et al. “Dark-Photon Search using Data from CRESST-II Phase 2”. In: *Eur. Phys. J.* C77.5 (2017), p. 299. DOI: `10.1140/epjc/s10052-017-4878-6`. arXiv: `1612.07662 [hep-ex]` (cit. on pp. 24, 25).

[66] F. Petricca et al. “First results on low-mass dark matter from the CRESST-III experiment”. In: *15th International Conference on Topics in Astroparticle and Underground Physics (TAUP 2017) Sudbury, Ontario, Canada, July 24-28, 2017.* 2017. arXiv: `1711.07692 [astro-ph.CO]` (cit. on pp. 24, 25).

[67] L. Hehn et al. “Improved EDELWEISS-III sensitivity for low-mass WIMPs using a profile likelihood approach”. In: *The European Physical Journal C* 76.10 (Oct. 2016), p. 548. ISSN: 1434-6052. DOI: `10.1140/epjc/s10052-016-4388-y`. URL: `https://doi.org/10.1140/epjc/s10052-016-4388-y` (cit. on p. 24).

[68] D. S. Akerib et al. “Results from a search for dark matter in the complete LUX exposure”. In: *Phys. Rev. Lett.* 118.2 (2017), p. 021303. DOI: `10.1103/PhysRevLett.118.021303`. arXiv: `1608.07648 [astro-ph.CO]` (cit. on pp. 25, 26).

[69] R. Ajaj et al. “Search for dark matter with a 231-day exposure of liquid argon using DEAP-3600 at SNOLAB”. In: *Phys. Rev.* D100.2 (2019), p. 022004. DOI: `10.1103/PhysRevD.100.022004`. arXiv: `1902.04048 [astro-ph.CO]` (cit. on p. 25).

[70] E. Aprile et al. “First Dark Matter Search Results from the XENON1T Experiment”. In: *Phys. Rev. Lett.* 119.18 (2017), p. 181301. DOI: `10.1103/PhysRevLett.119.181301`. arXiv: `1705.06655 [astro-ph.CO]` (cit. on p. 25).

[71] Andi Tan et al. “Dark Matter Results from First 98.7 Days of Data from the PandaX-II Experiment”. In: *Phys. Rev. Lett.* 117 (12 Sept. 2016), p. 121303. DOI: `10.1103/PhysRevLett.117.121303`. URL: `https://link.aps.org/doi/10.1103/PhysRevLett.117.121303` (cit. on pp. 25, 26).

[72] R. Bernabei et al. “First Model Independent Results from DAMA/LIBRA–Phase2”. In: *Universe* 4.11 (2018). [Nucl. Phys. Atom. Energy19,no.4,307(2018)], p. 116. DOI: `10.3390/universe4110116,10.15407/jnpae2018.04.307`. arXiv: `1805.10486 [hep-ex]` (cit. on pp. 25, 27).

[73] C. E. Aalseth et al. “CoGeNT: A Search for Low-Mass Dark Matter using p-type Point Contact Germanium Detectors”. In: *Phys. Rev.* D88 (2013), p. 012002. DOI: `10.1103/PhysRevD.88.012002`. arXiv: `1208.5737 [astro-ph.CO]` (cit. on p. 25).

[74] A. Aguilar-Arevalo et al. “First Direct-Detection Constraints on eV-Scale Hidden-Photon Dark Matter with DAMIC at SNOLAB”. In: *Phys. Rev. Lett.* 118.14 (2017), p. 141803. DOI: `10.1103/PhysRevLett.118.141803`. arXiv: `1611.03066 [astro-ph.CO]` (cit. on p. 25).

[75] Q. Arnaud et al. “First results from the NEWS-G direct dark matter search experiment at the LSM”. In: *Astropart. Phys.* 97 (2018), pp. 54–62. DOI: `10.1016/j.astropartphys.2017.10.009`. arXiv: `1706.04934 [astro-ph.IM]` (cit. on p. 25).

[76] E. Behnke et al. “Final Results of the PICASSO Dark Matter Search Experiment”. In: *Astropart. Phys.* 90 (2017), pp. 85–92. DOI: `10.1016/j.astropartphys.2017.02.005`. arXiv: `1611.01499 [hep-ex]` (cit. on p. 26).

[77] C. Amole et al. “Dark Matter Search Results from the PICO−60 C_3F_8 Bubble Chamber”. In: *Phys. Rev. Lett.* 118 (25 June 2017), p. 251301. DOI: `10.1103/PhysRevLett.118.251301`. URL: `https://link.aps.org/doi/10.1103/PhysRevLett.118.251301` (cit. on p. 26).

[78] Kiseki Nakamura et al. "NEWAGE - Direction-sensitive Dark Matter Search Experiment". In: *Physics Procedia* 61 (2015). 13th International Conference on Topics in Astroparticle and Underground Physics, TAUP 2013, pp. 737–741. ISSN: 1875-3892. DOI: `https://doi.org/10.1016/j.phpro.2014.12.091`. URL: `http://www.sciencedirect.com/science/article/pii/S1875389214007044` (cit. on p. 26).

[79] D. Santos et al. "MIMAC: A micro-tpc matrix for dark matter directional detection". In: *J. Phys. Conf. Ser.* 460 (2013), p. 012007. DOI: `10.1088/1742-6596/460/1/012007`. arXiv: `1304.2255 [physics.ins-det]` (cit. on p. 26).

[80] E Daw et al. "Spin-Dependent Limits from the DRIFT-IId Directional Dark Matter Detector". In: *Astroparticle Physics* 35 (Oct. 2010). DOI: `10.1016/j.astropartphys.2011.11.003` (cit. on p. 26).

[81] E. Aprile et al. "Dark Matter Search Results from a One Ton-Year Exposure of XENON1T". In: *Phys. Rev. Lett.* 121.11 (2018), p. 111302. DOI: `10.1103/PhysRevLett.121.111302`. arXiv: `1805.12562 [astro-ph.CO]` (cit. on p. 26).

[82] E. Aprile et al. "Light Dark Matter Search with Ionization Signals in XENON1T". In: (2019). arXiv: `1907.11485 [hep-ex]` (cit. on p. 26).

[83] C. Amole et al. "Dark matter search results from the complete exposure of the PICO-60 C_3F_8 bubble chamber". In: *Phys. Rev. D* 100 (2 July 2019), p. 022001. DOI: `10.1103/PhysRevD.100.022001`. URL: `https://link.aps.org/doi/10.1103/PhysRevD.100.022001` (cit. on p. 26).

[84] E. Aprile et al. "Constraining the spin-dependent WIMP-nucleon cross sections with XENON1T". In: *Phys. Rev. Lett.* 122.14 (2019), p. 141301. DOI: `10.1103/PhysRevLett.122.141301`. arXiv: `1902.03234 [astro-ph.CO]` (cit. on p. 26).

[85] Jingkai Xia et al. "PandaX-II Constraints on Spin-Dependent WIMP-Nucleon Effective Interactions". In: *Phys. Lett.* B792 (2019), pp. 193–198. DOI: `10.1016/j.physletb.2019.02.043`. arXiv: `1807.01936 [hep-ex]` (cit. on p. 26).

[86] D. S. Akerib et al. "Limits on spin-dependent WIMP-nucleon cross section obtained from the complete LUX exposure". In: *Phys. Rev. Lett.* 118.25 (2017), p. 251302. DOI: `10.1103/PhysRevLett.118.251302`. arXiv: `1705.03380 [astro-ph.CO]` (cit. on p. 26).

[87] C. Savage et al. "Compatibility of DAMA/LIBRA dark matter detection with other searches in light of new galactic rotation velocity measurements". In: 2009.9, 036 (Sept. 2009), p. 036. DOI: `10.1088/1475-7516/2009/09/036`. arXiv: `0901.2713 [astro-ph.CO]` (cit. on p. 27).

[88] Thomas Alexander et al. "Light yield in DarkSide-10: A prototype two-phase argon TPC for dark matter searches". In: *Astropart. Phys.* 49 (2013), pp. 44–51. DOI: `10.1016/j.astropartphys.2013.08.004`. URL: `http://linkinghub.elsevier.com/retrieve/pii/S0927650513001254` (cit. on p. 29).

[89] Paolo Agnes et al. “First results from the DarkSide-50dark matter experiment at Laboratori Nazionali del Gran Sasso”. In: *Phys. Lett. B* 743 (2015), pp. 456–466. DOI: `10.1016/j.physletb.2015.03.012`. URL: `http://linkinghub.elsevier.com/retrieve/pii/S0370269315001756` (cit. on pp. 29, 37, 47).

[90] E. Aprile et al. *Noble Gas Detectors*. Wiley, 2007. ISBN: 9783527609635. URL: `https://books.google.fr/books?id=tsnHM8x6cHAC` (cit. on pp. 29, 32).

[91] Paolo Agnes. “Direct Search for Dark Matter with the DarkSide Experiment”. PhD thesis. APC, Paris, 2016. URL: `https://tel.archives-ouvertes.fr/tel-01497505` (cit. on p. 29).

[92] Paolo Agnes et al. “Results from the first use of low radioactivity argon in a dark matter search”. In: *Phys. Rev. D* 93.8 (2016), p. 081101. DOI: `10.1103/PhysRevD.93.081101`. URL: `http://link.aps.org/doi/10.1103/PhysRevD.93.081101` (cit. on pp. 29, 47).

[93] C. Amsler et al. “Luminescence quenching of the triplet excimer state by air traces in gaseous argon”. In: *Journal of Instrumentation* 3.2 (Feb. 2008), p. 02001. DOI: `10.1088/1748-0221/3/02/P02001`. arXiv: `0708.2621 [physics.ins-det]` (cit. on p. 30).

[94] S. Kubota et al. “Recombination luminescence in liquid argon and in liquid xenon”. In: *Phys. Rev. B* 17 (6 Mar. 1978), pp. 2762–2765. DOI: `10.1103/PhysRevB.17.2762`. URL: `https://link.aps.org/doi/10.1103/PhysRevB.17.2762` (cit. on p. 32).

[95] Joshua Jortner et al. “Localized Excitations in Condensed Ne, Ar, Kr, and Xe”. In: *The Journal of Chemical Physics* 42.12 (1965), pp. 4250–4253. DOI: `10.1063/1.1695927`. eprint: `https://doi.org/10.1063/1.1695927`. URL: `https://doi.org/10.1063/1.1695927` (cit. on p. 32).

[96] G. W. Hutchinson. “Ionization in Liquid and Solid Argon”. In: *Nature* 162 (1948), pp. 610–611. DOI: `10.1038/162610a0`. URL: `https://doi.org/10.1038/162610a0` (cit. on p. 33).

[97] A.I. Bolozdynya. “Two-phase emission detectors and their applications”. In: *Nuclear Instruments and Methods in Physics Research Section A: Accelerators, Spectrometers, Detectors and Associated Equipment* 422.1 (1999), pp. 314–320. ISSN: 0168-9002. DOI: `https://doi.org/10.1016/S0168-9002(98)00965-6`. URL: `http://www.sciencedirect.com/science/article/pii/S0168900298009656` (cit. on p. 33).

[98] E. M. Gushchin, A. A. Kruglov, and I. M. Obodovskil. “Emission of ’hot’ electrons from liquid and solid argon and xenon”. In: *Journal of Experimental and Theoretical Physics* 55.5 (1982). URL: `http://jetp.ac.ru/cgi-bin/e/index/e/55/5/p860?a=list` (cit. on pp. 33, 34).

[99] C.M.B. Monteiro et al. “Secondary scintillation yield in pure argon”. In: *Physics Letters B* 668.3 (2008), pp. 167–170. ISSN: 0370-2693. DOI: `https://doi.org/10.1016/j.physletb.2008.08.030`. URL: `http://www.sciencedirect.com/science/article/pii/S0370269308010435` (cit. on p. 35).

[100] V Chepel and H Araújo. "Liquid noble gas detectors for low energy particle physics". In: *Journal of Instrumentation* 8.04 (2013). ISSN: 1748-0221. DOI: `10.1088/1748-0221/8/04/R04001`. arXiv: `1207.2292` (cit. on p. 35).

[101] A Buzulutskov. "Advances in Cryogenic Avalanche Detectors". In: *Journal of Instrumentation* 7.02 (Feb. 2012), pp. C02025–C02025. DOI: `10.1088/1748-0221/7/02/c02025`. URL: `https://doi.org/10.1088%2F1748-0221%2F7%2F02%2Fc02025` (cit. on p. 35).

[102] Wladyslaw Henryk Trzaska. "LBNO-DEMO (WA105): a large demonstrator of the Liquid Argon double phase TPC". In: *PoS* PhotoDet2015 (2016), p. 054. DOI: `10.22323/1.252.0054` (cit. on p. 35).

[103] P. Benetti et al. "Measurement of the specific activity of 39Ar in natural argon". In: *Nuclear Instruments and Methods in Physics Research Section A: Accelerators, Spectrometers, Detectors and Associated Equipment* 574.1 (2007), pp. 83–88. ISSN: 0168-9002. DOI: `https://doi.org/10.1016/j.nima.2007.01.106`. URL: `http://www.sciencedirect.com/science/article/pii/S0168900207001672` (cit. on p. 36).

[104] Akira Hitachi et al. "Effect of ionization density on the time dependence of luminescence from liquid argon and xenon". In: *Phys. Rev. B* 27.9 (1983), pp. 5279–5285. DOI: `10.1103/PhysRevB.27.5279`. URL: `http://link.aps.org/doi/10.1103/PhysRevB.27.5279` (cit. on pp. 37, 92, 190).

[105] Shinzou Kubota, Masahiko Hishida, and Akira Nohara. "Variation of scintillation decay in liquid argon excited by electrons and alpha particles". In: *Nucl. Inst. Meth.* 150.3 (1978), pp. 561–564. DOI: `10.1016/0029-554X(78)90128-3`. URL: `http://linkinghub.elsevier.com/retrieve/pii/0029554X78901283` (cit. on p. 37).

[106] M J Carvalho and G Klein. "Luminescence decay in condensed argon under high energy excitation". In: *Journal of Luminescence* 18-19 (1979), pp. 487–490. DOI: `10.1016/0022-2313(79)90167-4`. URL: `http://linkinghub.elsevier.com/retrieve/pii/0022231379901674` (cit. on p. 37).

[107] T. Alexander et al. "Observation of the Dependence on Drift Field of Scintillation from Nuclear Recoils in Liquid Argon". In: *Phys. Rev.* D88.9 (2013), p. 092006. DOI: `10.1103/PhysRevD.88.092006`. arXiv: `1306.5675 [physics.ins-det]` (cit. on pp. 37, 117, 190).

[108] P. -A. Amaudruz et al. "Measurement of the scintillation time spectra and pulse-shape discrimination of low-energy β and nuclear recoils in liquid argon with DEAP-1". In: *Astropart. Phys.* 85 (2016), pp. 1–23. DOI: `10.1016/j.astropartphys.2016.09.002`. arXiv: `0904.2930 [astro-ph.IM]` (cit. on p. 37).

[109] Paolo Agnes et al. "The veto system of the DarkSide-50 experiment". In: *JINST* 11.03 (2016), P03016–P03016. DOI: `10.1088/1748-0221/11/03/P03016`. URL: `http://stacks.iop.org/1748-0221/11/i=03/a=P03016?key=crossref.42fdff7a59143bab1664aa79499feffb` (cit. on p. 41).

[110] Gianpaolo Bellini et al. "Cosmic-muon flux and annual modulation in Borexino at 3800 m water-equivalent depth". In: *JCAP* 1205.05 (2012), pp. 015–015. DOI: `10.1088/1475-7516/2012/05/015`. URL: `http://stacks.iop.org/1475-7516/2012/i=05/a=015?key=crossref.b5476379a662efdbee55c00835b7ff60` (cit. on pp. 43, 192).

[111] Giuseppe Battistoni et al. "Overview of the FLUKA code". In: *Annals of Nuclear Energy* 82 (2015). Joint International Conference on Supercomputing in Nuclear Applications and Monte Carlo 2013, SNA + MC 2013. Pluri- and Trans-disciplinarity, Towards New Modeling and Numerical Simulation Paradigms, pp. 10–18. ISSN: 0306-4549. DOI: `https://doi.org/10.1016/j.anucene.2014.11.007`. URL: `http://www.sciencedirect.com/science/article/pii/S0306454914005878` (cit. on p. 44).

[112] T.T. Böhlen et al. "The FLUKA Code: Developments and Challenges for High Energy and Medical Applications". In: *Nuclear Data Sheets* 120 (2014), pp. 211–214. ISSN: 0090-3752. DOI: `https://doi.org/10.1016/j.nds.2014.07.049`. URL: `http://www.sciencedirect.com/science/article/pii/S0090375214005018` (cit. on pp. 44, 50).

[113] A. J. Koning, S. Hilaire, and M. C. Duijvestijn. "TALYS-1.0". In: *Proceedings ofthe International Conference on Nuclear Data for Science and Technology*. Les Ulis, France: EDP Sciences, May 2007. DOI: `10.1051/ndata:07767`. URL: `http://nd2007.edpsciences.org/10.1051/ndata:07767` (cit. on p. 44).

[114] Aaron Roodman. "Blind analysis in particle physics". In: *eConf* C030908 (2003). [,166(2003)], TUIT001. arXiv: `physics/0312102 [physics.data-an]` (cit. on pp. 46, 192).

[115] Tadayoshi Doke et al. "Let dependence of scintillation yields in liquid argon". In: *Nucl. Inst. Meth. A* 269.1 (1988), pp. 291–296. DOI: `10.1016/0168-9002(88)90892-3`. URL: `http://linkinghub.elsevier.com/retrieve/pii/0168900288908923` (cit. on pp. 63, 98, 99, 197).

[116] D S Akerib et al. "Low-energy (0.7–74 keV) nuclear recoil calibration of the LUX dark matter experiment using D-D neutron scattering kinematics". In: (2016). arXiv: `arXiv:1608.05381v2` (cit. on p. 66).

[117] Huajie Cao et al. "Measurement of scintillation and ionization yield and scintillation pulse shape from nuclear recoils in liquid argon". In: *Phys. Rev. D* 91.9 (2015), p. 092007. DOI: `10.1103/PhysRevD.91.092007`. URL: `http://link.aps.org/doi/10.1103/PhysRevD.91.092007` (cit. on pp. 66, 93, 95, 115, 117, 196–198).

[118] W. Creus et al. "Scintillation efficiency of liquid argon in low energy neutron-argon scattering". In: *JINST* 10.08 (2015), P08002. DOI: `10.1088/1748-0221/10/08/P08002`. arXiv: `1504.07878 [physics.ins-det]` (cit. on pp. 67, 93, 95, 196, 197).

[119] H. Laurent et al. “EDEN: A neutron time of flight multi-detector for decay studies of giant states”. In: *Nuclear Instruments and Methods in Physics Research Section A: Accelerators, Spectrometers, Detectors and Associated Equipment* 326.3 (1993), pp. 517–525. DOI: `https://doi.org/10.1016/0168-9002(93)90854-B`. URL: `http://www.sciencedirect.com/science/article/pii/016890029390854B` (cit. on p. 69).

[120] C Green et al. “The art framework”. In: *Journal of Physics: Conference Series* 396.2 (Dec. 2012), p. 022020. DOI: `10.1088/1742-6596/396/2/022020`. URL: `https://doi.org/10.1088%2F1742-6596%2F396%2F2%2F022020` (cit. on p. 71).

[121] J. Scherzinger et al. “The light-yield response of a NE-213 liquid-scintillator detector measured using 2–6MeV tagged neutrons”. In: *Nuclear Instruments and Methods in Physics Research Section A: Accelerators, Spectrometers, Detectors and Associated Equipment* 840 (2016), pp. 121–127. ISSN: 0168-9002. DOI: `https://doi.org/10.1016/j.nima.2016.10.011`. URL: `http://www.sciencedirect.com/science/article/pii/S0168900216310361` (cit. on p. 80).

[122] R. Brun and F. Rademakers. “ROOT: An object oriented data analysis framework”. In: *Nucl. Instrum. Meth.* A389 (1997), pp. 81–86. DOI: `10.1016/S0168-9002(97)00048-X` (cit. on pp. 86, 130).

[123] W. H. Lippincott et al. “Scintillation time dependence and pulse shape discrimination in liquid argon”. In: *Phys. Rev.* C78 (2008). [Erratum: Phys. Rev.C81,039901(2010)], p. 035801. DOI: `10.1103/PhysRevC.81.039901,10.1103/PhysRevC.78.035801`. arXiv: `0801.1531 [nucl-ex]` (cit. on pp. 89, 106, 195).

[124] E. Aprile et al. “Simultaneous measurement of ionization and scintillation from nuclear recoils in liquid xenon as target for a dark matter experiment”. In: *Phys. Rev. Lett.* 97 (2006), p. 081302. DOI: `10.1103/PhysRevLett.97.081302`. arXiv: `astro-ph/0601552 [astro-ph]` (cit. on pp. 89, 196).

[125] W. H. Lippincott et al. “Calibration of liquid argon and neon detectors with $^{83}\mathrm{Kr}^{m}$”. In: *Phys. Rev. C* 81 (4 Apr. 2010), p. 045803. DOI: `10.1103/PhysRevC.81.045803`. URL: `https://link.aps.org/doi/10.1103/PhysRevC.81.045803` (cit. on pp. 90, 195).

[126] Akira Hitachi et al. “Effect of ionization density on the time dependence of luminescence from liquid argon and xenon”. In: *Phys. Rev. B* 27 (9 May 1983), pp. 5279–5285. DOI: `10.1103/PhysRevB.27.5279`. URL: `https://link.aps.org/doi/10.1103/PhysRevB.27.5279` (cit. on p. 90).

[127] J Lindhard, M Scharff, and H. E. Schiott. “Range concepts and heavy ion ranges”. In: *Mat. Fys. Medd. K. Dan. Vidensk. Selsk* 33.1 (1963), p. 1. URL: `https://catalog.hathitrust.org/Record/009643906` (cit. on pp. 91, 93, 95, 120, 196, 197, 199).

[128] DongMing Mei et al. “A model of nuclear recoil scintillation efficiency in noble liquids”. In: *Astropart. Phys.* 30.1 (2008), pp. 12–17. DOI: 10.1016/j.astropartphys.2008.06.001. URL: http://linkinghub.elsevier.com/retrieve/pii/S0927650508000765 (cit. on pp. 92, 93, 95, 197).

[129] D. Gastler et al. “Measurement of scintillation efficiency for nuclear recoils in liquid argon”. In: *Phys. Rev.* C85 (2012), p. 065811. DOI: 10.1103/PhysRevC.85.065811. arXiv: 1004.0373 [physics.ins-det] (cit. on pp. 93, 95, 196, 197).

[130] P. Agnes et al. “Simulation of argon response and light detection in the DarkSide-50 dual phase TPC”. In: *JINST* 12.10 (2017), P10015. DOI: 10.1088/1748-0221/12/10/P10015. arXiv: 1707.05630 [physics.ins-det] (cit. on pp. 95, 104, 111, 197).

[131] D.L. Smith, R.G. Polk, and T.G. Miller. “Measurement of the response of several organic scintillators to electrons, protons and deuterons”. In: *Nuclear Instruments and Methods* 64.2 (1968), pp. 157–166. ISSN: 0029-554X. DOI: https://doi.org/10.1016/0029-554X(68)90189-4. URL: http://www.sciencedirect.com/science/article/pii/0029554X68901894 (cit. on p. 93).

[132] J Thomas and D A Imel. “Recombination of electron-ion pairs in liquid argon and liquid xenon”. In: *Phys. Rev. A* 36.2 (1987), pp. 614–616. DOI: 10.1103/PhysRevA.36.614. URL: https://link.aps.org/doi/10.1103/PhysRevA.36.614 (cit. on pp. 97, 197).

[133] George Jaffé. “Zur Theorie der Ionisation in Kolonnen”. In: *Ann. Phys.* 347.12 (1913), pp. 303–344. DOI: 10.1002/andp.19133471205. URL: http://doi.wiley.com/10.1002/andp.19133471205 (cit. on p. 97).

[134] K Deiters et al. “Test of a liquid argon multistrip ionization chamber with 8.5 mum RMS resolution”. In: *Nucl. Instrum. Methods* 180.CERN-EP-80-109 (1981), pp. 45–52. DOI: 10.1016/0029-554X(81)90008-2. URL: https://cds.cern.ch/record/134850 (cit. on p. 97).

[135] L. S. Miller, S. Howe, and W. E. Spear. “Charge Transport in Solid and Liquid Ar, Kr, and Xe”. In: *Phys. Rev.* 166 (3 Feb. 1968), pp. 871–878. URL: https://link.aps.org/doi/10.1103/PhysRev.166.871 (cit. on p. 97).

[136] K. Yoshino, U. Sowada, and W. F. Schmidt. “Effect of molecular solutes on the electron drift velocity in liquid Ar, Kr, and Xe”. In: *Phys. Rev. A* 14 (1 July 1976), pp. 438–444. URL: https://link.aps.org/doi/10.1103/PhysRevA.14.438 (cit. on p. 97).

[137] T. H. Joshi et al. “First measurement of the ionization yield of nuclear recoils in liquid argon”. In: *Phys. Rev. Lett.* 112 (2014), p. 171303. DOI: 10.1103/PhysRevLett.112.171303. arXiv: 1402.2037 [physics.ins-det] (cit. on pp. 98, 121).

[138] L. Onsager. “Initial Recombination of Ions”. In: *Phys. Rev.* 54 (8 Oct. 1938), pp. 554–557. DOI: 10.1103/PhysRev.54.554. URL: https://link.aps.org/doi/10.1103/PhysRev.54.554 (cit. on p. 98).

[139] D. V. Hinkley. “On the Ratio of Two Correlated Normal Random Variables”. In: *Biometrika* 56.3 (1969), pp. 635–639. ISSN: 00063444. URL: `http://www.jstor.org/stable/2334671` (cit. on p. 104).

[140] P. Cushman et al. “Snowmass CF1 Summary: WIMP Dark Matter Direct Detection”. In: (2013). arXiv: `1310.8327`. URL: `http://arxiv.org/abs/1310.8327` (cit. on pp. 109, 198).

[141] E. Aprile et al. “Low-mass dark matter search using ionization signals in XENON100”. In: *Physical Review D* 94.9 (2016), pp. 8–13. ISSN: 24700029. DOI: `10.1103/PhysRevD.94.092001`. arXiv: `1605.06262` (cit. on pp. 109, 198).

[142] Michael J. Travers, Daniel C. Cowles, and G.Barney Ellison. “Reinvestigation of the electron affinities of O2 and NO”. In: *Chemical Physics Letters* 164.5 (1989), pp. 449–455. ISSN: 0009-2614. DOI: `https://doi.org/10.1016/0009-2614(89)85237-6`. URL: `http://www.sciencedirect.com/science/article/pii/0009261489852376` (cit. on p. 112).

[143] Russell G. Tonkyn, Jerry W. Winniczek, and Michael G. White. “Rotationally resolved photoionization of O2+ near threshold”. In: *Chemical Physics Letters* 164.2 (1989), pp. 137–142. ISSN: 0009-2614. DOI: `https://doi.org/10.1016/0009-2614(89)85005-5`. URL: `http://www.sciencedirect.com/science/article/pii/0009261489850055` (cit. on p. 112).

[144] T. Trickl et al. “State-selective ionization of nitrogen in the X2+gv+=0 and v+=1 states by two-color (1+1) photon excitation near threshold”. In: *The Journal of Chemical Physics* 91.10 (1989), pp. 6006–6012. DOI: `10.1063/1.457417`. eprint: `https://doi.org/10.1063/1.457417`. URL: `https://doi.org/10.1063/1.457417` (cit. on p. 112).

[145] E. Segreto. “Evidence of delayed light emission of TetraPhenyl Butadiene excited by liquid Argon scintillation light”. In: *Phys. Rev.* C91.3 (2015), p. 035503. DOI: `10.1103/PhysRevC.91.035503`. arXiv: `1411.4524 [physics.ins-det]` (cit. on p. 113).

[146] P. Agnes et al. “Measurement of the liquid argon energy response to nuclear and electronic recoils”. In: *Physical Review D* 97.11 (Jan. 2018), pp. 1–15. ISSN: 24700029. DOI: `10.1103/PhysRevD.97.112005`. arXiv: `1801.06653`. URL: `http://arxiv.org/abs/1801.06653%20http://dx.doi.org/10.1103/PhysRevD.97.112005` (cit. on pp. 115, 198).

[147] R.B. Firestone, C.M. Baglin, and S.Y.F. Chu. *Table of Isotopes: 1999 Update*. A Wiley-Interscience publication vol. 4. Wiley, 1999. ISBN: 9780471356332. URL: `https://books.google.fr/books?id=W4JUAAAAMAAJ` (cit. on pp. 115, 116, 130, 198).

[148] D. H. W. Kirkwood, B. Pontecorvo, and G. C. Hanna. “Fluctuations of Ionization and Low Energy Beta-Spectra”. In: *Phys. Rev.* 74 (4 Aug. 1948), pp. 497–498. DOI: `10.1103/PhysRev.74.497`. URL: `https://link.aps.org/doi/10.1103/PhysRev.74.497` (cit. on pp. 115, 198).

[149] B. Pontecorvo, D. H. W. Kirkwood, and G. C. Hanna. “Nuclear Capture of L_I Electrons”. In: *Phys. Rev.* 75 (6 Mar. 1949), pp. 982–982. DOI: `10.1103/PhysRev.75.982`. URL: `https://link.aps.org/doi/10.1103/PhysRev.75.982` (cit. on pp. 115, 198).

[150] V. I. Barsanov et al. “A technology and facility for extraction, purification, and collection of 37Ar from calcium oxide”. In: *Instruments and Experimental Techniques* 49.4 (July 2006), pp. 454–460. ISSN: 1608-3180. DOI: `10.1134/S0020441206040026`. URL: `https://doi.org/10.1134/S0020441206040026` (cit. on p. 115).

[151] Odiot, Simone and Daudel, Raymond. “Contribution à l’étude de la capture des électrons du cortège par les noyaux d’atomes : Effet des corrélations existant entre les positions des électrons sur le rapport la probabilité de capture l a celle de capture K”. In: *J. Phys. Radium* 17.1 (1956), pp. 60–62. DOI: `10.1051/jphysrad:0195600170106000`. URL: `https://doi.org/10.1051/jphysrad:0195600170106000` (cit. on p. 116).

[152] H. Brysk and M. E. Rose. “Theoretical Results on Orbital Capture”. In: *Rev. Mod. Phys.* 30 (4 Oct. 1958), pp. 1169–1177. DOI: `10.1103/RevModPhys.30.1169`. URL: `https://link.aps.org/doi/10.1103/RevModPhys.30.1169` (cit. on p. 116).

[153] A. G. Santos-Ocampo and D. C. Conway. “$\frac{L}{K}$-Capture Ratio and $\frac{E_L}{E_K}$ for Ar^{37}”. In: *Phys. Rev.* 120 (6 Dec. 1960), pp. 2196–2200. DOI: `10.1103/PhysRev.120.2196`. URL: `https://link.aps.org/doi/10.1103/PhysRev.120.2196` (cit. on p. 116).

[154] S. Sangiorgio et al. “First demonstration of a sub-keV electron recoil energy threshold in a liquid argon ionization chamber”. In: *Nucl. Instrum. Meth.* A728 (2013), pp. 69–72. DOI: `10.1016/j.nima.2013.06.061`. arXiv: `1301.4290 [astro-ph.IM]` (cit. on p. 116).

[155] Fedor Bezrukov et al. “Interplay between scintillation and ionization in liquid xenon Dark Matter searches”. In: *Astropart. Phys.* 35 (2011), pp. 119–127. DOI: `10.1016/j.astropartphys.2011.06.008`. arXiv: `1011.3990 [astro-ph.IM]` (cit. on pp. 120, 121, 199).

[156] James F. Ziegler and Jochen P. Biersack. “The Stopping and Range of Ions in Matter”. In: *Treatise on Heavy-Ion Science: Volume 6: Astrophysics, Chemistry, and Condensed Matter*. Ed. by D. Allan Bromley. Boston, MA: Springer US, 1985, pp. 93–129. ISBN: 978-1-4615-8103-1. DOI: `10.1007/978-1-4615-8103-1_3`. URL: `https://doi.org/10.1007/978-1-4615-8103-1_3` (cit. on pp. 120, 121, 199).

[157] A Agnes. “Direct Search for Dark Matter with the DarkSide Experiment”. PhD thesis. Université Paris Diderot, 2016 (cit. on p. 126).

[158] Stephen L. Adler. “Axial-Vector Vertex in Spinor Electrodynamics”. In: *Phys. Rev.* 177 (5 Jan. 1969), pp. 2426–2438. DOI: `10.1103/PhysRev.177.2426`. URL: `https://link.aps.org/doi/10.1103/PhysRev.177.2426` (cit. on p. 135).

[159] J. S. Bell and R. Jackiw. “A PCAC puzzle: $\pi^0 \to \gamma\gamma$ in the σ model”. In: *Nuovo Cim.* A60 (1969), pp. 47–61. DOI: `10.1007/BF02823296` (cit. on p. 135).

[160] J. M. Pendlebury et al. “Revised experimental upper limit on the electric dipole moment of the neutron”. In: *Phys. Rev.* D92.9 (2015), p. 092003. DOI: `10.1103/PhysRevD.92.092003`. arXiv: `1509.04411 [hep-ex]` (cit. on p. 135).

[161] Cumrun Vafa and Edward Witten. “Parity Conservation in Quantum Chromodynamics”. In: *Phys. Rev. Lett.* 53 (6 Aug. 1984), pp. 535–536. DOI: `10.1103/PhysRevLett.53.535`. URL: `https://link.aps.org/doi/10.1103/PhysRevLett.53.535` (cit. on p. 136).

[162] Jihn E. Kim. “Weak-Interaction Singlet and Strong CP Invariance”. In: *Phys. Rev. Lett.* 43 (2 July 1979), pp. 103–107. DOI: `10.1103/PhysRevLett.43.103`. URL: `https://link.aps.org/doi/10.1103/PhysRevLett.43.103` (cit. on p. 136).

[163] M.A. Shifman, A.I. Vainshtein, and V.I. Zakharov. “Can confinement ensure natural CP invariance of strong interactions?” In: *Nuclear Physics B* 166.3 (1980), pp. 493–506. ISSN: 0550-3213. DOI: `https://doi.org/10.1016/0550-3213(80)90209-6`. URL: `http://www.sciencedirect.com/science/article/pii/0550321380902096` (cit. on p. 136).

[164] Michael Dine, Willy Fischler, and Mark Srednicki. “A simple solution to the strong CP problem with a harmless axion”. In: *Physics Letters B* 104.3 (1981), pp. 199–202. ISSN: 0370-2693. DOI: `https://doi.org/10.1016/0370-2693(81)90590-6`. URL: `http://www.sciencedirect.com/science/article/pii/0370269381905906` (cit. on p. 136).

[165] A. R. Zhitnitsky. “On Possible Suppression of the Axion Hadron Interactions. (In Russian)”. In: *Sov. J. Nucl. Phys.* 31 (1980). [Yad. Fiz.31,497(1980)], p. 260 (cit. on p. 136).

[166] Javier Redondo. “Solar axion flux from the axion-electron coupling”. In: *Journal of Cosmology and Astroparticle Physics* 2013.12 (2013). ISSN: 14757516. DOI: `10.1088/1475-7516/2013/12/008`. arXiv: `arXiv:1310.0823v1` (cit. on p. 137).

[167] Masahiro Kawasaki, Ken’ichi Saikawa, and Toyokazu Sekiguchi. “Axion dark matter from topological defects”. In: *Phys. Rev. D* 91 (6 Mar. 2015), p. 065014. DOI: `10.1103/PhysRevD.91.065014`. URL: `https://link.aps.org/doi/10.1103/PhysRevD.91.065014` (cit. on p. 138).

[168] Olivier Wantz and E. P. S. Shellard. “Axion Cosmology Revisited”. In: *Phys. Rev.* D82 (2010), p. 123508. DOI: `10.1103/PhysRevD.82.123508`. arXiv: `0910.1066 [astro-ph.CO]` (cit. on pp. 138, 139).

[169] C. Hagmann, Sanghyeon Chang, and P. Sikivie. “Axion radiation from strings”. In: *Phys. Rev.* D63 (2001), p. 125018. DOI: `10.1103/PhysRevD.63.125018`. arXiv: `hep-ph/0012361 [hep-ph]` (cit. on p. 138).

[170] Edward W. Kolb and Michael S. Turner. “The Early Universe”. In: *Front. Phys.* 69 (1990), pp. 1–547 (cit. on p. 139).

[171] Kyu Jung Bae, Ji-Haeng Huh, and Jihn E. Kim. “Update of axion CDM energy”. In: *JCAP* 0809 (2008), p. 005. DOI: `10.1088/1475-7516/2008/09/005`. arXiv: `0806.0497 [hep-ph]` (cit. on p. 139).

[172] Guillermo Ballesteros et al. “Standard Model—axion—seesaw—Higgs portal inflation. Five problems of particle physics and cosmology solved in one stroke”. In: *Journal of Cosmology and Astroparticle Physics* 2017.08 (Aug. 2017), pp. 001–001. DOI: `10.1088/1475-7516/2017/08/001`. URL: `https://doi.org/10.1088%2F1475-7516%2F2017%2F08%2F001` (cit. on pp. 139, 140).

[173] Maxim Pospelov, Adam Ritz, and Mikhail B. Voloshin. “Bosonic super-WIMPs as keV-scale dark matter”. In: *Phys. Rev.* D78 (2008), p. 115012. DOI: `10.1103/PhysRevD.78.115012`. arXiv: `0807.3279 [hep-ph]` (cit. on p. 139).

[174] Adrian Ayala et al. “Revisiting the bound on axion-photon coupling from Globular Clusters”. In: *Phys. Rev. Lett.* 113.19 (2014), p. 191302. DOI: `10.1103/PhysRevLett.113.191302`. arXiv: `1406.6053 [astro-ph.SR]` (cit. on p. 140).

[175] Georg G. Raffelt. “Astrophysical axion bounds”. In: *Lect. Notes Phys.* 741 (2008). [,51(2006)], pp. 51–71. DOI: `10.1007/978-3-540-73518-2_3`. arXiv: `hep-ph/0611350 [hep-ph]` (cit. on p. 140).

[176] Tobias Fischer et al. “Probing axions with the neutrino signal from the next galactic supernova”. In: *Phys. Rev.* D94.8 (2016), p. 085012. DOI: `10.1103/PhysRevD.94.085012`. arXiv: `1605.08780 [astro-ph.HE]` (cit. on p. 140).

[177] Maurizio Giannotti et al. “Stellar Recipes for Axion Hunters”. In: *JCAP* 1710.10 (2017), p. 010. DOI: `10.1088/1475-7516/2017/10/010`. arXiv: `1708.02111 [hep-ph]` (cit. on p. 140).

[178] Michael S. Turner. “Thermal Production of Not SO Invisible Axions in the Early Universe”. In: *Phys. Rev. Lett.* 59 (1987). [Erratum: Phys. Rev. Lett.60,1101(1988)], p. 2489. DOI: `10.1103/PhysRevLett.59.2489,10.1103/PhysRevLett.60.1101.3` (cit. on p. 140).

[179] John Preskill, Mark B. Wise, and Frank Wilczek. “Cosmology of the Invisible Axion”. In: *Phys. Lett.* B120 (1983). [,URL(1982)], pp. 127–132. DOI: `10.1016/0370-2693(83)90637-8` (cit. on p. 140).

[180] Davide Cadamuro and Javier Redondo. “Cosmological bounds on pseudo Nambu-Goldstone bosons”. In: *JCAP* 1202 (2012), p. 032. DOI: `10.1088/1475-7516/2012/02/032`. arXiv: `1110.2895 [hep-ph]` (cit. on p. 140).

[181] P. Sikivie. “Experimental tests of the ’invisible’ axion”. In: *Physical Review Letters* 51 (Oct. 1983), pp. 1415–1417. DOI: `10.1103/PhysRevLett.51.1415` (cit. on pp. 140, 141).

[182] V. Anastassopoulos et al. “New CAST Limit on the Axion-Photon Interaction”. In: *Nature Phys.* 13 (2017), pp. 584–590. DOI: `10.1038/nphys4109`. arXiv: `1705.02290 [hep-ex]` (cit. on p. 140).

[183] N. Du et al. “A Search for Invisible Axion Dark Matter with the Axion Dark Matter Experiment”. In: *Phys. Rev. Lett.* 120.15 (2018), p. 151301. DOI: `10.1103/PhysRevLett.120.151301`. arXiv: `1804.05750 [hep-ex]` (cit. on p. 141).

[184] B. M. Brubaker et al. “HAYSTAC axion search analysis procedure”. In: *Phys. Rev.* D96.12 (2017), p. 123008. DOI: `10.1103/PhysRevD.96.123008`. arXiv: `1706.08388 [astro-ph.IM]` (cit. on p. 141).

[185] Ben T. McAllister et al. “The ORGAN Experiment: An axion haloscope above 15 GHz”. In: *Phys. Dark Univ.* 18 (2017), pp. 67–72. DOI: `10.1016/j.dark.2017.09.010`. arXiv: `1706.00209 [physics.ins-det]` (cit. on p. 141).

[186] Y. Semertzidis et al. “Limits on the Production of Light Scalar and Pseudoscalar Particles”. In: *Phys. Rev. Lett.* 64 (1990), pp. 2988–2991. DOI: `10.1103/PhysRevLett.64.2988` (cit. on p. 141).

[187] E. Zavattini et al. “Experimental observation of optical rotation generated in vacuum by a magnetic field”. In: *Phys. Rev. Lett.* 96 (2006). [Erratum: Phys. Rev. Lett.99,129901(2007)], p. 110406. DOI: `10.1103/PhysRevLett.99.129901,10.1103/PhysRevLett.96.110406`. arXiv: `hep-ex/0507107 [hep-ex]` (cit. on p. 141).

[188] Pierre Pugnat et al. “First results from the OSQAR photon regeneration experiment: No light shining through a wall”. In: *Phys. Rev.* D78 (2008), p. 092003. DOI: `10.1103/PhysRevD.78.092003`. arXiv: `0712.3362 [hep-ex]` (cit. on p. 141).

[189] R. Ballou et al. “New exclusion limits on scalar and pseudoscalar axionlike particles from light shining through a wall”. In: *Phys. Rev. D* 92 (9 Nov. 2015), p. 092002. DOI: `10.1103/PhysRevD.92.092002`. URL: `https://link.aps.org/doi/10.1103/PhysRevD.92.092002` (cit. on p. 141).

[190] P. Sikivie, D. B. Tanner, and Karl van Bibber. “Resonantly enhanced axion-photon regeneration”. In: *Phys. Rev. Lett.* 98 (2007), p. 172002. DOI: `10.1103/PhysRevLett.98.172002`. arXiv: `hep-ph/0701198 [HEP-PH]` (cit. on p. 142).

[191] Mougeot, X., Bé, M.-M., and Bisch, C. “Calculation of beta spectral shapes”. In: *Radioprotection* 49.4 (2014), pp. 269–273. DOI: `10.1051/radiopro/2014017`. URL: `https://doi.org/10.1051/radiopro/2014017` (cit. on p. 144).

[192] E. Fermi. “An attempt of a theory of beta radiation. 1.” In: *Z. Phys.* 88 (1934), pp. 161–177. DOI: `10.1007/BF01351864` (cit. on p. 144).

[193] R. H. Good. “Effect of Atomic Electron Screening on the Shape of Forbidden Beta Spectra”. In: *Physical Review* 94.4 (May 1954), pp. 931–933. DOI: `10.1103/PhysRev.94.931`. URL: `https://link.aps.org/doi/10.1103/PhysRev.94.931` (cit. on p. 145).

[194] Leendert Hayen et al. “High precision analytical description of the allowed β spectrum shape”. In: *Reviews of Modern Physics* 90.1 (2018). ISSN: 15390756. DOI: `10.1103/RevModPhys.90.015008`. arXiv: `arXiv:1709.07530v2` (cit. on p. 145).

[195] Mougeot Xavier. “BetaShape : A new code for improved analytical”. In: 12015 (2017). DOI: `10.1051/epjconf/201714612015` (cit. on p. 145).

[196] D. S. Akerib et al. “First Searches for Axions and Axionlike Particles with the LUX Experiment”. In: *Physical Review Letters* 118.26 (2017), pp. 1–7. ISSN: 10797114. DOI: `10.1103/PhysRevLett.118.261301`. arXiv: `1704.02297` (cit. on p. 148).

[197] E. Aprile et al. “First axion results from the XENON100 experiment”. In: *Physical Review D - Particles, Fields, Gravitation and Cosmology* 90.6 (2014), pp. 1–7. ISSN: 15502368. DOI: `10.1103/PhysRevD.90.062009`. arXiv: `1404.1455` (cit. on p. 148).

[198] NIST. *XCOM: Photon Cross Sections Database*. 2010. URL: `https://physics.nist.gov/PhysRefData/Xcom/html/xcom1.html` (cit. on p. 148).

Résumé de la thèse

1 Introduction

Tout ce que nous pouvons voir lorsque nous regardons l'Univers avec nos yeux, nos télescopes et nos détecteurs représente à peine 5% de son contenu énergétique total. Le reste est divisé entre énergie noire ($\sim$ 70%) et matière noire ($\sim$ 25%). Cela seul est une raison suffisante pour consacrer nos efforts à l'étude de "l'univers sombre". Mais il y a plus. L'énergie noire est la raison qui explique l'accélération de l'expansion de l'univers. La découverte de ses propriétés nous donnerait des informations sur l'évolution future du cosmos. Quant à la matière noire, selon les modèles de l'univers primitif, elle a joué un rôle clé dans la formation des structures (galaxies, amas de galaxies, etc.). L'étude de la matière noire éclairera l'histoire de notre univers. Cette thèse porte sur la chasse aux particules de matière noire.

Nous ignorons la nature même de la matière noire. Cependant, les sondes astrophysiques ont fourni des contraintes sur ses propriétés. Nous savons que la matière noire est stable, non relativiste et a un très faible couplage avec la matière du Modèle Standard. Nous avons également des informations sur sa distribution dans l'univers. Mais d'autres paramètres, comme sa masse, ne sont presque pas contraints. Cela laisse enormément de possibilités d'expériences de detection. De nombreux moyens ont été explorés pour enfin "voir" la matière noire.

Le halo de matière noire englobant la Voie lactée, associé au mouvement de la Terre dans ce halo, permet une interaction DM-nucléon détectable avec des appareils basés sur la Terre. C'est la stratégie de détection directe. En raison de la très faible quantité d'énergie déposée par la matière noire, des détecteurs à seuil très bas, de grandes masses actives et une forte suppression du bruit de fond sont nécessaires.

Les liquides nobles sont d'excellents matériaux pour la recherche directe de matière noire, en raison de leurs rendements élevés en ionisation et en scintillation et de la facilité à les obtenir en grande quantité. Les chambres à projection de temporelle (TPCs) utilisant des liquides nobles sont la technologie de pointe dans le domaine de la détection de matière noire de haute masse. Ces détecteurs reposent sur la détection des signaux scintillation et d'ionisation produits lors de la diffusion d'une particule de matière noire sur un noyau cible (recul nucléaire). L'argon liquide (LAr), en particulier, offre une méthode de réjection des bruits de fond impressionnante contre les reculs électroniques (diffusion de la matière par des électrons des noyaux cibles) basée sur l'étude de la distribution temporelle du signal.

La collaboration DarkSide a mis au point un programme par étapes de recherche directe de la matière noire à l'aide de TPC LAr. L'étape actuelle du programme, DarkSide-50, a commencé en octobre 2013 au Laboratori Nazionali del Gran Sasso (LNGS, en Italie) et a produit ses derniers résultats de physique en 2018 [1, 2]. C'est le premier détecteur à utiliser de l'argon extrait de sources souterraines, ce qui réduit considérablement sa radioactivité interne.

De nombreux candidats à la matière noire ont été proposés. Pendant longtemps, l'hypothèse de départ a été l'hypothèse WIMP (Weakly Interacting Massive Particle). Les WIMPs sont des particules massives (GeV - TeV), qui interagissent via la force nucléaire faible. Cependant, même s'il reste fortement motivé, l'absence de detection de WIMPs pousse vers d'autres possibilités intéressantes. En particulier, les particules moins massives comme les axions apparaissent comme une éventualité de plus en plus prometteuse.

Au cours de ma thèse, j'ai été impliquée dans la caractérisation de la réponse de l'argon liquide aux reculs nucléaires et électroniques dans l'expérience ARIS. Puis je me suis intéressée à la recherche de WIMPs de faible masse avec les données de DarkSide. La dernière partie de ma thèse porte sur la recherche d'axions.

2 La matière noire : ce qu'on en sait

2.1 Pourquoi la matière noire ?

Il y a un faisceau d'observations astrophysiques, à plusieurs échelles, qui pointent toutes dans la direction de l'existence d'un type de matière "invisible".

Rotation des galaxies La preuve la plus connue de l'existence de matière noire a été révélée dans les années 1960 et 1970 dans les travaux de Vera Rubin [8]. Ils ont étudié le mouvement des étoiles dans les galaxies spirales. Ces galaxies consistent généralement en un bulbe central entouré d'un disque. Les progrès des technologies de télescopes ont rendu possible la mesure de la vitesse du disque galactique en fonction du rayon.

Comme les étoiles dans les galaxies se déplacent sans entrer en contact, leur mouvement est entièrement dicté par les lois de la gravitation. Cela permet de prédire la vitesse de rotation en fonction de leur orbite. La vitesse attendue, v_c, pour un objet en orbite à une distance r du centre de la galaxie est,

$$v_c(r) = \sqrt{\frac{GM(r)}{r}} \tag{14}$$

où G est la constante de gravitation et $M(r)$ est la masse totale incluse dans une sphère de rayon r. Pour les très grands rayons loin du bulbe central ($r \gg R_{bulbe}$), la masse incluse est approximativement constante par rapport au rayon r. Nous nous attendons donc à ce que la vitesse décroisse à mesure que que r augmente, $v(r) \propto r^{-1/2}$, selon l'équation 14. Vera Rubin

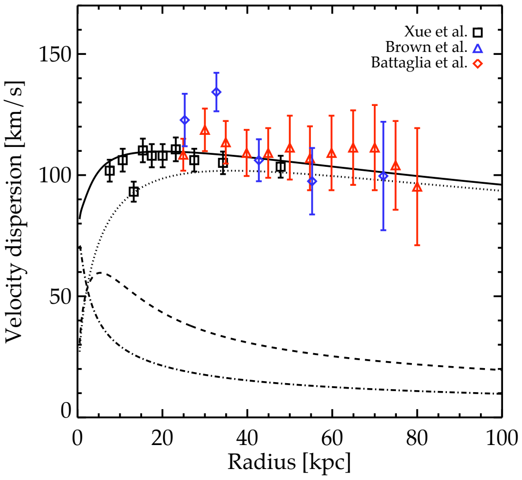

Figure 13 – Dispersion des vitesse des étoiles dans la Voie lactée en fonction de la distance du centre galactique [4]. Mesures extraites de [5, 6, 7]. Les contributions du bulbe (en pointillé), du disque (en pointillé) et du halo de matière noire (points) sont représentées. La dispersion de vitesse du halo de matière noire est supposée isotrope.

a mesuré les courbes de rotation de différentes galaxies. Mais les courbes de rotation observées tendent vers une vitesse constante non nulle pour les grands rayons au lieu de diminuer. Cette étude a été répétée dans la Voie lactée, donnant des résultats similaires [9] (voir Figure 13).

L'explication évidente d'un tel comportement est l'ajout d'une "masse invisible" sous la forme d'un halo de matière sphérique entourant les galaxies, augmentant ainsi le potentiel de gravitation. L'étude des courbes de rotation suggère qu'une densité de matière noire répartie au format $\rho(r) \propto r^{-2}$ permet de récupérer les courbes correctes. Cela correspond à un halo de matière noire avec une distribution sphérique symétrique autour du centre galactique.

Amas de galaxies Le premier indice suggérant l'existence de la matière noire a été donné par Fritz Zwicky dans les années 1930 [10, 11]. Il a observé la dispersion de vitesse des galaxies dans l'amas de Coma, contenant plus de 1 000 galaxies, et a calculé sa masse en utilisant deux méthodes différentes. La première était basée sur le théorème du viriel, à partir de la mesure des vitesses des galaxies à la périphérie de l'amas. Puisqu'il doit y avoir suffisamment de masse dans l'amas pour lier les galaxies externes, nous pouvons en déduire la masse qui doit être présente. La seconde méthode s'appuyait sur la luminosité des objets, estimant la masse à partir d'un comptage des objets visibles. La méthode du viriel conduit à une estimation de masse beaucoup plus élevée que la méthode de la luminosité. Pour expliquer ce phénomène, Zwicky a proposé l'existence d'une "matière noire", une matière qui ne pouvait pas être vue (échappant ainsi au compte de luminosité), mais dont l'influence gravitationnelle maintenait la cohésion des galaxies. Son article a rendit le terme célèbre.

Lentille gravitationelle La lentille gravitationnelle fournit un moyen supplémentaire d'estimer la masse d'un objet astrophysique. Selon la relativité générale, la lumière qui passe à proximité d'un objet massif est courbée, en raison de la perturbation spatio-temporelle causée par l'objet. La quantité de distorsion dépend de la masse de l'objet. Ainsi, la lumière émise par des objets lointains peut être perturbée par cet effet, qui faussera l'image que nous observons. Il peut en résulter plusieurs images observées (lentille forte) ou une image déformée (lentille faible) [13]. L'étude de la déformation permet de reconstruire la masse de l'objet qui l'induit. Dans de nombreux cas, la masse reconstruite est supérieure à la masse lumineuse, suggérant la présence de matière noire.

Les lentilles gravitationnelles permettent également de poser des limites supérieures à l'auto-interaction de la matière noire, grâce à des simulations hydrodynamiques détaillées et à des modèles théoriques [14].

Paramètres cosmologiques Le modèle standard de la cosmologie décrit remarquablement bien la formation des structures à grande échelle de l'univers. À petite échelle, la matière est distribuée de manière très irrégulière et s'accumule dans les galaxies, ou amas de galaxies, laissant de grandes zones de sous-densités. Si nous considérons l'Univers à ses plus grandes échelles, nous observons que la matière a tendance à être distribuée de manière homogène et isotrope. Le modèle standard actuel, le modèle Lambda Cold Dark Matter (Λ-CDM) stipule que la densité énergétique totale de l'univers, ρ_T est divisée en trois composantes [16]:

$$\rho_T = \rho_m + \rho_r + \rho_\Lambda \tag{15}$$

où ρ_m est la densité de matière, ρ_r est la densité de rayonnement et ρ_Λ représente la densité d'énergie sombre.

La densité de matière peut être vue comme la somme des contributions baryoniques et non-baryoniques: $\rho_m = \rho_b + \rho_{nb}$. La densité de rayonnement ρ_m inclut tous les composants relativistes (photons, neutrinos, etc.). La densité d'énergie sombre, ρ_Λ a été introduite pour expliquer l'accélération de l'expansion de l'Univers [17, 18].

Ces quantités sont généralement normalisées à l'aide du paramètre de densité totale $\Omega = \sum \Omega_i$, où $\Omega_i = \rho_i/\rho_c$, $i = m, r, \Lambda$. ρ_c est la densité dite critique, la densité requise pour un univers plat, homogène et isotrope.

Le modèle Λ-CDM a six paramètres libres, qui peuvent être contraints par plusieurs sondes astrophyiques, comme le fond diffus cosmologique [20, 19], les oscillations acoustiques de baryons [23, 24], les supernovae [27] ou la nucléosynthèse primordiale [29].

Le tableau ci-dessus résume les differentes valeurs des paramètres cosmologiques.

2.2 Candidats à la matière noire

Particules massives interagissant faiblement : les WIMPs Parmi tous les candidats à la matière noire, le WIMP (Weakly Interacting Massive Particle) est le plus étudié en ce moment. Les WIMPs sont des particules élémentaires hypothétiques, n'interagissant que par gravité et force

Component	Symbol	Measured density
Photons	Ω_r	$\sim 5.46 \times 10^{-5}$
Dark Energy	Ω_Λ	0.6911 ± 0.0062
Matter	Ω_m	0.3089 ± 0.0062
Baryonic matter	Ω_b	0.0486 ± 0.00072
Non-baryonic matter	Ω_c	0.2589 ± 0.0041

Table 3 – Mesures des paramètres cosmologiques, obtenues à partir des mesures du CMB du satellite PLANCK [22], combinées avec les BAOs et les supernovae. Ces résultats sont obtenus en supposant le modèle Λ-CDM avec six paramètres libres et un univers plat.

nucléaire faible. L'interaction faible les rend détectables par le biais de méthodes non gravitationnelles. L'introduction d'une nouvelle particule de masse à l'échelle faible ($m_{Weak} \sim 10$ GeV - 1 TeV) justifierait que la masse du boson de Higgs soit inférieure à la masse de Planck [36] (résolvant ainsi le problème dit de la hiérarchie), ce qui lui donne une autre motivation.

Des particules ayant les caractéristiques d'un WIMP apparaissent naturellement dans plusieurs théories autres que celles du Modèle Standard (BSM), telles que la supersymétrie (SUSY) [37] ou les modèles à extra-dimensions [39].

L'intérêt de la communauté scientifique pour les WIMP vient en partie de ce qu'on appelle parfois le "miracle des WIMPs". Si l'on calcule la densité relique de matière noire dans l'Univers, on se rend compte que la valeur obtenue est extrêmement proche de la section efficace typique de l'interaction faible. Donc, une population relique de particules de matière noire en interaction faible, avec des masses dans la gamme GeV - TeV aurait naturellement la bonne densité actuelle, fournissant une forte motivation pour de la matière noire composée de WIMPs.

Axions Alors que l'espace de paramètres pour les recherches WIMP commence à être de plus en plus exclu, la recherche de matière noire se tourne vers des candidats alternatifs. Un intéressant est l'axion.

Une des principales faiblesses du modèle standard est l'absence de mécanisme permettant d'expliquer le manque de violation de la parité charge (CP) dans les interactions fortes. Une solution, introduite par Peccei et Quinn [3], postule une symétrie supplémentaire brisée à une grande échelle d'énergie f_a. Cela se traduit par une nouvelle particule, appelée l'axion. Les résultats expérimentaux ont écarté cet axion original, mais les axions résultant d'une brisure de symétrie à une échelle beaucoup plus grande, les axions "invisibles" sont toujours autorisés [40]. En plus de ces axions, les particules de type axion (ALPs) sont des pseudo-scalaires qui ne résolvent pas nécessairement le problème de la violation de CP, mais qui ont été introduits par de nombreux modèles de BSM basés sur la théorie des cordes [41, 42, 43].

Les axions et les ALPs sont des candidats intéressants pour la matière noire. Ils peuvent avoir été produits comme des reliques [44], et même s'ils sont très légers, ils devraient être produits essentiellement au repos, satisfaisant ainsi aux critères de la matière sombre et froide.

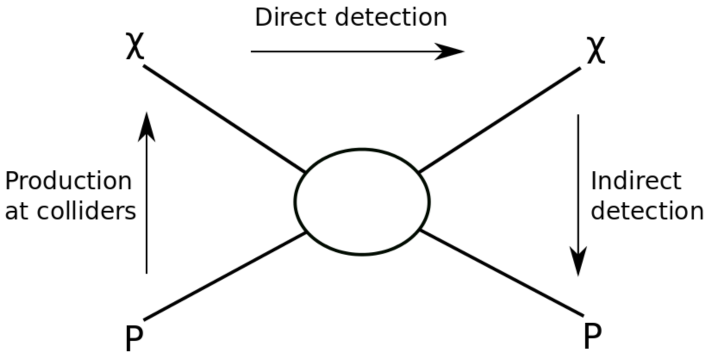

Figure 14 – Schéma décrivant les différentes startegies de recherche de WIMPs

2.3 À la recherche des WIMPs

La figure 14 illustre les différents types d'interactions entre matière noire et matière ordinaire. Toutes ces méthodes donnent accès à différentes informations et explorent différents espaces de paramètres. Elles sont donc complémentaires pour assurer la détection et l'identification des particules de matière noire.

Indirect detection En lisant la figure 14 de haut en bas, on obtient le processus d'annihilation des particules de matière noire, ce qui conduit à la détection indirecte. La détection indirecte utilise des observations astronomiques pour détecter les produits d'annihilation de la matière noire. Il y a en fait deux processus à considérer:

- l'annihilation de paires de particules de matière noire: $\chi + \chi \longrightarrow SM$
- la désintégration de particules de matière noire en particules du Modèle Standard: $\chi \longrightarrow SM$

Les recherches portent généralement sur trois canaux : les photons (γ et X), les neutrinos et l'anti-matière [45]. Les télescopes recherchent un excès de ces particules provenant d'une région dans laquelle une forte densité de matière noire est attendue, comme le centre de la Voie lactée ou le centre du Soleil.

Recherche dans les collisionneurs Les collisionneurs de particules tels que le LHC au CERN sont également des outils très utiles pour rechercher la matière noire [58]. SUSY et extra-dimension peuvent être testés au LHC. À ce jour, aucun signe de ces théories n'a été trouvé dans le LHC. Voir [40] pour des commentaires sur SUSY et les recherches d'extra-dimensions au LHC.

De la matière noire peut également être produite lors de collisions de particules de haute énergie résultant d'une collision proton-proton via la fusion de deux quarks. Les particules de DM risquent de traverser le détecteur sans laisser de traces, menant à de l'énergie manquante dans le signal detecté. Les bruits de fond étant généralement plus petits lorsque l'énergie manquante est importante, la recherche de collisionneur a tendance à être plus efficace pour les particules de matière noire de faible masse, qui sont plus facilement produites avec une quantité de mouvement élevée.

Recherche directe de WIMPs Puisque la matière noire est supposée être répartie dans un halo sphérique autour des galaxies, le mouvement de la Terre dans ce halo provoquera un ”vent” de WIMPs. Un tel flux serait détectable en mesurant le spectre d'énergie des reculs nucléaires provoqué par la diffusion élastique des WIMPs sur des noyaux cibles. Cette stratégie a été proposée en 1985 par M.W. Goodman et E. Witten [61]. L'énergie typique des reculs est $\sim$ 100 keV. Cela nécessite des détecteurs de seuil à très bas énergie et de grandes masses cibles.

3 L'expérience DarkSide

L'expérience DarkSide exploite la technologie de la chambre de projection temporelle (TPC) à double phases (liquide-gaz) avec une cible à argon liquide (LAr). La conception du détecteur a été orientée vers une recherche de WIMPs sans bruit de fond. Pour atteindre cet objectif, une sélection stricte des matériaux et une suppression efficace des sources de bruit de fond sont nécessaires.

Les liquides nobles sont d'excellentes cibles pour la détection directe de WIMPs de haute masse : ils sont relativement peu coûteux, naturellement stables, intrinsèquement plus purs que d'autres matériaux et peuvent être utilisés dans des détecteurs de plusieurs tonnes. Ils sont également denses et faciles à purifier chimiquement, ont des rendements élevés en ionisation et en scintillation, sont transparents à leur lumière de scintillation et ont une grande mobilité électronique. Argon et xénon sont les liquides nobles les plus utilisés en recherche de matière noire.

3.0.1 Scintillation dans les liquides nobles

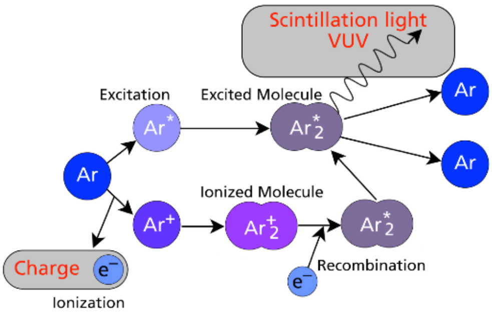

Figure 15 – Processus de scintillation de l'argon.

Le processus de scintillation est ici expliqué pour l'argon, mais est similiaire dans les autres liquides nobles. Lorsqu'une particule énergétique interagit dans un volume de LAr, son énergie est transférée aux atomes et molécules du milieu sous forme d'excitation ou d'ionisation. La particule peut subir une diffusion élastique par un électron tournant autour d'un noyau d'argon (recul électronique ou ER) ou par le noyau lui-même (recul nucléaire ou NR), produisant un électron libre ou un noyau reculant à travers l'argon liquide. Lorsque la particule chargée se déplace à travers l'argon, elle perd continuellement de l'énergie, soit par ionisation ou par excitation. Cela crée une trace d'atomes excités et ionisés. Les electrons libérés par l'ionisation peuvent se recombiner avec l'argon ionisé pour former de l'argon excité. L'argon excité revient ensuite à son état fondamental en émettant des photons UV.

3.0.2 Chambre à projection temporelle double phase à argon liquide

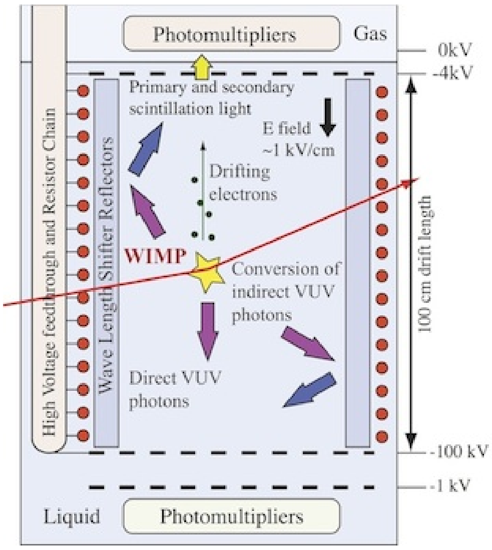

Figure 16 – Principe de fonctionnement d'une TPC double phase.

La chambre à projection temporelle est la principale technologie exploitant les liquides nobles pour la recherche directe de matière noire. En règle générale, un TPC double phase contient une couche mince ($\sim$ 1 cm) de gaz noble au-dessus d'un plus grand volume de gaz noble liquéfié. Le volume de liquide est immergé dans un champ électrique uniforme appliqué pour diriger les électrons qui survivent à la recombinaison vers la couche de gaz. Du liquide, ils sont extraits dans le gaz grâce au champ électrique d'extraction. Dans le gaz, un champ électrique plus intense provoque l'excitation (mais non l'ionisation) des atomes d'argon. La production de lumière dans le gaz est similaire à celle dans le liquide: les dimères d'argon se désexcitent et produisent de la lumière selon une exponentielle à deux composants (avec des temps de désintégration de 11 ns et 3.2 µs). Ce processus est illustré à la figure 16. Un ou plusieurs réseaux de photodétecteurs (généralement des photomultiplicateurs) visualisent le volume actif enregistrant à la fois le signal de scintillation primaire, appelé couramment S1, et le signal d'électroluminescence, appelé communément S2.

3.0.3 Bruit de fond dans une TPC à liquide noble

Les bruits de fond possibles incluent:

- ERs induit par la radioactivité interne et externe;
- NRs induits par les neutrons radiogéniques et cosmogéniques;
- particules α émises par les surfaces du détecteur;

Reculs electroniques Les reculs électroniques peuvent être classés selon leur origine : les reculs externes, provenant des matériaux du détecteur, et les reculs internes, induits par la contamination de l'argon en ^{39}Ar.

L'^{39}Ar est produit par intéractions des rayons cosmiques avec l'argon atmosphérique. L'argon souterrain, extrait de puits profonds, est protégé des rayons cosmiques. En conséquence, sa contamination ^{39}Ar est fortement réduite. C'est pourquoi DarkSide a choisi d'utiliser de l'argon souterrain pour ses campagnes de recherche de WIMPs.

La majeure partie du bruit de fond dû au rayonnement γ provient de la désintégration dans les chaînes d'uranium et de thorium naturels, ainsi que de la désintégration d'isotopes courants tels que ^{40}K, ^{60}Co et ^{137}Cs présents dans les matériaux entourant le détecteur. Plusieurs désintégrations αet γ dans les chaînes d'uranium et de thorium sont suivies de l'émission de plusieurs rayons γ d'une énergie allant de quelques dizaines de keV à quelques MeV. Lorsqu'ils interagissent avec l'argon, ces γ déposent de l'énergie dans la région d'énergie attendue pour les WIMPs.

	Xenon	Argon
τ_1	4 ns	7 ns
τ_2	22 ns	1.6μs

Table 4 – Decay time constant for singlet and triplet states in xenon and argon

Un atome d'élément noble peut être excité sur deux états différents, le singulet $^1\Sigma_u^+$ et le triplet $^3\Sigma_u^+$. La différence d'énergie entre les deux états est faible, de sorte qu'ils ne peuvent pas être distingués par spectroscopie, mais les constantes de temps de décroissance τ_1 et τ_2 des deux états sont différentes, comme résumé dans le tableau 4 (l'indice 1 signifie le singulet et 2 le triplet). Alors que dans le xénon liquide, les deux constantes de désintégration sont similaires, elles diffèrent par un facteur plus de 200 dans l'argon liquide [104]. La fraction de singulets typique pour les reculs d'électrons est d'environ 0.3 et environ 0.7 pour les reculs nucléaires dans l'argon liquide.

Cela implique que les distributions temporelles des signaux de scintillation induits par des reculs électroniques et nucleraires seront différentes. Il est donc possible de séparer les reculs electroniques et nucléaires en étudiant le signal de scintillation. L'expérience SCENE [107] a montré que la séparation maximale est obtenue en définissant le paramètre f_{90}. f_{90} est la fraction du signal S1 reçue dnas les 90 premières nanosecondes. Ce paramètre permet d'estimer la fraction prompte du signal $S(t)$:

$$\mathrm{f}_{90} = \frac{\int_0^{90ns} S(t)dt}{\int_0^{7\mu s} S(t)dt} \tag{16}$$

où la limite supérieure de 7 µs est choisie pour permettre à la partie tardive du signal de se désintégrer complètement. Avec le paramètre f_{90}, il est possible d'effectuer une discrimination entre le recul nucléaire et le recul électronique jusqu'à un facteur 10^8 dans l'argon liquide. Cette technique qu'on appelle Pulse Shape Discrimination (PSD) est un outil unique de l'argon liquide pour la discrimination du bruit de fond des reculs électroniques.

3.1 Les différents détecteurs de DarkSide-50

DarkSide-50, le détecteur actuellement en opération du programme DarkSide, consiste en trois détecteurs imbriqués. Le plus interne est la TPC, englobé dans deux enveloppes véto qui agissent comme un barrage contre les neutrons tout en permettant de les identifier. Ces détecteurs sont installés dans le hall C de la LNGS, sous ∼3400 m.w.e. de pierre. Ils sont décrits ici de l'intérieur vers l'extérieur.

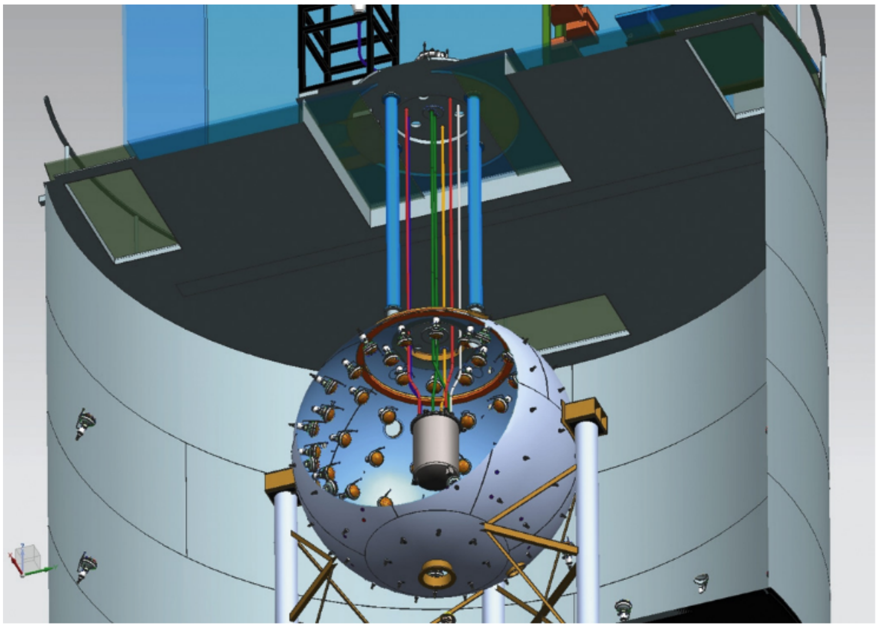

Figure 17 – Les détecteurs imbriqués de DarkSide-50.

La TPC La TPC est logée dans un cryostat en acier inoxydable cylindrique isolé par du vide pour maintenir l'argon à l'état liquide. Elle est constituée d'un cylindre réflecteur monolithique en PTFE (téflon) d'une épaisseur de 2.54 cm, mesurant 36 cm de diamètre et de hauteur. Le volume actif de (46.4±0.7) kg d'argon liquide est observé par 38 PMTs Hamamatsu R11065, disposés en deux réseaux hexagonaux (19 en haut et 19 en bas). Les surfaces supérieure et inférieure du volume sensible sont des fenêtres en silice fondue, d'une épaisseur de 6 mm et de 12 mm respectivement. L'oxyde d'indium et d'étain (ITO) est évaporé des deux côtés des fenêtres, ce qui en fait des électrodes à haute tension. Les faces internes des fenêtres en silice fondue sont alors l'anode (en haut) et la cathode (en bas) de la cage de champ electrique de la TPC. Une grille en acier inoxydable de 50 µm d'épaisseur avec un maillage hexagonal se trouve à environ 5 mm sous la surface du liquide. Une haute tension négative est appliquée entre la grille et la cathode pour produire le champ électrique vertical qui dérive les électrons d'ionisation vers le haut. Une tension est également appliquée entre l'anode et la grille pour extraire les électrons de dérive du liquide et produire le signal d'électroluminescence dans la poche de gaz. Les champs nominaux sont: 200 V/cm pour le champ de dérive, 2.8 kV/cm pour le champ d'extraction et 4.2 kV/cm pour le champ d'électroluminescence. À 200 V/cm, la vitesse de dérive des électrons est de 0.93 ±0.01 mm·µ^{-1} Puisque l'argon émet une lumière de scintillation à 128 nm environ, la surface interne des parois de la TPC sont recouvertes de tétraphényl butadiène (TPB), qui permet de décaler la longueur d'onde vers une valeur visible par les PMTs (420 nm).

En dehors de la paroi cylindrique en PTFE, 15 anneaux en cuivre en forme de T à potentiels gradués maintiennent l'uniformité du champ de électrique de dérive dans tout le volume actif.

Le Liquid Scintillator Veto (LSV) Le LSV est la première enveloppe veto de DarkSide, qui englobe complètement le cryostat de la TPC. C'est une sphère en acier inoxydable de 4 m de diamètre remplie de 30 tonnes de scintillateur liquide au bore, assurant une grande section effcicace de capture des neutrons. La couverture de 4π permet au LSV de détecter des rayons γ et des neutrons qui se dispersent dans la TPC et dans le LSV et produisent des signaux coïncidents, permettant un veto et une mesure *in situ* des neutrons dans DarkSide-50 .

Le Water Cerenkov Detector (WCD) Le WCD est un réservoir cylindrique en acier inoxydable de 11 m de diamètre et de 10 m de haut, rempli de 1000 tonnes d'eau ultra-pure. Il remplit deux fonctions: il constitue un bouclier passif contre les rayons et les neutrons γ externes, et il est un détecteur actif pour les muons traversant la TPC ou passant suffisamment près pour produire des neutrons qui interagiront dans le volume actif. Il est conçu pour détecter la lumière produite par Cerenkov par les muons ou d'autres particules relativistes traversant l'eau. Le WCD permet de marquer les neutrons induits par ces processus et de les rejeter. Le flux de muons à 3400 m.w.e. (la profondeur du LNGS), bien que réduit par rapport à celui à la surface de la Terre d'un facteur $\sim 10^6$, est de l'ordre de 1.1 muons/m^2/h [110]. Cela correspond à environ 2 000 muons par jour traversant la WCD, environ 380 muons par jour à travers le LSV, et environ 4 muons par jour à traverser le TPC LAr.

3.2 Résultats sur les WIMPs de haute masse

Les derniers résultats de DarkSide proviennent d'une analyse en aveugle réalisée sur 532.4 jours de données en temps réel. L'objectif de l'analyse en aveugle est de réduire les biais non intentionnels d'un résultat dans une direction donnée. Il existe plusieurs techniques d'analyse en l'aveugle pour la physique des particules, et il est important de choisir correctement celle qui correspond à une recherche particulière. La technique *hidden signal box* choisie par DarkSide convient bien aux recherches d'événements rares, où la région du signal est connue à l'avance [114].

Dans cette technique, une "boîte aveugle" est définie, masquant les événements entrant dans la région du signal. La boîte est généralement choisie pour être plus grande que la région du signal, afin d'empêcher un biais dans le choix des coupes de signal finales. Une fois les sélections coupées et les estimations de bruit de fond finalisées, la boîte est ouverte et les limites d'exclusion peuvent être définies. Nous choisissons un niveau de bruit de fond prédéterminé dans la zone de signalisation WIMP et nous concevons nos découpes en conséquence. Nous avons choisi 0.1 événement de fond attendu comme niveau acceptable, ce qui donne une probabilité de Poisson <10% de voir un ou plusieurs événements de fond dans la région de recherche. Les différents types de bruits de fond ont été estimés séparément, et un jeu de coupures de sélection a été développé pour chacun d'entre eux. Une fois que l'objectif de bruits de fond a été atteint et que la zone de recherche des WIMPs a été définie, nous avons procédé à l'ouverture de la boîte. La figure 18 présente les données complet après les coupes de sélection, la région ombrée en bleu représentant la zone de recherche de WIMPs. Comme il est clairement visible, aucun événement n'a été observé dans la région d'intérêt. Ce résultat sans bruit de fond ni signal est compatible avec un maximum de 2.3 diffusions DM-nucléon attendues (90% C.L.), ce qui fixe une limite supérieure de la section efficace de diffusion indépendante du spin à $1.14 \times 10^{-44} cm^2$) pour $M_{WIMP} = 100GeV/c^2$. La figure 18 compare cette limite à celles obtenues par d'autres expériences.

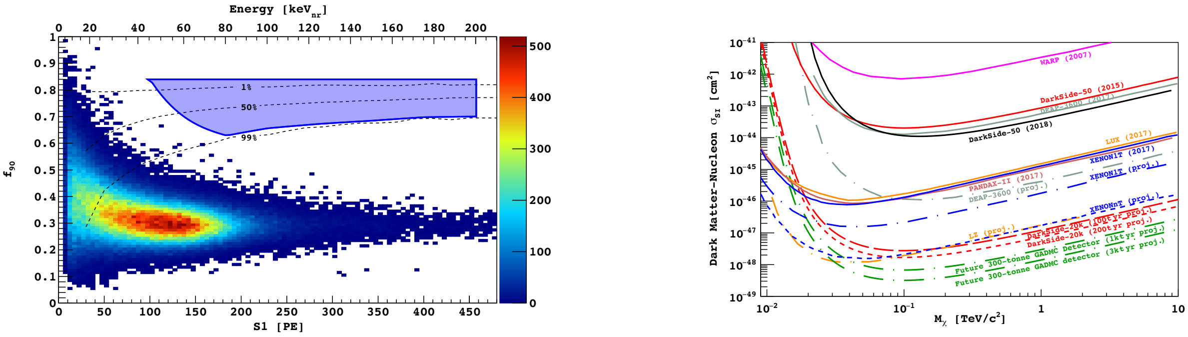

(a) Jeu de données de recherche WIMP final correspondant à 532.4 de prise de données. Le contour bleu indique la région de recherche WIMPs. Les contours d'acceptance 1%, 50% et 99% f_{90} pour les reculs nucléaires, dérivés de nos données de calibtration^{241}AmBe, sont indiqués par les lignes pointillées.

(b) Coupe transversale de DM-nucléon indépendante de la spin 90 % C.L. limites d'exclusion, comparée aux résultats d'autres expériences et projections.

Figure 18

4 Caractérisation de la réponse de l'argon : l'expérience ARIS

Un aspect critique des expériences de recherche de matière noire LAr TPC est la connaissance limitée de la réponse LAr pour les énergies de recul inférieures à 100 keV, à la fois dans les canaux à scintillation et à ionisation et en fonction du champ électrique de dérive. Il est particulièrement important de comprendre l'échelle d'énergie des reculs nucléaires et électroniques, c'est-à-dire de relier l'énergie reconstruite par le détecteur (S1) à l'énergie réelle de recul. Cette relation dépend de différents paramètres, tels que le rendement en photoélectrons, le champ électrique ou le rendement relatif de scintillation entre les contractions nucléaires et électroniques. En particulier, l'effet de la probabilité de recombinaison est non linéaire avec l'énergie de recul et doit être mesuré. Il existe des divergences dans la mesure des paramètres de réponse de LAr à basse énergie, comme l'efficacité relative de scintillation de NR comparée à celle de ER. Ces divergences sont une source énorme de systématique pour les recherches WIMP en LAr.

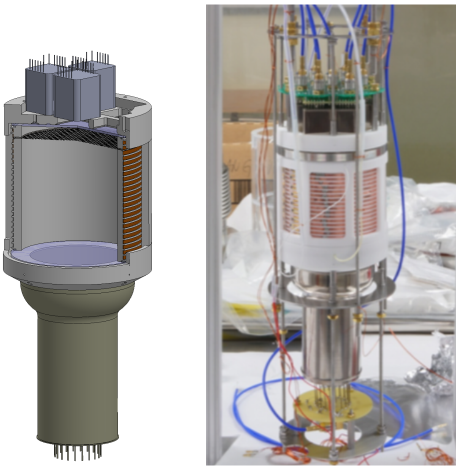

Figure 19 – Left panel: 3D drawing of the TPC. Right panel: picture of the TPC.

4.1 Setup expérimental

La TPC de ARIS a été conçue pour minimiser les interactions multiples des neutrons dans la TPC. La disposition du détecteur a été basée sur celle de DarkSide-50, à une échelle plus petite, comme indiqué sur la figure 19. La masse active $\sim$0.5 kg LAr est logée dans un cylindre en PTFE de 7.6 cm de diamètre, $\sim$1 cm d'épaisseur.

Les photons sont collectés par un PMT R11065 de 3 pouces sous la cathode et par un ensemble de sept PMT R8520 de 1 pouce au-dessus de l'anode. Une fibre optique connectée à une LED, alimentée par un générateur d'impulsions, est utilisée pour étalonner les PMT en régime de photoélectron unique.

Huit détecteurs de neutrons (ND) sont placés autour du TPC pour observer les neutrons dispersés, étiquetés de A0 à A7. Les détecteurs sont des cylindres de 20 cm de diamètre et de 5 cm de hauteur remplis de scintillateur liquide NE213. La PSD est disponible pour le signal ND, fournissant une bonne discrimination neutron/γ. Les distances entre les ND et la TPC vont de 1.3 à 2.5 m, et les angles par rapport à la direction du faisceau vont de 25.5 à 133.1 degrés.

4.1.1 Le faisceau de neutrons LICORNE

Les neutrons ont été fournis par le faisceau LICORNE de l'Institut de physique nucléaire d'Orsay (IPNO). LICORNE produit un faisceau de neutrons très collimé, grâce à la réaction cinématique inverse dans laquelle des ions lourds sont projetés sur une cible de protons (généralement de l'hydrogène). L'accélérateur tandem de l'IPNO fournit un faisceau intense d'ions ^{7}Li, avec des énergies allant de 13 à 17 MeV. L'énergie du noyau ^{7}Li détermine les caractéristiques (énergie et angle d'ouverture du cône) du faisceau produit, comme indiqué sur la figure 20. Toute la campagne ARIS a été réalisée avec une énergie ^{7}Li définie à 14.63 MeV.

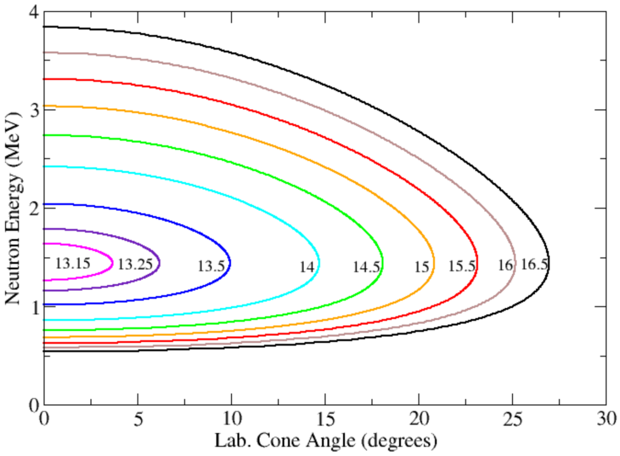

Figure 20 – Kinematic curves of the produced neutrons. Each curve is produced for a different ^{7}Li energy.

4.2 Resultats

Linéarité de la reponse en lumière *Lippincott et al.* [123] ont utilisé différentes sources γ pour mesurer la réponse ER de l'argon liquide. Ils ont observé que le rendement lumineux semblait varier linéairement par rapport à l'énergie des photons γ. Ceci suggère que LAr n'est pas sujet à des effets de *quenching* pour les reculs nucléaires. Cela serait intéressant pour les expériences futures, car cela signifierait que nous pouvons utiliser n'importe quelle source de rayons γ pour calibrer la réponse LAr, sans prêter attention au régime des pics utilisés. En effet, les γs du régime photoélectrique déposent leur énergie en une seule fois, ce qui provoque un seul événement de dispersion dans le TPC, tandis que les γs du régime de Compton se disperseront plusieurs fois dans le TPC. Si le rendement lumineux n'est pas linéaire, cela signifie que le régime des γs aura une incidence sur le rendement lumineux mesuré, faussant les mesures.

Cependant, le résultat de [123] ne repose que sur plusieurs sources de diffusion, comme les rayons γ dans le régime dominé par la diffusion de Compton: aucune mesure directe avec un seul électron n'a encore confirmé la linéarité.

La réponse en lumière, illustrée dans la figure 21, est extraite à partir de γs de différentes énergies: ^{241}Am (59.5 keV), ^{133}Ba (81 et 356 keV) et ^{22}Na (511 keV), ainsi γs de la de-excitation du ^{7}Li* qui subissent une diffusion Compton. Les pics d'absorption complets de 59.5 et 81 keV γs sont dominés par l'effet photoélectrique alors que les interactions 356 et 511 keV γ sont dominées par la diffusion Compton, produisant de multiples électrons de plus basse énergie qui interagissent à leur tour. L'effet d'extinction total pour des γs dans le régime Compton serait alors amplifié par rapport aux événements à diffusion unique.

En étudiant simultanément les points ^{241}Am, ^{133}Ba, ^{22}Na et Compton, la réponse en lumière dans la plage [41,5, 511] keV est constante à 1.6%, comme le montre la figure 21. Ce résultat confirme la linéarité de la réponse de scintillation de LAr au champ nul également observée chez [125] à 2%, en utilisant plusieurs sources de diffusion dans la plage [41.5, 662] keV. Ce résultat suggère que, pour un champ nul, les ER ne sont pas soumis à des effets d'extinction non linéaires.

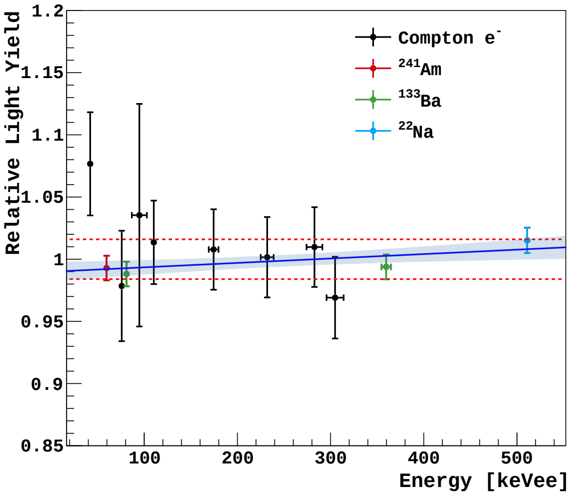

Figure 21 – LY relatif, extrait à partir des γs de la de-excitation du ^{7}Li* et de ^{241}Am (59,5 keV), ^{133}Ba (81 et 356 keV) et ^{22}Na (511 keV). Les points de données sont ajustés avec un polynôme du premier degré (ligne bleue) pour rechercher les déviations par rapport à l'unité. Les lignes rouges en pointillés correspondent à la bande ± 1.6% et contiennent le polynôme ajusté, y compris la déviation à 1 $sigma$(bande bleue), dans la plage [41.5, 511] keV.

La linéarité de la réponse en lumière de l'argon le différencie du xénon, pour lequel une réponse non linéaire aux reculs electroniques a déjà été observée [124].

Quenching des reculs nucléaires Dans le cas de reculs électroniques à champ nul, toute l'énergie déposée est convertie en scintillation. En effet, en l'absence de champ électrique pour les éloigner du site d'interaction, les electrons se recombinent avec les ion d'argon. Mais pour les reculs nucléaires, une densité d'ionisation élevée empêche la recombinaison et réduit le rendement de scintillation. Dans ce cas, l'efficacité de scintillation du recul nucléaire, q_f, est beaucoup plus petite que pour un recul électronique et dépend de l'énergie du recul.

Un bon indicateur de q_f est l'efficacité relative de la scintillation $\mathcal{L}_{eff}$. Elle est définie par rapport à une énergie de recul électronique particulière et représente le rapport de la lumière à scintillation pour un recul nucléaire par rapport à un recul électronique.

La figure 22 montre la mesure de $\mathcal{L}_{eff}$ en fonction de l'énergie des reculs nucléaires, comparée aux mesures précédentes [117, 129, 118] et aux modèles de Lindhard [127] et Mei [**Mei: 2008ca**]. Dans la région ~[20, 60] keV$_{nr}$, tous les ensembles de données concordent, alors que les écarts sont observés en dehors de cette plage. Aux faibles énergies, ARIS fournit une mesure $\mathcal{L}_{eff}$ jusqu'à ~ 7 keV$_{nr}$, l'énergie NR la plus basse de tous les ensembles de données. On remarque aussi que les modèles ne reproduisent pas les données sur l'ensemble de l'intervalle d'énergies considéré.

Probabilité de recombinaison Lorsqu'un champ électrique est appliqué, les électrons libres sont conduits loin du site d'interaction, ce qui diminue la probabilité de recombinaison et affecte donc le signal de scintillation. Il est important de prendre en considération cet effet pour des

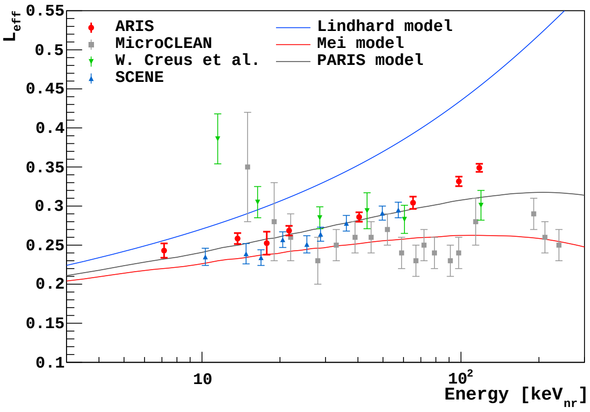

Figure 22 – Variation $\mathcal{L}_{eff}$ en fonction de l'energie des reculs nucléaires mesurée par ARIS, comparée à des mesures précédentes [117, 129, 118] et à des modèles théoriques [127, 128, 130].

détecteurs appliquant un champ électrique pour collecter le signal d'ionisation.

En plus des données de champ nul, ARIS a collecté des données à des champs de dérive de 50, 100, 200 et 500 V/cm.

Dans ARIS, les dépendances de recombinaison de l'énergie équivalente E_{ee} et du champ F de dérive des électrons sont étudiées par rapport à l'observable:

$$\frac{\mathrm{S1}}{\mathrm{S1}_0} = \frac{\alpha + R(E_{ee}, F)}{1+\alpha}, \tag{17}$$

où $\mathrm{S1}_0$ est la réponse à la scintillation dans un champ nul. Dans le cas de reculs nucléaires, $E_{ee} = \mathrm{L}_{eff}\ (\mathrm{E}_{nr}) \times E_{nr}$.

Nous comparons les ratios $\mathrm{S1}/\mathrm{S1}_0$, extraits des données avec les modèles Thomas-Imel [132], Doke-Birks [115] et PARIS (developed by DarkSide).

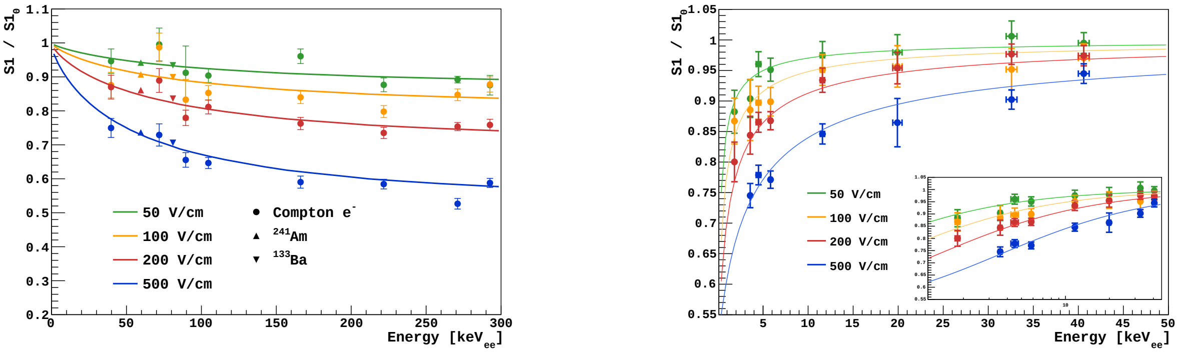

(a) Quenching de S1 pour les ERsinduit par différents champs de dérive comparé au modèle de Doke-Birks.

(b) Quenching de S1 pour les NRsinduit par différents champs de dérive comparé au modèle de Thomas-Imel.

Figure 23 – Quenching de S1 pour les reculs electroniques (gauche) et nucléaires (droite) comparé aux modèles théoriques.

Comme il est visible sur la Figure 23, les modèles théoriques reproduisent correctement les données à différentes valeurs du champs électriques, que ce soit pour les reculs nucléaires ou électroniques. Cependant, il est nécessaire de changer de paramétrisation.

5 Recherche de WIMPs de faible de masse avec DarkSide-50

Les TPCs à liquides nobles ont toujours visé les WIMPs de haute masse [140], la gamme de masse inférieure étant dominée par d'autres technologies telles que les bolomètres. Ceci est principalement dû au fait que, à basse énergie, l'efficacité de détection du signal S1 diminue. La séparation ER/NR donnée par la PSD disparait aussi à basse énergie. Cependant, en abandonnant le signal S1, le gain élevé du signal S2 assure une bonne efficacité de détection jusqu'aux énergies correspondant à un seul électron ($\sim$ 20 eV) extrait dans la phase gaseuse. Une analyse reposant uniquement sur le signal S2 pourrait alors avoir un seuil beaucoup plus bas. Des analyses similaires antérieures ont été effectuées dans des TPC au xénon à double phases [141], démontrant ainsi sa faisabilité de cette méthode et motivant notre recherche.

DarkSide a utilisé le nombre d'électrons, Ne, comme observable pour cette analyse. Toutes les variables d'énergie d'ionisation habituelles, S2, doivent être converties en Ne, ce qui nécessite l'étalonnage du détecteur afin de déterminer l'échelle de conversion d'énergie pour les reculs électroniques et nucléaires.

5.1 Calibration de l'échelle d'énergie

Afin de calibrer la réponse du détecteur, nous devons relier l'observable (S2 ou Ne) à l'énergie de recul. Cela doit être fait en mesurant le rendement d'ionisation, c'est-à-dire le nombre d'électrons produits pour une énergie donnée déposée dans le liquide, en fonction de l'énergie déposée (échelle d'énergie). En raison des effets d'extinction (quenching), les échelles d'énergie seront différentes pour ER et NR. L'échelle d'énergie ER est obtenue en utilisant des pics de ^{37}Ar et de ^{83}Kr comme points d'ancrage. L'échelle NR provient des données d'étalonnage *in-situ* issues des sources de neutrons ^{241}Am^{13}C et AmBe, ainsi que des données de diffusion du faisceau de neutrons provenant des expériences SCENE [117] et ARIS [146].

5.1.1 Echelle des reculs electroniques

L'échelle d'énergie ER est calibrée aux basses énergies grâce à la présence de ^{37}Ar, produite par activation cosmique. ^{37}Ar a une durée de vie de 35.04 jours [147] et se désintègre à 100% par capture électronique [148, 149] vers le ^{37}Cl.

Pour étendre la plage d'énergie de la calibration, un point de ^{83m}Kr a été ajouté aux données. Le ^{83m}Kr métastable se désintègre en ^{83}Kr en deux transitions de 32.1 keV et 9.4 keV [147]. Étant donné que les deux transitions se produisent avec une demi-vie intermédiaire de 154 ns, les deux pics ne sont pas résolus par le détecteur et le spectre ne présente qu'un seul pic à 41.5 keV.

La figure 24 montre le résultat de la calibration.

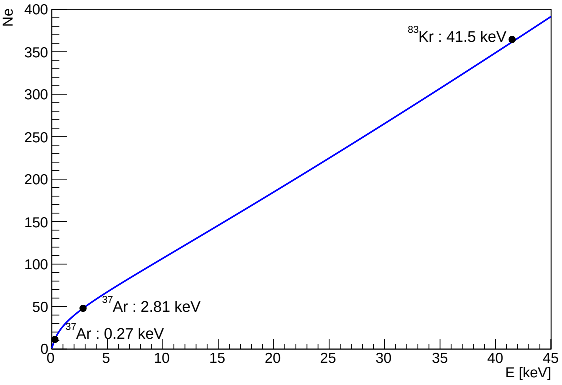

Figure 24 – Échelle d'énergie ER sur la plage d'énergie WIMP de faible masse utilisant les lignes de ^{37} Ar et ^{83m} Kr.

5.1.2 Echelle pour les reculs nucléaires

L'échelle d'énergie des reculs nucléaires a été obtenue à l'aide d'un étalonnage externe et *in situ.*

Les données des expériences ARIS et SCENE ont été utilisées pour calibrer l'échelle d'énergie NR. SCENE a directement mesuré le signal d'ionisation alors qu'ARIS n'avait accès qu'à la scintillation, mais atteignait des énergies inférieures. Le rendement d'ionisation dans ARIS a ensuite été extrapolé relativement à la mesure de S1 dans DS-50 pour ^{83}Kr.

Deux sources de neutrons ont été utilisées pour le calibrage *in-situ* de la réponse d'ionisation aux reculs nucléaires: ^{241}Am^{7}Be et ^{241}Am^{14}C. Les spectres des neutrons des deux sources sont générés avec un simulation Monte-Carlo. L'energie de recul simulée est ensuite convertie en nombre d'électrons Ne utilisant la probabilité de recombinaison de Lindhard-Ziegler-Bezrukov [127, 155, 156].

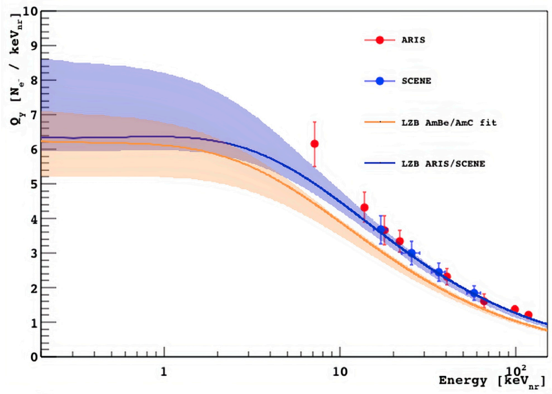

Figure 25 – Energy scale for nuclear recoils extracted from the fit the AmBe/AmC and ARIS/SCENE.

Le spectre simulé est ensuite ajusté aux données, ce qui permet d'extraire les paramètres d'ionisation. La figure 25 montre l'ionisation extraite de la calibration *in-situ* ainsi qu'externe.

5.2 Limites d'exculsion sur les WIMPs de basse masse

La limite sur la section efficace WIMP-nucléon dans la région des WIMPs de basse masse a été obtenue à l'aide d'une méthode de vraisemblance. Les limites obtenues sont présentées en figure 26.

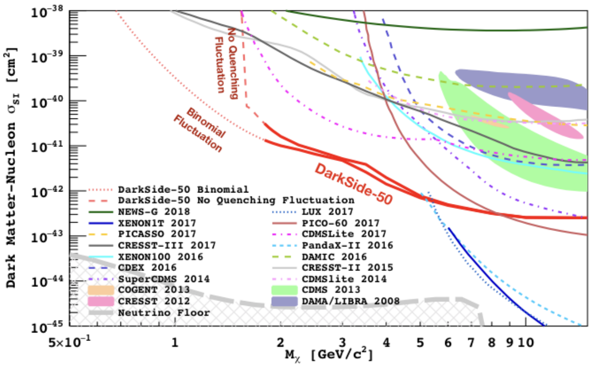

Figure 26 – Limites supérieures (90% C.L) sur la section efficace WIMP-nucléon indépendante du spin de DarkSide-50 dans la plage supérieure à 1.8 GeV/c^2.

6 Recherche d'axions

En l'absence de détection de WIMPs, il est naturel de se tourner vers des candidats alternatifs, comme les axions. La plupart des recherches portent sur leur couplage aux photons, mais récemment, des recherches exploitant le couplage à des électrons ont été effectuées. Le couplage des axions avec les électrons permettrait de les détecter dans les TPCs à liquides nobles, où leurs interactions entraineraient des reculs électroniques.

6.1 Les axions somme solution au problème CP fort

La violation de CP a des conséquences importantes pour la cosmologie. Les théories actuelles de la physique des particules et de la cosmologie prédisent que notre univers s'est formé avec des quantités égales de matière et d'antimatière, qui auraient dû s'annihiler. Cependant, l'Univers est aujourd'hui clairement dominé par la matière. Pour cette expliquer la dominance de la matière, la violation de CP doit exister. Or aucune violation de CP n'a été pour l'instant observé pour l'interaction forte.

Peccei et Quinn [3] ont proposé une solution pour expliquer ce phénomène. La théorie de Peccei-Quinn (PQ) postule l'existence d'une quasi-symétrie globale $U_{PQ}(1)$, c'est-à-dire une symétrie de la théorie au niveau lagrangien (c'est-à-dire classique). Cette symétrie doit être explicitement brisée par les effets non perturbatifs produisant le terme thêta et spontanément brisée à une échelle f_a. Étant une symétrie globale spontanément brisée, il doit exister une particule, l'axion a, associé à $U_{PQ}(1)$.

Plus généralement, on peut envisager des extensions de modèle standard avec de nouvelles symétries globales $\mathcal{U}(1)$ brisées spontanément par un mécanisme (caché) de type Higgs à une échelle de rupture de symétrie v_h beaucoup plus élevée que l'échelle electrofaible. Il est alors possible d'étendre la théorie PQ à d'autres échelles, produisant des particules similaires aux axions. Ces particules peuvent être appelées de manière générique "axion-like particles" (ALPs). La théorie des cordes, par exemple, prédit des ALPs. L'axion est couplé aux hadrons, aux photons et aux leptons avec des forces d'interaction inversement proportionnelles à f_a. Ainsi, les expériences n'ayant pas permis de détecter les axions, les plus petites valeurs de f_a ont été exclues expérimentalement.

6.2 Recherche d'axions dans DarkSide-50

Les recherches directes d'axions dans un détecteur de liquide noble reposent sur l'effet axion-électrique, qui est similaire à l'effet photo-électrique, remplaçant le photon par un axion. En raison de cet effet, une interaction axion ou ALP dans le détecteur entraînerait un recul visible des électrons. L'énergie de recul peut atteindre ~15 keV pour les axions solaires, alors que spectre des axions galactiques culminera autour de la masse de l'axion, étant donné que le halo de matière noire est considéré au repos par rapport à la Terre.

La section efficace axio-électrique est donnée, pour les axions et les ALPs, par:

$$\sigma_{Ae} = \sigma_{pe}(E_A)\frac{g_{Ae}^2}{beta_A}\frac{3E_A^2}{16\pi\alpha_{em}m_e^2}(1-\frac{\beta_A^{2/3}}{3}) \tag{18}$$

où σ_{pe} est la section efficace photoélectrique pour LAr, E_A est l'énergie des axions, α_{em} est la constante de structure fine, m_e est la masse de l'électron, β_A est la vitesse d'axion sur la vitesse de la lumière et et $g_{Ae} = 2m_e/f_a$[1] est la constante de couplage adimensionnelle axion-électron.

6.3 Spectre en energie

Nous générons les spectres axion visibles dans le détecteur en multipliant les flux d'émission par la section efficace axio-électrique.

Le taux d'évènements peut alors être écrit,

$$R[/kg/jour] = \Phi \times 24 * 3600 \times \frac{6\times 10^{23}}{A}\sigma_A(E) \tag{19}$$

avec Φ, le flux d'émission, et A, le numéro atomique de l'argon. Pour les axions solaires, le flux et la section dépendent de g_{Ae}^2, de sorte que le taux d'événements évoluera avec g_{Ae}^4.

Nous incluons ensuite l'influence de la réponse du détecteur. Nous supposons des fluctuations binomiales du nombre d'électrons produits par l'interaction. Nous incluons également la résolution dûe à la réponse des PMT.

Le spectre pour les axions solaires est produit en supposant que $g_{Ae} = 10^{-11}$, tandis que les spectres pour les axions galactiques sont produits en supposant que $g_{Ae} = 10^{-12}$.

La Figure 27 montre les spectres obtenus pour les axions solaires de masse nulle et les axions galactiques dont les masses vont de 1 à 13 keV/c^2.

---

[1] f_a est a force de l'interaction modèle standard-axion

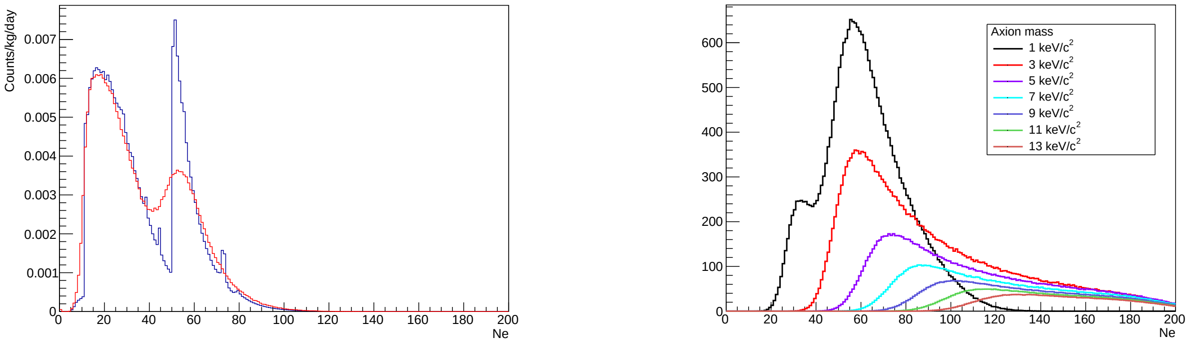

(a) Spectre des axions solaires sans fluctuations (noir), et en ajoutant la réponse du détecteur (rouge). Spectre généré avec $g_{Ae} = 10^{-11}$

(b) Spectre des axions galactiques, assumant $g_{Ae} = 10^{-12}$

Figure 27 – Spectres des axions solaires et galactiques dans DarkSide-50

6.4 Limites d'exclusion

Les données sont ensuite ajustées en utilisant le même cadre d'analyse que pour les WIMPs de basse masse. La recherche de WIMPs de basse masse a utilisé une incertitude de 15% sur la normalisation du bruit de fond. Afin de tenir compte de l'ajustement effectué sur la plage d'analyse des axions, ces incertitudes ont été élargies à 30%.

Nous obtenons une limite supérieure à $g_{Ae} = 4.75 \times 10^{-12}$ pour les axions solaires de masse nulle. L'analyse pour les axions galactiques est encore en développement. À titre d'exemple, je cite ici la limite préliminaire pour des ALPs galactiques de 1 keV/c^2. Pour cette masse, nous excluons les couplages supérieurs à $g_{Ae} = 1.87 \times 10^{-13}$.

7 Conclusions

Les cibles liquides nobles sont extrêmement bien adaptées à la recherche directe de matière sombre et posent les limites les plus strictes sur les WIMPs de haute masse. Parmi les différents éléments nobles disponibles, l'argon se distingue par son pouvoir de discrimination du bruit de fond extraordinaire, grâce à la PSD.

DarkSide-50 a été le premier détecteur à argon liquide à fonctionner avec de l'argon souterrain à faible radioactivité. Les résultats obtenus ont confirmé le potentiel de l'argon liquide pour la recherche WIMP en masse élevée. DarkSide fournit aussi les meilleures limites dans la plage ~ 2 à ~ 6 GeV·c^{-2}. Ce résultat a été rendu possible grâce à l'amélioration de nos connaissances sur la réponse en ionisation de l'argon à basse énergie, fournies par l'étalonnage externe ARIS et les mesures *in situ*.

La dernière partie de cette thèse a été consacrée aux recherches sur les axions dans DarkSide-50. Les axions sont des candidats prometteurs pour la matière sombre. Leur couplage aux électrons permettrait leur détection dans DarkSide. Les résultats préliminaires obtenus sont comparables aux meilleures limites actuelles obtenues avec les détecteurs au xénon. La sensibilité pourrait être améliorée par un raffinement supplémentaire du modèle de bruit de fond. Des études de sensibilité pour les recherches d'axions et d'ALPs dans le DS-20k devraient être menées. D'autres types de matière légère doivent également être envisagés.

Le voyage de DarkSide n'est pas terminé. La prochaine phase de DarkSide, DarkSide-20k, devrait commencer ses activités en 2022. En multipliant la masse cible par 400 par rapport à DarkSide-50, DS-20k augmente la sensibilité aux WIMP de masse élevée de plusieurs ordres de grandeur. Le DS-20k utilisera également des SiPMs pour remplacer les PMTs. Les SiPMs sont moins radioactifs, présentent une meilleure photodétection ainsi qu'une résolution électronique unique.

Toujours dans l'avenir, la Global Argon Dark Matter Collaboration envisage de créer un détecteur de 300 t, Argo, dont les applications pourraient aller au-delà de la recherche de matière noire pour devenir également un observatoire de neutrinos.

Les performances inattendues de l'argon liquide pour les recherches WIMPs de faible masse et les résultats encourageants des axions ouvrent également une nouvelle porte pour les détecteurs à base d'argon liquide. DarkSide a un projet de petite TPC à argon liquide, DarkSide-LowMass, dédiée à la recherche WIMPs de faible masse. D'autres modèles de matière sombre de faible masse pourraient être explorés, comme la matière sombre leptophilique, les photons cachés, etc.